

INTEGRATING MACHINE LEARNING AND WEATHER ANALYTICS  
FOR SIZING VARIABLE GENERATION WITH  
UTILITY-SCALE ENERGY STORAGE

by

Fei Sun, M.S

A dissertation submitted to the Graduate Council of  
Texas State University in partial fulfillment  
of the requirements for the degree of  
Doctor of Philosophy  
with a Major in Materials Science, Engineering, and Commercialization  
May 2021

Committee Members:

Tongdan Jin, Chair

Zhijie Sasha Dong

Tahir Ekin

Byron J Gao

Yijuan Lu

Byoung Hee You

**COPYRIGHT**

by

Fei Sun

2021

## **FAIR USE AND AUTHOR'S PERMISSION STATEMENT**

### **Fair Use**

This work is protected by the Copyright Laws of the United States (Public Law 94-553, section 107). Consistent with fair use as defined in the Copyright Laws, brief quotations from this material are allowed with proper acknowledgement. Use of this material for financial gain without the author's express written permission is not allowed.

### **Duplication Permission**

As the copyright holder of this work I, Fei Sun, refuse permission to copy in excess of the "Fair Use" exemption without my written permission.

## ACKNOWLEDGEMENTS

Foremost, I would like to express my deepest appreciation to my advisor Dr. Tongdan Jin in the Ingram School of Engineering at Texas State University, for giving me the opportunity to work with him. He also provides me with an excellent research atmosphere for me. His support, supervision, and inspiration encourage me to accomplish course work and the dissertation throughout my graduate study at Texas State University.

Besides my advisor, I would like to thank the rest of the committee members: Dr. Zhijie Sasha Dong, Dr. Tahir Ekin, Dr. Byron J Gao, Dr. Yijuan Lu, and Dr. Byoung Hee You for their encouragement, insightful comments, providing me valuable suggestions to improve research. My sincere thanks also go to Dr. Clara Novoa in the Ingram School of Engineering at Texas State University who is always there to provide insightful help and support me in all the time of research. I am extremely grateful to Dr. Irvin in the Materials Science, Engineering, and Commercialization at Texas State University creating great opportunities throughout my school years. I wish to express my appreciation to Ms. Karla M Pizana, Ms. Kelsie L Crumpton, Ms. Sarah D Rivas, and Ms. Carla J Batey for their great assistance in the past years. I would express my appreciation to the National Science Foundation for supporting me under the NSF CBET Grant (No. 1704933).

Last but not least, I would like to thank my husband Dong and my son Zongyan. They are supporting me throughout my life and encouraging me with their best wishes.

## TABLE OF CONTENTS

	<b>Page</b>
ACKNOWLEDGEMENTS .....	iv
LIST OF TABLES .....	ix
LIST OF FIGURES .....	xiii
LIST OF ABBREVIATIONS .....	xvii
ABSTRACT .....	xix
CHAPTER	
1. INTRODUCTION AND LITERATURE REVIEW .....	1
1.1. Introduction.....	1
1.2. Literature Review.....	4
1.2.1. Energy Storage Devices and Materials .....	4
1.2.2. Hybrid Energy Storage System.....	9
1.2.3. Wind and Solar Generation Forecast Models .....	12
1.2.4. Distributed Renewable Generation System .....	19
1.3. System Configuration and Research Methodology .....	22
1.3.1. System Configuration .....	22
1.3.2. Research Methodology .....	24
1.3.3. Outline of Dissertation.....	25
2. CLIMATE DATA ANALYSIS .....	27
2.1. Raw Data and Clean Methodology .....	28
2.1.1. Classify Data Structure .....	29
2.1.2. Remove Redundant Data .....	30
2.1.3. Locate Missing Observations.....	30
2.1.4. Impute Missing Value.....	31
2.2. Climate Data Information .....	33
2.2.1. Wind Speed.....	35
2.2.2. Weather Features .....	43
2.3. Data Transformation .....	45
2.4. Extreme Climate Event .....	46

3. FORECASTING MODEL.....	47
3.1. Research Methodology .....	47
3.2. Artificial Neural Network Forecasting Model.....	50
3.2.1. Topology of FNN.....	51
3.2.2. Backpropagation Algorithm.....	53
3.2.3. Activation Function .....	54
3.3. Performance Evaluation Approaches.....	56
3.4. Wind Speed Forecasting Models and Results.....	58
3.4.1. Persistence Forecasting Model .....	59
3.4.2. ARIMA Forecasting Model .....	59
3.4.3. Hybrid Short-term Forecasting Model.....	64
3.4.4. Short-term Wind Speed Forecasting Result and Comparison ...	65
3.4.5. Deep Learning Long-term Wind Speed Prediction Model .....	74
3.5. Weather Features Forecasting Models and Results .....	76
3.5.1. Markov Model .....	77
3.5.2. Hidden Markov Model.....	79
3.5.3. Recurrent Neural Network Model .....	82
3.5.4. Weather Features Forecasting Results and Comparisons .....	84
4. MATHEMATICAL FUNCTIONS IN MODELS .....	90
4.1. Modeling Wind Turbine Generation .....	91
4.1.1. Wind Source Property.....	92
4.1.2. Mathematics Model of Wind Turbine Generation.....	94
4.1.3. Simulate Generation of Wind Turbine.....	96
4.2. Modeling Solar Panel Generation.....	97
4.2.1. Mathematics Model of Solar Panel Generation .....	97
4.2.2. Simulate Generation of Solar PV .....	104
4.3. Modeling Hybrid Energy Storage System .....	106
4.3.1. Mathematics Model of Lithium-ion Battery .....	108
4.3.2. Mathematics Model of Graphene-based SC .....	109
4.4. Modeling Charging and Discharging Process of HESS .....	110
4.4.1. Mathematical Function in Charging Process .....	111
4.4.2. Mathematical Function in Discharging Process .....	112
4.4.3. State of Charge.....	112
4.4.4. Modeling Cycle Life of Battery .....	113
4.5. Modeling Load Demand .....	113

5. LCOE PROSUMER MODEL .....	116
5.1. Cost Analysis .....	118
5.1.1. Installation Cost .....	118
5.1.2. Operation and Maintenance (O&M) Cost.....	119
5.1.3. Electricity Bill.....	119
5.2. Income Analysis.....	120
5.2.1. Carbon Credit Incentive.....	120
5.2.2. Net Metering Income .....	120
5.3. System Reliability Criterion .....	121
5.4. MLCOE Model .....	122
5.5. Numerical Experiment Results .....	124
6. VPP-BASED MULTI-TIER PRODUCTION INVENTORY MODEL.....	128
6.1. Problem Statement.....	130
6.2. Dispatch Strategy .....	134
6.3. PSC-VPP Optimization Model .....	135
6.3.1. Objective Function.....	135
6.3.2. Production-inventory Constraints .....	136
6.3.3. Energy Demand Constraints .....	137
6.3.4. CHP Constraints.....	139
6.3.5. Capacity Constraints .....	140
6.3.6. Chance Constraint.....	141
6.4. Capacity Factor of WT and PV in Testing Cities .....	141
6.5. Numerical Experiments .....	142
6.5.1. Model Parameters .....	142
6.5.2. Numerical Experiment Result for 2F-1W-2S Network .....	144
6.5.3. Result for Production Planning.....	145
6.5.4. Result for Microgrid Allocation and Scheduling.....	147
6.6. Sensitivity Analysis .....	149
6.6.1. Sensitivity Analysis on Production Planning.....	150
6.6.2. Sensitivity Analysis on Microgrid Allocation .....	151
6.6.3. Sensitivity Analysis on CHP Operation.....	154
6.7. Conclusions of Analysis .....	155
7. BATTERY TECHNOLOGY DEVELOPMENT AND SIMULATION.....	157
7.1. Lithium-ion Electrochemical Energy Storage Device .....	157
7.2. Supercapacitor Energy Storage Device .....	158
7.3. Nanomaterial for SC Electrode.....	160

7.3.1. Graphene and graphene oxide.....	161
7.3.2. Graphene and Metal Oxide Nanocomposite Electrode.....	162
7.3.3. Graphene and CNT Flexible Electrode.....	164
7.4. Simulate Performance of Lithium-ion Battery .....	166
7.5. Commercialization.....	174
7.5.1. Supercapacitor Penetration Rate Forecast .....	174
7.5.2. Li-ion Battery Financial Forecast .....	176
8. CONCLUSIONS AND FUTURE WORK.....	179
8.1. Conclusions.....	179
8.2. Future Studies .....	183
8.2.1. Multi-Objective Optimization Model .....	183
8.2.2. Joint Long- and Short-Term Forecasting Model .....	184
8.2.3. Energy Storage Technology.....	184
APPENDIX SECTION.....	186
REFERENCES .....	201

## LIST OF TABLES

<b>Table</b>	<b>Page</b>
1.1 Mechanical Energy Storage Characteristics and Cost .....	6
1.2 Commercial LIBs Performance .....	7
1.3 Parameters of Various Energy Storage Technologies .....	11
2.1 Summary of Cities Geographic Information.....	27
2.2 Raw Dataset Sample .....	28
2.3 Classes Description in Forecasting Model.....	30
2.4 Cleaning Dataset Sample .....	33
2.5 Summary of Climate Condition on Testing Cities.....	34
2.6 Two-Parameter Weibull Distribution Expression of Wind Speed.....	37
2.7 Statistics for Wind Speed (m/s), Temperature (°C), and Dew Point (°C) .....	42
2.8 Proportion of Weather Features in Testing Cities (%).....	44
2.9 Cloud Fraction in Five States.....	45
2.10 Number of Observations in Training, Validation, and Testing Datasets .....	46
3.1 ARIMA Model Structure for Testing Cities .....	64
3.2 Forecasting Results of ARIMA Model with Five Forecasting Horizons .....	66
3.3 Models with Various Input Features for Wellington .....	68
3.4 Comparisons with Persistence Model in 1-hour Ahead Forecasting .....	70
3.5 Comparisons between Hybrid Model and FNN Model .....	71
3.6 Input Variables for Long-term Deep Learning Prediction Model .....	75

3.7 Performance of Deep Learning Model with Different Layers and Neurons .....	75
3.8 Weather States Summary of Phoenix and New York .....	77
3.9 Random 48-hour of Weather States in Phoenix and New York .....	77
3.10 Comparisons of Different Predictors for Weather States Forecasting Model .....	83
3.11 Confusion Matrix with Threshold Value in Phoenix.....	85
3.12 Confusion Matrix without Threshold Value in Phoenix.....	85
3.13 Forecasting Accuracy over Five Forecasting Horizations .....	86
3.14 Comparisons between 5- and 7-state Model with Seasonal Data.....	87
3.15 Ten-state Weather Features Prediction Result in New York.....	88
3.16 Comparisons among MC,HMM, and ANN Model in Phoenix .....	88
3.17 Comparisons of One-hour Ahead Forecasting Accuracy .....	89
4.1 Parameters of Current Wind Turbine Technologies .....	92
4.2 Wind Speed at Different Height Levels in Wellington.....	94
4.3 2MW GE Wind Turbines Platform.....	96
4.4 Summary of Key Factors that Impact PV Output Power.....	103
4.5 Weather Coefficients under Different States .....	103
4.6 Specifications of PV Module .....	104
4.7 Cost and performance of Energy Storage Devices based on Materials .....	107
4.8 Mean and Standard Deviation of Monthly Load .....	115
5.1 Summary of Climate Conditions .....	116
5.2 Operation Modes of Manufacturer.....	117

5.3 Notation of Parameters .....	117
5.4 Notation of Decision Variables.....	118
5.5 Experimental Results for Case I .....	124
5.6 Experimental Results: Cases I vs. Cases II.....	125
5.7 DoD Impact on Installation Capacity of Devices in Boston.....	126
6.1 Notation of Sets in PSC-VPP Model .....	131
6.2 Notation of Parameters in PSC-VPP Model .....	132
6.3 Notation of Variables in PSC-VPP Model .....	134
6.4 Capacity Factors of WT and PV in Five Cities.....	142
6.5 Weekly Product Demands from Stores.....	142
6.6 Parameters for Production Planning in Model.....	143
6.7 Parameter value in PSC-VPP.....	144
6.8 Production-inventory Cost.....	145
6.9 Size of WT, PV and ESS for the 2F-1W-2S Network.....	147
6.10 Sensitivity Analysis on Production Planning.....	150
6.11 Comparisons of Annual Cost among Cases.....	151
6.12 Size of WT, PV, and ESS from Case 1 to Case 7 .....	152
6.13 Size of WT, PV, and ESS from Case 8 to Case 14.....	153
7.1 Comparisons of Specific Surface Area with EDLC Capacitance .....	161
7.2 Electrode Materials of SCs .....	166
7.3 Notation of Parameters .....	167

7.4 Factors and Levels of Parameters in Model.....171

7.5 Simulation Result Based on Various Levels of Three Factors .....173

7.6 Five Year Cash Flows Statement.....178

## LIST OF FIGURES

Figure	Page
1.1 Graphene Band Structure .....	8
1.2 Rolling of Graphene Sheet into CNT.....	9
1.3 24-h Residential Load Profile and PV Output Power .....	9
1.4 Comparisons of Energy and Power Density of Energy Storage Techniques.....	10
1.5 A Grid-connected Distributed onsite Power Generation System with HESS.....	23
1.6 Operation Strategy of HESS .....	24
2.1 Probability of $B_i$ Given $A$ .....	32
2.2 Weather Climate in Wellington, Phoenix, and San Francisco.....	34
2.3 Wind Portfolios of Testing Cities in 2014 .....	35
2.4 Hourly Wind Speed Density Distribution.....	36
2.5 Monthly Average Wind Speed.....	38
2.6 Diurnal Wind Speed variation .....	39
2.7 Wind Rose of Testing Cities .....	40
2.8 Correlation between Variables.....	41
2.9 Histogram Graph of Weather States in Phoenix and New York .....	43
2.10 Weather States in Four Seasons in Phoenix and New York .....	44
3.1. Scheme of Methodology .....	48
3.2 Multiple Forecasting Horizons .....	49
3.3 Structure of FNN.....	51

3.4 Model Development and Training Process .....	53
3.5 Output Characteristic Curve of Sigmoid Function .....	55
3.6 Output Characteristic Curve of Softmax Function .....	56
3.7 Confusion Matrix for a Two-class Model.....	58
3.8 Real and Differenced Wind Speed Data in a Month of Wellington .....	61
3.9 ACF and PACF of Wind Data in Wellington .....	63
3.10 Flowchart for Construct Proposed Model.....	65
3.11 ARIMA Model Forecasting Result in Wellington.....	67
3.12 Comparisons of Forecasting Models under Different Predictors .....	68
3.13 Structure of Hybrid Wind Speed Forecasting Model .....	70
3.14 Comparisons of 1-hour Ahead Forecasting Models in Wellington .....	71
3.15 Comparisons of RMSE and MAE among Five Models for Three Cities .....	72
3.16 Prediction Intervals in Day-ahead Prediction Models .....	73
3.17 Markov Chain with Two States .....	78
3.18 5×5 States Transition Matrix .....	79
3.19 HMM Model with Two States and Three Observations.....	81
3.20 Emission Matrix with Five States and Ten Observations.....	81
3.21 Comparison of Accuracy among Eight Models.....	83
3.22 Structure of Multi-classification Model.....	84
3.23 Visualization of Forecasting Accuracy .....	86
4.1 Microgrid Power System with HESS .....	91

4.2 Wind Resource Distribution across World .....	93
4.3 Wind Speed Variety with Different Height and Roughness .....	93
4.4 Schematic of Wind Energy Conversion System.....	95
4.5 Wind Turbine Power Curve .....	95
4.6 Hourly Generation of Wind Turbine through 2015 in Boston.....	96
4.7 Surface Downward Solar Irradiance across World.....	97
4.8 Equivalent Circuit of Photovoltaic Cell.....	98
4.9 Solar Irradiance on Solar PV in a Day .....	100
4.10 Solar Irradiance on Jan 1 <sup>st</sup> , 2015 at Phoenix.....	102
4.11 I-U and P-U Curve of the PV Cell under Different Temperatures .....	104
4.12 I-U and P-U Curve of PV Cell under Different Solar Irradiance .....	105
4.13 Hourly Generation of Solar PV through 2015 in Phoenix .....	106
4.14 Wafer Fab Load Profile .....	114
4.15 Simulate Load Demand in a Day .....	115
5.1 Experimental Results: Cases I, III, and IV .....	126
6.1 Block Diagram of VPP .....	131
6.2 Energy, Product, and Transportation Flow across Facilities .....	143
6.3 Production and Inventory Decision of the 2F-1W-2S Network .....	146
6.4 Transportation between Warehouse and Stores of the 2F-1W-2S Network.....	147
6.5 Hourly Energy Transactions in 1 <sup>st</sup> and 3 <sup>rd</sup> Quarter in Factories .....	149
6.6 Status of ES in 24 hours.....	154

6.7 Scheduling CHP Operation Hours in One-year at Facilities. ....	155
7.1 Charging and Discharging Process of Li-ion Battery .....	158
7.2 Schematic of an EDLC .....	158
7.3 Schematic of Two Devices with Different Spacer Thickness .....	162
7.4 Graphitized MWCNT with Varying Foliate Density.....	165
7.5 Discharge Curve Comparison under Various Cycle Numbers .....	170
7.6 Specific Capacity under Various Conditions.....	170
7.7 Voltage Behavior for Various Designs .....	172
7.8 Energy Efficiency under Various Conditions.....	172
7.9 SC Penetration Rate vs. Capacity Cost.....	175
7.10 Cost Ratio (%).....	177
7.11 24-Month Cash Flow .....	177

## LIST OF ABBREVIATIONS

<b>Abbreviation</b>	<b>Description</b>
AI	Artificial Intelligence
ANN	Artificial Neural Network
CAES	Compressed Air Energy Storage
LCOE	Levelized Cost of Energy
CDF	Cumulative Distribution Function
CHP	Combine Heat and Power
CRF	Capital Recovery Factor
DG	Distributed Generation
DOD	Depth of Discharging
EDLC	Electrical Double Layer Capacitors
ES	Energy Storage
HESS	Hybrid Energy Storage System
LIB	Lithium-ion Battery
MIP	Mixed Integer Programming
O&M	Operation & Maintenance
PDF	Probability Density Function
PPA	Power Purchase Agreement
PV	Solar Photovoltaic Panel
PSC	Product Supply Chain

RNN	Recurrent Neural Network
SC	Supercapacitor
TS	Thermal Storage
VPP	Virtual Power Plant
WT	Wind Turbine

## **ABSTRACT**

To reverse climate change, both manufacturing and power sectors are undergoing a paradigm change by integrating renewable energy for sustainability operations. The goal of this study is to model and design a cost-effective, eco-friendly microgrid system to meet the uncertain load of large industrial and commercial users. The microgrid consists of wind turbines, solar photovoltaics, utility-scale hybrid energy storage system (HESS), and feed-in tariff program. HESS comprises the battery and supercapacitor made by lithium-ion and graphene materials, respectively.

First, hybrid forecasting models combining multi-layer neural network and statistical inference are developed to predict the wind speed and weather states. The proposed models are implemented in six US cities with diverse climate profiles. The results show that proposed models outperform time series models in 3-to-24 hours ahead of wind speed forecasting by reducing 20 percent error. The weather state model shows yearly forecasting outperforms season-based prediction. A stochastic optimization program is further proposed to minimize the levelized cost of energy based on estimated power capacity factor. Finally, a virtual power plant system accommodating both electricity and thermal generation is proposed to minimize the operation cost of a three-tier supply chain network. Various uncertainties are considered, including random power demand, time-of-use rate, government incentives, and the loss of load probability. Through sensitivity analysis, it is found the optimal sizing of renewable generators and lithium-ion battery is not only correlated with the climate conditions, but also depends on

time-of-use rate and reliability criteria.

Design of experiments is applied to investigate the capacity fade degree with three levels of factors: state of charge, the porosity of positive electrode, and the particle radius size of positive active electrode material. Simulation results show lithium-ion battery yields a better performance when the positive active electrode material has a smaller size, while the porosity of positive electrode and state of charge are at a high level. In conclusion, Lithium-ion battery and graphene-based supercapacitor are the promising technology due to their declining cost and improving performance. The study shows that the distributed generation with utility-scale HESS is cost-effective in the long term and enhances power resilience against extreme weather.

**Keywords:** Lithium-ion Battery, Graphene-based Supercapacitor, Hybrid Energy Storage System, Multi-layer Neural Network, Levelized Cost of Energy, Virtual Power Plant.

# 1. INTRODUCTION AND LITERATURE REVIEW

## 1.1 Introduction

To attain a sustainable future for the world, many manufacturing firms have adopted renewable energy in their daily business operations, including production, warehousing, transportation, and logistics. With heavy power demand and environmental effects, energy-intensive industries are striving to reduce energy costs by embracing renewable power through onsite or distributed generation. Hence, designing sustainable products and providing eco-friendly services become the goal for worldwide enterprises.

For the reasons stated above, one promising solution is to power manufacturing facilities with onsite renewable energy. Due to technological advancement, solar and wind generation have become economically viable technologies as onsite power generators. The renewable energy used by the industrial facilities can be generated by rooftop solar photovoltaic (PV) arrays, backyard wind turbines (WT), biogas fuel cells, or other distributed renewable resources. According to IEA (2020), the major large industry worldwide will be powered by 20 - 40% renewable energy by 2030. At present there are two renewable energy solutions adopted by manufacturing sectors: 1) onsite renewable generators; and 2) power purchase agreement contract.

The research solves the problem of minimizing the levelized cost of energy (LCOE) as well as maximizing the reliability of power systems. The scheme is focused on discussing the system planning method and the implementation procedure. Three phrases are designed to assist in achieving the goals: 1) analyzing big data; 2) constructing forecasting models; and 3) applying forecasting value in the models to minimize the LCOE by integrated hybrid energy storage system and operation cost in

three-tires production supply chain.

The capacity of WT, solar PV, and hybrid energy storage devices are the decision variables in the model, and their values are influenced by the facility size, load demand, geographical location, and local climate conditions. Accurate forecasting of wind speed and weather features is important for optimizing the capital investment and the reliability of the distributed power system. The historic weather data information retrieved from the database over one decade is used to predict the wind speed and weather features, then the forecasting result is used to estimate capacity factor of renewable generators. The hybrid model, combined with the feedforward artificial neural network (FNN) and time series model of autoregressive integrated moving average (ARIMA), is employed to forecast the wind speed and weather features. The forecasting result has a significant economic impact on operating an integrated renewable generation system. It also can substantially reduce the lifecycle costs of the energy storage system.

To enhance power resilience against extreme weather events, a HESS comprised of supercapacitor (SC) and lithium-ion battery (LIB) is integrated into the microgrid power system. SC is designed to meet the fast charging-discharging power requirement due to its high-power density and excellent cycling stability. LIB is adopted to meet the large-scale capacity requirement due to its high energy density. A hybrid energy storage method plays an important role in balancing the gap of power response and energy duration. It also helps to create a more flexible and reliable power system. The capacity of the SC and LIB will be optimized based on the output of renewable generation, power demand, and loss of power supply probability criterion (LPSP).

Multiple factors need to be considered in the future, such as building a multi-stage

recourse stochastic model by considering the operation pattern of the manufacturing and load demand. Reducing missing data effect and deploying advanced prediction models is to enhance the forecasting accuracy of wind speed and weather features. In this study, the input attributes for the proposed model are also investigated in terms of the root of mean squared error (RMSE) and mean absolute error (MAE).

The system costs include the capacity installation, maintenance and operation, and the utility bills. Meanwhile, green energy incentives such as carbon credit and feed-in-tariff programs will be subtracted from the system cost. A large linear mixed-integer mathematical programming model is formulated to minimize system cost. The simulation programs are developed to mimic intermittent power output of WT and PV generation in representative cities according to the forecast value of wind speed and weather states, respectively. In addition, the LCOE will be computed in each testing city with diverse climate profiles, which gives additional information about renewable energy costs for manufacturers in those corresponding areas. It is anticipated that the results of weights and biases configuration post the training process leading to the minimum output error. The proposed forecast model will be tested by evaluating the performance using various input features, number of hidden layers, and neurons in each hidden layer. The performance of the proposed method will also be compared with existing forecasting strategies.

The study will provide the solutions for the following questions:

- 1). Minimizing the LCOE and annual operation cost of renewable DG system, respectively.
- 2). Optimizing size of WT, solar PV, and HESS in each location under power

supply reliability criteria.

3). Constructing appropriate wind speed and weather feature forecast models based on big data analysis and machine learning algorithm.

## **1.2 Literature Review**

Renewable energy resources include solar, wind, tides, biomass, and geothermal heat. All of these are considered as alternatives to replacing conventional coal, gas, and oil. Both wind power and solar energy are the two main alternative energy resources among them. The main challenge to harness renewable energy as the power supply is its intermittent and uncertain generation. The output is impacted by climate conditions, such as wind speed, wind speed direction, weather features, or temperature. Thus, forecasting models with higher accuracy of wind speed and weather features can assist the integration of renewable power systems in both public and private sectors. The literature review is divided into four parts to survey the current research. The first part reviews the material and structure of the current energy storage devices. The second subsection explores a retrospective analysis of the current electrical storage system in a renewable power system. The third subsection reviews the prediction methodologies for the time series climate data. The fourth part focuses on constructing mathematical models and optimization algorithm for an onsite renewable power system.

### **1.2.1 Energy Storage Devices and Materials**

The electrical energy storage device converts electrical energy into another form that can be stored and releases the stored energy when it is desired. In brief, global storage power capacity was 4.67 TWh in 2017. The capacity will reach approximately 11.89-15.72 TWh in 2030 (Ralon et al., 2017). The energy storage device demonstrates

multiple functions through mitigating intermittency of the renewable generation system, improving the quality and reliability of power supply, meeting peak demands, and supporting smart grid operation. This research will focus on the application of the energy storage devices in microgrid, i.e., the onsite renewable power system. Available large-scale applications of energy storage technologies can be divided into four categories: kinetic energy (flywheels or compressed air), chemical energy (batteries), gravitational potential energy (pumped hydroelectric), and energy in the form of electrical (capacitors) and magnetic fields.

According to the US Energy Information Administration (EIA, 2020), existing grid-scale energy storage is dominated by pumped hydroelectric, around 99% in capacity. The rest of the installed storage capacity worldwide is nearly 127 GW composed by compressed air (440 MW), sodium-sulfur (304 MW), lithium-ion (100 MW), lead-acid (70 MW), nickel-cadmium (27 MW), and flywheel (25 MW). However, pumped hydro has very low energy density, and the amount of delivered energy is limited by constructing volume. In addition, pumped hydro is not a cost-effective technology due to requiring both a huge area and the proper terrain to store water. The capital cost is \$5,595/kW and the fixed operations and maintenance (O&M) cost is \$13.03/kW for a 250 MW pumped hydroelectric plant.

Compressed air energy storage (CAES) is a relatively mature technology. The first CAES facility was installed in Huntorf, Germany in 1978 (DOE, 2017). It is used to store off-peak baseload energy from a nuclear power plant. Currently, this facility has been used to level variable power from integrated wind energy. The second CAES facility was built in 1991 and located in McIntosh, Alabama. Flywheel has large up-front

costs, which is in the range of \$7,800 to 8,800/kWh for a 5 MWh capacity facility. Table 1.1 summarizes the technology parameters and cost of three main mechanical energy storage devices.

Table 1.1: Mechanical Energy Storage Characteristics and Cost (EIA, 2016).

Metric	Unit	Pumped Hydro	Compress Air	Flywheel
Specific Energy	Wh/kg	0.30~1.33	3.2~60	100~200
Energy Density	kWh/m <sup>3</sup>	0.5~1.33	2~6	20~80
Specific Power	kW/kg	10~120	2.2~24	~1.2
Power Density	kW/m <sup>3</sup>	0.01~0.12	0.04~10	~
Energy Capacity cost	\$/kWh	250~430	390~430	7,800~8,800
Power Capacity cost	\$/kW	1,500~2,700	1,900~2,350	1950~2,200
Life Cycle	Cycles	>10,000	>10,000	>100,000

Lithium-based battery technology was commercially introduced by Sony in the early 1990s based on the use of lithium intercalation compounds. According to the Lithium-Ion Battery Market report, the global market will be worth \$152.3 billion for the rechargeable Lithium-ion battery (LIB) by 2025 and will continue to grow by 16.4% every year. LIB is commonly used as the power supply device for consumer electronics. Moving forward, the market expansion shifts from consumer electronics applications to electric vehicle and industrial applications for storing renewable energy. Since 2000, LIB has become a popular choice, however, it is still considered a less mature technology compared with lead-acid batteries which are cost-competitive. Based on the research from National Renewable Energy Laboratory, the price of LIB is projected to drop below \$100/kWh by 2030, as opposed to the current cost of \$200-300/kWh.

LIB is applied for the areas that have high requirements in the response time,

weight, and cycle efficiencies (e.g., milliseconds response time, 1500-10,000 W/L, 75-200Wh/kg, 150-2000W/kg, up to 97%) (Chen et al., 2009). LIB needs a computer to manage the operation process due to the depth of discharging impacting the battery lifetime, hence increasing the overall cost of LIB.

Table 1.2: Commercial LIBs Performance (Hesse et al., 2017).

Parameter	Unit	LIB Cell Data Sheet Values			
Cell Identification	-	SDI94Ah	NCR18650B	US26650FTC1	SCiB Titanate
Manufacturer	-	Samsung	Panasonic	Murata	Toshiba
Cell Chemistry	-	NMC:C	NCA:C	LFP:C	MO <sub>x</sub> :LTO
Cell Format	-	Prismatic	Cylindrical	Cylindrical	Prismatic
Cell Capacity	Ah	94.0	3.2	3.0	20
Vol. Energy Density	Wh/L	355	676	278	177
Cont. Power Cap.(DCH/CH)	C-rate	3C/1C	2C/0.5C	6C/1C	8C/>3C
Cycle Life(80% SOH)	FEC	>5.000	320	>6.000	10.0
Voltage Range	V	2.70-4.15	2.50-4.20	2.0-3.6	1.5-2.7
Normal Voltage	V	3.7	3.6	3.2	2.3

Some researchers focus on increasing power capacity and specific energy by developing nanoscale electrode materials and electrolyte solutions. The relationship between materials and LIB performance is listed as follows: 1) the difference between the oxidation reduction potential of the positive and negative electrode becomes the operating voltage, which means the operating voltage of LIB is determined by the materials of cathode and anode; 2) power density and energy density are also determined by the materials of electrodes; 3) safety is impacted by the material of electrolytes; and 4) the battery life span is correlated with the type of cathode material in term of performance degradation. Table 1.2 lists LIB performance based on the cell material composite and manufacturers.

The supercapacitor (SC) is a novel energy storage device that can be applied in many fields due to its long-life cycle (over 10<sup>5</sup> times charging-discharging cycles), high

specific power density, and fast charging-discharging process (Zhang et al., 2010).

Graphene (GR) becomes the most promising material for energy storage due to the high surface area and electrical conductance. GR is a single, tightly packed layer of carbon atoms that are bonded together in a hexagonal honeycomb lattice. In 2004, GR was first prepared by micromechanical cleavage from graphite flakes. Its specific area is  $2,630 \text{ m}^2/\text{g}$ . It is a zero-overlap semimetal with very high electrical conductivity as shown in Figure 1.1.

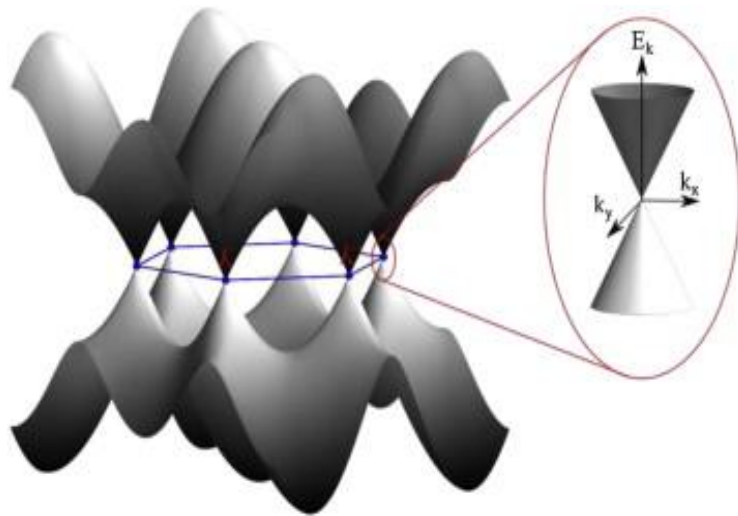


Figure 1.1: Graphene Band Structure (Rao and Sood, 2013)

GR/CNT (carbon nanotube) film shows unique electrical and mechanical properties as well as high stability in electrolyte due to the properties of GR. In fact, CNT can be made by rolling up a sheet of GR into a cylinder as shown in Figure 1.2. The hollow tubes have a diameter in the nanometer range and the length usually at the micro-scale. Based on the number of tube walls, CNT can be classified into single-walled CNT and multi-walled CNT.

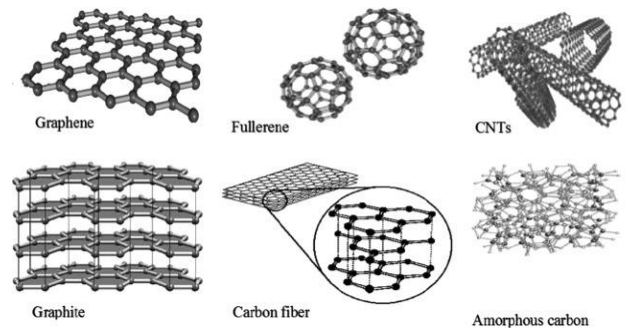


Figure 1.2: Rolling of Graphene Sheet into CNT (Hanaei et al., 2016).

### 1.2.2 Hybrid Energy Storage System

Due to the intermittent generation of renewable technologies, the uncertain load, and the dynamic energy pricing, energy storage devices (battery, supercapacitor, pump hydro, etc.) are usually installed to overcome these challenges. The energy storage device acts as a load when energy is stored (e.g., in charging process), while acts as an electrical resource when the energy is returned to the consumer (e.g., in discharging process).

Renewable power generation and the load profile are important factors to determine the capacity and type of the energy storage components. Figure 1.3, originally from Zhou et al. (2011), depicts the load profile curve and the variation of output curve.

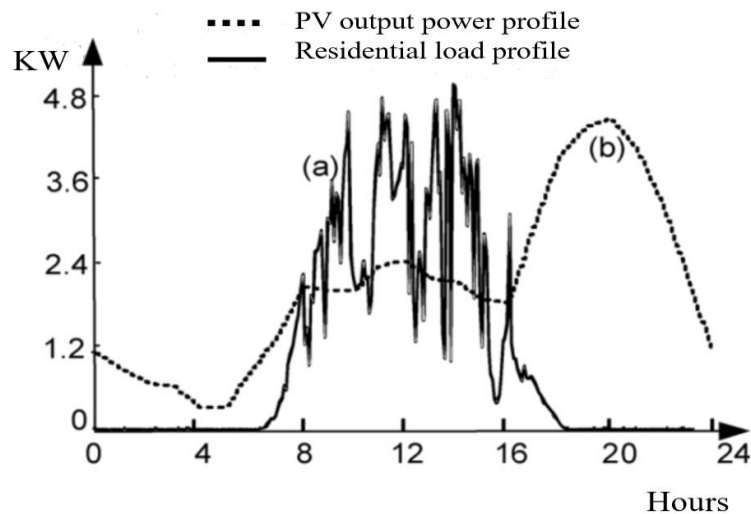


Figure 1.3: 24-h Residential Load Profile and PV Output Power.

The power fluctuation is decomposed into a high-frequency component and a low-frequency component. The hybrid energy storage devices are adopted to smooth the power fluctuation according to its own response characteristics and storage property. There are a few related discussions on how to select appropriate energy storage technologies for utility-scale applications.

Hadjipaschalis et al. (2009) present a review article concentrating on several energy storage technologies and provide an insightful analysis of advanced materials for several devices, i.e., battery, supercapacitor, superconducting magnetic energy storage, and flywheel. Chen et al. (2009) provide a well-organized, comprehensive, and critical review on progress in energy storage systems, which covers various types of storage technologies with their applications and deployment status. Figure 1.4 plots multiple storage devices in the current market.

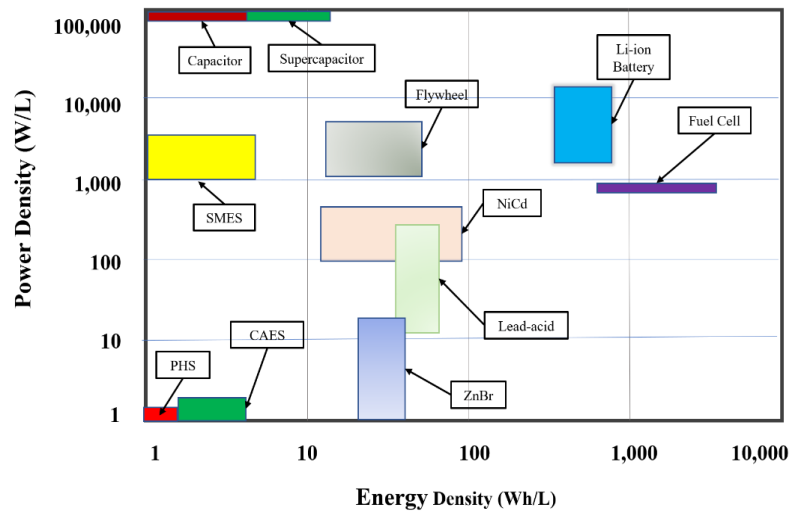


Figure 1.4: Comparisons of Energy and Power Density of Energy Storage Techniques.

Table 1.3 lists the characteristics and performance of both energy type and power type storage devices, including energy density, power density, investment cost, cycle time, and response speed.

Table 1.3: Parameters of Various Energy Storage Technologies.

Energy Storage Device Type		Energy Density (kWh/m <sup>3</sup> )	Power Density (kW/m <sup>3</sup> )	Investment Cost (\$/kWh)	Cycle Times	Response Speed
Energy type	Li-ion battery	94~500	56~800	100~4,000	10 <sup>3</sup>	medium
	Lead-acid battery	25~90	10~400	50~1,200	10 <sup>3</sup>	medium
	Alkaline battery	360~400	12~100	100~1,000	200	medium
Power type	Supercapacitor	3~50	0~10,000	1,000~10,000	10 <sup>5</sup>	milliseconds
	Flywheel	0.25~424	40~2,000	200~150,000	10 <sup>6</sup>	Fast

It is obvious that these two types of energy storage devices are complementary to each other. A hybrid storage system can provide enhanced power supply capability. Hence, a hybrid energy storage system is chosen to be proposed in this study. Glavin et al. (2008) show that hybrid energy storage performs better than battery storage alone for a stand-alone PV system. Dougal et al. (2002) analytically demonstrate hybrid energy storage can extend battery life. Based on these studies, a conclusion can be drawn that the capacity of energy type devices must be oversized in order to meet the peak load demand, if the storage system only has a battery unit; on the other side, the capacity of power type device also has to be oversized for storing a sufficient amount of energy if the system only adopts the supercapacitor.

Currently, the study on the optimal capacity of the hybrid energy storage system (HESS) under wind and solar generation is inadequate. Navaeefard et al. (2010) obtain the global optimal solution for capacity cost. The uncertainty of wind energy and reliability index are considered as system constraints in their work. Mohammadi et al. (2012) optimize the microgrid cost, which includes electricity bill, operation and maintenance cost, and production cost for microgrid units.

### 1.2.3 Wind and Solar Generation Forecast Models

The WT or solar PV generation forecast model is normally based on two approaches, i.e., the direct method and the indirect method (Gao et.al., 2019). The historical power output data is used as input variables of the model that directly forecast power output, called a direct method. In the indirect method, the output of the model is meteorological variables, such as wind speed and weather condition, which impact the generation of the renewable system. The renewable generation is estimated through the forecasted value of meteorological variables. Currently, researchers have been studying on forecasting wind speed or sunshine intensity for a long period, which have been widely applied in agricultural production, construction, and estimating the generation of WT and solar PV.

The forecasting model can be classified into two types based on the data type of output: the regression model and classification model. The dependent variables are the numerical or categorical, respectively. The wind forecasting model belongs to the former because the output is a continuous value. The weather feature forecasting model belongs to the classification problem and the output is a discrete value or called categorical data.

Based on the forecasting strategy, the weather forecasting techniques can be classified into four types: 1) physical method, 2) statistical model, 3) artificial intelligence model, and 4) hybrid forecasting method (Lei et al., 2009; Costa et al., 2008). A physical method is usually used to establish a rigorous mathematical model based on the principles of geophysical fluid dynamics and thermodynamics. The numerical weather prediction (NWP) model is one type of physical model that can generate satisfactory results for a relatively long prediction horizon up to several days. Carvalho et

al. (2012) point out NWP requires a considerable amount of computational time due to the complex mathematical formula that typically needs topography information. Hence, NWP is often used by meteorologists for long-term weather prediction in a large-scale area. However, the model does not guarantee the accuracy in short-term prediction.

The physical model for wind prediction is usually built upon meteorological features (e.g., temperature, pressure, and humidity) and geographical information (e.g., surface roughness and latitude). Both Ren et al. (2014) and Zhang et al. (2016) utilize sophisticated meteorological data for wind speed and wind generation prediction. Due to the complexity in mathematical formulas, a considerable amount of computational time is often required.

Weather Research and Forecast Model (WRF) is one of the most popular NWP approaches. It has been used to forecast air chemistry, hydrology, wildland fires, hurricanes, and regional climate (Powers et al., 2017). For instance, Carvalho et al. (2012) apply the WRF model in an area of Portugal under different numerical and physical options. The area contains complex terrain and is characterized by significant wind energy resources. However, WRF usually requires large and detailed terrain information in order to achieve better performance. As pointed by Wu and Hong (2007), NWP models including WRF have two drawbacks. First, they do not update the predictions very frequently. Second, they require a large amount of computing resources.

Statistical models can explicitly reveal the linear relation between the input and output variables. The simplest time series forecasting model, called persistence forecast, predicts the future weather as the same as the present conditions, which would quickly forecast weather events for short-term prediction. Time series models, including the

autoregressive integrated moving average (ARIMA) family, are widely used in forecasting time series data (Ziel et al., 2016).

Studies show that the performance of statistical models often exceeds NWP in short-term prediction. For instance, Kavasseri and Seetharaman (2009) propose a fractional-ARIMA model to predict the wind speed in one- or two-day ahead horizon, respectively. The expected wind energy throughput is further derived from the predicted wind speed along with the power curve of the wind turbine. Fang and Chiang (2016) derive a multivariate wind power prediction model that accommodates multiple weather features. The forecasting accuracy is further improved by considering the interdependency of different features.

In general, time series models, such as ARIMA, perform well for the short-term prediction due to the use of Box-Jenkins methodology for model construction. The limitation is that the model structure is linear, hence the accuracy is not guaranteed in the long-term prediction (Barbounis et al., 2006 and Senjyu et al., 2006). In addition, the trend and seasonal factors in the time series data need to be decomposed before the model is applied. Since the model structure is limited to the linear form, statistical models become less effective in handling data with large variations.

Most of the statistical models also assume the data follows certain predefined distributions, such as normal or the Weibull. Considering the existence of nonlinearity in time series data, research interests are shifting towards artificial intelligence (AI) and machine learning algorithms. AI techniques such as artificial neural network (ANN) and support vector machine are also adopted to forecast time series data, like wind speed.

ANN has been considered as a powerful tool to solve non-linear problems and

differs from physical and statistical methods, because it can learn the input-output relation from historical data, recognize hidden patterns based on past observations, and use them to forecast future values. ANN (Mohandes et al., 2004) model can also tolerate data errors and ease in adaptability to online measurements. Therefore, AI-based prediction methods turn out to be more capable of handling the non-linear relation with no assumptions on the statistical distribution of underlying data. However, ANN could become computationally intensive as the number of neurons or hidden layers increase. Another limitation of an ANN model is that it needs to be trained by a large data set to achieve the minimum forecasting error. Otherwise, the performance goal or accuracy becomes difficult to achieve if no sufficient training data are available.

ANN can easily accommodate different meteorological features, such as air pressure, temperature, and dew point to improve the wind forecast accuracy. For instance, Li et al. (2001) utilize a three-layer model with 4-, 8-, and 1-neuron for input, hidden, and output layers to estimate wind power. The four inputs are the wind speed and wind directions from two meteorological towers records, respectively. Mabel and Fernandez (2008) use wind speed, relative humidity, and hourly generation as input variables to construct an ANN wind speed model. They claim that better performance is obtained by incorporating additional climate conditions. Peng et al. (2013) propose prediction method for short-term wind power generation forecasting by considering temperature, wind speed, and wind direction features. The study concludes that the model yields more accurate result than the ANN model with a single feature.

Feedforward neural network (FNN) is a classical multi-layer perceptron (MLP) neural network consisted of an input layer, an output layer, and one or more hidden

layers. Each node in hidden layers is fully connected to the input layer connections and output layer connections. The neurons in the same layer are mutually independent, and each neuron has a transfer function. Based on multi-layer perceptron and nonlinear autoregressive exogenous model with multivariable features, Amellas et al. (2020) predict the short-term wind speed. The model aims to assist wind farms and utilities in maximizing the economic benefits. The studies by Khashei et al. (2010) indicate that FNN is more effective than the statistical prediction techniques, especially for input data with non-linearity relation. Wang et al. (2017) utilize deep learning-based ensemble approach for probabilistic wind power forecasting. Convolutional neural network is designed for probabilistic wind power forecasting.

Hybrid approach combines any two methodologies from the physical method, statistical, or AI method in the predicted procedure to obtain a better forecasting performance with reduced error. To combine the advantages of AI-based algorithm and statistical method, Cadenas and Rivera (2010) propose a hybrid forecasting approach that consists of a time series model and FNN model. The former characterizes the linear component and the latter captures the nonlinear relation between the input and the output data. However, most hybrid models ignore the impact from the other climate features, such as air pressure, humidity, and temperature. They are often suitable to one-step ahead forecasting.

Liu et al. (2012) design hybrid ARIMA-ANN and ARIMA-Kalman methods for hourly wind speed forecasting. Both methods result in good prediction and can effectively handle the dynamics of the wind profile. Damousis et al. (2004) dominate a genetic algorithm-based learning scheme to predict the wind speed and power generation

at a wind park. Their model focuses on short-term forecasting in a range from 0.5-hour to 2-hour ahead. Comparative studies are also carried out between ANN and time series model. Zhou et al. (2019) propose a hybrid wind forecasting method comprised of four modules: data analysis, model selection, multi-criteria forecasting, and performance evaluation. Their approach allows for selecting an optimal forecasting model given a set of wind speed data without prior knowledge.

For a solar PV system, the solar irradiance received by the PV array is generally impacted by many other meteorological impact factors, such as temperature, latitude of location, and weather features. The climate data, such as temperature, dew point, humidity, visibility, wind speed, and weather features, are available from most of the weather forecast portals, while the irradiance forecasting data are often unavailable. In the current research, a variety of models have been proposed to forecast the generation of solar PV based on the predicted value of the solar irradiance (Dong et.al., 2020; Kamadinata et al., 2019). However, for a known location, the amount of solar irradiation is a known value when the tilt angle of the solar PV panel, the time of day, and the latitude of location are given (Pham et al., 2019).

The weather feature is the main factor to affect the generation of a solar system. Weather feature causes the various cloud coverage, such as "clear" or "cloudy". The weather feature forecasting model is the typical classification model. Currently, there are multiples Algorithms, such as statistic model, support vector machine, and machine learning model that are working on the classification problem. Based on the level of outputs, the classification can be classified into the binary model and multinomial model. The dependent variable only has two levels in the former model. The outputs have more

than two levels in the latter model. Each level would be assigned a probability between 0 and 1, with the sum equals to one.

The logistic regression model, Markov chain model (MC), and hidden Markov model (HMM) are the statistic models. Sanjari and Gooi (2016) design a higher-order MC that describes a stochastic process that may characterize a system at any horizon. HMM provides a probabilistic framework with a fixed number of states for multivariate observations. In recent years researchers proposed HMM as a classifier or predictor for speech recognition (Palaz et al., 2019), DNA sequence analysis (Huang et al., 2017), handwritten character recognition (Wang et al., 2020), etc. Analysis of HMM seeks to recover the sequence of states from the observed data. This model hinges on the estimation of transition and emission probabilities.

AI-based techniques have been applied for the classification forecasting model, such as fuzzy logic method, support vector machine, ANN, and hybrid method (Notton et al., 2019). Shi et al. (2012) apply a support vector machine (SVM) method to build a forecasting model based on the four types of weather features (clear sky, cloudy day, foggy day, and rainy day). Yang et al. (2014) present an alternative approach combining a self-organizing map, a learning vector quantization network, and fuzzy inference approach to make 1-day ahead hourly forecasting of PV power generation based on three types of weather features (sunny, cloudy, and rainy), but three types of weather states cannot represent all the possible cases for the weather features.

The multi-output forecasting strategy involves the development of the multi-step forecasting model that can predict a sequence of outputs in a one-shot manner. Kline et al. (2004) construct a multi-output neural network where each output node corresponds to

one prediction horizon. This approach can prevent the accumulation of prediction errors and avoid performance degradation as the forecasting horizon increases. Zhang (1998) deploys an ANN model for multi-period time series forecasting and concludes that the direct method produces better results than the recursive strategy. In their paper, the proposed model can perform multi-output forecasting, hence capturing the dynamic behavior of future wind speed and weather state. This is crucial for improving the security and economic benefit of renewable generation system.

#### 1.2.4 Distributed Renewable Generation System

The distributed generation (DG) system produces alternative and environmentally benign electricity onsite where the generated energy is consumed by the local users. Distributed renewable power systems can take many forms, including WT, solar PV, energy storage devices, combined heat and power, and micro-hydroelectric, fuel cells, and geothermal systems. To alleviate factors affecting global climate change, a growing number of firms and manufacturers are installing renewable DG systems. For instance, Honda in Russell Point, Ohio installs two units of WT that contribute 10% of electric power to its auto transmission plant. Budweiser facility in Fairfield, California installs two units of WT with the total capacity of 3 MW and 1.2 MW solar PV arrays (6,500 panels), together providing 40% of the green electricity to meet the demand. Laurel Mountain project of AES in Elkins, West Virginia (Hart and Sarkissian, 2016) has installed a 32 MW Li-ion battery storage array that is sited with a 98 MW wind farm.

The cost-benefit analysis for renewable DG system is made subject to generation and demand variation when HESS is applied (Ruangpattana et al., 2011). Jin et al. (2017) propose the assessment based on the return on investment (ROI) analysis. To estimate a

project's ROI, all relevant factors shall be taken into account on the cost and the benefit side, including installation, operation and maintenance, equipment depreciation for a technology lifetime, and government incentives or subsidies.

Taboada et al. (2012) and Zhang et al. (2017) propose a single objective optimization function. They take an early step to design an onsite, grid-tied PV system to power a 15 MW wafer fab in conjunction with a substation. The numerical experiments show that up to 10,000 tons of carbon could be avoided when the PV capacity reaches one-third of the mean load. Villarreal et al. (2013) and González et al. (2015) expand the renewable generation portfolio by incorporating WT and solar PV into local DG systems. The model is applied to minimize the DG lifecycle cost. Moon and Park (2014) solve a multi-machine, multi-process manufacturing scheduling problem by considering the onsite renewable power and with a single type of energy storage technology.

Based on these approaches, a mixed-integer programming (MIP) model is formulated for the DG planning problem. Vafaei and Kazerani (2011) construct a MIP model to select and size different power generation technologies and storage devices for a microgrid power system to minimize operational costs. Bahramirad et al. (2012) and Chen et al. (2012) adopt the MIP approach to minimize the investment in storage devices and microgrid operational costs by optimizing the capacity of the energy storage system, in which the problem is analyzed from an economical point of view.

Due to the changing load pattern, the time of use (TOU) rate was introduced in early 1997. Under the TOU policy, the utility price would be either higher during the peak period or lower during the off-peak. It also becomes a factor to impact the sizing of WT, solar PV, and energy storage devices. Li et al. (2016) and Li et al. (2017) propose an

optimal model for onsite PV and battery systems to minimize energy costs. Electricity cost savings potentially are influenced by the capacity of solar PV and the size of the battery. The capacity of the ESS affected by TOU rate has been addressed in Lee and Chen (1995). Datta (2017) analyzes a production-inventory model involving a cycle of product under a carbon tax system. This model provides the optimal policy in an inventory system under carbon tax levied by the emission regulatory authority.

With the growing penetration of wind and solar energy in the utility market, it is imperative to incorporate the energy supply variability and the carbon constraints into the production-inventory planning model to lower the manufacturing cost with superior environmental performance. Integrating renewable energy sources to power production-inventory systems is a significant approach to achieve a low carbon emission for manufacturing. Jin et al. (2017) design a linear optimization model to integrate onsite wind and solar power for a multi-site manufacturing supply chain. The model is developed at the strategic level to identify the sizing and siting of WT and PV units with minimum cost.

A case study of supply chain planning in a multi-site pulp company is analyzed by Waldemarsson et al. (2013). Authors extend the model from monthly period over a one-year planning horizon, including decisions about the supply of materials, production, and distribution. Golari et al. (2017) integrate onsite WT, solar PV, hydro, and conventional energy in a multi-facility, production-inventory system to meet the green energy coefficient target. Intermittent power, optimal production plan, and energy supplies are jointly coordinated in each period such that the total expected cost is minimized over the whole planning horizon. Fattahi et al. (2018) and Hasani et al. (2020) present a novel

cost-efficient multi-stage stochastic program in which operational and tactical planning decisions are made for mining industry. The model consists of multi-manufacturing, warehouses, and demand sites. Lin et al. (2019) study carbon emission policies with emissions reduction technology investment in a two-stage supply chain inventory policy.

Virtual power plant (VPP) has recently emerged as one of the most promising solutions for coordinating intermittent renewable energy resources in different regions to achieve coordinated optimization control of distributed generation. Kuznia et al. (2013) have proposed a stochastic mixed integer programming model for a comprehensive hybrid power system design, including wind turbines, storage device, transmission network, and thermal generators in remote areas. Wang et al. (2015) construct an interactive dispatch model for the bidding strategy and consider the demand response based on time-of-use pricing mechanism and interruptible load to the maximum profit of the VPP system. A maximum VPP operation income model is designed by Ju et al. (2016) and Duarte et al. (2020), which is optimized the scheduling with the day-ahead prediction output of wind turbine and solar PV generation. Naval et al. (2020) design a mixed-integer model for Large-scale distributed renewable generation. The research proves that the VPP power system reduces grid dependence and final electricity costs.

### **1.3 System Configuration and Research Methodology**

#### **1.3.1 System Configuration**

The onsite renewable DG system consists of the WT, solar PV panels, HESS, substation, and a feed-in tariff (FIT) program in this study. The configuration of the system is shown in Figure 1.5. The DG system exchanges electric power with the substation when the output generation of WT and solar PV plus the stored energy drop

below the load. The short-term energy gap can be filled by importing electricity from the main grid. On the other hand, the surplus energy can be stored in the storage system or feed into the main grid via feed-in tariff program. The HESS plays a dual role that works as the energy consumer or producer depending on the output of wind and PV generation. The system can reduce the carbon footprint, mitigate the electricity transmission losses, and environmental risks of forest fires caused by downed power lines.

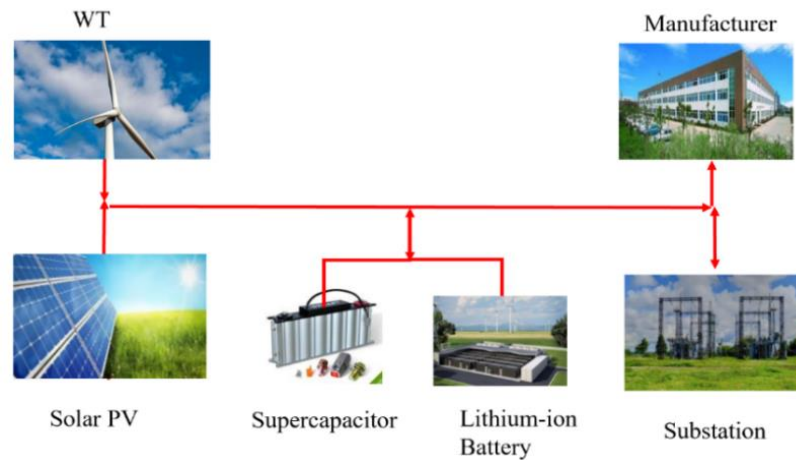


Figure 1.5: A Grid-connected Distributed onsite Power Generation System with HESS.

In case study, the hybrid energy storage system operates as the following strategy shown in Figure 1.6:

1) If  $P_{\text{gen}} = D_t$ , the aggregate renewable generation ( $P_{\text{gen}}$ ) equals the load ( $D_t$ ). It means that the generation meets the demand. There are no energy exchanges with grid and storage system.

2) If  $P_{\text{gen}} > D_t$ , it has surplus power which would inject into main grid via FIT scheme or recharging HESS depends on whether the devices are in fully charged status or not.

3) If  $P_{\text{gen}} < D_t$ , the shortage of demand will be supplemented by discharging HESS or importing energy from the main grid. During peak hours, the system will draw

the energy from HESS first, then import shortage energy from the main grid. The opposite operation process occurs during off-peak hour.

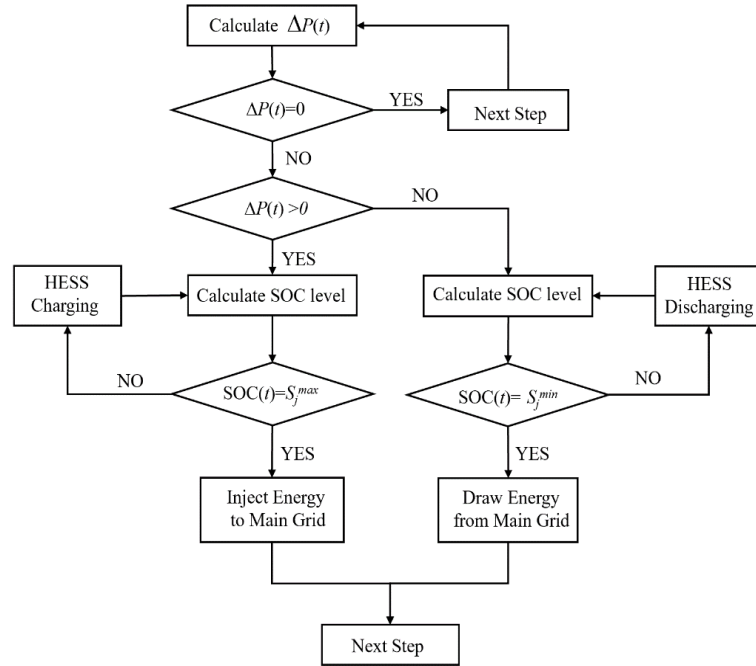


Figure 1.6: Operation Strategy of HESS.

### 1.3.2 Research Methodology

In this research, the mathematical model of a DG planning problem is formulated as a mixed-integer linear program (MILP) and mixed-integer non-linear program (MINLP) to optimize system cost and LCOE, respectively. The binary variables are the charging or discharging status of the HESS units. The model will be not only considering the degradation of HESS energy capacity but also accounting dynamic output, load profile, and various utility price constraints.

The proposed models are tested in cities with different climate conditions. Even though the model parameters, such as the capacity cost and maintenance cost, remain unchanged, the optimal decision on the capacity of WT, solar PV, Li-ion battery and SC are various in testing cities. The system cost will be reduced as the cost of WT, PV

modules, and energy storage device goes down. The energy stored in the HESS should not be dropped below 20% of initial capacity at any time, which can extend or maintain a good lifespan of battery.

The entire study can be divided into five modules and the research goals of each module are given below:

- 1) Data collection, evaluation, and statistical analysis.
- 2) Development, evaluation, and implementation of hybrid forecasting model.
- 3) Modeling and simulation of the wind turbine and solar PV power system.
- 4) Constructing prosumer model to minimize the LCOE for single location .
- 5) Design production-inventory model for the three-echelon network supply chain system.

### 1.3.3 Outline of Dissertation

The dissertation consists of eight chapters and the main content of each chapter is described as follows:

Chapter 1 is the introduction and discusses the research background, motivation, and significance of this research. This section also conducts the literature review, including the overview of existing research methodology.

Chapter 2 analyzes the weather data, which includes wind speed and weather features. The statistical approach is applied to interpret the time series data.

Chapter 3 proposes hybrid forecast models. Both wind speed and weather feature forecasting models are constructed to predict the short-term and long-term, respectively. The renewable generation will be simulated based on the long-term forecasting results of wind speed and weather features.

Chapter 4 presents a mathematical model for onsite renewable generation and hybrid energy storage technologies by considering their different working principle and application conditions. The hybrid storage devices focus on LIB and SC. It also explains the charging-discharging principle of LIB, and the key factors that affect the battery service life.

Chapter 5 displays numerical experiment results for each testing city under four operation modes to minimize LCOE. It also compares the optimization results based on the city and operation mode.

Chapter 6 formulates a multi-product, multi-period production model for a multi-echelon supply chain network under energy supply and product demand uncertainty to minimize the annual operation cost. It also performs a comprehensive sensitivity analysis in terms of model scalability and applicability.

Chapter 7 deploys the battery technology and analyzes the performance of the battery made by lithium-ion material through the computer simulation experiment.

Chapter 8 makes a summary of the research and projects the future research. It embarks upon the current energy storage technology, market analysis, and cutting-edge research in the field of energy storage technology.

## 2. CLIMATE DATA ANALYSIS

The hourly climate data in a particular location is retrieved from the Weather Underground Database (2017), which archives the weather records of cities across the world. The data attributes comprise wind speed, wind direction, air pressure, humidity, and temperature as the hourly interval. The timeframe spans from 2004 to 2014 with approximately 96,360 records for each city. Six cities around the world are selected to represent the diverse profiles of wind speed and weather patterns by comparing their weather information. Koeler (2013) states that weather is the original big data problem and weather forecasting is an initial value problem. As the size of initial data increases, the accuracy of forecasting increases.

Table 2.1 lists the geographic information such as elevation, longitude, and latitude of testing cities under investigation. These cities cover the majority of areas where the human being lives across the Northern and Southern hemispheres. Wellington is the capital city of New Zealand and it is in the Southern hemisphere. The rest of cities are in the Northern hemisphere.

Table 2.1: Summary of Cities Geographic Information.

Continent	Country	City	Elevation (meter)	Longitude (degree)	Latitude (degree)
Asian	China	Sanya	729	109.51	18.25
Australia	New Zealand	Wellington	18	174.78	-41.29
North American	USA	New York	10	-74.01	40.71
		San Francisco	67	-122.43	37.78
		Phoenix	332	-112.07	33.44
		Boston	43	-71.06	42.36

\*negative latitude means South of the Equator; A negative longitude means West of the Prime Meridian

## 2.1 Raw Data and Clean Methodology

Table 2.2 shows a sample record, containing attributes of the climate data range from temperature, wind speed to humidity, and weather features. The sample record has two types of data. One is the numerical data type, like wind speed and temperature that belong to continuous value. The other type is called the categorical variable or discrete variable, such as weather feature, describing as "raining" or "overcast". The meteorological data (e.g., wind, wind direction, and humidity) is the most widely recognized as time series data. The dataset needs to be transformed to obtain the uniformity granularities on every hour interval in this study.

Table 2.2: Raw Dataset Sample.

date	temp (F)	dew point	hum	wind speed	wind gust	wind direction	vis	pressure	wind chill	precip	state
12/18/2014 12:51	59	45	60	0	NA	North	10	30.08	NA	NA	MC
12/18/2014 13:51	59	43	55	0	NA	North	10	30.06	NA	NA	MC
12/18/2014 14:51	61	42.1	50	6.9	NA	Variable	10	30.06	NA	NA	MC
12/18/2014 15:51	61	42.1	50	5.8	NA	WNW	10	30.06	NA	NA	SC
12/18/2014 16:51	60.1	41	49	8.1	NA	WNW	10	30.07	NA	NA	SC
12/18/2014 17:51	59	42.1	53	8.1	NA	West	10	30.08	NA	NA	PC
12/18/2014 18:51	57	43	59	6.9	NA	West	10	30.11	NA	NA	Clear
12/18/2014 19:51	54	44.1	69	5.8	NA	WSW	10	30.13	NA	NA	Clear
12/18/2014 20:51	54	43	66	3.5	NA	SW	10	30.14	NA	NA	Clear
12/18/2014 21:51	55	42.1	62	4.6	NA	NW	10	30.15	NA	NA	Clear
12/18/2014 22:51	52	43	71	0	NA	North	10	30.17	NA	NA	Clear
12/18/2014 23:51	51.1	43	74	4.6	NA	East	10	30.16	NA	NA	Clear
12/19/2014 0:51	48.9	44.1	83	3.5	NA	East	10	30.16	NA	NA	Clear

\*Data source: Weather Underground <https://www.wunderground.com/>

\*Note: MC=mostly cloudy, SC= scattered cloudy, PC=partly cloudy.

Some records from the original data resource are not completed with missing values, which are represented by “NA” or “Unknown”. It also has multiple records within

an hour period. For example, the climate data has three duplicated records within one hour, but only one observation is needed for that hour. In other cases, there are quite a few observation points not being recorded. For example, the worst situation in Wellington appears from 12/16/2012 to 12/17/2012. More than ten records are missing across two days. The total number of missing observations is 313, and 2,758 observations have incomplete records. Together, incomplete values and missing observations make up around 3.4% of the entire observations. Before the climate data are applied to the forecasting model, the raw data needs to be cleaned or pre-processed by imputing the missing value and deleting the redundant records.

#### 2.1.1 Classify Data Structure

The weather feature belongs to categorical variable. There are more than thirty different states in over one decade climate data, which are described as "clear day", "drizzle", "fog", "funnel cloud", "hail", "haze", "heavy drizzle", "heavy rain", "heavy rain showers", "heavy thunderstorms and rain", "light drizzle", etc. Since some of them represent rare situations and extreme events compare with other states, the type of weather states can be compressed by combining similar features. For instance, thunderstorms and light thunderstorms are both referred to as the thunderstorms state. In this study, three classification models are posted to predict weather features with five states, seven states, and ten states output, respectively. Table 2.3 below lists three situations with detailed information in the model. The number of states in one model can be set as  $N$ . These states are ranked from 0 to  $N-1$  in the forecasting model based on the amount of cloud in the sky.

Table 2.3: Classes Description in Forecasting Model.

Levels	Description
5 classes	"clear", "scattered cloudy" (SC), "partly cloudy" (PC), "most cloudy" (MC), " overcast"
7 classes	"clear", "scattered cloudy" (SC), "partly cloudy" (PC), "most cloudy" (MC), " overcast", "rain", "snow"
10 classes	"clear", "scattered cloudy" (SC), "partly cloudy" (PC), "most cloudy" (MC), " overcast", "rain", "light rain", "Thunderstorm", "fog/haze", "snow"

### 2.1.2 Remove Redundant Data

Before splitting the raw data into the train, test, and validation dataset, the data needs to be cleaned and standardized. The input data of the model needs to be as an hourly interval. Table 2.2 shows the dataset before cleaning process. The redundant or unnecessary data need to be removed. The date column is the timestamp, which contains the "year", "month", "day", "hour", and "minute" information. This column is split into five columns, represented by "year", " month", " day", "hour", and "minute", respectively. If there are multiple rows having the same value of "year", "month", "day" and " hour", only the first appearance is kept. Hence the task becomes to filter out duplicate timestamps and form a new data table.

### 2.1.3 Locate Missing Observations

In addition to redundant data, the sample data set also contains quite a few missing observations, which means an entire row is missing in the sample data. It is imperative to identify where these missing observations are located. A new data frame needs to be created with the hourly time step. The table created by the previous step in (2.1.2) joins the new table, then the missing row is located and a completed timestamp in

the dataset is constructed.

#### 2.1.4 Impute Missing Value

In this study, the missing data could be an empty cell or recorded as "N/A" or "unknown". Two situations are considered to deal with these missing data. In the first situation, the missing record is associated with a totally lost observation in a specific hour, called the missing row. For a single row, the value in each column equals the value of its previous row, regardless of the data type. The second situation is the incomplete records for a given row. For the missing numerical value, like wind speed, the missing data is filled by averaging the nearest two rows of data prior to and post the missing data. For categorical data like weather states, the missing state information for that row is taken as the worst-case scenario between the previous and following hours. For instance, if the weather state is sunny and overcast at 1 pm. and 3 pm., respectively, then the missing weather state is assumed to be overcast at 2 pm.. This makes the weather forecasting model more conservative when estimating the generation of solar PV.

In this research, Bayes' theorem is used to infer the missing weather conditions. This theorem describes the probability of an event occurrence based on the prior knowledge that might be related to the event. By replacing the missing values with simulated values, it creates complete data. For example,  $A$  and  $B$  are two events, Bayes' theorem allows us to calculate the probability of  $A$  given  $B$ , if known the probability of  $B$  given  $A$  and the probabilities of each event. Denoted  $P(A/B)$  as the probability of  $A$  given  $B$ ;  $P(B|A)$  as the probability of  $B$  given  $A$ ; and  $P(A \cap B)$  as the joint probability of  $A$  and  $B$ . The conditional probability of  $A$  given  $B$  is,

$$P(A|B) = \frac{P(A \cap B)}{P(B)} \quad (2.1)$$

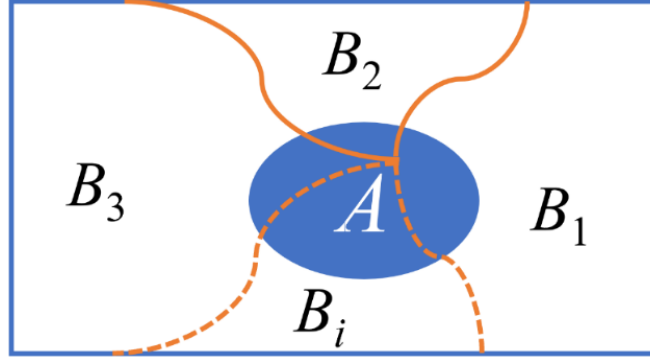


Figure 2.1: Probability of  $B_i$  Given  $A$ .

As in Figure 2.1, the total probability of formula  $A$  is:

$$P(A) = \sum P(A | B_i)P(B_i) \quad (2.2)$$

The probability of  $B_i$  given  $A$  can be obtained by Bayes' theorem formula:

$$P(B_i | A) = \frac{P(A | B_i)P(B_i)}{P(A)} = \frac{P(A | B_i)P(B_i)}{\sum P(A | B_i)P(B_i)} \quad (2.3)$$

where

$P(A)$  = prior probability of  $A$ .

$P(B)$  = prior probability of  $B$ .

$P(A/B_i)$  = likelihood of  $A$  if  $B_i$  occurs.

$P(B_i | A)$  = posterior probability of  $B_i$  given  $A$ .

The missing value like weather condition at  $t$ -hour can be predicted by probability of weather features in previous hours. For the continuous distribution of wind speed, the approach can be made based on the Bayesian model of the density functions, that is

$$\begin{aligned} f_{x|y}(x|y) &= \frac{f_{x,y}(x,y)}{f_y(y)} \\ &= \frac{f_{y|x}(y|x)f_x(x)}{f_y(y)} \end{aligned} \quad (2.4)$$

Table 2.4 is the dataset after cleaning process of Phoenix. The original measurement unit of wind speed is mile per hour and temperature is Fahrenheit. All of

them are converted into meter per second and Celsius, respectively.

Table 2.4: Cleaning Dataset Sample.

Date	States	WD	Pressure	Humidity	DP	WS (m/s)	Temp (°C)
12/18/2014 12:51	MC	North	30.08	60	45	0	15
12/18/2014 13:51	MC	North	30.06	55	43	0	15
12/18/2014 14:51	MC	Variable	30.06	50	42.1	3.08	16.11
12/18/2014 15:51	SC	WNW	30.06	50	42.1	2.59	16.11
12/18/2014 16:51	SC	WNW	30.07	49	41	3.62	15.61
12/18/2014 17:51	PC	West	30.08	53	42.1	3.62	15
12/18/2014 18:51	Clear	West	30.11	59	43	3.08	13.89
12/18/2014 19:51	Clear	WSW	30.13	69	44.1	2.59	12.22
12/18/2014 20:51	Clear	SW	30.14	66	43	1.56	12.22
12/18/2014 21:51	Clear	NW	30.15	62	42.1	2.06	12.78
12/18/2014 22:51	Clear	North	30.17	71	43	0.00	11.11
12/18/2014 23:51	Clear	East	30.16	74	43	2.06	10.61
12/19/2014 0:51	Clear	East	30.16	83	44.1	1.56	9.39

\*Note: MC=mostly cloudy, SC= scattered cloudy, PC=partly cloudy, WD=wind direction, DP=dew point, WS=wind speed.

## 2.2 Climate Data Information

The selected testing cities represent the diverse profiles of wind speed and weather patterns. The detailed information about wind speed and weather features in each city are in Table 2.5. These cities have the unique meteorological profile and diverse climate conditions. Among these cities, Wellington has a very strong wind profile. It is the windiest city in the world, but the weather state is mostly cloudy throughout the year. Phoenix has plentiful solar energy resources and the hottest climate, but a low wind profile over the year, while San Francisco has both abundant wind resource that varies from medium to high, and strong solar irradiance due to large amounts of sunny days.

Table 2.5: Summary of Climate Condition on Testing Cities.

City	Average (m/s)	Std Dev (m/s)	City	Clear (day)	Scattered (day)	Partly Cloudy (day)	Mostly Cloudy (day)	Overcast (day)	Rain (day)	Snow (day)
Wellington	6.8	3.6	Phoenix	178	69	65	30	19	4	0
New York	5.1	2.7	Sanya	112	87	66	59	26	15	0
Boston	4.7	2.4	San Francisco	80	58	83	77	52	15	0
San Francisco	4.6	3.2	New York	75	55	75	66	54	26	14
Sanya	3.1	2.2	Wellington	62	69	91	88	15	37	4
Phoenix	2.8	1.9	Boston	58	58	58	66	84	26	15

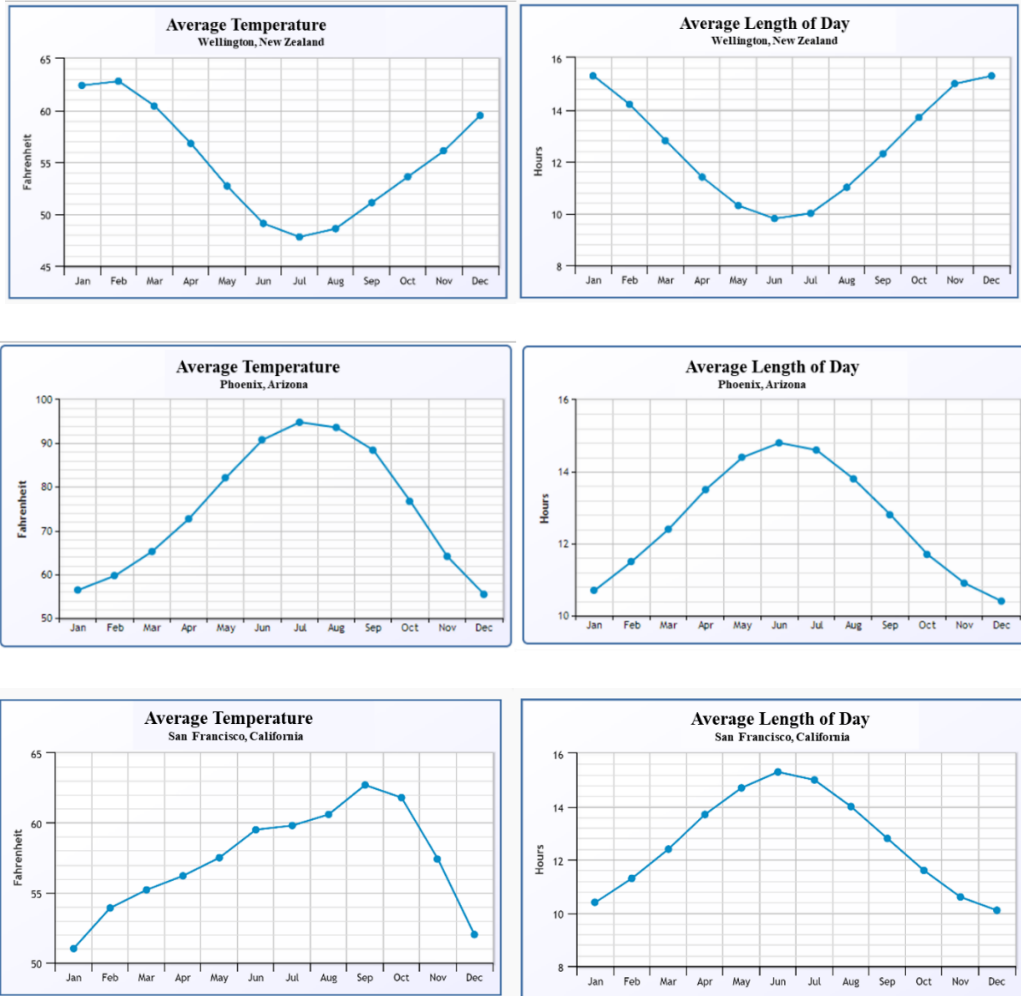
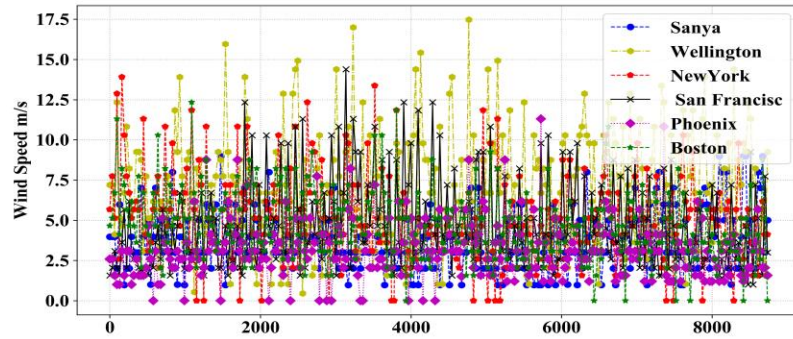


Figure 2.2: Weather Climate in Wellington, Phoenix, and San Francisco.

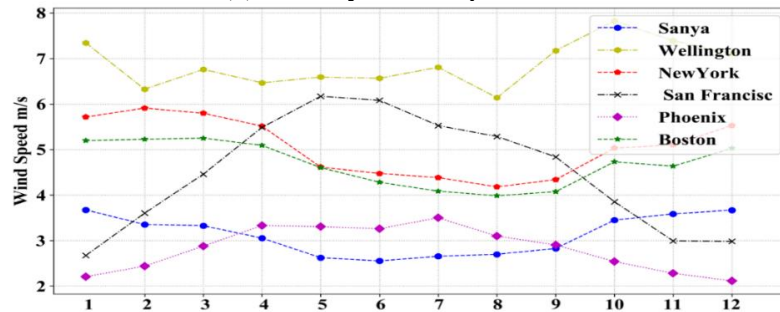
For further illustration, Figure 2.2 plots the climate conditions such as the average temperature in a month, the length of day, and the rainy days in a month in Wellington, Phoenix, and San Francisco. The average temperature and average length of daytime follow the same curve, but the curves of temperature and length of day are opposite between Wellington and the remaining cities, because they are in opposite hemispheres.

### 2.2.1 Wind Speed

Wind speed is the most important parameter in the integration and operations of wind energy generation system. The average wind speed, recorded at a height of 10 meters above the ground, is over 6.8 m/s in Wellington and it is only 2.8 m/s in Phoenix. The wind speeds at other four cities fall between these two values. The wind profiles and average monthly wind speed of the testing cities in 2014 are shown in Figure 2.3 (a) and Figure 2.3 (b), respectively.



(a). Hourly Wind Speed.



(b). Average Monthly Wind Speed.

Figure 2.3: Wind Portfolios of Testing Cities in 2014.

In practice, it is very important to describe the variation of wind speed during the design and optimization of renewable generation systems, resulting in the low upfront investment and future maintenance costs. The random behavior of wind speed is usually characterized by the normal distribution (Justus et al., 1978) or Weibull distribution (Justus et al., 1978; Seguro and Lambert, 2000). Figure 2.4 (a) plots the hourly wind speed histogram in 2014 with 8,760 data points per city. The corresponding Weibull distributions of wind speed for testing cities are depicted in Figure 2.4 (b). All distribution curves have a bell shape with an extended right tail, but the curve of Sanya's distribution is more trended to a normal distribution shape.

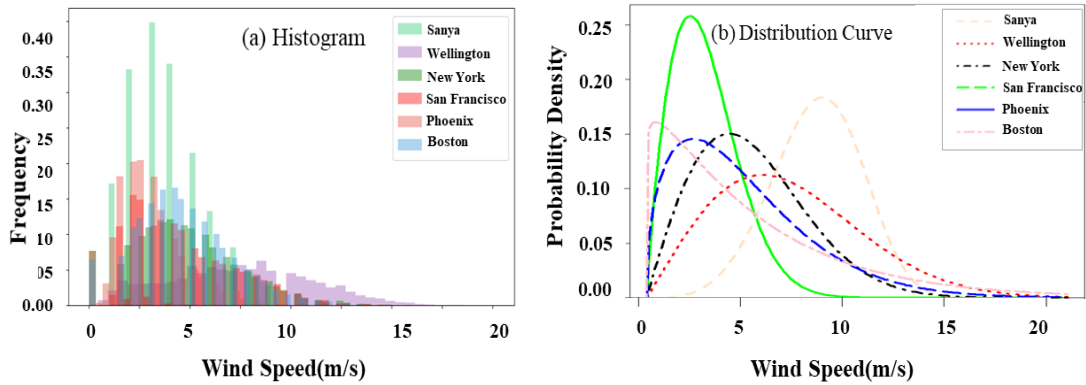


Figure 2.4: Hourly Wind Speed Density Distribution.

Table 2.6 presents the Weibull wind speed distribution parameters of testing cities. Note that  $c$  and  $k$  are the scale and shape parameters of Weibull distribution, respectively. For a given  $c$ , a larger  $k$  makes the distribution curve more concentrated around the mean value. For a given  $k$ , a larger  $c$  pushes the distribution curve to the right side.

The seasonality of wind speed varies in different cities. The average monthly wind speed of San Francisco is plotted in Figure 2.5 based on 11-year data. The wind speed exhibits a strong seasonality with the fastest speed occurring in the second quarter and the lowest speed in the fourth quarter. In other words, the wind profile in each year swings from spring to winter. The windy season spans from April to August, and May is the peak wind period. A similar pattern also appears in Phoenix where the windy season is from April to August, yet the average wind speed in Phoenix is much slower than in San Francisco. Wellington does not show a strong seasonality, rather the wind speed patterns remain homogeneous across 12 months.

Table 2.6: Two-Parameter Weibull Distribution Expression of Wind Speed.

cities	$c$ (m/s)	$k$
Sanya, China	8.87	4.303
Wellington, New Zealand	7.685	2.022
New York, USA	5.63	1.964
San Francisco, USA	5.067	1.434
Phoenix, USA	3.152	1.836
Boston, USA	5.206	1.079

The wind profiles of testing cities also have a strong diurnal variation. Figure 2.6 plots the hourly wind records in a day in Wellington and San Francisco. In Wellington, the peak speed appears around 2 am. The wind speed decreases and reaches the valley at 1 pm. The curve and trend of wind speed in San Francisco and Phoenix are opposite to Wellington. In San Francisco, the windiest time is around 4 pm. and the speed declines to the lowest level in a day around 5 to 7 am. The wind speed tends to increase after sunrise and decrease after sunset in San Francisco. Figures 2.5 and 2.6 show that wind speed exhibits both seasonal and diurnal variations.

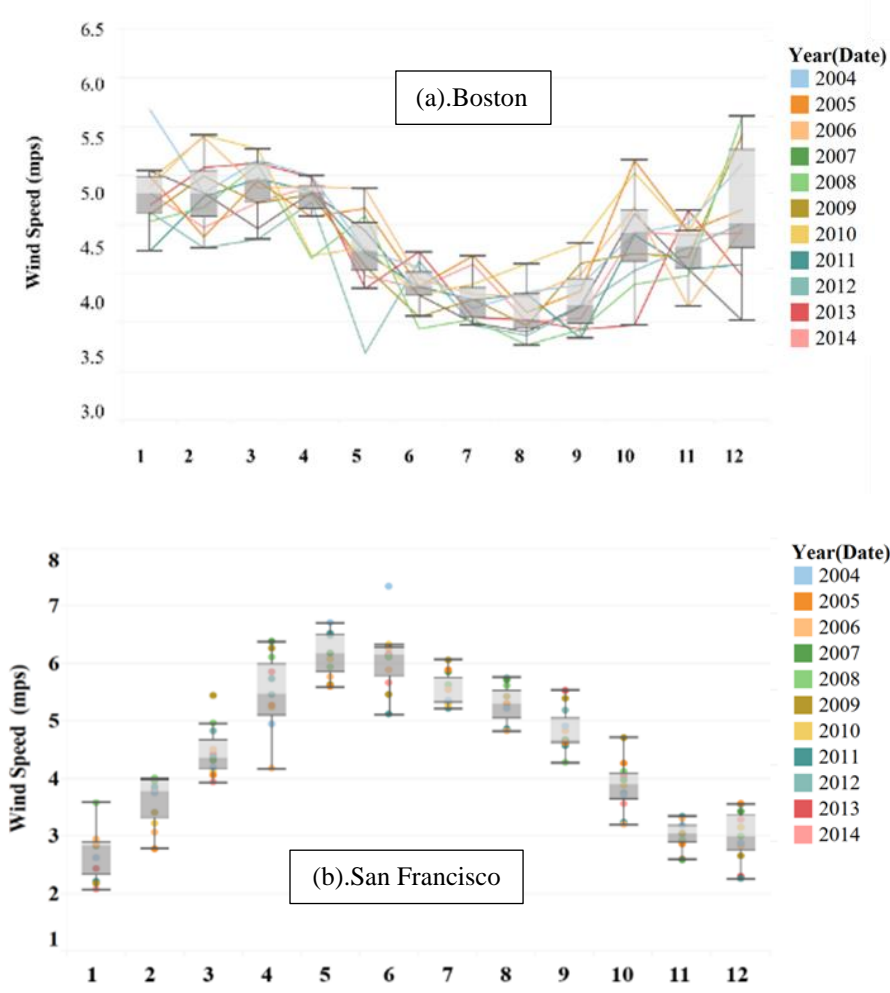


Figure 2.5: Monthly Average Wind Speed.

Obviously, the wind speed dataset exhibits two types of variations: diurnal (i.e., 24 hours) and seasonal variations (i.e., 365 days). Although a neural network can handle seasonal time series data quite well in theory, the model is expected to be more accurate if the seasonal factor could be removed from the data.

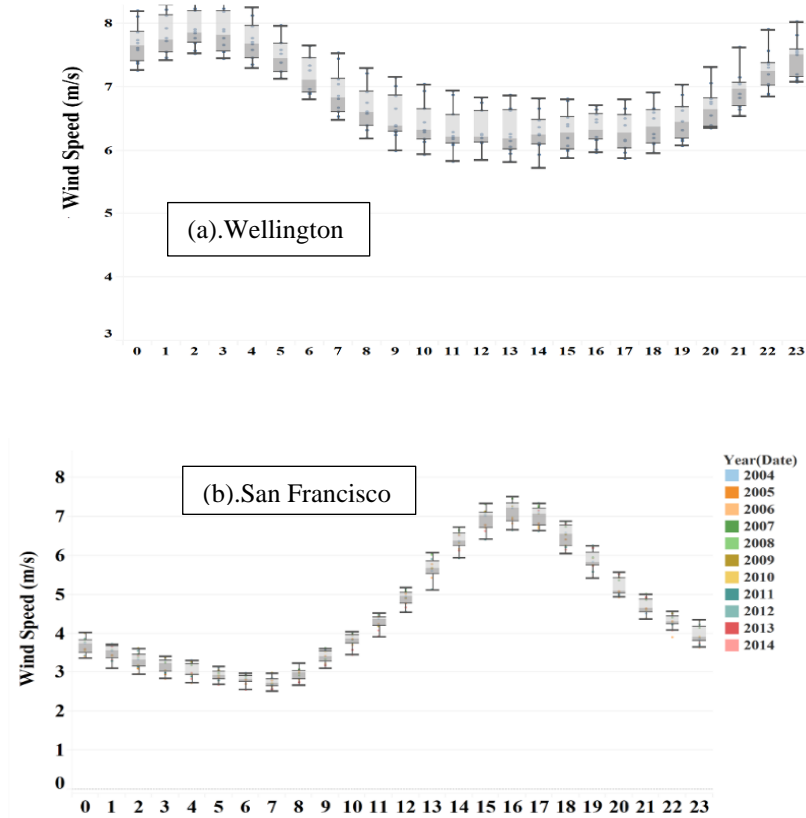


Figure 2.6: Diurnal Wind Speed Variation.

A wind rose is a graphic tool that gives a succinct view of how wind speed, wind direction, and frequency are typically distributed in one location. The length of the bars indicates the frequency in percentage unit. Figure 2.7 depicts the wind rose for the testing cities, where  $0^\circ$ ,  $90^\circ$ ,  $180^\circ$ , and  $270^\circ$  denote north, east, south, and west directions, respectively. In Wellington and Phoenix, the dominant wind direction is from the north (N). For example, the wind blows from the north about 19.1% of the time at speeds between 6.1 and 11.6 m/s in Wellington. In Phoenix, the average wind speed blows from the northeast at over 3.9 m/s. In San Francisco, the dominant wind direction is from the southwest–northwest (SW–NW), in the range between  $260^\circ$  and  $300^\circ$ . The wind rose of these cities shows that the wind speed is highly correlated with the wind direction.

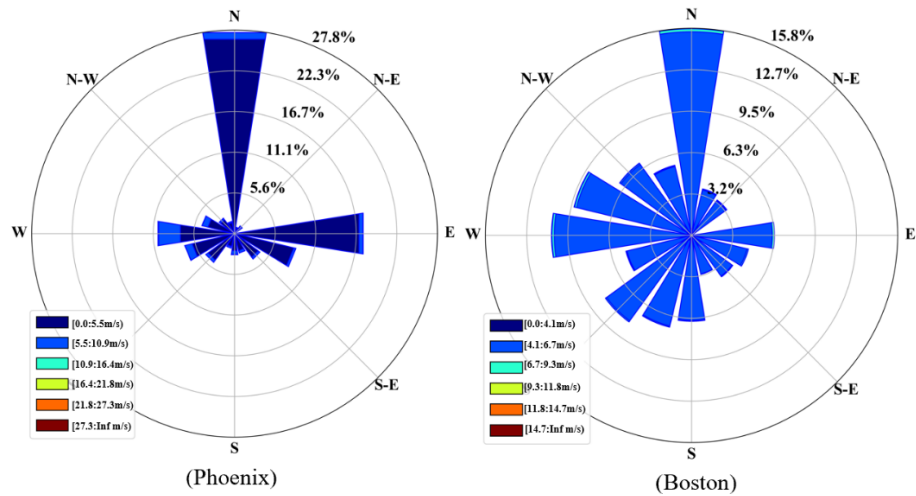
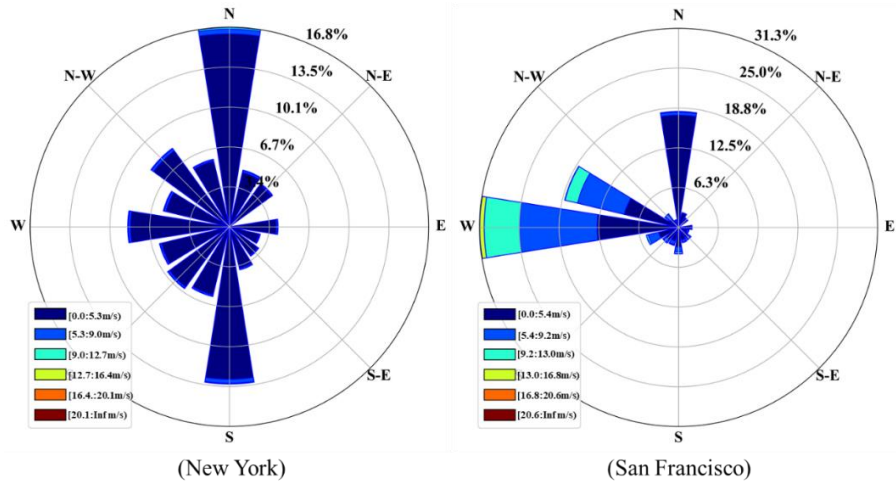
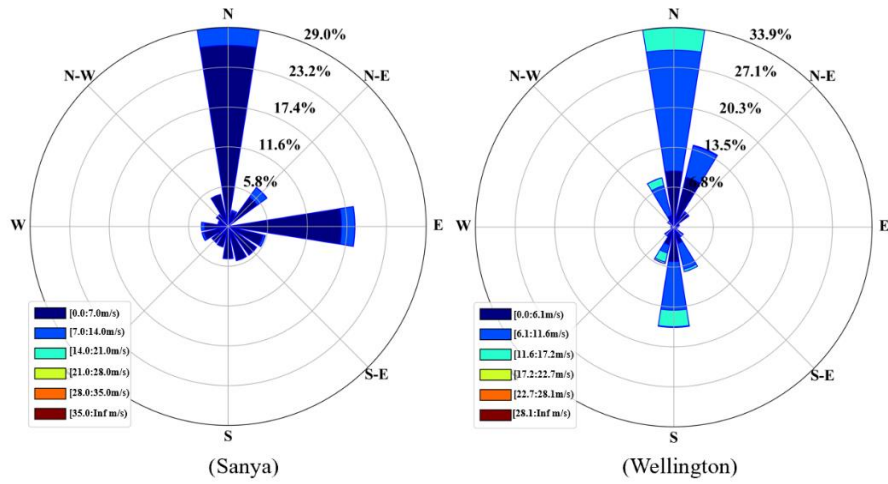


Figure 2.7: Wind Rose of Testing Cities.

The raw dataset includes the temperature, weather condition, dew point, air pressure, humidity, wind speed, and wind direction variables. Their correlation between meteorological data would impact the output of renewable generation. To do that, the correlations are analysed to determine the input neuron number for the forecasting model. Understanding the correlation among meteorological data is important and beneficial to predict wind speed and weather features. One of the tasks of our study is to determine the number of input neurons for the proposed model because these neurons represent different meteorological data.

Figure 2.8 graphically depicts the correlation matrix between any two features. The sign and magnitude of the correlation coefficient are represented by two colors and the intensity of color. It shows that the wind speed has a positive correlation with wind direction and a negative correlation with humidity. The temperature has a strong positive correlation with the dewpoint.

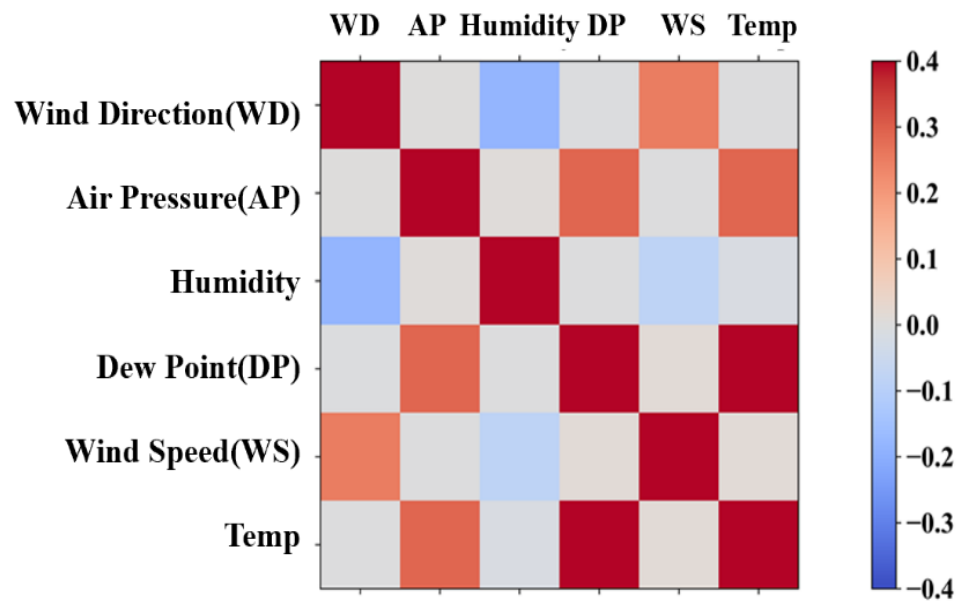


Figure 2.8: Correlation between Variables.

Table 2.7 below summarizes the basic statistics of meteorological features for testing cities. In Wellington, about 50% of wind direction is observed between the north and the northwest. In San Francisco, about 40% of wind direction is observed between the west and the northwest. The wind direction is a circular function resulting in a discontinuity at 0° and 360°. The wind direction feature is transferred into two input series in the forecasting model by using trigonometric functions of sine and cosine. One value of wind direct becomes two values in a range from 0 to 1.

Table 2.7: Statistics for Wind Speed (m/s), Temperature (°C), and Dew Point (°C).

Category	Sanya				Wellington				New York			
	Dir	Speed	Temp	DP	Dir	Speed	Temp	DP	Dir	Speed	Temp	DP
<b>Median</b>	110	2.9	15.6	22.1	180	7.9	14	10	220	4.7	6.7	6.8
<b>Mean</b>	132	3.1	16.4	21.2	191	6.8	13.6	9.4	211	4.7	7.3	5.6
<b>Max</b>	350	35.0	34.0	29.1	360	28.3	29	19	350	20.1	36.1	29.0
<b>25%</b>	40	2.0	15.6	19.1	40	4.1	11	7	150	4.6	6.7	-2.2
<b>50%</b>	110	3	15.6	22.1	180	7.1	14	10	220	4.6	6.7	6.8
<b>75%</b>	220	3.9	15.6	24.1	340	9.7	16	12	310	4.6	6.7	14.5
<b>Std</b>	115	2.2	3.1	4.0	128	3.7	3.4	3.6	105	0.7	3.2	10.8
Category	San Francisco				Phoenix				Boston			
	Dir	Speed	Temp	DP	Dir	Speed	Temp	DP	Dir	Speed	Temp	DP
<b>Median</b>	280	4.1	13.3	8	200	2.5	25	2.2	220	6.2	3.9	4.4
<b>Mean</b>	253	4.6	24.5	8.6	188	2.8	24.8	3.2	211	6.1	4.5	3.3
<b>Max</b>	360	20.6	50	19.4	360	17.4	47.2	23	350	14.4	34.4	25.7
<b>25%</b>	260	2.1	10.6	5.6	80	2.1	17.8	3.2	130	6.2	3.9	-5.6
<b>50%</b>	280	4.1	13.2	8	200	2.6	25	2.2	220	6.2	3.9	4.4
<b>75%</b>	300	6.7	16.7	10.6	300	4.1	32.2	10	290	6.2	3.9	13.3
<b>Std</b>	84	3.3	4.2	4	117	1.6	9.2	8.9	104	0.8	3.6	12.2

\*Note: Dir= wind direction, Temp=temperature, Std=standard deviation, DP= dew point.

### 2.2.2 Weather Features

More than thirty weather states are described in the dataset for each testing city. Figure 2.9 plots weather states in Phoenix (a) and New York (b) from 2012 to 2014. The number of hours in "clear," "scattered cloudy," and "partly cloudy" state represents over 50% in Phoenix. It means this city has plentiful solar energy. Comparing Figure 2.9 (a) and Figure 2.9 (b), the weather features in New York are more diverse than in Phoenix. This situation may impact the forecasting accuracy of the model of New York and make the forecasting result having big variation between them.

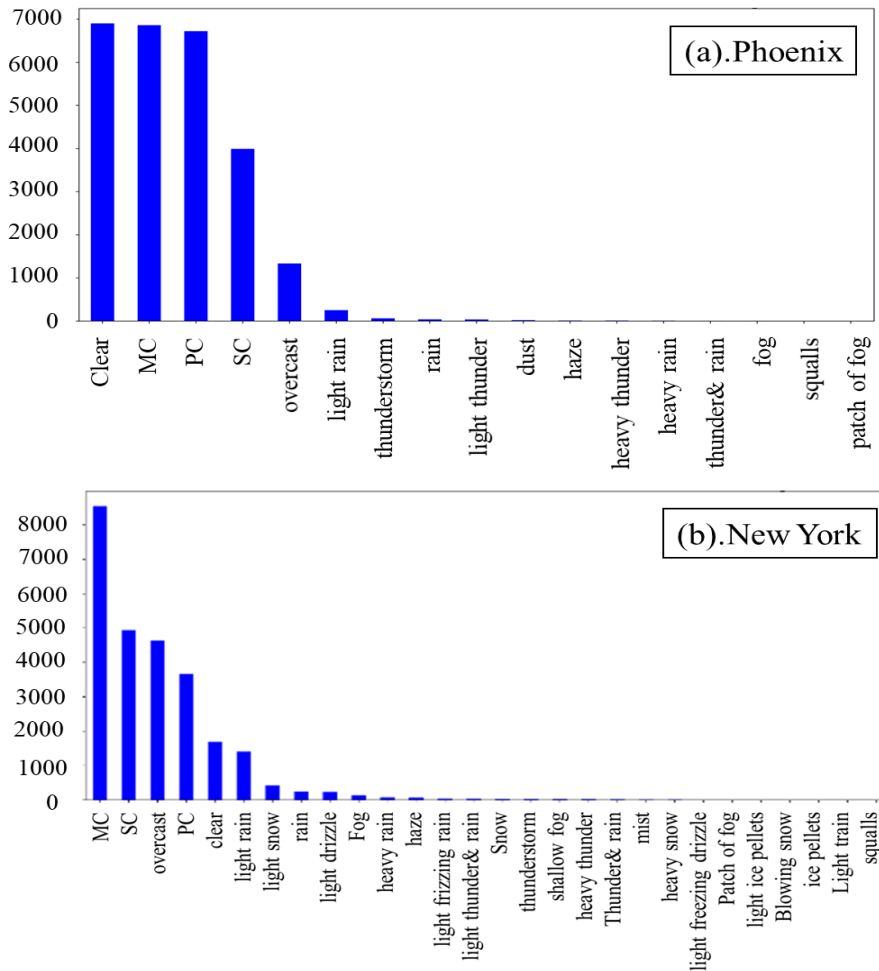


Figure 2.9: Histogram Graph of Weather States in Phoenix and New York.

Table 2.8 summarizes the proportion of the top seven feature states for the testing city by counting the frequency of weather state from 2004 to 2014. For instance, the highest frequency weather state in Wellington is "mostly cloudy, " which is the same as New York. Meanwhile, almost a half ration with "clear" and "scattered cloudy" states appear in Phoenix and Sanya.

Table 2.8: Proportion of Weather Features in Testing Cities (%).

Cities	clear	SC	PC	MC	overcast	rain	snow
Wellington	6.5	19.2	27.2	28.9	4.24	13.54	..
San Francisco	20.7	14.6	23.4	20.6	13.9	0.06	..
Phoenix	27.2	14.8	26.4	25.4	4.3	0.2	..
New York	6.2	18.1	17.1	33.1	16.1	6.7	1.6
Boston	15.5	15.6	14.2	19.8	22.7	0.8	0.6
Sanya	21.5	24.1	17.5	25.8	4.2	6.9	..

Figure 2.10 plots ten weather states in four seasons. The weather in New York is more complicated and changeable than in Phoenix. Some weather states only appear in specific seasons. For instance, the event of snow and thunderstorms likely occur in winter and summer, respectively. Both have a limited frequency.

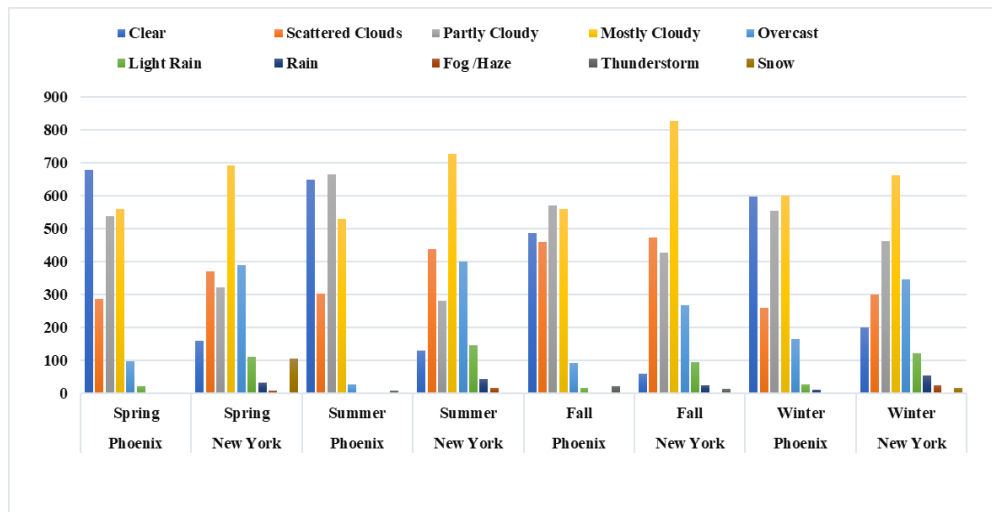


Figure 2.10: Weather States in Four Seasons in Phoenix and New York.

Table 2.9 declares the cloud cover fraction for "clear", "mostly cloudy", "overcast", "partly cloudy", and "scattered cloudy" states. "Clear" state means there is only 0~25% amount of cloud in the sky.

Table 2.9: Cloud Fraction in Five States.

States	Cloud fraction
clear	0.00~0.25
SC	0.26~0.50
PC	0.51~0.75
MC	0.76~0.99
overcast	1.00

### 2.3 Data Transformation

The input data are normalized because different meteorological features have a different range. For example, the value of temperature is less than 50°C and wind direction is in the range from 0 to 360°. They cannot be compared meaningfully. Therefore, the normalization method is used to adjust for the scale variations. Min-Max scaling is applied to transform the original data and retains the original distribution. The original data are converted into a common range between [0, 1]. The input value  $X_i$  is mapped to the new value as follows,

$$X_i' = \frac{X_i - X_{\min}}{X_{\max} - X_{\min}} \quad (2.5)$$

where

$X_{\max}$  = the maximum value of a feature.

$X_{\min}$  = the minimum value of a feature.

The influence of prediction accuracy from other atmospheric variables besides wind speed is investigated. Each dataset is divided into three parts: training, validation,

and testing. Table 2.10 shows the detailed breakdown of the dataset for training, validation, and testing in each testing city.

Table 2.10: Number of Observations in Training, Validation, and Testing Datasets.

Cities	No. of Training Data	No. of Validation Data	No. of Testing Data	Total
Wellington	70,124	8,760	8,760	87,644
San Francisco	96,457	8760	8760	113,976
Phoenix	78,910	8760	8760	96,432
Boston	78,910	8760	8760	96,432
New York	70,124	8,760	8,760	87,644
Sanya	70,124	8,760	8,760	87,644

## 2.4 Extreme Climate Event

In Wellington, the wind speed over 25m/s only appears twice on 6/20/2013 from ten years historical data record. The average wind speed is 6.8 m/s with the 3.7 m/s standard deviation ( $\sigma$ ). Six  $\sigma$  covers roughly 99.7% of the data population below the 17.8 m/s. Therefore, the wind speed data fall outside of the six  $\sigma$  range is filtered out in this study.

Some types of weather states, such as fog, thunderstorms, and haze only represent a very limited portion, like the snowstorm in Texas in 2021. Thus, they are treated as extreme weather states or climate events. These states will not be considered as the input states in the model because their occurrence rate is too low. To be conservative in PV generation, these weather states are classified as "overcast". The generation of solar PV is zero under these events.

### **3. FORECASTING MODEL**

The accurate prediction of the WT and PV power generation is an efficient way to mitigate power supply risk, facilitate real-time grid operation, and optimize asset usage. Therefore, a prediction method with the best possible accuracy over multiple time periods is critical for maintaining and operating a variable generation system. The climate behavior of future year could be conjectured and forecasted based on current and historical meteorological data. The prediction models for hourly weather features and wind resources will be presented. The principles of artificial neural network (ANN) model and statistical model will be explained in this chapter. Hybrid forecasting models are constructed by combining the advantages of the ANN-based algorithm and statistical method.

Recently, artificial intelligence (AI) techniques, such as feedforward neural network (FNN), attract more attentions. FNN is a multi-layer perceptron (MLP) neural network, which differs from physical and statistical methods in that it can learn the input-output relation from historical data, recognize hidden patterns based on past observations, and use them to forecast future values. FNN also can tolerate data errors and ease in adaptability to online measurements. Therefore, AI-based prediction methods are more capable of handling non-linear relationship.

#### **3.1 Research Methodology**

The motivation of this research is to develop weather forecasting models for estimating the wind speed and weather features, respectively, implementing advanced computer algorithms. In this study, the meteorological and geographical information of each location is considered as variables in the forecasting model. In this chapter, the

performance of the proposed models is compared with several existing methods, such as ARIMA, persistence model, and univariate neural network model in 1- to 24-hour ahead prediction. The root mean square error (RMSE) and mean absolute error (MAE) are used as comparison criteria. The proposed model is applied to various testing cities with a broad scope of climate conditions. The preliminary study shows that the proposed forecasting model exceeds the existing models and reduces the prediction error by 20% compared with univariate neural networks.

Weather information is a typical example of time series data which require a special approach in data mining. In multi-step forecasting, a univariate time series  $\{y_1, \dots, y_n\}$  is comprised of  $N$  observations. The model will then forecast for one, three, or twenty-four hours ahead of the last observations  $\{y_{n+1}, \dots, y_{n+h}\}$ , where  $h$  is 1, 3, or 24, respectively. Namely, the forecasting horizon is in a range between 1 and 24 hours.

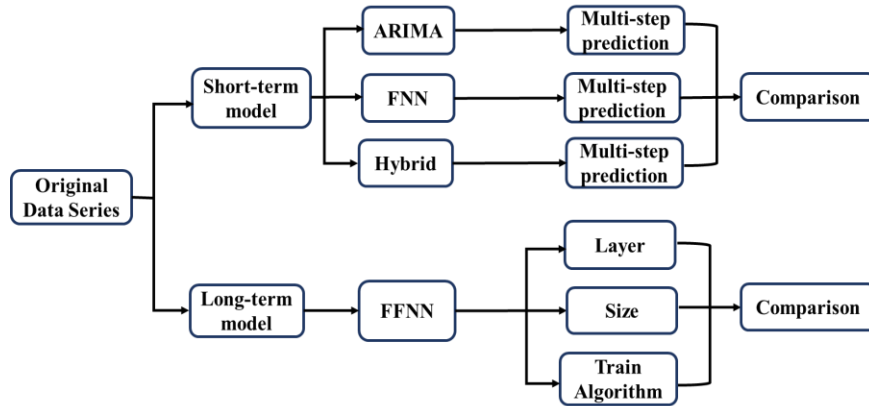


Figure 3.1: Scheme of Methodology.

It is known that forecasting the climate is a challenging task because of the involvement of large uncertainties. A desired FNN model should generate a small prediction error not only within the training dataset but also in the testing dataset (Kamruzzaman, 2006). Due to this reason, it becomes critical to obtain the optimal prediction output by appropriately choosing the input feature, the number of hidden

layers, the size of each hidden layer, activation function, and the initial values of weight and bias. Figure 3.1 depicts the flowchart and the framework of the proposed hybrid models.

To compare the performance of forecasting models, direct multiple forecasting horizons are adopted in this study. As indicated by Figure 3.2, five different forecasting horizons are assumed. These are 1-, 3-, 8-, 12-, and 24-hour. The 24-hour is also known as day-ahead forecasting. An out-of-sample forecast method is adopted, meaning the prediction data outside the dataset is used to develop and train the model. Croonenbroeck and Stadtmann (2019) emphasize that the out-of-sample forecasting strategy is essential in constructing wind forecasting model. The sliding-window-technique is used as prediction strategy. The input data are normalized because different meteorological features have a different range. For example, wind speed varies between 0 and 30 m/s, and the temperature changes from -20°C to 40°C. Min-max scaling is applied to transform the original data into a common range between [0, 1]. The proposed hybrid model allows us to obtain multiple outputs over different horizons at the same time. This can be easily realized through the implementation of multiple neurons in the output layer. For instance, in the 1-hour ahead prediction model, the output layer only has one neuron. However, in the 12-hour ahead forecasting model, the output layer contains 12 neurons, each representing the individual wind speed of the upcoming twelve hours.

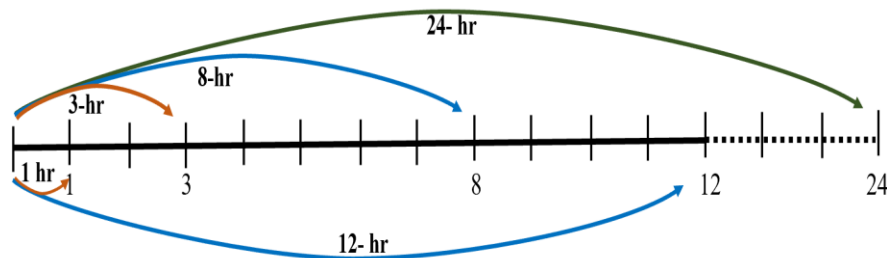


Figure 3.2: Multiple Forecasting Horizons.

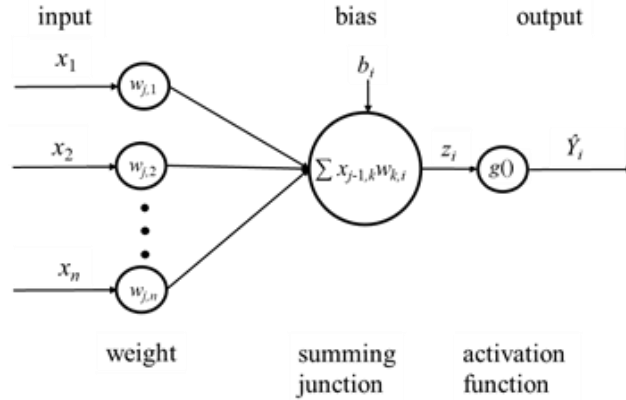
First, we need to identify the desired output in this study, then decide which type of model and activity function can be applied. In the wind speed forecasting model, the output is associated with the changes in numerical value. This can be defined as a regression problem with numerical or continuous values.

In the weather state forecasting model, the model is dealing with predefined weather features. The model can be considered as a classification problem and the prediction output of the model is classified as "clear", "scattered cloudy", "partly cloudy", "most cloudy", "overcast" and so on. Both types of outputs are computed hourly in this research.

### **3.2 Artificial Neural Network Forecasting Model**

Since the mid-1980s, ANN methods have received much attention and are treated as a powerful computational tool to solve the weather forecasting problem. ANN is the computing mechanism with studying and learning capability, inspired by biological brain, and widely applied for time series data forecasting. The feed-forward ANN (FNN) model consists of at least three layers. For instance, the architecture of a three-layer FNN model with a supervised learning technique can be graphically described in Figure 3.3. The three layers are namely an input layer, an output layer, and a hidden layer.

Unlike other statistical techniques, FNN does not make any prior assumptions on the statistical distribution of the input data. The number of units at the input and output layers is defined by the problem as mentioned in previous part. The input neuron is related to each input vector, while the output provides the forecasted value for the desired structure. The input vector fed to the model is normalized between [0, 1].



Input vector:  $\mathbf{X} = [x_1, x_2, \dots, x_n]$ ; Output vector:  $\hat{\mathbf{Y}} = [\hat{Y}_1, \hat{Y}_2, \dots, \hat{Y}_i]$

Figure 3.3: Structure of FNN.

### 3.2.1 Topology of FNN

The neural network model uses parallel processing of the information from the data to approximate a large class of functions with a high degree of accuracy. In this study, the validation dataset contains one-year hourly meteorological data to evaluate the model performance and the testing dataset consists of one-year of hourly data to make forecasting. The remaining data are used to train and tune the parameters in the model. During the training process, the model is repeatedly applied with the training data. The weight  $w$  and bias  $b$  are adjusted automatically until the desired output mapping occurs. The parameters in the model are captured based on a gradient descent optimization algorithm by using the Python compiler.

In the dataset, each observation has multiple independent variables, therefore various features need to be identified before being chosen as the input vector. Feature evaluation and integration are very important for the forecasting problem under study. The number of input neurons helps reveal the relations between observations, hence influencing the performance of the model. The neurons in the hidden layer establish the computational relation between the neurons in the input layer and output layer.

Note that  $\mathbf{X}$  is the input vector of the model, and  $\hat{\mathbf{Y}}$  is the output vector or the forecast values. An appropriate transfer function is stored in the hidden layer and used for processing the data from the input nodes. Each neuron in the hidden layer receives weighted inputs plus bias from each neuron in the previous layer, and is defined as,

$$z_i = \sum_{k=1}^{N_{j-1}} x_{j-1,k} w_{k,i} + b_i \quad (3.1)$$

where

$w_{k,i}$  = the weighted connection between node  $k^{\text{th}}$  and all the nodes in the previous layers.

$x_{j-1,k}$  = input value form  $k^{\text{th}}$  node in the  $j^{\text{th}}$  layer.

$b_i$  = the bias to the node.

$N_{l-1}$  = the number of nodes in the layer  $l-1$ .

This sum is passed along to an activation function,  $g()$  is activation function to capture the nonlinear behaviors and produce the output of the node. It is calculated as:

$$\hat{Y}_k = g(z_i) \quad (3.2)$$

The task of the backpropagation algorithm is to minimize the cost function  $J_w$  that is often expressed as mean square error as follows,

$$J_w = \frac{1}{N} \sum_{n=1}^N (Y_n - \hat{Y}_n)^2 \quad (3.3)$$

where  $N$  represents the number of observations used in the training set. However, the determination of the number of input and hidden layer nodes is vitally important, yet cumbersome. Architectures with different numbers of hidden layers and the size of a hidden layer need to be compared to identify the model with the best performance. To avoid the overfitting issue, the available data set should be divided into three parts:

training dataset, validation dataset, and testing dataset. The validation dataset is used to monitor and handle the model whether it is overfitting or not. The key-process of constructing the model is illustrated in Figure 3.4.

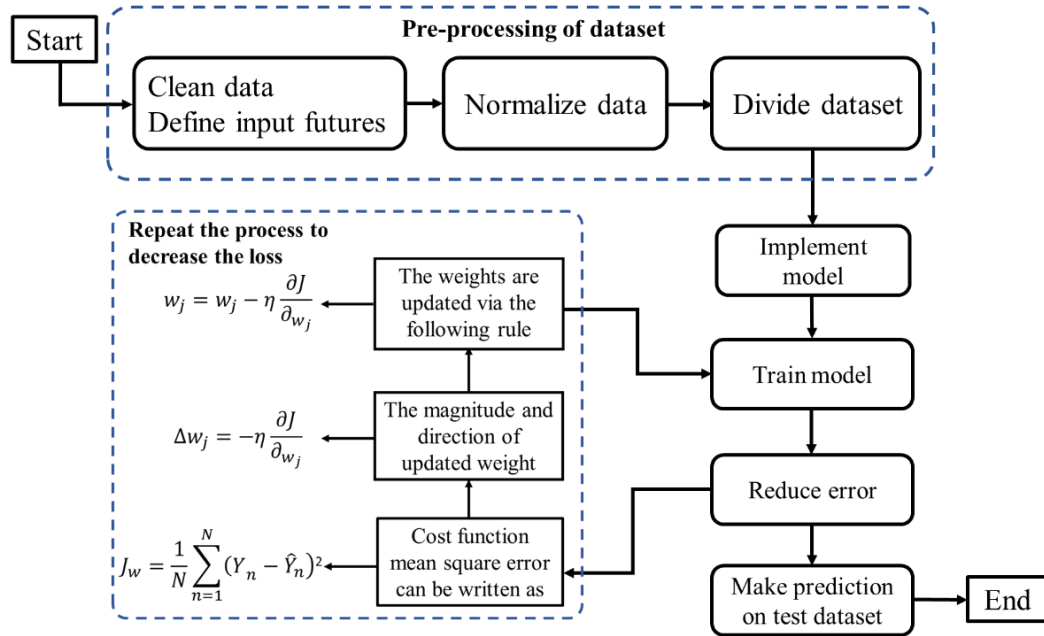


Figure 3.4: Model Development and Training Process.

### 3.2.2 Backpropagation Algorithm

The ability to self-improving performance through the training process is the neural network's fundamental capability. Backpropagation (BP) is the most popular algorithm to train the FNN model. The BP algorithm is widely used in solving classification and regression forecasting problems. The learning mechanism involves two phases: Phase 1 is a feed-forward process in which the information at the input nodes is propagated to compute the output at the output neurons; Phase 2 is called a backward process in which the connection weights and biases are adjusted through gradient descent optimization. The BP algorithm calculates the error gradients and distributes them backward to update the weights in the next iteration.

Suppose,  $\mathbf{Y}$  is the observation vector. In the first phase (i.e., forward-pass),  $x_i$  is fed into the input layer, and the output value is generated based on the current weights  $w$ . The goal is to find a well-trained mathematical model and adjust the weights by minimizing the mean square error (MSE) as follows,

$$\text{Min: } MSE = \frac{1}{n} \sum (Y - \hat{Y})^2 \quad (3.4)$$

In the second phase, a gradient descent in the weights,  $w$ , is used to locate the optimal solution under the delta rule. The weight adjustment can be done via stochastic gradient descent using the following equation,

$$w_{new} = w_{old} - \eta \nabla E(w) , \quad (3.5)$$

where  $\eta$  is the learning rate between 0 and 1. The learning rate governs the change amount of the weight as per the effect of the weight on the total error.  $\nabla$  is gradient operator, and  $\nabla E$  is the gradients of error function.

### 3.2.3 Activation Function

The activation function, also called the transfer function, translates the input signals into output signals, such that the output is between certain values. In this study, two activation functions are adopted in the computation of Softmax for logistic regression problem and linear function for regression problem.

A sigmoid function is a mathematical function having an S-shaped curve. It belongs to the non-linearity function family. Quite often sigmoid function refers to the standard logistic function. A sigmoid function, denoted by  $g()$ , with logistic function is given as

$$g(x) = \frac{1}{1 + e^{-x}} \quad (3.6)$$

Sigmoid function produces a curve with an S-shape in Figure 3.5. It can be used in the binary classification model. Sigmoid function maps input data into a value in the range between [0,1].

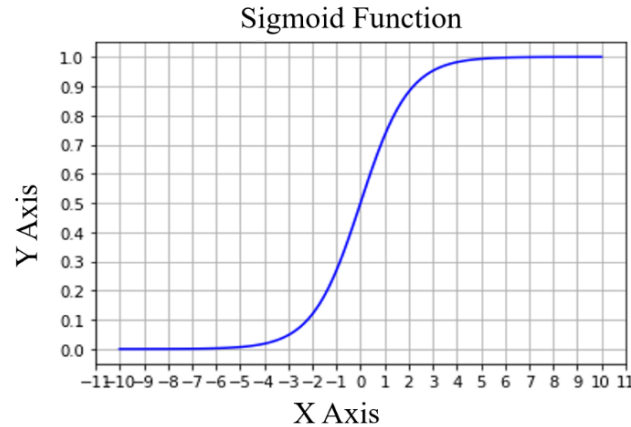


Figure 3.5: Output Characteristic Curve of Sigmoid Function.

Softmax is an activation function frequently used in multi-classification tasks. It is an exponential function as shown in Equation (3.7), which can enlarge differences, i.e., pushing the biggest value of  $Z_i$  closer to one while the smallest closer to zero. It turns scores logits into probability values that sum to one. The essential goal of Softmax is to turn a number into a probability value. That is,

$$f(Z_i) = \frac{e^{Z_i}}{\sum_{j=1}^M e^{Z_j}}, \quad i=1, 2, \dots, k. \quad (3.7)$$

In Equation (3.7),  $Z_i$  is the score for neuron  $i$  in hidden layer. Figure 3.6 shows the fundamental property of Softmax function. A higher input value results in a larger probability.

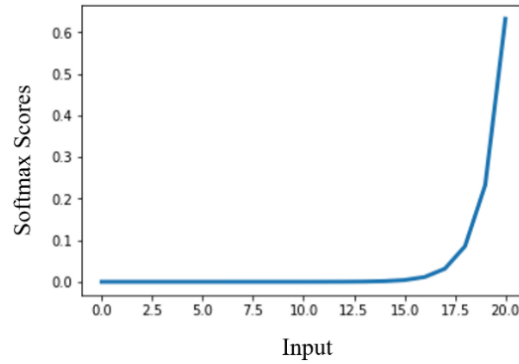


Figure 3.6: Output Characteristic Curve of Softmax Function.

### 3.3 Performance Evaluation Approaches

This study adopts the two popular performance measures to test the efficiency of the proposed model: the mean absolute error (MAE), and the root mean square error (RMSE). The performance measures of MAE and RMSE are utilized to quantify the errors of forecasting values. Both RMSE and MAE have the same unit as the observation data. MAE is a measure of the average of the absolute error, and the advantage is that the metric is relatively easy for non-specialists to understand. MAE is defined as follows

$$\text{MAE} = \frac{1}{HN} \sum_{n=1}^N \sum_{h=1}^H |Y_{n,h} - \hat{Y}_{n,h}| \quad (3.8)$$

RMSE is a quadratic scoring rule that also measures the average magnitude of the error, which is more frequently used in error evaluation. RMSE differs from MAE in that it can amplify and punish large errors terms. RMSE is defined as

$$\text{RMSE} = \sqrt{\frac{1}{HN} \sum_{n=1}^N \sum_{h=1}^H (Y_{n,h} - \hat{Y}_{n,h})^2} \quad (3.9)$$

where

$n$  = the number of observations.

$h$  = the forecasting horizons.

$\hat{Y}_{n,h}$ ,  $Y_{n,h}$  = represented the forecast and observed values, respectively.

Cross entropy is the cost function for the classification model, which is used to measure the error between the predicted value and observation. In binary classification task, the cost can be estimated by

$$H(y, p) = - \sum_{i=1}^N (y_i \log(p_i) + (1 - y_i) \log(1 - p_i)) \quad (3.10)$$

In the multi-classification task model, a separate loss for each class label per observation is added first, then the loss function is listed below:

$$H(y_i^c, p_i^c) = - \sum_{i=1}^N \sum_{c=1}^M y_i^c \log(P_i^c) \quad (3.11)$$

where

$M$  = the number of classes.

$N$  = the number of observations.

$Y_i^c$  = binary indicator. If class label  $c$  is the correct classification for observation  $i$ ,

$Y_i^c$  equals one.

$P_i^c$  = predicted probability observation  $i$  is of class  $c$ .

The performance of weather classification models is assessed using confusion matrix (Provost and Kohavi, 1998) and percentage of correct classification. The confusion matrix is a standard tool for evaluating model performances for classification problems and widely employed in the machine learning field. It contains information about actual and predicted classifications done by a classification system. The performance of such systems is commonly evaluated using the data in the  $n$ -by- $n$  matrix, where  $n$  is the number of classes. Figure 3.7 shows a confusion matrix for a two-class classifier.

		Predicted class	
Actual class		True Positive (TP)	False Negative (FP)
		False Positive (FN)	True Negative (TN)
		Precision $\frac{TP}{TP + FP}$	Negative Predictive Value $\frac{TN}{TN + FN}$
		Sensitivity $\frac{TP}{TP + FN}$	Specificity $\frac{TN}{TN + FP}$
		Accuracy $\frac{TP + TN}{TP + TN + FP + FN}$	

Figure 3.7: Confusion Matrix for a Two-class Model.

Accuracy is a criterion how to evaluate the ability of a classifier. The accuracy of the predictor indicates how well a given predictor can guess the value of the predicted attribute for new data. Accuracy (ACC, %) for two classes can be calculated and given in Figure 3.7. The following accuracy assessment approach is used to estimate the performance of the model with multi-classes.

$$ACC = \frac{TP+TN}{TP+TN+FP+FN} \quad (3.12)$$

The accuracy is simplified as follows,

$$ACC_{(Y_i-\hat{Y}_i)} = \frac{1}{N} \sum_{i=1}^N 1 \quad \text{when } \hat{Y}_i = Y_i \quad (3.13)$$

### 3.4 Wind Speed Forecasting Models and Results

The climate behavior of future years can be conjectured and forecasted based on current and historical climate data. The prediction models for short-term and long-term wind speed forecasting are presented in this subsection. The existing forecasting methods including the persistence model, ARIMA model, and univariate FNN are briefly reviewed as they are used for comparison with the proposed model.

### 3.4.1 Persistence Forecasting Model

The persistence method is adopted as the benchmark to compare the forecasting performances with ARIMA, FNN, and the proposed hybrid model. Persistence method is a simple way to forecast the wind speed and is often used as a reference to evaluate the performance of other prediction methods. This method assumes that the wind speed at time  $t+\Delta t$  is the same as it was at time  $t$  where  $\Delta t$  is the time increment or step size. The ideal is derived from the fact that a high correlation exists between the present and the future wind speed. Let  $Y_t$  and  $\hat{Y}_{t+\Delta t}$  be the observed wind speed at  $t$  and the predicted speed at  $t+\Delta t$ , respectively. The persistence model is given as follows,

$$\hat{Y}_{t+\Delta t} = Y_t, \quad \text{for } t=1, 2, \dots, T. \quad (3.14)$$

### 3.4.2 ARIMA Forecasting Model

ARIMA model is built upon the Box-Jenkins methodology, which best fits the time series data with non-seasonal behavior. A time series model reproduces future value based on the prior pattern of variables. The univariate method employs ARIMA model with only one type of data information as the variable. A standard notation is used for ARIMA  $(p, d, q)$ , where the integers represent the parameters of a ARIMA model. Let  $y_t$  be the prediction value at time  $t$ . The ARIMA model with  $d = 0$ ,  $p > 0$  and  $q > 0$  is expressed as,

$$\begin{aligned} y_t &= \sum_{i=1}^p \varphi_i y_{t-i} + \mu + \sum_{j=1}^q \phi_j \varepsilon_{t-j} + \varepsilon_t \\ &= \mu + \varphi_1 y_{t-1} + \varphi_2 y_{t-2} + \dots + \varphi_p y_{t-p} + \varepsilon_t + \phi_1 \varepsilon_{t-1} + \phi_2 \varepsilon_{t-2} + \dots + \phi_q \varepsilon_{t-q} \end{aligned} \quad (3.15)$$

where

$p$  = the number of lag observations in the model, also called the lag order.

$d$  = the number of times that the raw observations are different, also called the degree of differencing.

$q$  = the size of the moving average window, called order of moving average.

$\varphi_i$  = the  $i^{\text{th}}$  autoregressive coefficient.

$\phi_j$  = the  $j^{\text{th}}$  moving average coefficient.

$\varepsilon_t$  = error term at time  $t$ .

$\varepsilon_{t-j}$  = the random error of a prior points at time  $t-j$ .

$\mu$  = constant term.

An autoregression (AR) model involves the regressing on its own logged value, a moving average (MA) model uses past errors as the explanatory variables. Discussed by Cochrane (2005), Box et al. (2015), and Hipel and McLeod (1944), the AR ( $p$ ) is a linear model that predicts the present value of a time series using the immediately prior value in time as follows,

$$\begin{aligned}
 y_t &= c + \sum_{j=1}^p \varphi_j y_{t-j} + \varepsilon_t \\
 &= c + \varphi_1 y_{t-1} + \varphi_2 y_{t-2} + \dots + \varphi_p y_{t-p} + \varepsilon_t
 \end{aligned}
 \tag{3.16}$$

Here,  $c$  is a constant,  $\varphi_j$  for  $j=1, 2, \dots, p$  are the model parameters, and  $p$  is the order of the model. Similarly, the MA ( $q$ ) model given by Box et al. (2015), takes the following form,

$$\begin{aligned}
 y_t &= \mu + \sum_{j=1}^q \phi_j \varepsilon_{t-j} + \varepsilon_t \\
 &= \mu + \phi_1 \varepsilon_{t-1} + \phi_2 \varepsilon_{t-2} + \dots + \phi_q \varepsilon_{t-q} + \varepsilon_t
 \end{aligned}
 \tag{3.17}$$

Here,  $\mu$  is the mean of series,  $\phi_j$  for  $j=1, 2, \dots, q$  are the model parameters, and  $q$  is the order of the model.

Real-world time series data is often diverse and may change seasonally, such as energy consumption, temperature change, and wind speed. Since wind speed possesses seasonality, the measured data exhibit non-stationary behavior. A stationary time series means its statistical properties, like the mean and variance, are constant over time. If the time series data is not stationary, it should be differentiated to become stationary.

Many statistical forecasting methods assume that the time series data can be rendered stationary through the transformation. The data is prepared by a degree of differencing to make it stationary, i.e., to remove the trend and seasonal structures that negatively affect the regression model. Data should be differenced and converted into a stationary dataset prior to fitting model. Figure 3.8 shows one-month wind speed data of Wellington after differencing. The differenced data possess a good stationarity behavior compared with the original data. Once the prediction is made on the stationary data, it must be converted back to the original series using the same transformation that made it stationary.

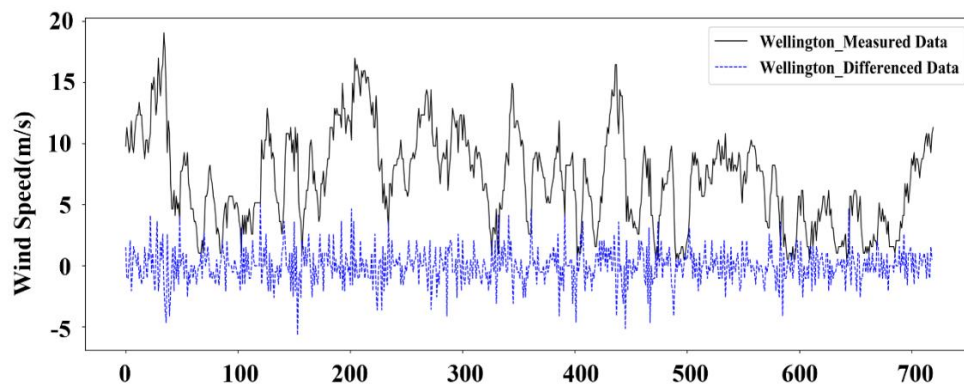


Figure 3.8: Real and Differenced Wind Speed Data in a Month of Wellington.

Three steps are involved in building an ARIMA model: 1) model identification, 2) parameter estimation, and 3) diagnostic checking (Box and Jenkins, 1970). These steps are elaborated next.

Step 1. Model Identification. Autocorrelation function (ACF) and partial autocorrelation function (PACF) can be applied to obtain the preliminary orders of the ARIMA model. This can be done after the original data is transformed with stabilized mean and variance. Graphing the original and the differenced data series, along with autocorrelation and partial autocorrelation functions, are the useful tools. Figure 9 shows the ACF and PACF graphs presented for wind speed time series data of Wellington. If both ACF and PACF show exponential decay and damped sinusoid, other techniques such as Akaike's information criterion, Bayesian information criterion, and grid search could be used to optimize the model structure (Kuha., 2004; Pho et al., 2019).

Step 2. Parameter Estimation. After the model structure is determined, the parameters resulting in the lowest residual need to be estimated. Yule–Walker estimation or maximum likelihood estimation can be applied to estimate the parameter values, and uncorrelated residuals can be identified using non-significant P-values.

Step 3. Diagnostic Checking. After the model structure and parameters are determined, diagnostic checks are used to examine the model adequacy and make further improvements. If the model is a good fit to the data, the residuals would be white noise with little or no autocorrelation.

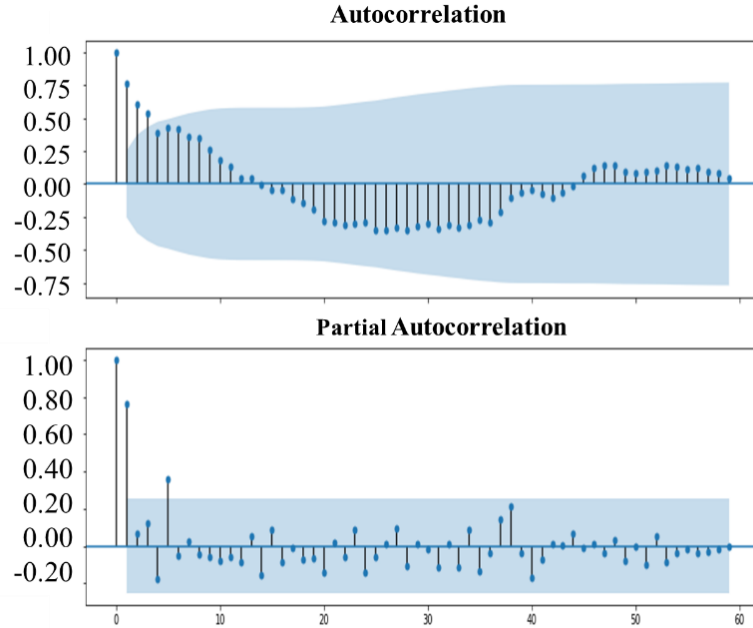


Figure 3.9: ACF and PACF of Wind Data in Wellington.

The ARIMA model is used to detect the existing relation between the current observation and the previous observations. It further determines the optimal input neuron that is associated with the autocorrelation between wind speeds. To ensure the best performance of ARIMA model, its most effective structure in terms of model parameters  $(p, d, q)$  should be established.

In this study, let the order of the model vary within  $p \in \{1, 2, \dots, 8\}$ ,  $q \in \{1, 2, \dots, 8\}$ , and  $d \in \{0, 1\}$ . Five days of learning interval is used to select the best performance of ARIMA model based on minimum RMSE or MAE. By running the combinations of each parameter, the ARIMA model with the best preference for each city is selected and summarized in Table 3.1. The sign and the coefficient indicate the relation and strength between wind speed data. For instance, the current wind speed  $y_t$  has the positive correlation with  $y_{t-1}$ ,  $y_{t-3}$ ,  $y_{t-4}$  and negative correlation with  $y_{t-2}$  in Wellington. The ARIMA model with  $(4, 0, 2)$  appears to be the best fit for the wind speed forecasting in

Wellington and Phoenix. Similarly, ARIMA (2, 0, 1) becomes the best structure for San Francisco, and ARIMA (3, 0, 1) is the best for Boston, etc.

Table 3.1: ARIMA Model Structure for Testing Cities.

Cites	ARIMA ( $p, d, q$ )	Model
Wellington	(4, 0, 2)	$y_t = 2.12y_{t-1} - 1.59y_{t-2} + 0.36y_{t-3} + 0.02y_{t-4} + \varepsilon_t - 1.3\varepsilon_{t-1} + 0.56\varepsilon_{t-2}$
San Francisco	(2, 0, 1)	$y_t = y_{t-1} - 7.4y_{t-2} + \varepsilon_t - 2.3\varepsilon_{t-1}$
Phoenix	(4, 0, 2)	$y_t = -0.5y_{t-1} - 0.12y_{t-2} + 0.76y_{t-3} + 0.08y_{t-4} + \varepsilon_t + 1.1\varepsilon_{t-1} + 0.99\varepsilon_{t-2}$
Boston	(3, 0, 1)	$y_t = 0.2y_{t-1} - 0.32y_{t-2} + 0.43y_{t-3} + \varepsilon_t - 0.91\varepsilon_{t-1}$
New York	(4, 0, 1)	$y_t = 1.4y_{t-1} - 0.81y_{t-2} + 0.76y_{t-3} + 0.48y_{t-4} + \varepsilon_t + 0.1\varepsilon_{t-1}$
Sanya	(3, 0, 2)	$y_t = -1.25y_{t-1} + 0.82y_{t-2} + 0.54y_{t-3} + \varepsilon_t + 2.1\varepsilon_{t-1} - 0.89\varepsilon_{t-2}$

### 3.4.3 Hybrid Short-term Forecasting Model

The hybrid approach combines at least two different methods among physical methods, statistical methods, or AI approaches, to construct the prediction function and obtain the optimal forecasting results with reduced error. The proposed hybrid model in this study integrates meteorological features, time series techniques, and BP algorithm for short-term wind speed prediction. Compared with traditional approach, the hybrid model not only considers the wind speed attribute but also incorporates other meteorological features.

It is well documented in the literature that ARIMA and neural network models have their own advantages, and none of them can exceed the other in terms of forecasting accuracy. ARIMA ( $p, d, q$ ) model can capture linearity information and decide the number of input neurons correlated with wind speed. Compared with FNN, ARIMA has a deficiency in handling nonlinear characteristics of data series, such as wind speed. Hence, the performance of both forecasting methods largely depends on the data characteristics.

The proposed methodology is expected to capture both linear and nonlinear characteristics between the inputs and outputs. Since, the future climate condition involves large amounts of uncertain factors, choosing the input features of the model becomes a critical issue to obtain the optimal prediction result. In this study, the meteorological information of each location is considered as variables in the model.

Based on above materials, the development of the hybrid forecasting model consists of four steps shown in Figure 3.10: 1) using ARIMA model to capture wind speed autocorrelation; 2) obtaining the correlation between different feature pairs; 3) training various input features model and identifying the one with minimum error; and 4) generating the forecasting data based on the selected model.

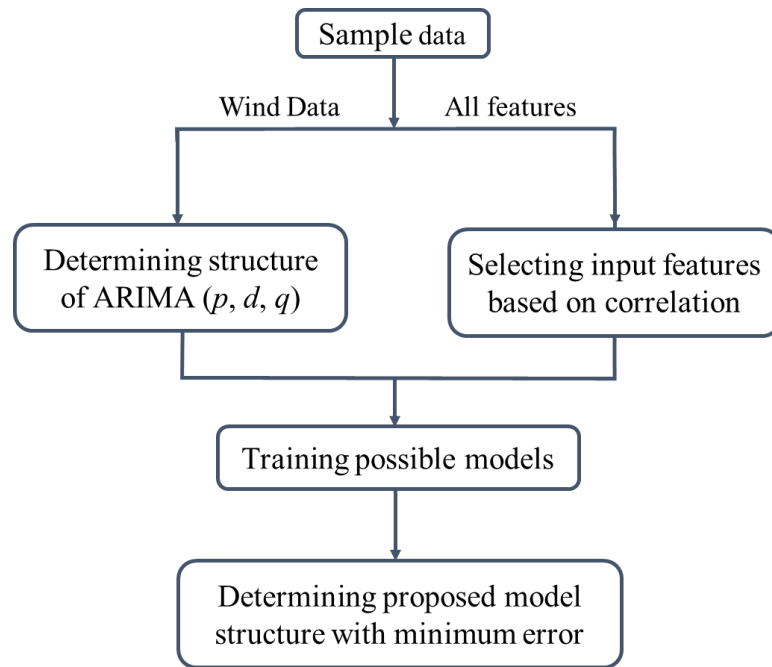


Figure 3.10: Flowchart for Construct Proposed Model.

#### 3.4.4 Short-term Wind Speed Forecasting Result and Comparison

According to Table 3.2, the prediction accuracy decreases with the increase of the forecasting horizon, but the degradation of accuracy is non-linear in terms of RMSE and

MAE. For example, the MAE value for 1-hour ahead forecasting based on ARIMA is 0.82 m/s, while the values for 3-, 8-, 12-, and 24-hour ahead forecasting is 1.2 m/s, 1.68 m/s, 1.75 m/s, and 2.3 m/s in Wellington, respectively. Similar trends can be observed in other testing cities.

To see the gap between the ARIMA prediction values and the actual wind speed observations, Figure 3.10 shows 1-hour and 24-hour ahead predictions along with the measured wind speeds over a 24-hour period in Wellington. The solid line is the actual observation curve, the dot dash curve is the 1-hour ahead forecasting and the dashed curve is the day-ahead forecasting. The 1-hour ahead forecasting is quite close to the actual observation, whereas the day ahead forecasting becomes more flattened out and smoother. For instance, the lowest wind speed in a day happens at 11am. and the occurrence time based on 1-hour ahead forecasting is at 12 noon time.

Table 3.2: Forecasting Results of ARIMA Model with Five Forecasting Horizons.

Location	Error (m/s)	ARIMA				
		1-hr	3-hr	8-hr	12-hr	24-hr
Wellington	RMSE	0.93	1.8	1.92	2.1	3.0
	MAE	0.82	1.2	1.68	1.75	2.3
San Francisco	RMSE	0.91	1.39	1.41	1.48	1.5
	MAE	0.96	1.22	1.22	1.26	1.28
Phoenix	RMAE	0.4	0.836	0.85	0.87	0.96
	MAE	0.409	0.73	0.736	0.75	0.84
Boston	RMSE	0.78	1.41	1.51	1.81	2.63
	MAE	0.67	1.28	1.33	1.2	1.58
New York	RMSE	0.81	1.39	1.39	1.41	1.98
	MAE	0.76	1.22	1.22	1.2	1.77
Sanya	RMAE	0.88	0.99	1.59	1.92	2.32
	MAE	0.82	0.88	1.42	1.71	2.05

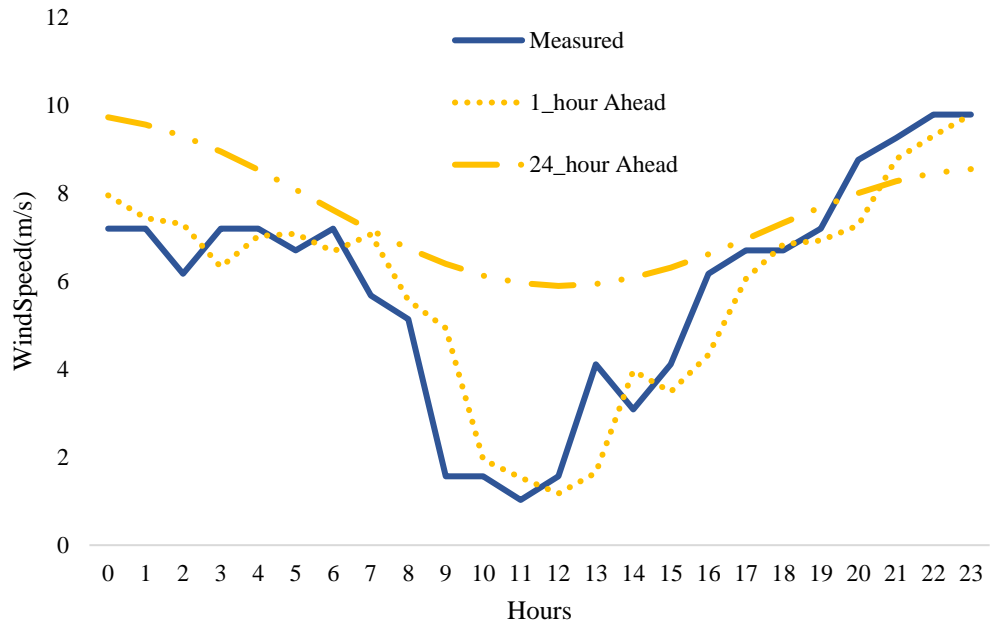


Figure 3.11: ARIMA Model Forecasting Result in Wellington.

In this section, the meteorological information of each city is considered as multivariable in the hybrid short-term forecasting models. Table 3.1 shows the parameter value of ARIMA model of the wind speed. Figure 2.8 depicts the correlation between wind speed and other critical variables. The grey boxes represent some insignificant correlations. For instance, wind speed and wind direction are correlated because they are influenced by the Earth’s rotation. Thus, the approach may consider wind direction, air pressure, temperature, and dew point as predictors or input variables.

Table 3.3 presents five multivariate forecast models for Wellington wind data with the aim of selecting the optimal input features. Similar models can also be constructed for other cities.

Table 3.3: Models with Various Input Features for Wellington.

Models	Predictors
Model 1	'WindSpd <sub>(t-4)</sub> ', 'WindSpd <sub>(t-3)</sub> ', 'WindSpd <sub>(t-2)</sub> ', 'WindSpd <sub>(t-1)</sub> ', 'WindDir_sin <sub>(t-1)</sub> ', 'WindDir_cos <sub>(t-1)</sub> '
Model 2	'WindSpd <sub>(t-4)</sub> ', 'WindSpd <sub>(t-3)</sub> ', 'WindSpd <sub>(t-2)</sub> ', 'WindSpd <sub>(t-1)</sub> ', 'WindDir_sin <sub>(t-1)</sub> ', 'WindDir_cos <sub>(t-1)</sub> ', "AirPressure <sub>(t-1)</sub> "
Model 3	'WindSpd <sub>(t-4)</sub> ', 'WindSpd <sub>(t-3)</sub> ', 'WindSpd <sub>(t-2)</sub> ', 'WindSpd <sub>(t-1)</sub> ', 'WindDir_sin <sub>(t-1)</sub> ', 'WindDir_cos <sub>(t-1)</sub> ', "AirPressure <sub>(t-1)</sub> ", "Humidity <sub>(t-1)</sub> "
Model 4	'WindSpd <sub>(t-4)</sub> ', 'WindSpd <sub>(t-3)</sub> ', 'WindSpd <sub>(t-2)</sub> ', 'WindSpd <sub>(t-1)</sub> ', 'WindDir_sin <sub>(t-1)</sub> ', 'WindDir_cos <sub>(t-1)</sub> ', "AirPressure <sub>(t-1)</sub> ", "Humidity <sub>(t-1)</sub> ", 'Temperature <sub>(t-1)</sub> '
Model 5	'WindSpd <sub>(t-4)</sub> ', 'WindSpd <sub>(t-3)</sub> ', 'WindSpd <sub>(t-2)</sub> ', 'WindSpd <sub>(t-1)</sub> ', 'WindDir_sin <sub>(t-1)</sub> ', 'WindDir_cos <sub>(t-1)</sub> ', "AirPressure <sub>(t-1)</sub> ", "Humidity <sub>(t-1)</sub> ", 'Temperature <sub>(t-1)</sub> ', 'Dewpoint <sub>(t-1)</sub> '

Since the wind direction is a circular variable, it is decomposed into sine and cosine parts. Among these models, Model 4 has the best performance because RMSE and MAE are the smallest as shown in Figure 3.12. If more features are incorporated in the input set, the model may not always improve the prediction accuracy compared with Model 4. Therefore, it can be concluded that wind direction, humidity, air pressure, and temperature are among the most important data for wind speed forecasting model in Wellington because they lead to the minimum RMSE and MAE errors.

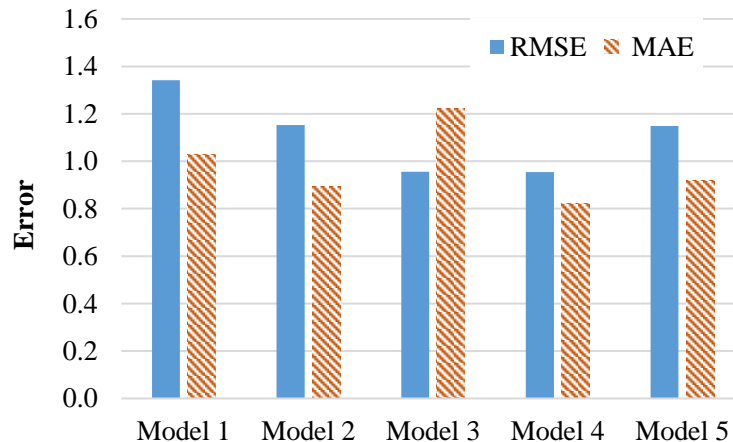
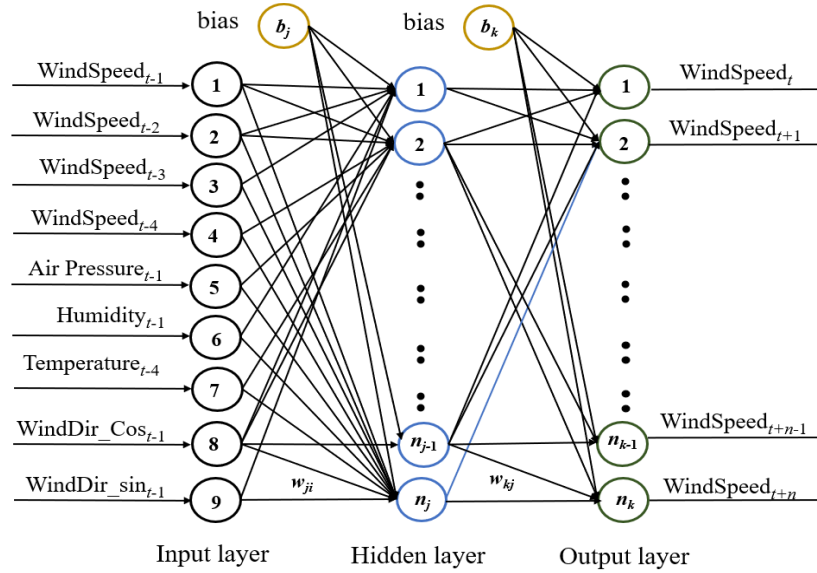
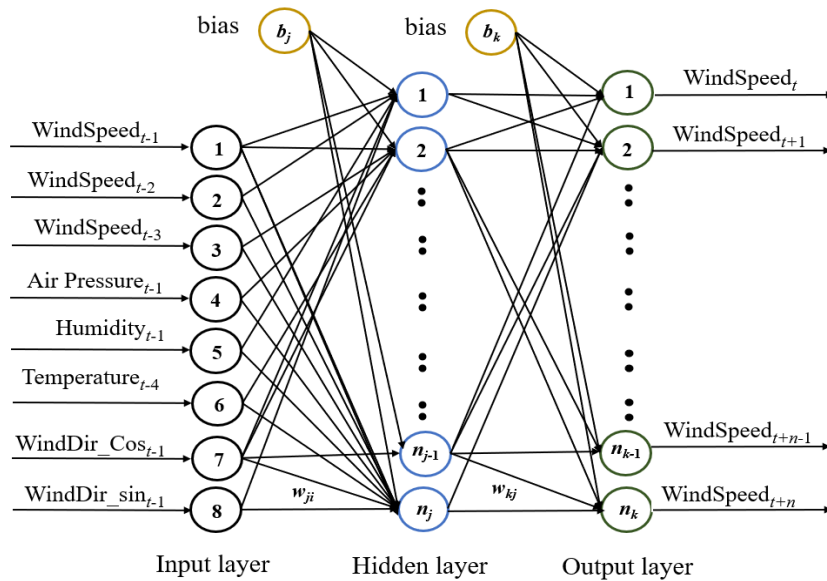


Figure 3.12: Comparisons of Forecasting Models under Different Predictors.

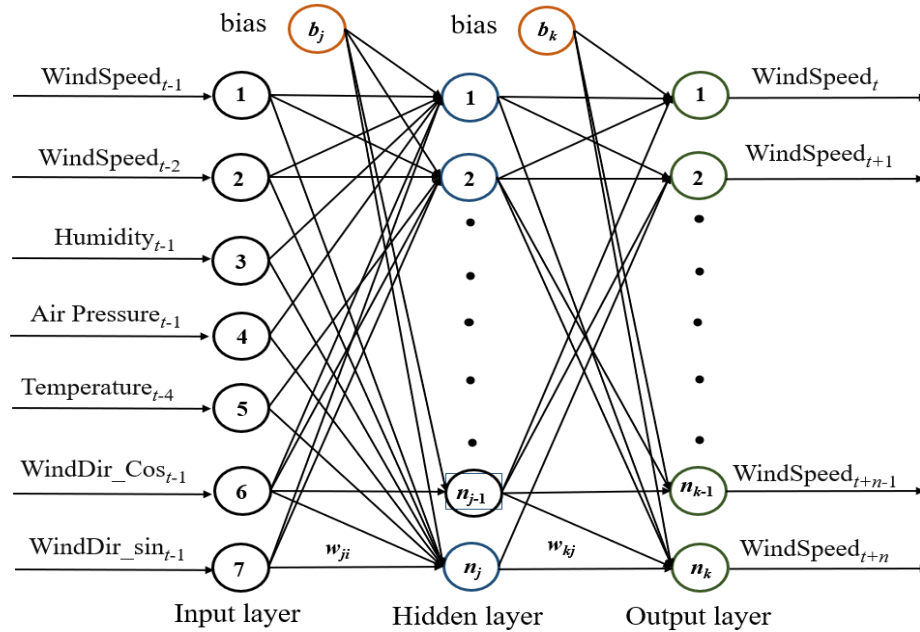
Based on the comparison results, the neurons at the input and output layers are shown in Figure 3.13(a) for Wellington, Phoenix, and New York. Figure 3.13(b) is for Boston and Sanya, and Figure 3.13(c) represents San Francisco. There are nine input neurons for Wellington, Phoenix, and New York. However, only seven input neurons are needed for San Francisco.



(a). Wellington, Phoenix and New York.



(b). Boston and Sanya.



(c). San Francisco.

Figure 3.13: Structure of Hybrid Wind Speed Forecasting Model.

The comparison in Table 3.4 shows that the performance of ARIMA is still better than the proposed model and persistence model in 1-hour ahead forecasting. RMSE is reduced by 6.1% compared to ARIMA with persistence model. The proposed hybrid model only improves 5.6% of RMSE compared with the persistence model.

Table 3.4: Comparisons with Persistence Model in 1-hour Ahead Forecasting.

Improvement	ARIMA model	Proposed model
RMSE	6.1%	5.6%
MAE	3.4%	1.3%

Figure 3.14 displays the 1-hour ahead forecasting results obtained with the ARIMA, FNN, and proposed models with the actual data in Wellington. The proposed model and ARIMA model follow the actual data quite well, meanwhile, a delay exists in the prediction obtained from the ANN model. It is observed that MAE and RMSE for the ARIMA model are considerably lower than the other two models.

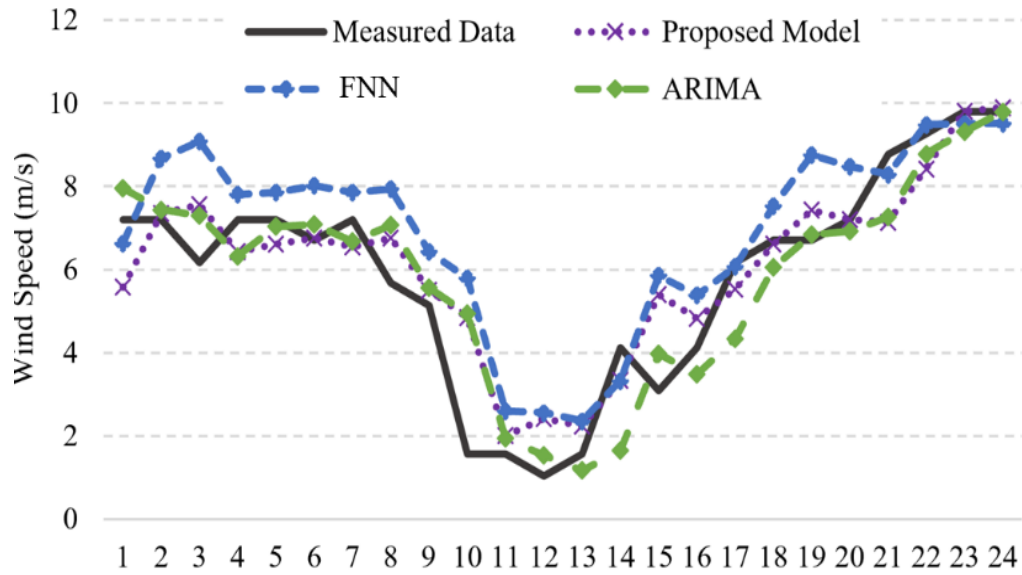
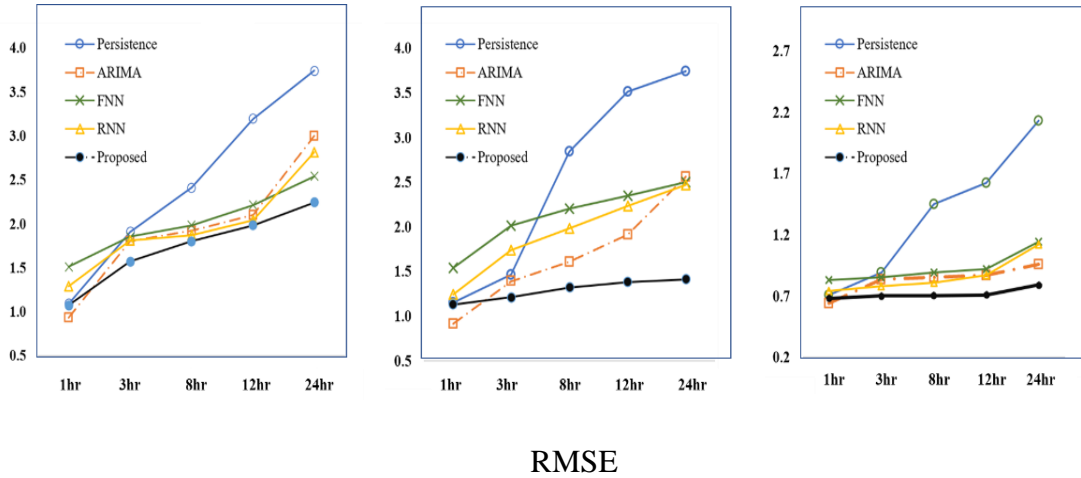


Figure 3.14: Comparisons of 1-hour Ahead Forecasting Models in Wellington.

Table 3.5 shows the measured errors of various forecasting horizons based on ANN and the proposed forecasting model of testing cities. The performance of FNN model becomes worse than the proposed model when the forecasting horizons extended.

Table 3.5: Comparisons between Hybrid Model and FNN Model.

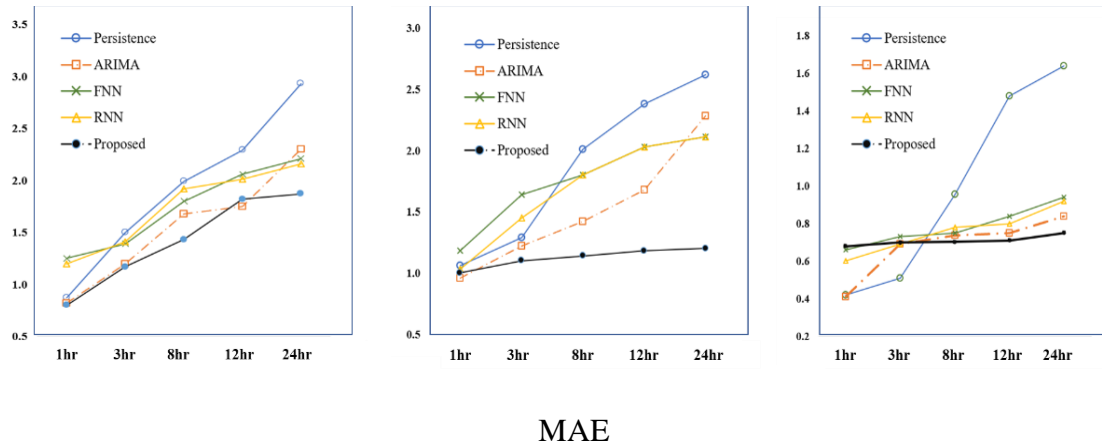
Cities	Indexes (m/s)	FNN					Proposed				
		1- hr	3- hr	8- hr	12- hr	24- hr	1- hr	3- hr	8- hr	12- hr	24- hr
Wellington	RMSE	1.5	1.8	1.9	2.1	2.4	1.07	1.57	1.8	1.98	2.24
	MAE	1.2	1.3	1.8	2.0	2.2	0.8	1.17	1.43	1.82	1.87
San Francisco	RMSE	1.5	2.0	2.2	2.3	2.5	1.23	1.31	1.32	1.38	1.41
	MAE	1.1	1.6	1.8	2.0	2.1	1.0	1.1	1.14	1.18	1.2
Phoenix	RMSE	0.8	0.9	0.9	0.9	1.1	0.71	0.74	0.76	0.79	0.93
	MAE	0.7	0.7	0.7	0.8	0.9	0.68	0.7	0.70	0.71	0.75
Boston	RMSE	0.9	1.2	1.5	1.7	2.4	0.89	0.98	1.31	1.68	2.03
	MAE	0.8	1.1	1.3	1.4	2.2	0.76	0.86	1.11	1.24	1.89
New York	RMSE	1.1	1.2	1.4	1.8	2.4	1.03	1.17	1.39	1.65	2.28
	MAE	0.9	1.1	1.2	1.6	2.1	0.94	1.08	1.18	1.47	2.04
Sanya	RMSE	0.9	1.2	1.2	1.6	2.2	0.91	1.02	1.23	1.59	1.93
	MAE	0.9	0.9	1.1	1.4	1.9	0.87	0.89	1.11	1.42	1.85



(a). Wellington

(b). San Francisco

(c). Phoenix



(a). Wellington

(b). San Francisco

(c). Phoenix

Figure 3.15: Comparisons of RMSE and MAE among Five Models for Three Cities.

It is observed that the MAE and RMSE of the proposed model are considerably lower than other models. Tables 3.2, 3.4, 3.5, and Figure 3.15 indicate that: 1) the larger number of forecasting horizon, the lower the accuracy; 2) the proposed model yields better performance in multi-hour forecasting. The most significant drop in performance occurs when the forecasting horizon increases from 3-hour to 8-hour. The degradation of performance tends to be flat as the forecasting horizon increases from 8-hour to 24-hour. The 8-hour and 12-hour ahead forecasting result are quite acceptable. The 24-hour ahead

forecasts appeared to be too rough estimates. Therefore, the additional techniques should be added to ARIMA model, FNN, and RNN model to improve the performance on one day ahead forecasting model; 3) by combining the physical features and statistical prediction techniques, the hybrid model exhibits high accuracy which is up to 45% than the FNN method in the day ahead forecasting. On the other hand, the proposed method does not outperform the ARIMA model for 1-hour ahead forecasting.

The black solid line and dashed line represent the actual observation and the forecasting value, respectively. The shaded areas display 95% prediction interval (PI) for various models in Figure 3.16. The smallest width of PI is obtained by the proposed model.

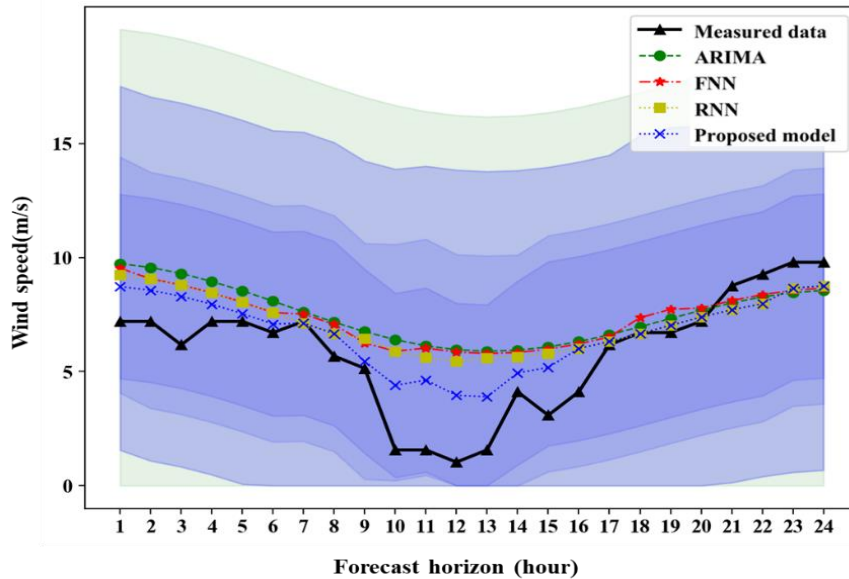


Figure 3.16: Prediction Intervals in Day-ahead Prediction Models.

To assess the performance of the hybrid model, several findings are obtained from the numerical comparisons. First, wind direction is found to be the most significant feature in the multivariate hybrid model, and it improves the prediction performance and leads to much better forecasting. Second, the proposed hybrid model outperforms the

benchmark results of four existing models in 3- to 24-hour ahead prediction. Third, ARIMA model generally outperforms neural network models in 1-hour ahead forecasting. Hence, it is concluded that the proposed methods cannot always improve the prediction result, especially in 1-hour ahead prediction. Fourth, all models result in a good prediction if wind speed involves smaller variations between consecutive hours. The prediction error exhibits a certain relation with wind speed, and a small prediction error can be achieved for the wind speed with a small-scale standard deviation. The forecasting result in Phoenix is better than all other cities owing to the lowest standard deviation of wind speed.

There are two interesting directions worth further investigation. First, wind and solar are complementary in terms of renewable power generation. Utility companies often purchase both wind and solar from the day-ahead market, hence it is desirable to develop an integrated model that jointly forecasts wind speed and weather conditions. Second, with the advance of sensor technology and Internet of Things, it is foreseeable that in-situ measurement of topography parameters can be realized cost-effectively. Hence more accurate and reliable wind speed prediction will be anticipated by combining physical and data-driven methods. The proposed approach provides a new and viable option for wind forecasting applications in that they outperform the single forecasting models on many occasions by incorporating both physical and data-driven methods.

#### 3.4.5 Deep Learning Long-term Wind Speed Prediction Model

Long-term forecasting of wind speed has attracted much attention in many different areas, such as restructured electricity markets, wind farm optimal design, especially in the renewable power system with the energy storage device, wind turbine,

and solar PV generator. Table 3.6 describes the input variables for the long-term wind speed forecast model.

Table 3.6: Input Variables for Long-term Deep Learning Prediction Model.

Input Variable	Explanation
Input 1	The monthly trend variable.
Input 2	The daily trend variable.
Input 3	Previous year' hourly record variable.
Input 4	Geography impact factors latitude.
Input 5	Geography impact factors longitude.
Input 6	Geography impact factors evaluation.
Input 7	Meteorology impact factors wind speed.

To determine the best model architecture, the experiment is conducted with the basic validation method. In this study, the number of hidden layers in testing models increases from one, two, and four. The nodes number in each hidden layer varies from 5, 10, and 20, respectively. The performance of each model is recorded in Table 3.7.

Table 3.7: Performance of Deep Learning Model with Different Layers and Neurons.

Number of hidden layers	Size of neurons in each hidden layer	Performance	
		RMSE	MAE
One layer	5	2.122	1.691
Two layers	Hidden_layer_1=5 Hidden_layer_2=5	2.1168	1.677
	Hidden_layer_1=10 Hidden_layer_2=10	2.1165	1.664
	Hidden_layer_1=20 Hidden_layer_2=20	2.106	1.662
	Hidden_layers =5	2.034	1.636
Four layers	Hidden_layers =10	2.013	1.613
	Hidden_layers =20	1.994	1.591

Based on the forecasting result, the accuracy of the model obviously improves when adding one more hidden layer. However, the improvement of accuracy is not significant when increasing the number of hidden layers and neurons in each hidden layer. Hence, a model with a complex structure cannot guarantee the significant enhancement of performance.

### **3.5 Weather Features Forecasting Models and Results**

The objective of this subsection is to predict the weather states based on historical data information. The model will be designed as logistic regression due to the categorical nature of the weather state. Generation of solar PV is depended on the solar irradiation and its own manufactured materials. Logistic regression can be classified into two types: binary classification or multi-classification. Binary logistic regression handles two classes problem when the observed outcome for a dependent variable can only have two possible values (e.g., "clear", "non-clear"). In binary logistic regression, the outcome is usually coded as "0" or "1". Multi-classification strategy works on the model that the outcome of the model has more than two possible values for a dependent variable (e.g., "clear", "partly cloudy", or "overcast"). For this research, a multi-classification model is designed to predict weather state with either continuous or categorical data as the predictor variables.

Some weather states, such as fog, thunderstorms, and haze, account for a very small portion in Phoenix. Hence, they are treated as extreme weather or climate events. These states will not be considered as the input states due to a very tiny portion over the decades. To be conservative in PV generation, these weather states can be grouped as "overcast". Table 3.8 summarizes the proportion of weather states in Phoenix and New

York. In Phoenix, the number of "clear" days accounts for the largest portion, on the contrary, the "MC" has the largest portion in New York.

Table 3.8: Weather States Summary of Phoenix and New York.

States	Proportion (New York)	Proportion (Phoenix)	Cloud fraction (%)
Clear	6.2	27.2	0~25
SC	18.1	14.8	26~50
PC	17.1	26.4	51~75
MC	33.1	25.4	76~99
OC	16.1	4.3	1
Sum	90.6	98.1	1
Rain	6.7	1.5	1
Snow	1.6	0	1

\*Note: Scattered Cloudy = SC, Partly Cloudy = PC, Mostly Cloudy = MC, Overcast = OC.

Table 3.9 displays the consecutive 24 records from two cities in one day that are randomly selected in January and May, respectively. The daily weather profile exhibits various feature events.

Table 3.9: Random 48-hour of Weather States in Phoenix and New York.

Hour	0	1	2	3	4	5	6	7	8	9	10	11	12	13	14	15	16	17	18	19	20	21	22	23
New York																								
Phoenix																								
New York																								
Phoenix																								

### 3.5.1 Markov Model

Berger (2012) defines that a Markov chain (MC) describes a stochastic process that may characterize a system at any time step. It has a wide range of applications in the last decade due to its strong mathematical structure and theoretical basis.  $\mathbf{S} = \{S_1, S_2, \dots, S_n\}$  is a finite set representing a sequence of random variables. This random process is called Markov chain with the following probability,

$$\Pr(S_{t+1}=s | S_1 = s_1, S_2 = s_2, \dots, S_t = s_t) = \Pr(S_{t+1} = s | S_t = s_t) \quad (3.18)$$

Equation (3.18) is referred to as the memoryless property. The Markovian property implies that given the present state, the future probabilistic behavior depends only on the current process state, and independent of its history.

$N$  = the number of the state.

$\mathbf{P}=\{p_{ij}\}$  representing the conditional probabilities, called transition matrix with  $N \times N$  size. The sum of the transition probability from state  $i$  to state  $j$  for all  $j$  must be satisfied.

$$\sum_{j=1}^N p_{ij} = 1, \quad p_{ij} \geq 0 \text{ for } \forall j \text{ and } \forall i \quad (3.19)$$

$$\mathbf{P} = \begin{bmatrix} p_{11} & p_{12} & \cdots & p_{1n} \\ p_{21} & p_{22} & \cdots & p_{2n} \\ \vdots & \vdots & & \vdots \\ p_{n1} & p_{n2} & \cdots & p_{nn} \end{bmatrix}$$

$\boldsymbol{\pi} = \{\pi_i\}$  the initial state distribution, where  $\pi_i$  represents the probability of being in state  $i$  at the beginning of the experiment.

$$\sum_{i=1}^N \pi_i = 1, \quad \pi_i \geq 0, \text{ for } \forall i \quad (3.20)$$

A conditional probability transition matrix governs the probabilities of remaining in the same state or changing to other states. The parameter is obtained by calculating the state occurrence probabilities. Figure 3.17 sets as an example to illustrate the transition matrix with two states.

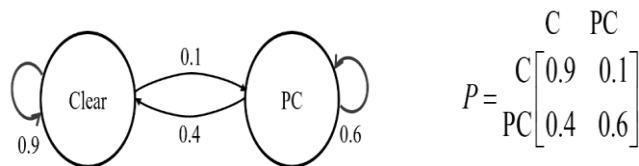


Figure 3.17: Markov Chain with Two States.

First, a 5×5 transition matrix is obtained from categorizing groups of similar states as individual states as in Figure 3.18. **P** is the transition matrix for the weather state of Phoenix (a) and New York (b) by five states.

$$\mathbf{P} = \begin{matrix} & \begin{matrix} \text{Clear} & \text{MC} & \text{PC} & \text{SC} & \text{OC} \end{matrix} \\ \begin{matrix} \text{Clear} \\ \text{MC} \\ \text{PC} \\ \text{SC} \\ \text{OC} \end{matrix} & \begin{bmatrix} 0.8977 & 0.0037 & 0.0001 & 0.0849 & 0.0136 \\ 0.0029 & 0.8190 & 0.0493 & 0.0125 & 0.1163 \\ 0.0008 & 0.2442 & 0.7386 & 0.0012 & 0.0152 \\ 0.1206 & 0.0208 & 0.0004 & 0.7492 & 0.1090 \\ 0.0162 & 0.1397 & 0.0018 & 0.1282 & 0.7141 \end{bmatrix} \end{matrix}$$

(a). Phoenix

$$\mathbf{P} = \begin{matrix} & \begin{matrix} \text{Clear} & \text{MC} & \text{PC} & \text{SC} & \text{OC} \end{matrix} \\ \begin{matrix} \text{Clear} \\ \text{MC} \\ \text{PC} \\ \text{SC} \\ \text{OC} \end{matrix} & \begin{bmatrix} 0.7817 & 0.0079 & 0.1712 & 0.0384 & 0.0009 \\ 0.0002 & 0.7618 & 0.0082 & 0.1183 & 0.1115 \\ 0.1096 & 0.0299 & 0.6538 & 0.2053 & 0.0014 \\ 0.0027 & 0.1981 & 0.0080 & 0.6410 & 0.1502 \\ 0.0002 & 0.1161 & 0.0010 & 0.0096 & 0.8731 \end{bmatrix} \end{matrix}$$

(b). New York

Figure 3.18: 5×5 States Transition Matrix.

### 3.5.2 Hidden Markov Model

Hidden Markov model (HMM) is a statistical model that was first introduced in the 1970s as a tool in speech recognition. It has been extensively used for pattern recognition or character classification problem. HMM is a finite state machine that has a fixed number of states. It provides a probabilistic framework for modeling a time series of multivariate observations. In this research, instead of analyzing the weather state data as a stand-alone time series, it is assigned to be a hidden process of an observation process of atmospheric pressure. Consequently, the aim of this study is to establish the

time transition properties of weather states, given the atmospheric pressure observations. Weather state is treated as a hidden state, whereas air pressure data is treated as the observation in this model.

Except for the number of states in the model, transition matrix and initial state distribution, the following notations will be used in the HMM:

$M$  = the number of distinct observation symbols per state (observation symbols correspond to the physical output of the system being modelled).

$T$  = the length of observation sequence.

$O = (O_1, O_2, O_3, \dots, O_T)$  observation sequence.

$\mathbf{B} = \{b_j(o_t)\}$  observation emission matrix, where  $b_j(o_t)$  represents the probability of observing  $O_t$  at state  $j$ .

$\mathbf{A} = \{a_{ij}\}$  transition matrix, where  $a_{ij}$  represents the transition probability from state  $i$  to state  $j$ .

$$\sum_{m=1}^M b_j(o_m) = 1 \quad (3.21)$$

with

$$a_{ij} \geq 0, \quad b_j(o_t) \geq 0, \quad \text{for } \forall j \text{ and } \forall t \quad (3.22)$$

The atmospheric pressure is selected as the observation of the hidden process of weather state due to the well-known meteorological relation between these two parameters (Khatani and Ghose, 2017). The weather states are discrete data as mentioned above. The simple structure with two weather states under three air pressure observations is plotted in Figure 3.19. The observations have been selected as the numerically rounded air pressure values in a fixed interval and air pressure are classified into 10 levels in this study. The transition matrix of this study is displayed in Figure 3.20.

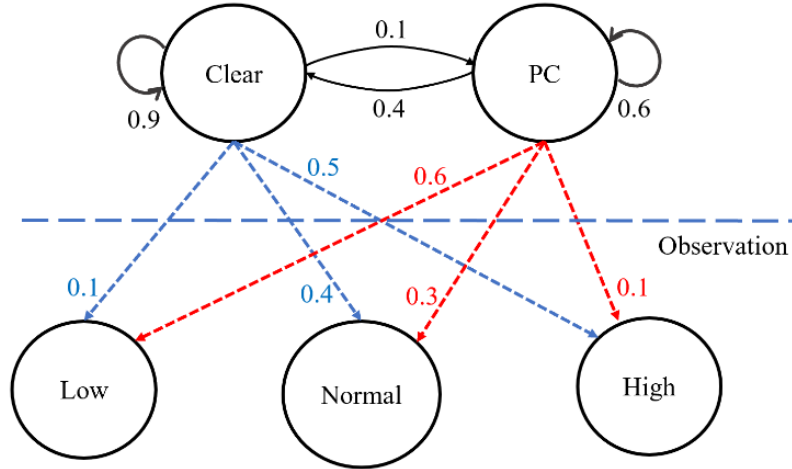


Figure 3.19: HMM Model with Two States and Three Observations.

$$\mathbf{B} = \begin{bmatrix} 0.009 & 0.056 & 0.12 & 0.26 & 0.193 & 0.118 & 0.121 & 0.071 & 0.03 & 0.031 \\ 0.08 & 0.0051 & 0.117 & 0.307 & 0.268 & 0.134 & 0.075 & 0.029 & 0.008 & 0.003 \\ 0.017 & 0.073 & 0.145 & 0.255 & 0.209 & 0.111 & 0.088 & 0.067 & 0.027 & 0.007 \\ 0.006 & 0.103 & 0.181 & 0.25 & 0.213 & 0.134 & 0.063 & 0.035 & 0.013 & 0.003 \\ 0.0 & 0.034 & 0.065 & 0.279 & 0.32 & 0.128 & 0.086 & 0.076 & 0.013 & 0.0 \end{bmatrix}$$

Figure 3.20: Emission Matrix with Five States and Ten Observations.

Overall,  $\lambda = (\mathbf{A}, \mathbf{B}, \boldsymbol{\pi})$  is the definition of HMM model. As mentioned above, the HMM model is characterized by five parameters:  $N$ ,  $M$ ,  $\mathbf{A}$ ,  $\mathbf{B}$  and  $\boldsymbol{\pi}$ . After the HMM structure is determined, the following issues are of interest:

- 1). Given the observation sequence  $O$  and the model  $\lambda = (\mathbf{P}, \mathbf{B}, \boldsymbol{\pi})$ , make an efficient computation of the probability of occurrence for that observation.
- 2). Given the observation sequence  $O$  and the model  $\lambda = (\mathbf{P}, \mathbf{B}, \boldsymbol{\pi})$ , find the optimal state sequence which contributes the maximum probability.
- 3). Given the observation sequence  $O$  and the dimensions  $N$  and  $M$ , adjust model  $\lambda = (\mathbf{P}, \mathbf{B}, \boldsymbol{\pi})$  to maximize the probability of occurrence of the observation.

The proposed problem in this research can be treated as the second issue. The solution to this problem is to obtain the maximum likelihood (ML) and estimate of the

state sequence at  $t$  time, given the transition observations (of size  $t-1$ ) in Equation (3.23):

$$\sigma(t) = \arg \max P(s_t / o_{t-1}), \quad (3.23)$$

where

$O$  = the observations.

$O_{t-1}$  = the observation sequence until the instance ( $t-1$ ).

The Viterbi algorithm aims to find the most likely state sequence by searching for the maximum of  $P(s_t / o_{t-1})$  over all possible transitions. It works by calculating the maximum probability of observing a state after each transition step. In the last step, the state with the maximum probability is selected and traced back to recover the most likely transition sequence (Viterbi, 1967).

### 3.5.3 Recurrent Neural Network Model

In this research, the weather condition data set includes more than ten attributes. Only the most useful or the most relevant features can be taken as the inputs of the model. Guyon and Elisseeff (2003) state that the objective of variable selection is three-fold. First, improving the prediction performance of the predictors. Second, providing faster and more cost-effective predictors. Third, providing a better understanding of the underlying process that generated the data. Eight weather state forecasting models are constructed in order to select the input variables with the best performance.

Table 3.10 shows that a sensible model for the weather state includes  $Y_{t-1}$ . By comparing Models 1 with 2,  $Y_{t-1}$  is clearly a significant predictor. In addition, Models 3-7 do not substantially enhance the fitted model, leading to the conclusion that higher order lagged values of the response are not significant predictors. Model 8 shows the accuracy can be improved when different factors are added in the model. All these models are

trained under the same hyper-parameters' value using the learning rate 0.01 and 20 epochs training process.

Table 3.10: Comparisons of Different Predictors for Weather States Forecasting Model.

Model	Predictors	Accuracy
Model 1	$X_{1,t-1}, X_{2,t-1}, X_{3,t-1}, X_{4,t-1}, X_{5,t-1}$	0.39
Model 2	$X_{1,t-1}, X_{2,t-1}, X_{3,t-1}, X_{4,t-1}, X_{5,t-1}, Y_{t-1}$	0.816
Model 3	$X_{1,t-1}, X_{2,t-1}, X_{3,t-1}, X_{4,t-1}, X_{5,t-1}, Y_{t-1}, Y_{t-2}$	0.8157
Model 4	$X_{1,t-1}, X_{2,t-1}, X_{3,t-1}, X_{4,t-1}, X_{5,t-1}, Y_{t-1}, Y_{t-2}, Y_{t-3}$	0.819
Model 5	$X_{1,t-1}, X_{1,t-2}, X_{2,t-1}, X_{3,t-1}, X_{3,t-2}, X_{4,t-1}, X_{5,t-1}, Y_{t-1}$	0.8167
Model 6	$X_{1,t-1}, X_{1,t-2}, X_{2,t-2}, X_{3,t-1}, X_{3,t-2}, X_{4,t-1}, X_{4,t-2}, X_{5,t-1}, X_{5,t-2}, Y_{t-1}$	0.8153
Model 7	$X_{1,t-1}, X_{1,t-2}, X_{1,t-3}, X_{2,t-2}, X_{2,t-3}, X_{3,t-1}, X_{3,t-2}, X_{4,t-1}, X_{4,t-2}, X_{4,t-3}, X_{5,t-1}, X_{5,t-2}, X_{5,t-3}, Y_{t-1}, Y_{t-2}, Y_{t-3}$	0.8149
Model 8	$X_{1,t-1}, X_{2,t-1}, X_{3,t-1}, X_{4,t-1}, X_{5,t-1}, X_{6,t}, X_{7,t}, Y_{t-1}$	0.8209

\*  $X_{1,t}$  : air pressure at  $t$ ;  $X_{2,t}$ : humidity at  $t$ ;  $X_{3,t}$ : dew point at  $t$ ;  $X_{4,t}$ : wind speed(m/s) at  $t$ ;  $X_{5,t}$ : temperature at  $t$ ;  $X_{6,t}$ :hour sin at  $t$ ;  $X_{7,t}$ :hour cos at  $t$ ;  $Y_t$ : weather states at  $t$ ;

Figure 3.21 (a) displays the comparison of forecasting accuracy from Models 2 to 8. Figure 3.21 (b) plots the comparison of forecasting accuracy between Models 1 and 8, respectively. All denote that the one hour ahead weather condition is a significant estimator in the forecasting process.

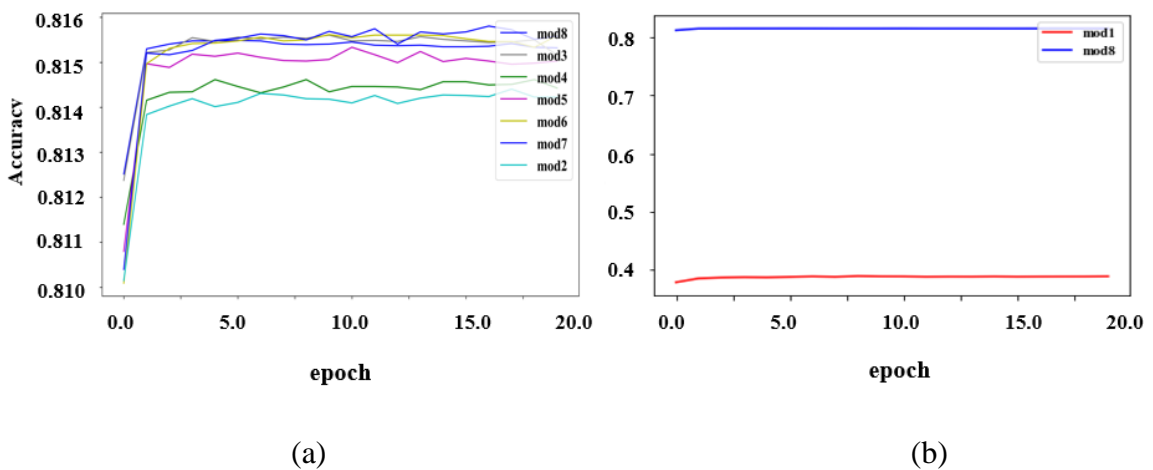


Figure 3.21: Comparison of Accuracy among Eight Models.

Based on the comparison of these eight models, the input features are determined. Figure 3.22 shows the model's structure to predict five weather states. The number of neurons in output layer represents the class levels. Each node represents the one state. The output is the state having the maximum likelihood compared to the other states. For example, if the output is 'Clear', the value signed to each node is {1, 0, 0, 0, 0}.

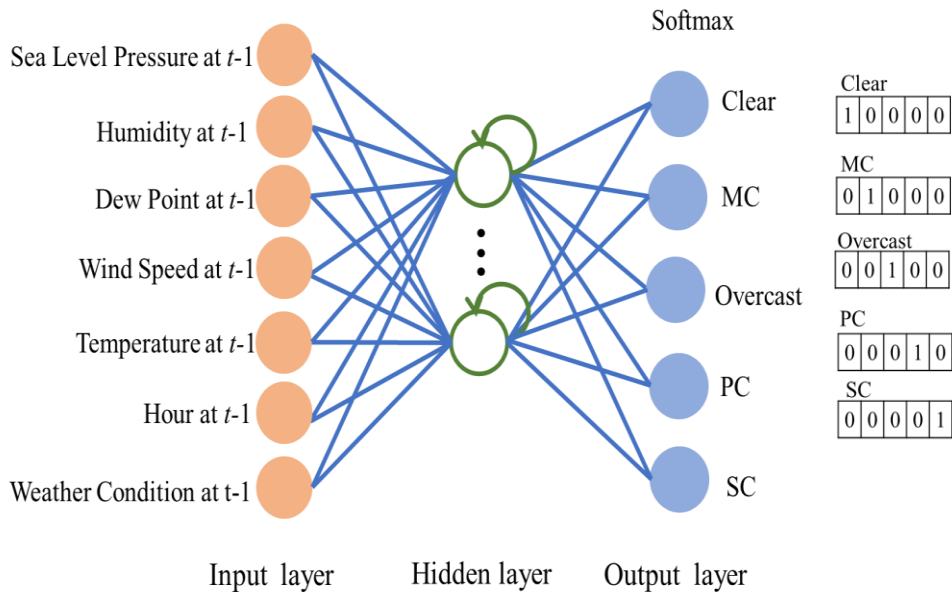


Figure 3.22: Structure of Multi-classification Model.

### 3.5.4 Weather Features Forecasting Results and Comparisons

The confusion matrix is applied in evaluating the quality of the output of a classifier on the weather state dataset, also known as the error matrix. It has a specific table layout that allows visualization of the performance of an algorithm. The diagonal elements represent the instances that the predicted state is equal to the observed state, while off-diagonal elements are those that are mislabeled by the classifier.

The prediction result in Table 3.11 sets the threshold for the "clear" state with 88.36% accuracy. Only the probability of "clear" state is greater than 50%, the outcomes

for the dependent variable is "clear" state. Otherwise, the state with second larger probability in output is adopted.

Table 3.11: Confusion Matrix with Threshold Value in Phoenix.

Predicated \ Observed	Clear	MC	Overcast	PC	SC
Clear	5691	16	0	620	57
MC	24	4584	262	87	611
Overcast	0	299	793	3	11
PC	510	91	2	3733	577
SC	75	626	19	489	3122

Table 3.12 is the same model without setting the threshold with accuracy of 89.9%. It indicates the model works very well for predicating "clear" state. When adopting the threshold, the forecasting result becomes conservative to estimate the solar PV generation at the expense of the accuracy. The model shows a quite good performance, when classifying the states between "clear" and "overcast". The state of "overcast" is never predicted as "clear" state. The state with the highest proportion shows more accuracy, like "clear" state in Phoenix and "overcast" in New York, than other weather states.

Table 3.12: Confusion Matrix without Threshold Value in Phoenix.

Predicated \ Observed	Clear	MC	Overcast	PC	SC
Clear	5715	16	0	596	57
MC	24	4584	262	87	611
Overcast	0	299	793	3	11
PC	527	91	2	3716	577
SC	82	625	19	483	3122

Figure 3.23 plots the accuracy of one-step ahead forecasting result. The model has

better performance in Phoenix with 89.9% accuracy and New York with 80.36% accuracy. The darkest blue color square represents the highest accuracy for that state.

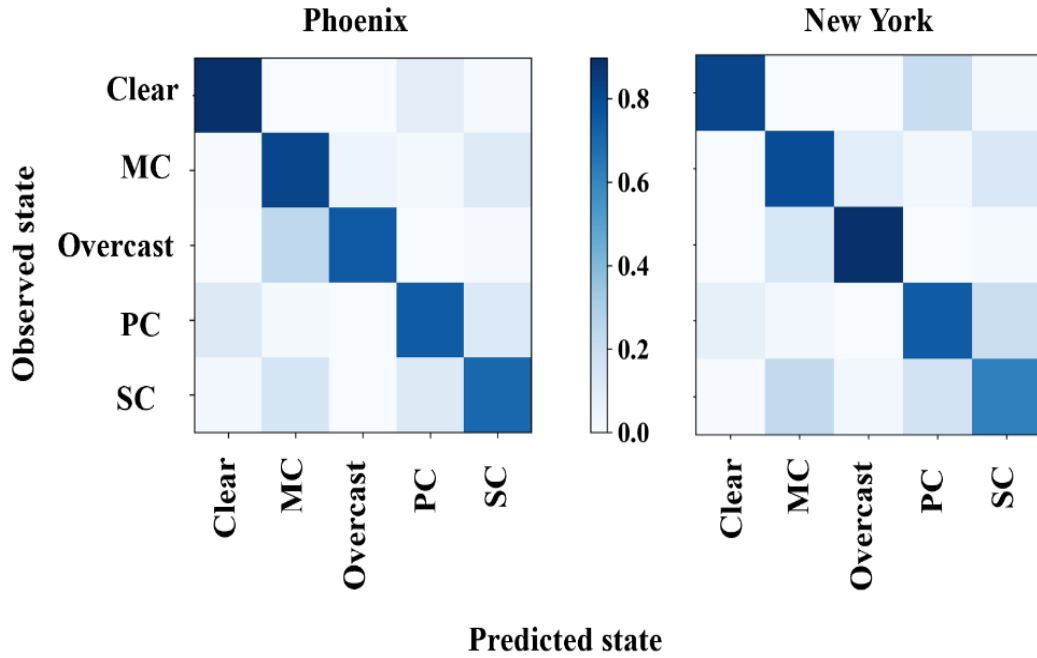


Figure 3.23: Visualization of Forecasting Accuracy.

Table 3.13 lists the multi-step ahead forecasting accuracy with the five-state output in Phoenix. The forecasting accuracy decreases with extended forecasting horizon, dropping from 89.9% in 1-hour ahead to 56.9% in 24-hour ahead.

Table 3.13: Forecasting Accuracy over Five Forecasting Horizons.

Model	Accuracy (%)
1-hour	89.9
3-hour	75.45
8-hour	71.74
12-hour	62.8
24-hour	56.9

The model is constructed with five different weather states and the results are compared with seven weather states. To better gauge the model performance, different weather profiles of two cities are compared. In addition, the proposed models are also

constructed by season and year to make the models more granular and gain insight as to whether the seasonal and yearly models yield better predictions for the corresponding period.

The results in Table 3.14 show the comparisons between the seasonal and yearly forecasting models with five and seven weather states. Their performances are drastically different. Interestingly, the five-state forecasting model yields higher accuracy than ten-state model. The model with yearly data has better performance than the seasonal one, because some states behave more randomly, such as snow or thunderstorms with zero occurrence frequency in summer or winter, which coincide with the real data record.

Table 3.14: Comparisons between 5- and 7-state Model with Seasonal Data.

Performance		Accuracy (%)			
		spring	summer	fall	winter
5 States	New York	74.3	74.7	74.6	73.9
	Phoenix	87.8	81	79.2	89.9
7 States	New York	63.3	65.3	65.1	67.1
	Phoenix	76.3	70.8	70.4	79.4

Table 3.15 presents the normalized confusion matrix of the forecasting accuracy of the entire year with ten states. The average accuracy is 68.8% in New York. The proposed model cannot achieve high prediction accuracy for states such as rain and thunderstorm, light rain, and fog/haze. The model also does not differ from fog/haze between overcast and partly cloudy and mixes the state of rain and light rain. This is because rain, light rain, thunderstorm, and fog/haze have a limited number of observations.

Table 3.15: Ten-state Weather Features Prediction Result in New York.

Predicted \ True	Clear	Fog /Haze	Light Rain	MC	OC	PC	Rain	SC	Snow	Thunder storm
Clear	0.78	0.00	0.00	0.00	0.00	0.19	0.00	0.03	0.00	0.00
Fog/Haze	0.00	0.44	0.00	0.22	0.33	0.00	0.00	0.00	0.00	0.00
Light Rain	0.00	0.00	0.76	0.13	0.00	0.00	0.10	0.01	0.00	0.00
MC	0.00	0.00	0.00	0.87	0.11	0.02	0.00	0.10	0.00	0.00
OC	0.00	0.01	0.06	0.17	0.73	0.00	0.02	0.00	0.01	0.00
PC	0.06	0.00	0.00	0.03	0.00	0.73	0.00	0.18	0.00	0.00
Rain	0.00	0.01	0.40	0.01	0.26	0.00	0.29	0.01	0.03	0.01
SC	0.00	0.00	0.00	0.23	0.01	0.17	0.00	0.58	0.00	0.00
Snow	0.00	0.00	0.00	0.04	0.15	0.00	0.00	0.02	0.80	0.00
Thunderstorm	0.00	0.00	0.05	0.42	0.32	0.00	0.00	0.11	0.00	0.11

Table 3.16 shows that the proposed model forecasting accuracy is 35.7% and 32% higher than the Markov model and the hidden Markov model (HMM), respectively.

Table 3.16: Comparisons among MC, HMM, and ANN Model in Phoenix.

Type \ Amount	Clear	MC	PC	SC	OC	Total
Measured	2462	2247	2344	1324	383	8760
MC	2946	1620	2086	2031	77	8760
HMM	3236	2323	315	2745	141	8760
RNN	2463	2248	2344	1324	381	8760

Table 3.17 shows the comparison result between the proposed model and the statistical models under five states. The accuracy in Phoenix shows the best performance compared to other cities due to the top five states accounting for over 98%, while less than 90% in other cities. Furthermore, the model prediction accuracy decreases when the number of states involved in the model increases.

Table 3.17: Comparisons of One-hour Ahead Forecasting Accuracy.

Cities	Accuracy (%)		
	MC	HMM	RNN
Wellington	65	77.6	81.4
San Francisco	71	80.6	87.9
Phoenix	74	83.6	89.9
Boston	66	75.6	84.4
New York	63	79.4	80.3
Sanya	68	82.4	86.7

#### 4. MATHEMATICAL FUNCTIONS IN MODELS

In this chapter, the working principle of renewable generators and energy storage devices is illustrated. The output of renewable generation, charging and discharging process, and the lifetime of battery are converted into mathematic functions, respectively. The challenge with the integration of the distributed energy resources (DER), such as wind turbine and solar photovoltaic (PV), is the uncertain nature of such electricity resources. DER and energy storage devices improve the security of supply and mitigate the impact to the grid power system.

A microgrid power system can operate either in connection with the main grid or in isolation mode. In this study, the grid-connected operation mode is adopted, meanwhile, the onsite renewable generation system has two ways of energy flow. The utility-scale hybrid energy storage system (HESS) manufactured by advanced materials is installed in the grid-connected microgrid distribution system as shown in Figure 4.1. The power in the microgrid system keeps the balance as below,

$$P_{HRE} = P_s + P_{Load} \quad (4.1)$$

$$P_{HRE} = P_{PV} + P_{WT} + P_{HESS} \quad (4.2)$$

$$P_{HESS} = P_{bat} + P_{sc} \quad (4.3)$$

where

$P_{HRE}$  = power output of HESS and renewable generations.

$P_s$  = exchange power between grid and micropower system.

When  $P_s > 0$  means system imports energy from grid;  $P_s < 0$  means onsite generation system exports energy to grid;  $P_s = 0$  means there is exchange between microgrid and main grid.

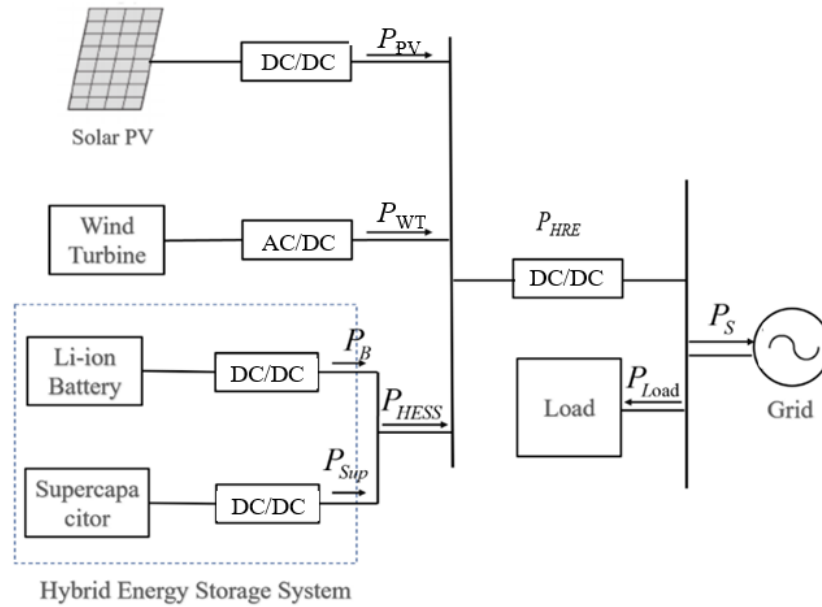


Figure 4.1: Microgrid Power System with HESS.

#### 4.1 Modeling Wind Turbine Generation

Wind energy is at the forefront of renewable energy sources. According to Global wind statistics (2019), the worldwide cumulative installed wind capacity reached nearly 591 gigawatt (GW) at the end of 2018, with an annual growth rate of 9.6%. Most countries make efforts to help wind power development from technology, policy, and budget aspects. The installed capacity of the United States has increased more than twentyfold in the past 16 years, from 4.2 GW in 2001 to 82 GW in 2017 surpassing hydropower capacity and becoming the largest installed generator (EIA, 2017). China has been the largest wind energy provider worldwide since 2010 and installed capacity reaches 149 GW in 2016 (Sullivan and Liu-Sullivan, 2019).

In 2016, wind turbines accounted for 8% of the operating electric generating capacity in the United States. The wind energy policy is a strong incentive to increase wind power generation as well as stimulate the energy industry. The largest onshore

turbines are in Texas, with capacity of 4 Megawatts (MW) each. According to EIA (2017), one of the largest wind farms in the world has installed 420 wind turbines spread over 47,000 acres at Horse Hollow Wind Energy Center in Texas. The project has 735 MW of combined generation capacity.

According to collected data from EIA (2016), utility-scale wind turbines typically exceed 2 MW and the diameter of the rotor is more than 76 meters. Table 4.1 summarizes the current wind turbine technologies based on the hub height, rotor, and rated power output.

Table 4.1: Parameters of Current Wind Turbine Technologies.

Category	Hub Height (m)	Swept area (m <sup>2</sup> )	Rated Capacity (kW)
Small	0~8	0~50	0~10
	8.1~11	50.1~100	10~25
	11.1~16	100.1~200	30~60
Medium	16.1~22	200.1~400	70~130
	22.1~32	400.1~800	150~330
	32.1~45	800.1~1600	300~750
Utility Scale	45.1~64	1600.1~3200	600~1500
	64.1~90	3200.1~6400	1500~3100
	90.1~128	6400.1~12800	3100~6400

#### 4.1.1 Wind Source Property

Wind generation utilizes airflow through the blades of wind turbine by mechanically rotating the generator to produce electricity. In general, wind resources vary with height above the terrain and the wind speed increases from the ground surface to the upper level. The wind program (energy.gov) estimates that the land-based wind energy potential is 10,500 GW at 80 meters height and 12,000 GW capacity at 100 meters height across the United States. Figure 4.2 is the heat map of wind speed worldwide over 100 meters height above ground.

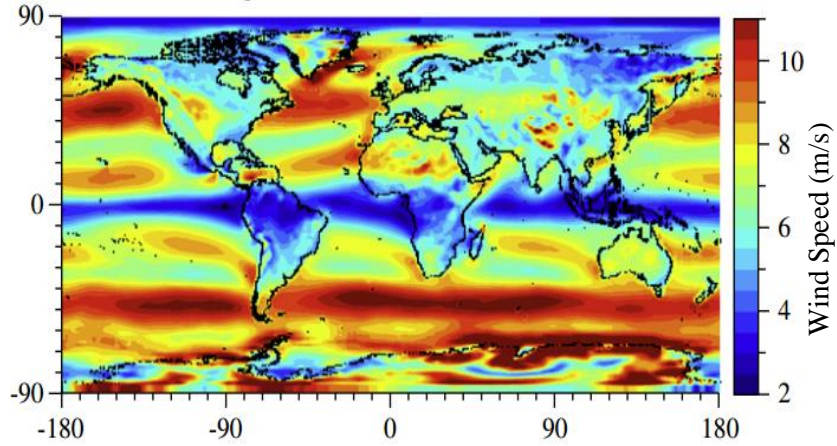


Figure 4.2: Wind Resource Distribution across World (Alkholidi, 2013).

The wind speed is also impacted by the surface roughness of terrain in a certain area shown in Figure 4.3. The wind speed at height  $H$  can be estimated by following equation (Ilinka et al., 2003),

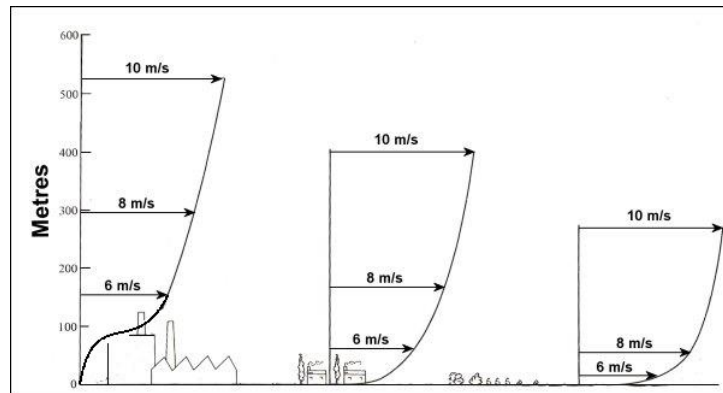


Figure 4.3: Wind Speed Variety with Different Height and Roughness.

$$v = \frac{v_{ref} \ln\left(\frac{H}{Z_0}\right)}{\ln\left(\frac{H_{ref}}{Z_0}\right)} \quad (4.4)$$

where

$v_{ref}$  = known wind speed at reference height (m/s, usually 10 m as reference).

$Z_0$  = surface roughness length of terrain.

$H$  = height above ground level for  $v$  (m).

$H_{ref}$  = reference height (m).

The wind data source from the weather underground is measured at 10 meters above the ground surface,  $H_{ref} = 10$  and hub height of wind turbine is 89 meters applied in this study,  $H = 89$ . Suppose the roughness length,  $Z_0 = 0.4$ , at the urban and farmland area. The wind speed equals 5.5 m/s,  $v_{ref} = 5.5$ , the wind speed,  $v$ , can be calculated:

$$v = \frac{5.5 \times (\ln(89) - \ln(0.4))}{\ln(10) - \ln(0.4)}$$

$$= 14.14 \text{ m/s}$$

Table 4.2 lists the wind speed under different height levels at the first hour in each year from 2006 to 2015 in Wellington, New Zealand given that the value of surface roughness length ( $Z_0$ ) is 0.4.

Table 4.2: Wind Speed at Different Height Levels in Wellington.

Category	2006	2007	2008	2009	2010	2011	2012	2013	2014	2015
measured value (10 m)	7.32	6.50	6.66	6.97	6.87	6.65	6.59	6.89	7.09	7.41
80 m above ground	18.3	16.25	16.65	17.42	17.17	16.62	16.47	17.22	17.72	18.52
100 m above ground	19.5	17.29	17.71	18.54	18.27	17.68	17.52	18.32	18.85	19.71

#### 4.1.2 Mathematics Model of Wind Turbine Generation

The aerodynamics are converted into mechanical energy through blades and a gearbox. The energy is further converted into electricity via a generator that is rotated by the torques from the gearbox. A wind energy conversion system is a combination of a wind turbine, generator, and power electronics converters for AC-DC-AC conversion as shown in Figure 4.4.

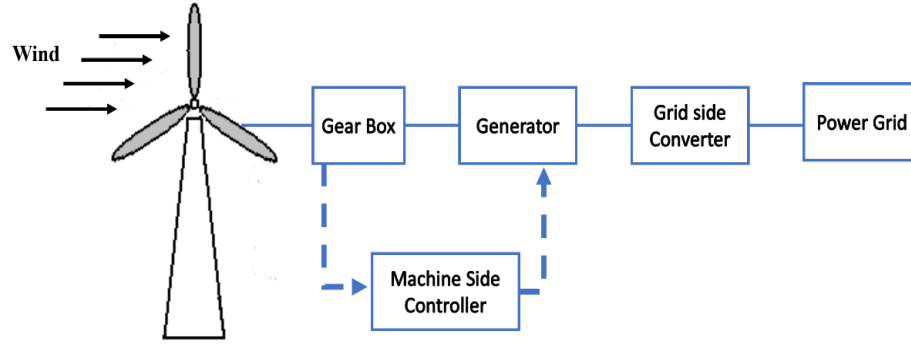


Figure 4.4: Schematic of Wind Energy Conversion System.

Depending on the wind speed, the operation of a WT can be broken into four phases: standby, non-linear production, constant production, and shutdown. Figure 4.5 plots the wind power curve, where  $v_c$  is called cut-in wind speed,  $v_r$  is called rated wind speed, and  $v_s$  is the cut-off wind speed.

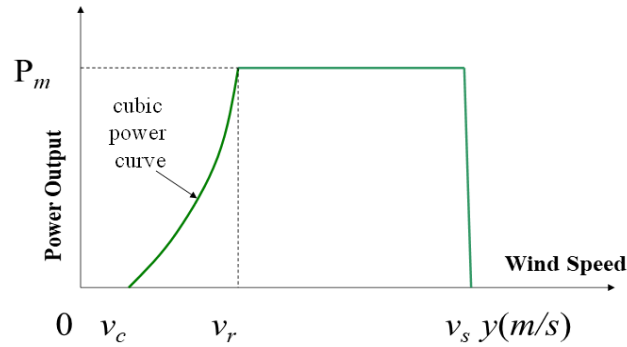


Figure 4.5: Wind Turbine Power Curve.

The relationship of the output power and the wind speed is regarded as a non-linear function when the turbine operates between  $v_c$  and  $v_r$ . Cubic power curve model is developed based on the kinetic theory of the airflow dynamics (Jangamshetti and Rau, 2001). Let  $Y$  be the random wind speed, and  $y$  is its realization. The output power of wind turbine in four phases can be modeled as,

$$p_{(Y)} = \begin{cases} 0 & y < v_c, y > v_s \\ 0.5\eta_{\max}\rho Ay^3 & v_c \leq y \leq v_r \\ P_r & v_r \leq y \leq v_s \end{cases} \quad (4.5)$$

where

$\rho$  = air density (1.225 kg/m<sup>3</sup>).

$A$  = the covered area of blades.

$y^3$  = the cube of wind speed across a wind turbine.

$\eta_{max}$  = the maximum conversion rate as 59.26%.

$P_r$  = related power or the capacity of the WT.

#### 4.1.3 Simulate Generation of Wind Turbine

In this study, a 2 MW wind turbine with hub height of 89 m and 124 m diameter of blade is chosen for simulation. The characteristic of the wind turbine made by glass fiber reinforced plastic material is given in Table 4.3.

Table 4.3: 2MW GE Wind Turbine Platform.

Category	Cut-in (m/s)	Rated (m/s)	Cut-out (m/s)
Wind Speed	3	10	25

The forecasting results of wind speed across a year from Chapter 3 are plugged into Equation (4.5). Assuming the WT is installed in Boston, MA, the hourly generation of a 2 MW wind turbine is plotted in Figure 4.6. The maximum output power is 2 MW when the wind speed falls in 10 m/s and 25 m/s.

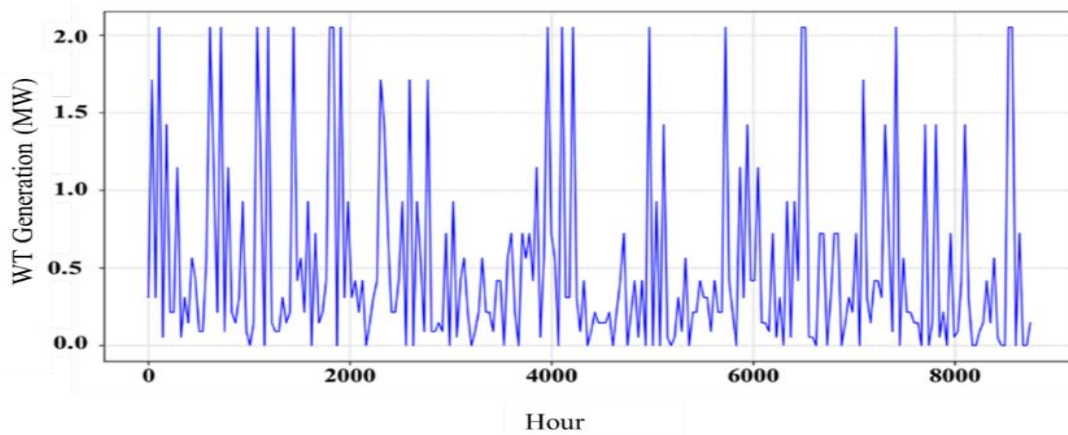


Figure 4.6: Hourly Generation of Wind Turbine through 2015 in Boston.

## 4.2 Modeling Solar Panel Generation

Solar is one of the most important sources of sustainable renewable energy. The sun provides energy for the earth through radiant light and heat. All living creatures on earth depend on the energy from the sun to survive. The amount of energy that the earth obtains from the sun per hour is more than the amount of energy that humans consume across an entire year. Solar PV is a technology that harnesses solar radiation and converts it into electric power. However, the solar PV generator has some limitations. It heavily depends on the weather features and is only available in the daytime. Figure 4.7 plots solar radiation resources across the world.

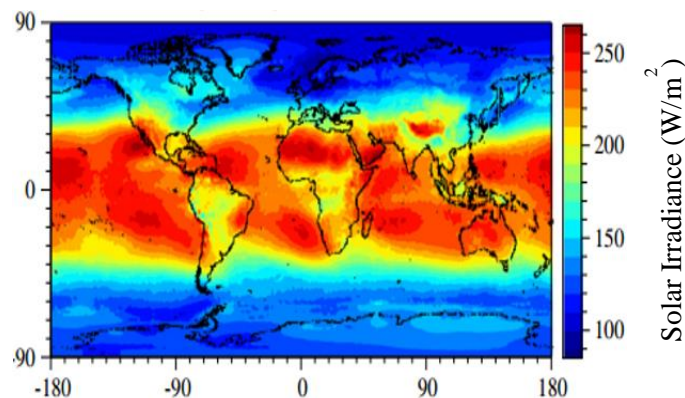


Figure 4.7: Surface Downward Solar Irradiance across World (Alkholidi, 2013).

### 4.2.1 Mathematics Model of Solar Panel Generation

A PV system typically includes a charge regulator, DC-AC power inverter, and a transformer. The maximum lifespan of a PV module is estimated at around 25 years. A typical PV module consists of about 36 or 72 solar cells connected in a series or parallel. The two principal classifications in the renewable power system are grid-connected (utility-interactive systems) and stand-alone systems. Photovoltaic systems can be operated as interconnected with or island to the utility grid. It also can be connected with other energy sources or storage systems, such as integrated with battery storage devices

to prevent the power shortage in night.

A solar cell is configured as a large area p-n junction made from silicon, which absorbs light to generate electron-hole pairs. The configuration of the simulated ideal solar cell with a single diode is shown in Figure 4.8.

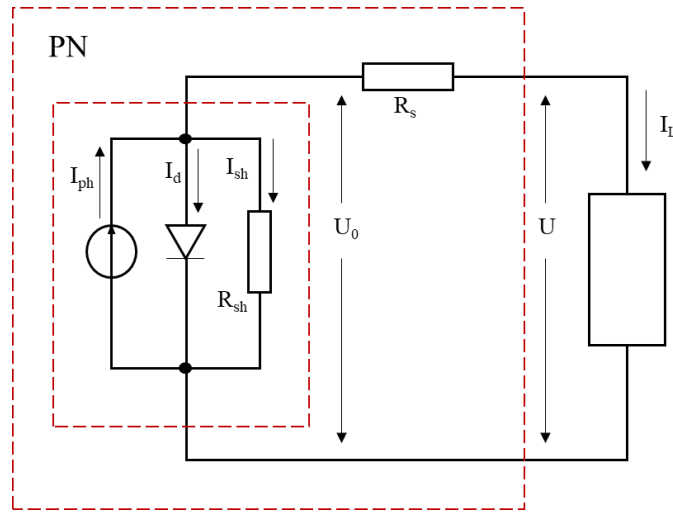


Figure 4.8: Equivalent Circuit of Photovoltaic Cell.

The output current  $I_L$  of solar panel is calculated by the following equation (Azzouzi, 2016),

$$\begin{aligned}
 I_L &= I_{ph} - I_d - I_{sh} \\
 &= I_{ph} - I_s \left[ \exp\left(\frac{q(U + I_L R_s)}{nKT}\right) - 1 \right] - \frac{U + I_L R_s}{R_{sh}}
 \end{aligned} \tag{4.6}$$

where

$I_{ph}$  = current generated by the incident light (A).

$I_d$  = diode current (A).

$q$  = electron charge ( $1.60217646 \times 10^{-19}$  C).

$I_{sh}$  = shunt current (A).

$K$  = Boltzmann's constant ( $1.38 \times 10^{-23}$  J/K).

$T$  = temperature of p-n junction (K).

$R_s$  = series resistance ( $\Omega$ ).

$R_{sh}$  = shunt resistance ( $\Omega$ ).

$$I_L = I_{sc} (1 - C_1 (\exp(U / C_2 U_{oc}) - 1)) \quad (4.7)$$

with

$$C_1 = \left(1 - \frac{I_m}{I_{sc}}\right) \exp\left(-\frac{U_m}{C_2 U_{oc}}\right)$$

$$C_2 = \left(\frac{U_m}{U_{oc}} - 1\right) \ln\left(1 - \frac{I_m}{I_{sc}}\right)^{-1}$$

It is difficult to directly use Equations (4.6) and (4.7) to estimate the generation of solar cells. In this study,  $I_{sc}$ ,  $U_{oc}$ ,  $U_m$ , and  $I_m$  are used to deduce the output current of the solar cells under the standard solar radiation and temperature. For any temperature and solar radiation levels, the corresponding values of  $I'_{sc}$ ,  $U'_{oc}$ ,  $U'_m$ , and  $I'_m$  can be obtained as follows,

$$I'_{sc} = I_{sc} \times \frac{S}{S_{ref}} (1 + \alpha \Delta T) \quad (4.8)$$

$$U'_{oc} = U_{oc} \times ((1 - c \Delta T)) \ln(e + b \Delta S) \quad (4.9)$$

$$U'_m = U_m \times ((1 - c \Delta T)) \ln(e + b \Delta S) \quad (4.10)$$

$$I'_m = I_m \times \frac{S}{S_{ref}} (1 + \alpha \Delta T) \quad (4.11)$$

where

$$\alpha = 0.0025/^\circ C$$

$$b = 0.5$$

$$c = 0.00288/^\circ C$$

$$\Delta T = T - T_{ref}$$

$$\Delta S = S - S_{ref}$$

The output power of the solar PV at a specific temperature and solar radiation level can be calculated as,

$$P_{PV} = I'_m \times U'_m \quad (4.12)$$

In this part, a simulation program is designed to emulate the whole year output power of a solar PV panel at the testing cities. In this model, the amount of solar irradiance can be calculated based on the latitude of the location, the date in a year, and the hour in a day. The weather features are also considered when simulate the power generation of solar PV. A three-step procedure is applied in modeling and simulation the solar PV generation for this study. Figure 4.9 displays the relation between tilt angle, latitude, and the amount of solar irradiance hit on a solar PV during a course of a day.

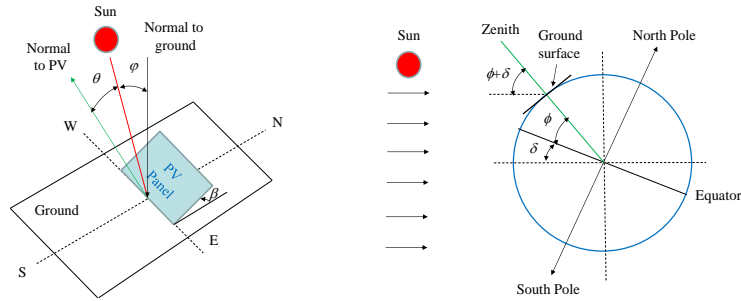


Figure 4.9: Solar Irradiance on Solar PV in a Day.

Step 1: compute the sunrise and sunset time for date  $d \in \{1, 2, \dots, 365\}$

$$\cos(-\omega_{rise}) = \cos(\omega_{set}) = \tan(\phi - \beta) \tan \delta \quad (4.13)$$

with

$$\delta = 0.40928 \sin\left(\frac{2\pi(d + 284)}{365}\right) \quad (4.14)$$

where

$\delta$  = The declination angles.

$\omega_{rise}$  = The sunrise angles in day  $d$  perceived from the solar panel.

$\omega_{set}$  = The sunset angles in day  $d$  perceived from the solar panel.

Step 2: provides the detailed model to compute  $S_t$  at  $t = 1, 2, \dots, 24$  hours in date  $d$  for  $d = 1, 2, \dots, 365$ . This model is applicable in any geographical region of the world. Table 4.4 summarizes the key parameters related to the computation of solar PV generation.

Computing the total amount of solar irradiance incident on the PV surface at time  $t$  in day  $d$  that is following,

$$S_t = 1370 \left( 0.7^{(\cos \phi)^{-0.678}} \right) \left( 1 + 0.034 \cos \left( \frac{2\pi(d-4)}{365} \right) \right) \times \left( \cos \theta + 0.1 \left( 1 - \frac{\beta}{\pi} \right) \right) \quad (4.15)$$

with

$$\cos \phi = \cos \delta \cos \varphi \cos \omega + \sin \delta \sin \varphi \quad (4.16)$$

$$\begin{aligned} \cos \theta = & \sin \delta \sin \phi \cos \beta - \sin \delta \cos \phi \sin \beta \cos \alpha \\ & + \cos \delta \cos \phi \cos \beta \cos \omega \\ & + \cos \delta \sin \phi \sin \beta \cos \alpha \cos \omega + \cos \delta \sin \alpha \sin \omega \sin \beta \end{aligned} \quad (4.17)$$

Where,  $s_t$  is the solar irradiance ( $\text{W/m}^2$ ) received by the PV at time  $t$  in date  $d$ , and  $\varphi$  is the solar zenith angle which is given by Equation (4.16).  $\omega$  is the solar hour angle determined by the local time. For instance,  $\omega = -\pi/2$  represents 6 am., and it increases  $15^\circ$  every hour until reaching  $\omega = \pi/2$  at 6 pm.

To maximize the solar power yield, the solar PV panel shall be oriented towards the south (i.e.,  $\alpha = 0$ ), then Equations (4.16) and (4.17) can be simplified as follows,

$$\cos \theta = \sin \delta \sin(\phi - \beta) + \cos \delta \cos(\phi - \beta) \cos \omega \quad (4.18)$$

Based on Equation (4.15), the hourly solar irradiance is calculated on the first day in 2015 at Phoenix and the result is plotted in Figure 4.10.

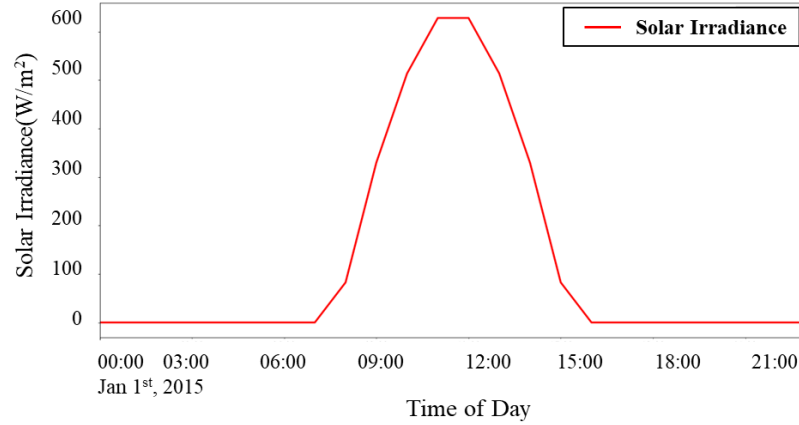


Figure 4.10: Solar Irradiance on January 1<sup>st</sup>, 2015 at Phoenix.

Step 3: the actual power output of a PV system considering the weather features now can be expressed by

$$P_{(W_t)} = W_t \eta \frac{S_t}{S_{ref}} (1 - 0.005(T_o - T_{ref})) P_{ref} \quad (4.19)$$

where

$P_{(W_t)}$  = output power of the PV system.

$S_t$  = solar irradiance incident on the PV surface at time  $t$  ( $t = 1, 2, \dots, 24$  hours)

on day  $d$  for  $d = 1, 2, \dots, 365$ .

$P_{ref}$  = rated output generated by the module under test conditions in watts.

$A$  = PV area ( $m^2$ ).

$T_o$  = PV operating temperature ( $C^\circ$ ).

$T_{ref}$  = temperature of the module under standard test condition.

$S_{ref}$  = solar irradiance under standard test condition ( $W/m^2$ ).

Note that there is no power output when  $\omega < \omega_{rise}$  or  $\omega > \omega_{set}$ , i.e., before sunrise and after sunset. The generation of PV system is dependent on multiple factors, including the panel size, the operating temperature, the PV orientation, the panel tilt angle, the weather condition, and the solar irradiance incident on the PV (Taboada et al., 2012).

Table 4.4: Summary of Key Factors that Impact PV Output Power.

Factor	Symbol	Explanations
Weather coefficient	$W_t$	random variable
PV size (m <sup>2</sup> )	$A$	PV module area
PV efficiency	$\eta$	Between 10-25% for conventional PV.
Date	$d$	$d \in \{1, 2, \dots, 365\}$
Solar hour (rad)	$\omega$	related to the local time
PV temperature (°C)	$T_o$	operating temperature
latitude (rad)	$\phi$	depends on geographical location
PV azimuth angle (rad)	$\alpha$	if facing south, $\alpha=0$
PV tilt angle (rad)	$\beta$	between PV and ground
Local hours	$t$	$t = 1, 2, \dots, 24$

To address the random amount of clouds, the weather coefficient  $W_t$  is used to adjust the actual  $P_t(s_t)$ . For instance, if it is “Clear”,  $W_t = 1$ , meaning 100% of  $S_t$  incident on the PV. If it is “PC,” then only 50 percent of  $S_t$  reaches the PV surface. On a snowy day,  $W_t = 0$  because the PV surface is likely to be covered by snow. The values of  $W_t$  under different weather states are listed in Table 4.5.

Table 4.5: Weather Coefficients under Different States.

No.	1	2	3	4	5	6	7	8	9	10
state	Clear	SC	PC	MC	OC	Light Rain	Rain	Fog	Storm	Snow
$W_t$	1	0.8	0.5	0.3	0.2	0.1	0.1	0.1	0.1	0

#### 4.2.2 Simulate Generation of Solar PV

Solar cells are primarily made from semiconductors which are manufactured using different processes and materials. The photovoltaic effect is a capability of semiconductor converting the sunlight energy directly into electricity. One type of m-Si PV module is selected in this study. The detail of electrical parameters for this type of solar cell is provided in Table 4.6.

Table 4.6: Specifications of PV Module.

Category	Notation	Value	Unit
Rated maximum power	$P_{max}$	250	W
Rated voltage	$U_{max}$	29.9	V
Rated circuit	$I_{max}$	8.36	A
Short-circuit current	$I_{sc}$	8.79	A
Open-circuit voltage	$U_{oc}$	37.8	V

Based on the electrical property of the solar cell, Figures 4.11 and 4.12 plot I-U and P-U curves under different levels of solar irradiance and temperature, respectively. Both factors simply impact the output voltage (V) and current (I).

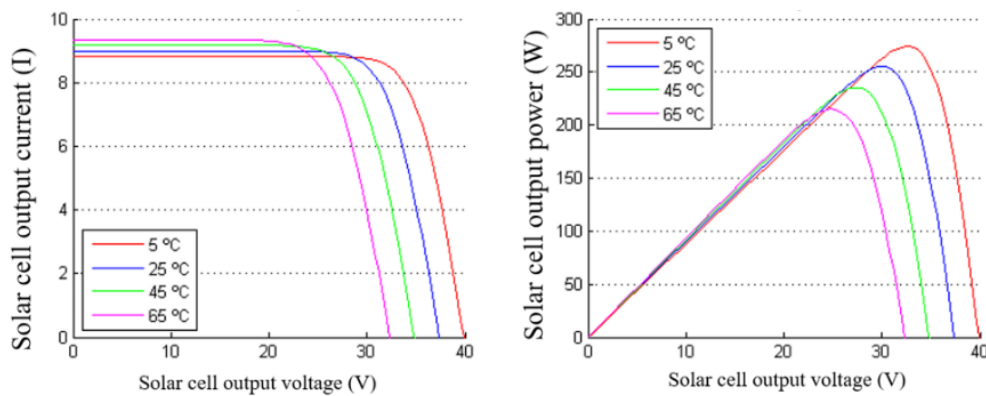


Figure 4.11: I-U and P-U Curve of PV Cell under Different Temperatures.

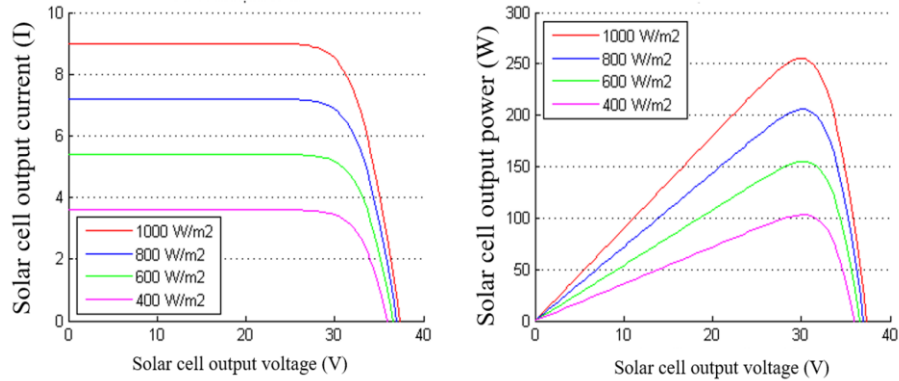


Figure 4.12: I-U and P-U Curve of PV Cell under Different Solar Irradiance.

Through analyzing Figures 4.11 and 4.12, the solar cell working principle can be summarized as:

- 1). The amount and intensity of solar irradiance control the amount of output current.
- 2). The operating temperature affects the output voltage of the solar cell.
- 3). The output voltage is more sensitive than the output current when the temperature changes.

During the operation, the generation of a solar PV module is uncertain due to the changes in temperature and solar irradiance throughout the year. These two factors should be considered when designing a PV power system. Therefore, the predicted results of solar PV generation will be closer to the actual operation condition and improve accuracy. In summary, the optimal generation for a solar panel performs best in a sunny and cold environment.

Based on Equation (4.19), the hourly power generation of solar PV is simulated. The generations of solar PV in one year are shown in Figure 4.13.

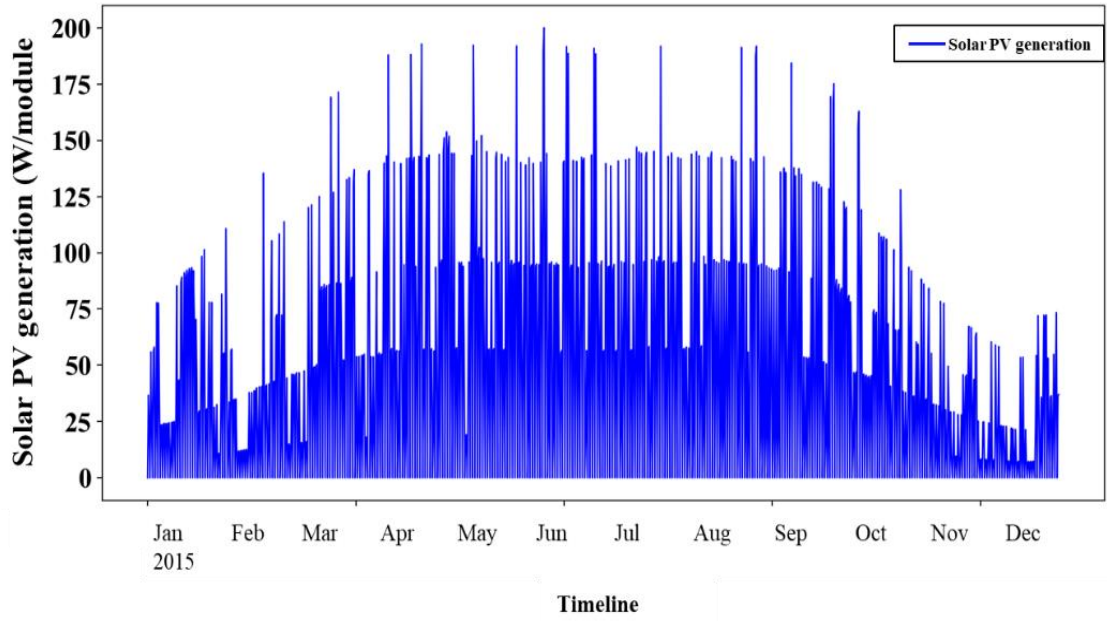


Figure 4.13: Hourly Generation of Solar PV through 2015 in Phoenix.

### 4.3 Modeling Hybrid Energy Storage System

Energy storage systems (ESS) will be integrated with WT and solar PV in a generation system to mitigate the power fluctuation and improve the power quality. ESS can continuously maintain energy supply for a long duration or quickly provide the power to fill the gap between the power generation and the demand. Schmidt et al. (2017) point out that an average annual cost prominently declining by 30% on the cell level can lead to 12% cutting on the system level in the ESS. Energy storage technologies available for large-scale applications can be divided into four types: mechanical, electrical, chemical, and electrochemical (Dunn et al., 2011). Some grid-scale storage technologies have already matured and been used for many years. For instance, pumped hydroelectric storage and compressed air energy storage (CAES) are excellent for storing large amounts of energy over a long duration. Table 4.7 lists the cost of utility-scale energy storage technologies.

Table 4.7: Cost and performance of Energy Storage Devices based on Materials.  
(Yamchi et al., 2019).

Technology option	Capacity cost (\$/kWh)	Replacement cost (\$/kWh)	O&M cost (\$/kWh)	Overall efficiency (%)
Na-S	298	180	4.4	82
Ni-Cd	780	525	11	66
Zn-Br	195	195	4.3	65
ZEBRA	509	182	5.5	87
Li-ion	170	110	4	85

In general, electrochemical energy storage device possesses several desirable features, including pollution-free operation, high round-trip efficiency, long cycle life, low maintenance, and flexible power and energy characteristics to meet different grid requirements. The utility-scale storage needs long service life to reduce the replacement cost. The SC can be cycled millions of times or virtually unlimited cycle life. It responds faster to discharge when demand increases. Hajiaghahi et al. (2019) make a summary that hybrid energy storage performs better than battery-alone energy storage for a stand-alone PV system. Jing et al. (2016) testify that hybrid storage has the virtues of both high energy and power density, and such systems increase battery lifespan. They analytically demonstrate that hybrid can extend the power output and life of battery. Hence, a hybrid energy storage system (HESS) is adopted in this study. HESS consists of lithium-ion battery (LIB) and supercapacitor (SC), which combines the advantages of both storage technologies. The main function of HESS can temporarily store surplus energy from WT and PV generation if empty capacity is available. On the other hand, if the aggregate generation from WT and PV is less than the demand, HESS is in discharge mode to complement the electricity gap.

#### 4.3.1 Mathematics Model of Lithium-ion Battery

The specific energy, specific power, and energy density are the important parameters of battery which decide their performance. In this research, the constant power discharging is required to meet the load demand. Based on this condition, the capacity of a battery can be calculated by the following,

$$C = \frac{2 \times P \times t}{U_0^2 - U_1^2} \quad (4.20)$$

where

$t$  = discharge time (s).

$C$  = capacity (Ah).

$U_0$  = charging voltage (V).

$U_1$  = discharging voltage (V).

$P$  = power (W).

Suppose the cut-off voltage, nominal capacity, and current discharging rate of each battery cell is  $U_b$  (V),  $C_b$  (A.h), and  $I_b$  (I), respectively. The battery subsystem consists of one array battery unit with  $m$  units, and the total storage energy  $E_b$  (Wh) and  $P_b$  (W) are generally calculated according to following equation,

$$\begin{aligned} E_b &= m \times C_b \times U_b \\ P_b &= m \times I_b \times U_b \end{aligned} \quad (4.21)$$

The batteries are more prone to failure if they are discharged below a certain threshold, approximately the depth of discharge (DoD), around 80% in this study. Under this criterion, the minimum residual electric energy is always greater than 20% of the initial battery capacity during the discharging process at any time for the protecting purpose. If the cells are discharged below this threshold, their capacity can be permanently reduced, it is important to avoid fully discharging a battery.

#### 4.3.2 Mathematics Model of Graphene-based SC

Graphene-based SC can deliver high power and achieve nearly 100% cycle efficiency (Zhang et al., 2014) and exhibit negligible aging effects. Unfortunately, SC suffers from severe self-discharge with 20% per day (Zhang et al., 2014), low energy density, and high capital cost. In 2013, SC system was installed in La Palma power system with a 4 MW maximum power and a 5.5 kWh content energy to meet peak demand. The SC system provides power until a backup generator is started and the switch-over is stabilized during the power outage.

It is generally known that the use of SC needs to be expanded through series or parallel connection because single SC only stores limited energy and cannot bear high voltage (Zhang et al., 2014). Suppose SC are connected in series with  $l$  and in parallel with  $n$  groups, the equivalent capacitance of SC group can be calculated as,

$$C = \frac{n}{l} C_f \quad (4.22)$$

Suppose  $U_{c \max}$  and  $U_{c \min}$  are the maximum and minimum voltages of SC groups, respectively. The storage energy  $E_c$  (Wh) is expressed as follows,

$$\begin{aligned} E_c &= \frac{0.5 \times C \times (U_{c \max}^2 - U_{c \min}^2)}{3.6 \times 10^3} \\ &= \frac{0.5 \times n \times C_f \times (U_{c \max}^2 - U_{c \min}^2)}{l \times 3.6 \times 10^3} \end{aligned} \quad (4.23)$$

where

$C_f$  = capacitance of single SC.

$U_{c \max}$  = maximum voltage of SC.

$U_{c \min}$  = minimum voltage of SC.

$I_{c \max}$  = maximum current of SC.

It is shown that the stored energy of SC group is related to the number of single SC in series and parallel arrangement. The maximum power of an SC array can be provided as follows,

$$P_{c \max} = \frac{n}{l} \times U_{c \max} \times I_{c \max}^2 \quad (4.24)$$

#### 4.4 Modeling Charging and Discharging Process of HESS

Suppose  $E_j$  is capacity of energy storage system.  $E_{j,t}$  is the stored energy at  $t^{\text{th}}$  hour in HESS is formulated by following,

$$\begin{aligned} E_j^{\min} &= DoD \times E_j \\ E_j^{\min} &\leq E_{j,t} \leq E_j \end{aligned} \quad (4.25)$$

In Equation (4.25), the lower bound thresholds for stored energy  $E_{j,t}$  in HESS at each hour,  $j \in \{\text{LIB}, \text{SC}\}$ . When the  $E_{j,t}$  reaches  $E_j$ , the HESS stops charging, while  $E_{j,t}$  reaches  $E_j^{\min}$ , the HESS stops discharging to protect the lifetime of HESS. The gap between  $E_j$  and  $E_j^{\min}$  represents the maximum amount of energy taken out from system. Lithium-ion batteries can be continually discharged at 100% DoD level with expected 3,000 cycles.

The optimal energy storage system control problem is treated as a discrete-time problem with the time step of one hour. Then, the power is equal to the value of energy.

$$E(\text{Wh}) = P(\text{W}) \times 1(\text{h}) \quad (4.26)$$

Hence, for any time  $t$  hour,  $P_{j,t}$  obtained by the following equation :

$$\left\{ \begin{array}{l} t = 1 \rightarrow E_j^{\min} - E_{j,0} \leq P_{j,1} \leq E_j - E_{j,0} \\ t = 2 \rightarrow E_j^{\min} - E_{j,1} \leq P_{j,1} + P_{j,2} \leq E_j - E_{j,1} \\ t = 3 \rightarrow E_j^{\min} - E_{j,2} \leq P_{j,1} + P_{j,2} + P_{j,3} \leq E_j - E_{j,2} \\ \vdots \\ t = T \rightarrow E_j^{\min} - E_{j,(T-1)} \leq P_{j,1} + P_{j,2} + P_{j,3} \dots + P_{j,T} \leq E_j - E_{j,(T-1)} \end{array} \right. \quad (4.27)$$

Where  $E_{j,0}$  is the initial stored energy in HESS at the beginning of operational epoch. Equation (4.27) can be rewritten as

$$E_j^{\min} - E_{j,0} \leq \sum_{t=1}^T P_{j,t} \leq E_j - E_{j,t} \quad (4.28)$$

$$t = 0, 1, \dots, T.$$

The stored energy at the end time  $T$  should be equal to the initial energy in the HESS for each operation cycle.  $E_{j,0} = E_{j,T}$ , in which the energy drawn from HESS during the discharging process equals energy recharged to HESS after a completed operational epoch.

#### 4.4.1 Mathematical Function in Charging Process

Let  $E_{j,t}$  be the energy stored in battery at time  $t$ . After charging in time  $\Delta t$ , the residual electric energy as

$$E_{j,(t+\Delta t)} = E_{j,t} + P_{j,t}^c \eta_j^c \Delta t \quad (4.29)$$

where

$t$  = operation hour, for  $\forall t$

$\Delta t$  = the charging duration (hour).

$P_{j,t}$  = charging power at  $t$ .

$\eta_j^c$  = charging power rate.

#### 4.4.2 Mathematical Function in Discharging Process

Let  $E_{j,t}$  be the battery energy state at time  $t$ , then after discharging over  $\Delta t$ , the residual electric energy as

$$E_{j,(t+\Delta t)} = E_{j,t} - P_{j,t} \eta_j^d \Delta t \quad (4.30)$$

where

$t$  = operation hour, for  $\forall t$

$\Delta t$  = the discharging duration (hour).

$P_{j,t}$  = discharging power at  $t$ .

$\eta_j^d$  = discharging power rate.

#### 4.4.3 State of Charge

State of charge (SoC) is used to describe the energy storage in a battery and is defined as:

$$\text{SoC} = \frac{E_{j,t}}{E_j} \times 100\% \quad (4.31)$$

Where  $E_{j,t}$  is the residual energy at time  $t$  and  $E_j$  is the storage capacity of the device. The SoC at  $t+1$  can be obtained as follows,

$$\begin{aligned} \text{SoC}_{j,(t+1)} &= \text{SoC}_{j,t} (1 - \sigma_j) - \frac{P_{j,t}}{E_j} \times 100\% \\ \text{SoC}_{j,(t+1)} &= \text{SoC}_{j,t} (1 - \sigma_j) - \frac{P_{j,t}}{E_j} \times 100\% \end{aligned} \quad (4.32)$$

with

$$P_{j,t} = P_{L,t} - P_{pv,t} - P_{wt,t}$$

In this study,  $\sigma_j$  is equal to 0.3% for LIB and 2% for supercapacitor. The SC performs the full discharging procedure without any impact on capacity unlike LIB. Hence, the DoD of SC can reach to 100%.

#### 4.4.4 Modeling Cycle Life of Battery

After significant amounts of charge-discharge cycles, the battery may fail to meet a specific performance criterion. Lithium-based batteries delivers between 300 and 500 full charge-discharge cycling before the capacity drops below 80 percent. The actual operating life of the battery is affected by DoD and other conditions, such as temperature and humidity. A higher DoD accelerates the shrinking of battery lifespan. For example, a battery may have 15,000 cycles at the 10 % of DoD, but only 3,000 cycles at the 80% of DoD. The amount of charge-discharge cycle of battery at a specific DoD level can be calculated as,

$$\begin{cases} N_{bat,ch} = \sum_t (SoC_{(t+1)} - SoC_t) & SoC_t < SoC_{t+1} \\ N_{bat,dis} = \sum_t (SoC_t - SoC_{(t+1)}) & SoC_t > SoC_{(t+1)} \end{cases} \quad (4.33)$$

where

$N_{bat,ch}$  = value of charging percentage in one operation period.

$N_{bat,dis}$  = value of discharging percentage in one operation period.

Based on  $N_{bat,ch}$  or  $N_{bat,dis}$  to calculate the lifetime loss of a battery, when  $N_{bat,ch}$  or  $N_{bat,dis}$  reaches the maximum number of charge-discharge cycles, the battery will be considered to replace.

#### 4.5 Modeling Load Demand

The electricity demand of a wafer fab is used as a case study to characterize the power use in an energy-intensive manufacturing facility. The results can be extended to other business sectors such as automobile assemblies, chemical and refinery industry, cloud computing, and data centers, because they usually operate in 24/7 mode. The load demand data, comprised of 12 months, is obtained from a local industry partner in

Austin, Texas. Figure 4.15 shows the load profile possesses strong seasonal patterns coupled with short-term demand variations and the probability of load demand. The power demand between late January and early April is among the lowest around 8.8 MW. It increases from April and reaches the peak of 10.4 MW in September, and then declines to 9.3 MW in later November.

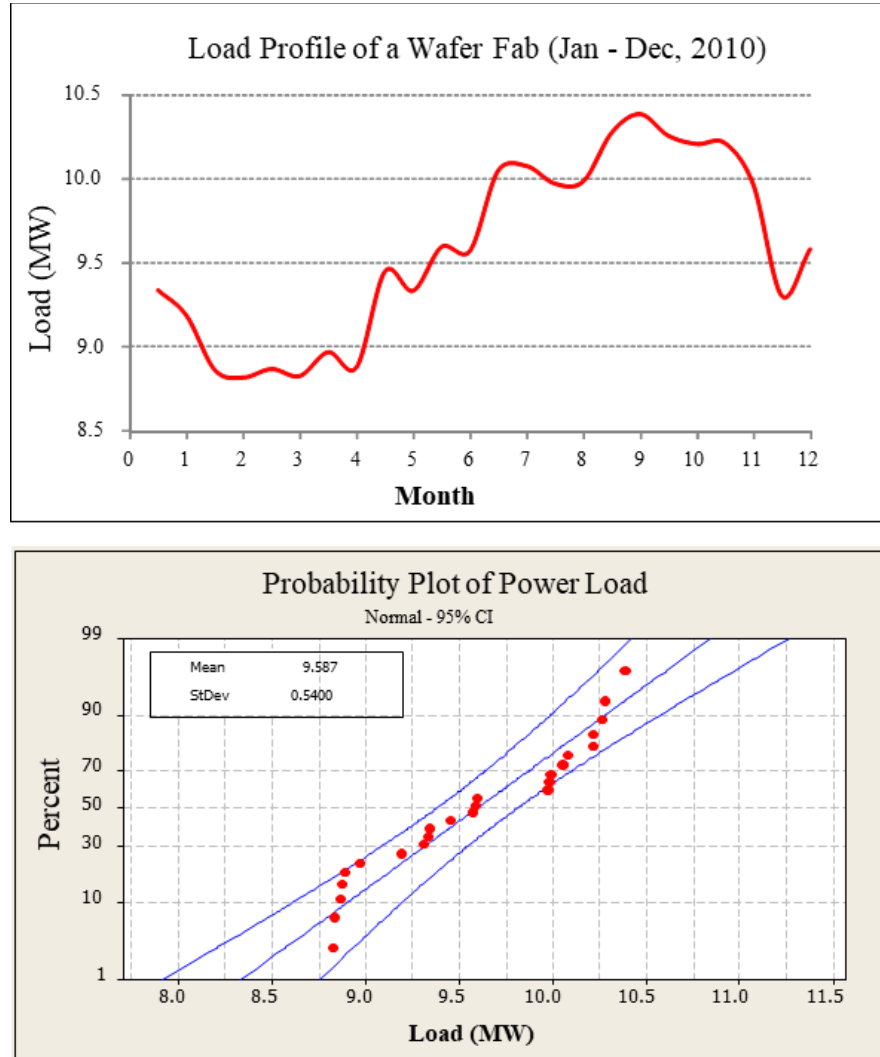


Figure 4.15: Wafer Fab Load Profile.

To capture the load seasonality as well as the short-term variation, the monthly mean load and standard deviation are estimated. The results of monthly mean load and standard deviation are presented in Table 4.8.

Table 4.8: Mean and Standard Deviation of Monthly Load.

Month	January	February	March	April	May	June
Mean (MW)	9.267	8.846	8.853	8.930	9.397	9.588
StDev (MW)	0.232	0.221	0.221	0.223	0.235	0.240
Month	July	August	September	October	November	December
Mean (MW)	10.068	9.983	10.334	10.237	10.093	9.448
StDev (MW)	0.252	0.250	0.258	0.256	0.252	0.236

\*Note: StDev = standard deviation.

Figure 4.16 plots the hourly demand in one day on September 1<sup>st</sup>. Due to the factory reduced the production during the night shift, the energy demand during the daytime is higher than in the night.

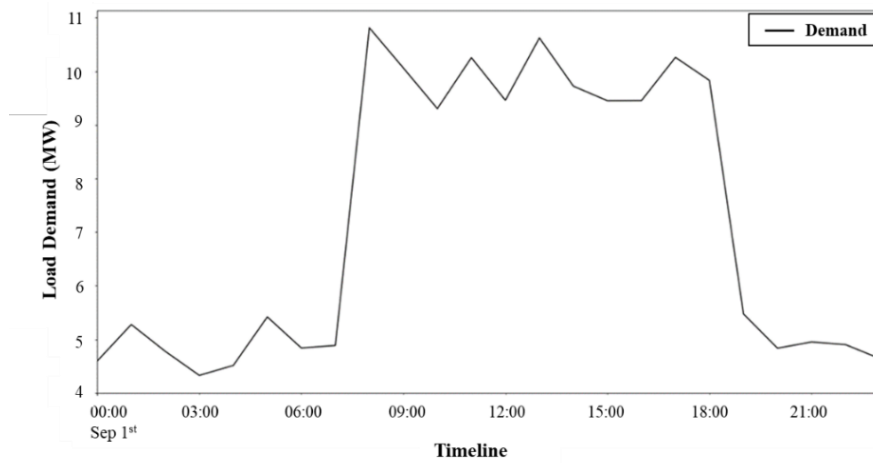


Figure 4.16: Simulate Load Demand in a Day.

## 5. LCOE PROSUMER MODEL

Levelized cost of energy (LCOE) is defined as the net present value of the unit cost of electricity over the lifetime of a generation asset. It is a critical criterion to evaluate the cost of energy based on the generation technology. In this study, the LCOE is the ratio between annualized operation cost of a power system divided by total delivered energy through a year. A quantitative approach is proposed to minimize the LCOE of each individual manufacturing facility by considering the power supply reliability criterion and time of use (TOU) rate. The manufacturer, as the prosumer, can export surplus energy or import energy to complement the shortage from the main grid. The model is tested and implemented in six testing cities with a variety of climate conditions. Table 5.1 summarizes the climate conditions of testing cities.

Table 5.1: Summary of Climate Conditions.

City	Wind Speed	Clear Sky
Wellington	H	L
San Francisco	M	M
Phoenix	L	H
Boston	M	L
New York	M	M
Sanya	L	H

In this chapter, optimization model will be designed based on the four operation modes shown in Table 5.2 for testing cities. In Case I, the goal is to minimize the LCOE within a one-year period under certain variables, such as manufacturer operated 24/7, carbon credit only applied for the solar PV generator, and \$70/MWh flat utility rate policy implement. Case I serves as the benchmark in this study. The one variable has been modified from Case II to Case IV. In case II, the manufacture is operated 12/7 during the daytime. In Case III, there are no incentive policies for stimulating investment

in renewable energy. TOU policy is applied for case IV.

Table 5.2: Operation Modes of Manufacturer.

Case	Operating mode	Carbon credit of PV (\$/MWh)	Pricing policy	Utility rate (\$/MWh)
1	24/7	10	Flat	70
2	12/7	10	Flat	70
3	24/7	0	Flat	70
4	24/7	10	TOU	\$140/MWh from 9 am. to 9 pm. \$70/MWh from 10 pm. to 8 am.

The mission of this chapter is to size the capacity of renewable generations and the capacity of energy storage devices in testing cities under four operation modes. Wind turbine is made by glass fiber reinforced plastic material and solar PV is m-Si module. Lithium-ion battery and graphene-based SC are adopted in the model. Table 5.3 states the value and unit of parameters in the mathematical function and Table 5.4 lists the variables in the model.

Table 5.3: Notation of Parameters (IEA, 2020).

Notation	Value	Unit	Comment
$a_1$	$1.5 \times 10^6$	\$/MW	Capacity cost of WT
$a_2$	$2 \times 10^6$	\$/MW	Capacity cost of PV
$a_3$	$0.6 \times 10^6$	\$/MWh	Capacity cost of LIB
$a_4$	$1.2 \times 10^6$	\$/MWh	Capacity cost of SC
$b_1$	12	\$/MWh	O&M cost of WT
$b_2$	4	\$/MWh	O&M cost of solar PV
$b_3$	3	\$/MWh	O&M cost of LIB
$b_4$	0	\$/MWh	O&M cost of SC
$c_1$	0	\$/MWh	Carbon credits of WT
$c_2$	0 or 10	\$/MWh	Carbon credits of PV
$\rho$	70	\$/MWh	Electricity rate
$q$	35	\$/MWh	Feed-in-tariff rate

Table 5.4: Notation of Decision Variables.

Notation	Unit	Variable Type	Comment
$P_{wt}^c$	MW	Continuous	Capacity of WT
$P_{pv}^c$	MW	Continuous	Capacity of PV
$B_{BS}^c$	MWh	Continuous	Capacity of Lithium-ion battery
$B_{SC}^c$	MWh	Continuous	Capacity of supercapacitor

## 5.1. Cost Analysis

The costs of system include the capital investment, operation and maintenance cost, and the utility bill (Sanders et al., 2012).

### 5.1.1 Installation Cost

$$C_{ln(p_g^c, B_j^c)} = \varphi_1(n_1, r) \sum_{g=1}^G a_g P_g^c + \varphi_2(n_2, r) \sum_{j=1}^E a_j B_j^c \quad (5.1)$$

with

$$\varphi(n, r) = \frac{r(1+r)^n}{(1+r)^n - 1}$$

where

$P_g^c$  = capacity of renewable energy technology (MW),  $G \in \{\text{WT, solar PV}\}$ .

$B_j^c$  = capacity of HESS (MWh),  $J \in \{\text{Battery, Supercapacitor}\}$ .

$a_g$  = capacity cost of renewable energy technology WT (\$/MW).

$a_j$  = capacity cost of HESS (\$/MWh).

$n_1$  = payment periods (Year) of renewable generators.

$n_2$  = payment periods (Year) of energy storage devices..

$r$  = interest rate (such as 5-6%).

$\varphi$  = capital recovery factor.

Note  $P_g^c$  and  $B_j^c$  are decision variables, they are unknown to be optimized in the model. The  $\varphi$  converts a present value into a stream of equal annual payments over a

specified time, at a specified discount interest rate.

### 5.1.2 Operation and Maintenance (O&M) Cost

Though wind and solar energy resources are free, the operation and maintenance cost have to do with two aspects: 1) leasing the land to install and place WT, PV units, and HESS systems; 2) repair and maintenance of WT, PV, and Li-battery due to component aging and wear-out.

$$C_{OM(P_g^c, B_j^c)} = \sum_{t=1}^T \sum_{g=1}^G b_g P_g^c \lambda_{gt} + \sum_{t=1}^T \sum_{i=1}^E b_j B_j^c \quad (5.2)$$

where

$\lambda_{gt}$  = the capacity factor of renewable generator at time  $t$ , for  $G \in \{\text{WT, PV}\}$

$b_g$  = annual O&M cost of renewable generation (\$/MWh).

$b_j$  = annual O&M cost of battery units (\$/MWh), O&M cost of supercapacitor is zero.

$T$  = number of hours in a year (i.e.,  $T=8,760$  hours).

### 5.1.3 Electricity Bill

When wind and solar generation are unavailable to meet the load, the manufacturer needs to purchase electricity from a utility company.  $p_t^B$  is the imported power from the substation. In this study, two pricing schemes are considered for the utility electricity: flat rate or time-of-use (TOU) pricing policy.  $\rho_t$  is the dynamic price expression at time  $t$ . For instance, the program contains two scenarios stage: first the price is \$140/MWh between 9:00 am. to 9:00 pm. on-peak period; and second, utility rate is down 50% during the off-peak period, \$70/MWh. The variation of the market price of electricity significantly affects the operation of the energy storage. The energy cost will be calculated based on the two scenarios.

$$C_{Ebill(P_i^c, P_j^c)} = \sum_{t \in T} p_t^B \rho_t y_t^B \quad (5.3)$$

where

$\rho_t$  = real-time utility price (\$/MWh), range from \$70/MW to \$140/MW.

$y_t^B$  = status of purchasing  $y_t^B \in \{0, 1\}$  at  $t$  for  $\forall t \in T$ .

$p_t^B$  = the amount of energy purchasing at time  $t$  for  $\forall t \in T$ .

## 5.2. Income Analysis

The system income consists of the carbon credit by generating renewable energy and the payment from the utility because of exporting the extra energy to the grid via feed-in-tariff program.

### 5.2.1 Carbon Credit Incentive

The carbon credit is the compensation due to the adoption of renewable energy technology. It is given to the manufacturer based on the amount of renewable energy produced. That is,

$$C_{cr(P_g^c)} = \sum_{t=1}^T \sum_{g=1}^G c_g P_g^c \lambda_{gt} \quad (5.4)$$

where

$c_g$  = carbon credits received by using renewable generation (\$/MWh).

Note carbon credit is only applied for WT generation technique as they actively produce the green electricity.

### 5.2.2 Net Metering Income

Net metering occurs when the output from onsite WT and PV units exceeds the power demand plus available storage of HESS. In this case, the surplus energy is stored in the HESS first, if they are not in the fully charged state, then fed to the main grid through feed-in-tariff program to create profit. Financially, the income by selling surplus

energy to the utility company can be calculated as,

$$C_{nm(P_g^c)} = \sum_{t=1}^T p_t^s q_t y_t^s \quad (5.5)$$

where

$q_t$  = the price by selling surplus electricity to the main grid,  $q_t = 0.5p_t$  at time  $t$ .

$y_t^s$  = binary variable, status of selling energy  $y_t^s \in \{0, 1\}$  at  $t$  for  $\forall t \in T$ .

$p_t^s$  = the amounts of energy purchasing at time  $t$  for  $\forall t \in T$ .

### 5.3 System Reliability Criterion

The loss of power supply probability (LPSP) is the criterion to measure and evaluate the reliability of the power supply system. LPSP is defined as the probability that an insufficient power supply results when the hybrid system (PV module, wind turbine, and hybrid energy storage system) is unable to satisfy the load demand (Yang et al., 2003). If the value of LPSP equals zero then the load will always be satisfied or the value of LPSP equals one then the load will never be satisfied. Let  $\alpha$  be the loss of power supply probability criterion, and typically  $\alpha < 0.001$ . Under this assumption, there is at most one outage event that occurred in one hour out of 1,000 hours. For one-year operation, power outage event is less than 9 times. In this study, LPSP of the microgrid power system can be formulated as below,

$$LPSP = \Pr \left\{ \frac{\sum_{t=1}^T \text{powerfailuretime}}{T} \right\} \quad (5.6)$$

Where  $T$  equals 8,736 operation hours in one year. The definition of power failure is the load cannot be satisfied when the power generated by both the wind turbine and PV array plus depleted HESS. Equation (5.6) also can be rewritten as follows:

$$LPSP = \frac{\sum_{t \in T} y_t^B}{T} \quad (5.7)$$

Where  $y_t^B$  is the binary variable and represents the purchasing status of the power system. If the system purchases energy from grid,  $y_t^B$  is one, otherwise,  $y_t^B$  equals zero.

#### 5.4 MLCOE Model

This section constructs a grid-connected micro-power system consisting of WT, PV, and hybrid energy storage devices by considering the system reliability. Here is the aggregate annualized cost model incorporating all the terms discussed previously. Note that carbon credits and net metering income as the revenue are negative with respect to the installation, operation, and maintenance costs, and so on in the system. Below is the annualized cost of system,

Aggregate Annulized Cost =

$$\left\{ \varphi_1(n_1, r) \sum_{g=1}^G a_g P_g^c + \varphi_2(n_2, r) \sum_{j=1}^E a_j B_j^c + \sum_{t=1}^T \sum_{g=1}^G b_g P_g^c \lambda_{gt} + \sum_{t=1}^T \sum_{i=1}^E b_i B_i^c - \sum_{t=1}^T \sum_{g=1}^G c_g P_g^c \lambda_{gt} \right\} \quad (5.8)$$

The objective function is to minimize the levelized cost of energy for prosumer model, which is defined as annualized energy cost divided by the total renewable energy generation in one year. The LCOE can be formulated as,

**Model 5.1:** minimize the levelized cost of energy (MLCOE)

$$f(P_i^c, B_j^c) = \frac{1}{\sum_{t=1}^T \sum_{i=1}^G P_{it}} \left\{ \varphi_1(n_1, r) \sum_{i=1}^G a_i P_i^c + \varphi_2(n_2, r) \sum_{j=1}^E a_j B_j^c + \sum_{t=1}^T \sum_{i=1}^G b_i P_{it} + \sum_{t=1}^T \sum_{i=1}^E b_j B_{jt}^{Dh} + \sum_{t=1}^T p_t^B \rho_t y_t^B - \sum_{t=1}^T p_t^s q_t y_t^s - \sum_{t=1}^T \sum_{i=1}^G c_i P_{it} \right\} \quad (5.9)$$

Subject to:

$$\sum_{i=1}^G P_{it} + p_t^B - p_t^s + \sum_{j=1}^E (B_{jt} - B_{j(t-1)}) = p_t^L \quad \text{for } \forall t \in T. \quad (5.10)$$

$$B_{jt} = B_{j(t-1)} + B_{jt}^{Ch} - B_{jt}^{Dh} \quad \text{for } \forall t \in T. \quad (5.11)$$

$$B_j^c S_j^{\min} \leq B_{jt} \leq B_j^c S_j^{\max} \quad \text{for } \forall t \in T. \quad (5.12)$$

$$B_{j0} = B_{jT} = B_j^c S_j^{\text{int}} \quad T=8760. \quad (5.13)$$

$$\sum_{t \in T} y_t^B \leq T * \alpha \quad \text{for } \forall t \in T; \quad (5.14)$$

$$p_t^B \leq M * y_t^B \quad \text{for } \forall t \in T. \quad (5.15)$$

$$y_t^B, y_t^s \in \{0,1\} \quad \text{for } \forall t \in T. \quad (5.16)$$

$$y_t^B + y_t^s \leq 1 \quad \text{for } \forall t \in T. \quad (5.17)$$

$$B_{jt}, B_{jt}^{Ch}, B_{jt}^{Dh}, p_t^s, p_t^B \geq 0 \quad \text{for } \forall t \in T. \quad (5.18)$$

$$P_1^c, P_2^c, B_1^c, B_2^c \geq 0 \quad (5.19)$$

Constraint (5.10) deploys the energy balance equation for any of the periods  $t$  in 1, ..., 8760; Constraint (5.11) states the energy conservation in the energy storage system at each operation period; Constraint (5.12) formulates the lower and upper bound on the storage level in HESS; Constraint (5.13) point out that the energy storage level at the end of operation period  $t = 8760$  equals initial stored energy level at  $t = 0$  in the HESS; Constraint (5.14) stipulates the service reliability in terms of loss-of-power supply probability; Constraint (5.15) ensures the purchasing energy is less than the biggest

demand in the whole operation process; Constraint (5.16) states the purchasing status and selling status and they are the binary variables; Constraint (5.17) ensures the purchasing status and selling status, and it ensures only one status or none of them occurs at the same period; Constraint (5.18) sets the sign of variable in the model; Constraint (5.19) is the sign constraint for the decision variables.

### 5.5 Numerical Experiment Results

All cases are compiled by the AMPL program, solved by the KNITRO solver. Each case has around 70K constraints, and computation time for each city of each operation mode is approximately 15min with Intel i7 8G memory.

Case I is the benchmark for this study and the experimental results are shown in Table 5.5. LCOE in Wellington and San Francisco is below \$70/MWh of referenced utility rate. The LCOE in the rest of the cities is still higher than the referenced utility rate. Suppose the utility price is increasing with 3% annual rate, the LCOE in all cities is less than \$126/MWh after 20 years. In the long-term, the renewable power system is cost-effective compared with the traditional power system.

Table 5.5: Experimental Results for Case I.

No.	Cities	WT (MW)	PV (MW)	LIB (MWh)	SC (MWh)	LCOE (\$/MWh)	Reference Utility Price	Cost difference after 20 years (\$/MWh)
<b>1</b>	<b>Wellington</b>	<b>16</b>	<b>11</b>	<b>105</b>	<b>0</b>	<b>54.7</b>	<b>70</b>	<b>-71.3</b>
<b>2</b>	<b>San Francisco</b>	<b>35</b>	<b>12</b>	<b>91</b>	<b>0</b>	<b>67.3</b>	<b>70</b>	<b>-58.7</b>
3	New York	30	16	67.2	9.7	77.3	70	-48.7
4	Phoenix	38	22	105	7	95.1	70	-30.9
5	Sanya	29	19	136	0	104	70	-22
6	Boston	27	23	132	12.4	118	70	-8

In Case II, the manufacturer is only operating 12 hours from 7:00 am. to 7:00 pm. in the daytime. The LCOE in Wellington reduces with limited scale. However, the LCOE in the rest of the cities reduces sharply, especially in the cities Phoenix and Sanya, because they have plenty of solar energy resources in a year compared with other cities. The installation of WT capacity in Phoenix and Sanya reduces due to more solar PV generator adopted. Another reason for decreasing LCOE is caused by cutting down the installation capacity of the li-ion battery and no SC demanded at all for all testing cities, because the manufacturer is only operating during the daytime and there is no energy needed during night.

Figure 5.1 plots the experimental results of Case I, Case III, and Case IV. In Case III, the carbon credit is not applied for both wind power and solar power generation. The TOU policy is implemented in Case IV. Under Case III, the LCOE rises for all the testing cities. The grid-connect onsite power system more prefers to install the onsite renewable generators to meet the manufacture demand, because TOU rate is more expensive. The LCOE trends down in Case IV compared with Case I.

Table 5.6: Experimental results: Cases I vs. Cases II.

City	Case 1					Case 2				
	WT (MW)	PV (MW)	LIB (MWh)	SC (MWh)	LCOE (\$/MWh)	WT (MW)	PV (MW)	LIB (MWh)	SC (MWh)	LCOE (\$/MWh)
Wellington	16	11	105	0	54.7	17	15	121.8	0	51.5
San Francisco	35	12	91	0	67.3	29	15	53.4	0	51.1
New York	30	16	67.2	9.7	77.3	30	13	62.4	0	55.2
Phoenix	38	22	105	7	95.1	24	20	67.2	0	73.9
Sanya	29	19	136	0	104	22	16	71.4	0	78.5
Boston	27	23	132	12.4	118	20	16	82.2	0	92.7

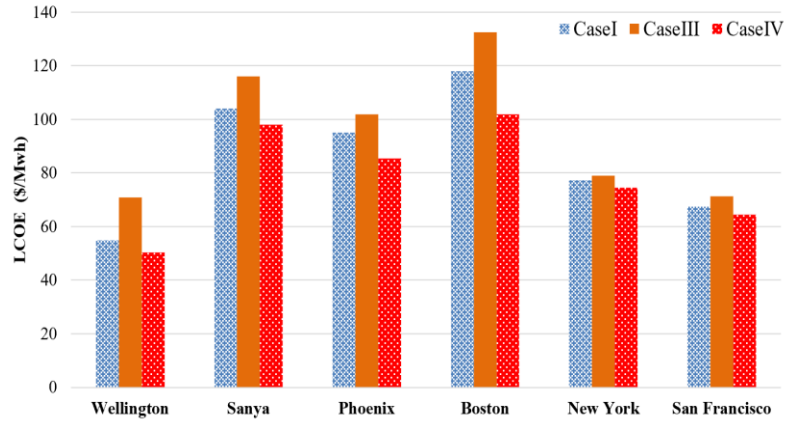


Figure 5.1: Experimental results: Cases I, III, and IV.

Table 5.7 illustrates the comparison of the installation capacity of renewable generation and HESS under two assumptions in Boston. The experiment results show the depth of discharging (DoD) impact on the system cost, capacity cost, and the lifetime of the battery. Increasing the depth of discharging is a double-edged sword, which can decrease the installation capacity of renewable generation meanwhile can shrink the lifetime of the li-based battery.

Table 5.7: DoD Impact on Installation Capacity of Devices in Boston.

Categories		DoD Rate				
		DoD (85%)	DoD (75%)	DoD (65%)	DoD (55%)	DoD (45%)
Without Consider DoD Impact	PV capacity	23	33.5	33.4	32.9	33.5
	WT capacity	27	33.5	36.4	42.9	46.5
	BS capacity	132	148	168	175.8	191.8
	SC capacity	12.4	19.4	29	39	52.4
Consider DoD Impact	PV capacity	26	37.5	39.4	43.9	45.5
	WT capacity	29	37	39	44.9	49.5
	BS capacity	144	156.1	188.2	193	196.8
	SC capacity	17.4	30	34	42	58
Lifetime of battery		13.3	23	33.5	33.4	32.9

The objective is to minimize the LCOE of the grid-connected onsite power system to size the installation capacity of renewable generation and energy storage devices. The hybrid energy storage system secures the reliability of the power supply. Some conclusions are deduced based on the numerical experiment results through all the cases in six testing cities: 1) WT is cost-effective if the local wind speed is above 6 m/s; 2) The local wind speed and weather features ultimately determine the mix of renewable generation portfolios; 3) The mix of installation capacity of HESS is the majority impacted by the operation mode of the manufacturer, not necessarily the carbon credit or TOU rate policy.

## 6. VPP-BASED MULTI-TIER PRODUCTION INVENTORY MODEL

With the growing penetration of wind and solar energy in the utility market, it is also imperative to incorporate the energy supply variability and the carbon constraints into the production-inventory management program to lower the manufacturing cost with superior environmental performance. Integrating renewable energy sources to power production-inventory systems is a viable approach to achieving low carbon industrial operations. Supply chain dive (2019) states Nike opens new distribution center running on 100% renewable energy.

This study is derived from the mechanism by installing renewable and combined heat and power (CHP) generators as the onsite power units for facilities in multi-tier production network model (Bhandari et al., 2019). Zidan et al. (2015) propose an optimal model to size capacity and select types of distributed generation for CHP systems within the microgrid. The objective of the model is to minimize the total net present cost of the microgrid system. The study proves the deployment of PV, electricity storage, and CHP hybrid systems can reduce consumer costs and carbon emissions. Shah et al. (2015) deploy a hybrid power system with PV, battery, and CHP at three regions in the U.S. which represent cold, warm, and hot areas. The sensitivity analysis has been carried out on the power generated of PV via varying the capacity factor of PV to maximize the environmental and financial benefits.

Two critical questions are addressed. First, how to design and optimize the virtual power plant (VPP) system for a multi-echelon, multi-period, production-distribution network under demand uncertainty and power intermittency. The network encompasses factories, warehouses, retail stores, and electrified logistics. Second, how to dispatch

renewable energy and schedule manufacturing operations in hourly biases with the participation of the transaction energy market to maximize the social-economic benefit. The cost of the system includes 1) production-inventory; 2) one-time investment of capacity renewable generators and ES units; and 3) operation and maintenance expense of renewable generators, CHP, and ES. Under the VPP scheme, the revenue of the system comprises renewable incentives and electricity sales to the transactive energy market. The selling price is time-varying and fluctuates in the trading market. The objective is to formulate a mixed integer programming model for minimizing the annual supply chain operation cost.

Energy consumed during production logistics network depends on the production plan and transportation between facilities. The contribution of this chapter can be summarized as follow:

- 1) A mixed integer linear (MIL) program is constructed to minimize the annual operation cost of the VPP system for multi-facility network over a one-year planning horizon. The goal is to size WT, PV, and ES units, which also provide an optimal energy production schedule under uncertain demand and energy supply.
- 2) Onsite power generators and energy storage are incorporated into the planning model to obtain low-carbon and cost-effective operations.
- 3) The strategic and tactical planning decisions are integrated, such as generation capacity decisions at each facility, inventory level at warehouses, production and backorder decisions, and shipment decisions.
- 4) Perform sensitivity analysis on the production plan and energy supply.

## 6.1 Problem Statement

Figure 6.1 exhibits the architecture of the VPP system. Typically, the VPP can be classified into source side VPP and load side VPP based on the operation condition. In this study, the source side VPP system consists of wind turbine (WT), solar photovoltaic (PV), combined heat and power (CHP), electricity storage (ES) unit, and thermal storage (TS) unit, providing both power and thermal to the local facilities. Wind turbine is made by glass fiber reinforced plastic material and solar PV is m-Si module. Lithium-ion battery is adopted in the model. Load side VPP consists of dynamic energy load due to the unpredicted product demand from stores. There is a single point of connection to the utility called the point of common coupling. The natural gas as the fuel input is needed only for the CHP, and the wind and sun as the energy input for the WT and solar PV. To meet the power demand, electricity can be produced directly by WT, PV, and CHP, meanwhile thermal load demand is also fulfilled by the CHP and thermal storage unit. CHP technology has a lower cost with higher efficiency. The system can export the surplus energy to the main grid in the day-ahead market.

In this study, the thermal energy is used locally within the facility and all microgrids are inter-connected with the main grid. This enables individual facilities to participate in energy trading market when excess electricity is generated. Since CHP and the thermal storage units are pre-installed in the facilities, the capacity cost of both units is not considered in the model. There are two levels of CHP operation in one year 1) unlimited operation, and 2) limited operation. A mixed integer linear programming model is proposed to allocate the microgrid capacity, sequentially schedule the production lot and the electric energy traded between the main grid and the microgrid.

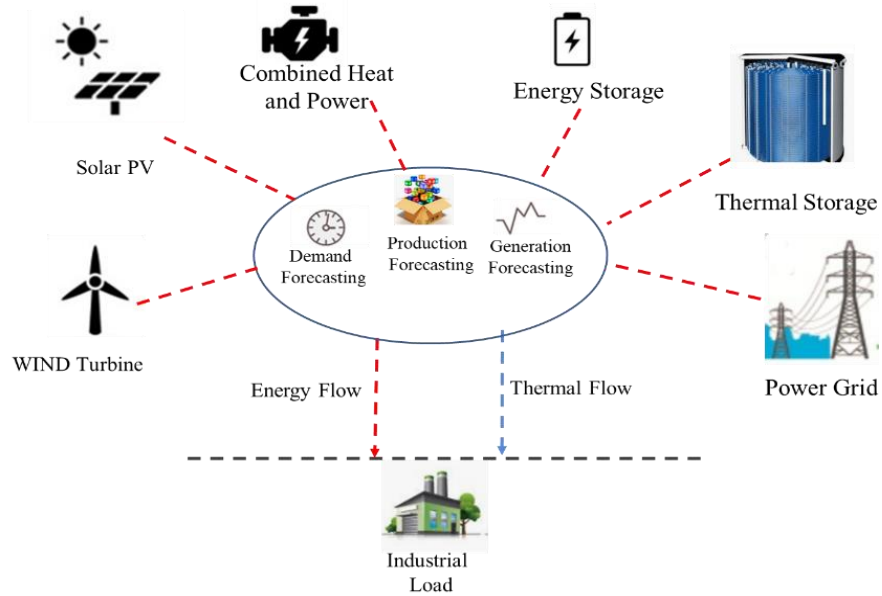


Figure 6.1: Block Diagram of VPP.

Assume the production supply chain VPP (PSV-VPP) network consists of  $K$  factories,  $N$  warehouses, and  $S$  stores. Each factory can produce  $I$  products to meet the aggregate demand of the stores. The goal is to optimize the production, inventory, backorders and capacity of WT, PV, and ES such that the annual operating cost is minimized. Tables 6.1 to 6.3 list the model sets, parameters, and the decision variables, respectively.

Table 6.1: Notation of Sets in PSC-VPP Model.

Indices	Definition
$I$	number of product type, for $I = 1, 2, \dots, I$ .
$J$	number of production period, for $j = 1, 2, \dots, J$ .
$G$	type of renewable energy generator, for $g = 1, 2, \dots, G$ .
$K$	number of factories in multi-location, for $k = 1, 2, \dots, K$ .
$N$	number of warehouses in multi-location, for $n = 1, 2, \dots, N$ .
$S$	number of stores in multi-location, for $s = 1, 2, \dots, S$ .
$R$	number of required production resources, for $r = 1, 2, \dots, R$ .
$T$	number of hours in a year, for $t = 1, 2, \dots, T$ .

Table 6.2: Notation of Parameters in PSC-VPP Model.

Notation	Definition
$\phi_g$	capital recovery factor of renewable energy generator $g$ .
$\phi_{BS}$	capital recovery factor of battery system.
$a_g$	capacity cost for renewable generator $g$ (unit: \$/MW).
$a_{BS}$	capacity cost for battery system (unit: \$/MWh).
$b_g$	operation and maintenance cost of renewable generator $g$ (unit: \$/MWh).
$b_{BS}$	operation and maintenance cost of battery system (unit: \$/MWh/year).
$b_{ijn}$	an intermediate or dependent variable for product $i$ in period $j$ at warehouse $n$ (unit: item).
$c_{CHP, k}$	operating cost of CHP in factory $k$ (unit: \$/MWh).
$c_{CHP, n}$	operating cost of CHP in warehouse $n$ (unit: \$/MWh).
$c_{CHP, s}$	operating cost of CHP in store $s$ (unit: \$/MWh).
$c_g$	carbon credits of renewable generator $g$ in the facility (unit: \$/MWh).
$\lambda_{gkt}$	capacity factor of renewable generator $g$ in factory $k$ at time $t$ .
$\lambda_{gnt}$	capacity factor of renewable generator $g$ in warehouse $n$ at time $t$ .
$\lambda_{gst}$	capacity factor of renewable generator $g$ in store $s$ at time $t$ .
$\rho_{DA,kt}$	price of day-ahead energy traded by factory $k$ at time $t$ (unit: \$/MWh).
$\rho_{DA,nt}$	price of day-ahead energy traded by warehouse $n$ at time $t$ (unit: \$/MWh).
$\rho_{DA,st}$	price of day-ahead energy traded by store $s$ at time $t$ (unit: \$/MWh).
$L_{E,nt}$	electric power demand in warehouse $n$ at time $t$ (unit: MW).
$L_{E,st}$	electric power demand in store $s$ at time $t$ (unit: MW).
$L_{TH,kt}$	thermal power demand in factory $k$ at time $t$ (unit: MW).
$L_{TH,nt}$	thermal power demand in warehouse $n$ at time $t$ (unit: MW).
$L_{TH,st}$	thermal power demand in store $s$ at time $t$ (unit: MW).
$c_{P,ijk}$	cost of making one unit of product $i$ in period $j$ at factory $k$ (unit: \$/item)
$c_{H,ijn}$	holding cost of product $i$ in period $j$ at warehouse $n$ (unit: \$/item/period).

$c_{B,ijn}$	backorder cost of product $i$ in period $j$ at warehouse $n$ (unit: \$/item).
$c_{NGI,kt}$	natural gas price in factory and warehouse (unit: \$/MWh).
$c_{NGC,nt}$	natural gas price in warehouse (unit: \$/MWh).
$c_{NGC,st}$	natural gas price in store (unit: \$/MWh).
$\pi_{ikn}$	shipping cost of product $i$ from factory $k$ to warehouse $n$ (unit: \$/item/km).
$\tilde{\pi}_{ins}$	shipping cost of product $i$ from warehouse $n$ to store $s$ (unit: \$/item/km).
$v_{ikr}$	resource $r$ consumed for making one unit of product $i$ at factory $k$ .
$w_{jkr}$	available production resource $r$ in period $j$ at factory $k$ .
$D_{ijs}$	random demand for product $i$ in period $j$ from store $s$ per period.
$\mu_{ijs}, \sigma_{ijs}$	mean and standard deviation of $D_{ijs}$ .
$\alpha$	probability of meeting the product demand.
$m_i$	unit weight of product type $I$ (unit: kg/item).
$e_{ik}$	energy use for making one unit of product $i$ at factory $k$ (unit: MWh/item).
$q_v$	e-truck electricity intensity rate (unit: MWh/kg/km).
$w_v$	e-truck self-weight (unit: kg).
$d_{kn}$	distance between factory $k$ and warehouse $n$ (unit: km).
$\tilde{d}_{ns}$	distance between warehouse $n$ and store $s$ (unit: km).
$n_{tkn}$	number of trips between factory $k$ and warehouse $n$ at time $t$ .
$\tilde{n}_{tns}$	number of trips between warehouse $n$ and store $k$ at time $t$ .
$\tau_{gk}$	operating time of generation $g$ at factory $k$ in a production period.
$\tau_{gn}$	operating time of generation $g$ at warehouse $n$ in a production period.
$\tau_{gs}$	operating time of generation $g$ at store $s$ in a production period.
$\tau_p$	time step size of a production period.
$\eta_k$	Electrical efficiency of CHP in factory $k$ (typically 30-40%).
$\eta_n$	Electrical efficiency of CHP in warehouse $n$ (typically 30-40%).
$\eta_s$	Electrical efficiency of CHP in store $s$ (typically 30-40%).
$\gamma_{CHP}$	Thermal to electric power ratio of a CHP (typical range is 2 to 10).

Table 6.3: Notation of Variables in PSC-VPP Model.

Variables	Definition
$x_{ijkn}$	number of product $i$ in period $j$ made by factory $k$ shipped to warehouse $n$ (unit: item).
$\tilde{x}_{ijns}$	number of product $i$ in period $j$ shipped from warehouse $n$ to store $s$ (unit: item).
$y_{ijn}$	inventory of product $i$ in period $j$ at warehouse $n$ (unit: item).
$z_{ijn}$	backorder of product $i$ in period $j$ at warehouse $n$ (unit: item).
$P_k^c$	power capacity of renewable generator $g$ in factory $k$ (unit: MW).
$P_n^c$	power capacity of renewable generator $g$ in warehouse $n$ (unit: MW).
$P_s^c$	power capacity of renewable generation $g$ in store $s$ (unit: MW).
$B_k^c$	capacity of electricity storage (ES) in factory $k$ (unit: MWh).
$B_n^c$	capacity of ES in warehouse $n$ (unit: MWh).
$B_s^c$	capacity of ES in store $s$ (unit: MWh).
$B_{E,kt}$	state of power energy level of ES at factory $k$ at time $t$ (unit: MWh).
$B_{E,nt}$	state of power energy level of ES at warehouse $n$ at time $t$ (unit: MWh).
$B_{E,st}$	state of power energy level of ES at store $s$ at time $t$ (unit: MWh).
$P_{DA,kt}$	electricity sold by factory $k$ at time $t$ (unit: MWh).
$P_{DA,nt}$	electricity sold by warehouse $n$ at time $t$ (unit: MWh).
$P_{DA,st}$	electricity sold by store $s$ at time $t$ (unit: MWh).
$B_{TH,kt}$	state of thermal energy level in TS at factory $k$ at time $t$ (unit: MWh).
$B_{TH,nt}$	state of thermal energy level in TS at warehouse $n$ at time $t$ (unit: MWh).
$B_{TH,st}$	state of thermal energy level in TS at store $s$ at time $t$ (unit: MWh).
$P_{CHP,E,kt}$	electricity power output of CHP in factory at time $t$ (unit: MW).
$P_{CHP,E,nt}$	electricity power output of CHP in warehouse at time $t$ (unit: MW).
$P_{CHP,E,st}$	electricity power output of CHP in store at time $t$ (unit: MW).
$P_{CHP,TH,kt}$	thermal power output of CHP in factory at time $t$ (unit: MW).
$P_{CHP,TH,nt}$	thermal Power output of CHP in warehouse at time $t$ (unit: MW).
$P_{CHP,TH,st}$	thermal Power output of CHP in store at time $t$ (unit: MWh).

## 6.2 Dispatch Strategy

The energy control and dispatch strategy for the VPP system is as follows. First, the PV and WT are prioritized, then energy storage, and finally the CHP unit to meet the demand.

- 1) If the energy generated by PV and WT is greater than the load, it will match the electrical demand. The surplus energy may be exported to the main grid or store in

ES units. The energy stored in the ES will be used during times when there is insufficient energy.

- 2) If the energy generated by PV and WT is less than the demand, the energy storage units are in discharge mode to complement the electricity gap.
- 3) If the energy gap still exists before ES depleted, the CHP unit is activated.

### **6.3 PSC-VPP Optimization Model**

The annualized cost of production supply chain integrated VPP system (PSC-VPP) is to minimize from three aspects. First, determining the production planning, namely  $\mathbf{x}$ ,  $\mathbf{y}$ , and  $\mathbf{z}$  are the decision variables representing the production, inventory, and backorders in each production period. Second, sizing the capacity of renewable generation and the energy storage units, namely  $\mathbf{P}^c$  and  $\mathbf{B}^c$  are the decision variables for renewable generators and ES capacity in each facility, respectively. Third, determine the amount of electric energy traded per facility  $\mathbf{P}_{DA}$  under the VPP scheme. Below are the mathematical formulations of the optimization model, including the objective function and constraints.

#### **6.3.1 Objective Function**

The objective function is to minimize the annualized operation cost of PSC-VPP system. The cost of PSC consists of production, inventory holding, backorder and transportation. The cost of VPP includes capacity investment, operation and maintenance (O&M), and revenue generated from selling electricity to main grid through day-ahead market as below,

### Model 6.1 PSC-VPP:

$$\begin{aligned}
& f(\mathbf{x}, \mathbf{y}, \mathbf{z}, \mathbf{P}^c, \mathbf{B}^c, \mathbf{P}_{DA}) \\
&= \sum_{k=1}^K \sum_{n=1}^N \sum_{i=1}^I \sum_{j=1}^J (c_{P,ijk} + \pi_{ijn}) x_{ijkn} + \sum_{n=1}^N \sum_{i=1}^I \sum_{j=1}^J c_{H,ijn} y_{ijn} + \sum_{n=1}^N \sum_{s=1}^S \sum_{i=1}^I \sum_{j=1}^J c_{B,ijn} z_{ijns} + \sum_{n=1}^N \sum_{s=1}^S \sum_{i=1}^I \sum_{j=1}^J \tilde{\pi}_{ins} \tilde{x}_{ijns} \\
&+ \sum_{k=1}^K \left( \sum_{g=1}^G \phi_g a_g P_{gk}^c + (\phi_{BS} a_{BS} + b_{BS}) B_k^c + \sum_{g=1}^G \sum_{t=1}^T \tau_{gk} (b_g - c_g) \lambda_{gkt} P_{gk}^c + \sum_{t=1}^T (c_{CHP,k} P_{CHP,E,kt} - \rho_{DA,kt} P_{DA,kt}) \right) \\
&+ \sum_{n=1}^N \left( \sum_{g=1}^G \phi_g a_g P_{gn}^c + (\phi_{BS} a_{BS} + b_{BS}) B_n^c + \sum_{g=1}^G \sum_{t=1}^T \tau_{gn} (b_g - c_g) \lambda_{gnt} P_{gn}^c + \sum_{t=1}^T (c_{CHP,n} P_{CHP,E,nt} - \rho_{DA,nt} P_{DA,nt}) \right) \\
&+ \sum_{s=1}^S \left( \sum_{g=1}^G \phi_g a_g P_{gs}^c + (\phi_{BS} a_{BS} + b_{BS}) B_s^c + \sum_{g=1}^G \sum_{t=1}^T \tau_{gs} (b_g - c_g) \lambda_{gst} P_{gs}^c + \sum_{t=1}^T (c_{CHP,s} P_{CHP,E,st} - \rho_{DA,st} P_{DA,st}) \right) \quad (6.1)
\end{aligned}$$

In the first line of objective function or Equation (6.1), the first term is the production cost in factory and shipping cost from factories to warehouses; second term is the holding cost in warehouses, the third term is the backorder cost, and last term is the shipping cost between warehouses and stores.

From the second to the fourth line, the first term is the installation cost of the renewable generation. The second term is the installation and operation cost of the ES units. The third term captures the annual O&M cost of the renewable generation and the reward of carbon credit. The fourth term is the operations cost of the CHP and the total revenue obtained through electricity sales in the day-ahead energy market.

#### 6.3.2 Production-inventory Constraints

$$\sum_{k=1}^K x_{i1kn} + y_{i0n} - y_{in} = \sum_{s=1}^S \tilde{x}_{i1ns}, \quad \text{for } j=1, \forall i, \text{ and } \forall n \quad (6.2)$$

$$\sum_{k=1}^K x_{ijkn} + y_{i(j-1)n} - y_{ijn} = \sum_{s=1}^S \tilde{x}_{ijns}, \quad \text{for } j=2, 3, \dots, J-1, \forall i, \text{ and } \forall n \quad (6.3)$$

$$\sum_{k=1}^K x_{iJkn} + y_{i(J-1)n} - y_{iJn} = \sum_{s=1}^S \tilde{x}_{iJns}, \quad \text{for } j=J, \forall i, \text{ and } \forall n \quad (6.4)$$

$$\Pr \left\{ \sum_{n=1}^N \tilde{x}_{ijns} + \sum_{n=1}^N z_{ijns} - \sum_{n=1}^N z_{i(j-1)ns} \geq D_{ijs} \right\} \geq \alpha, \quad \text{for } \forall i, \forall j, \text{ and } \forall s \quad (6.5)$$

$$\sum_{i=1}^I \sum_{n=1}^N v_{irk} x_{ijkn} \leq w_{jkr}, \quad \text{for } \forall j, \forall k, \text{ and } \forall r \quad (6.6)$$

$$y_{i0n} = 0, \quad \text{for } j = 0, \forall i \text{ and } \forall n \quad (6.7)$$

$$y_{iJn} = 0, \quad \text{for } j = J, \forall i \text{ and } \forall n \quad (6.8)$$

$$z_{i0ns} = 0, \quad \text{for } j = J, \forall i \text{ and } \forall n \quad (6.9)$$

$$z_{iJns} = 0, \quad \text{for } j = J, \forall i \text{ and } \forall n \quad (6.10)$$

$$\tau_p x_{itkn} = x_{ijkn}, \quad \text{for } \forall i, \forall j, \forall k, \text{ and } \forall n \quad (6.11)$$

$$\tau_p \tilde{x}_{itns} = \tilde{x}_{ijns}, \quad \text{for } \forall i, \forall j, \forall k, \text{ and } \forall n \quad (6.12)$$

Constraints (6.2) to (6.4) are the production-inventory balance equations between factories and warehouses for each product. Constraint (6.5) is the chance constraint and states that for given product  $i$  in period  $j$ , the demand of stores  $s$  must be satisfied with  $100 \times \alpha\%$  confidence. Constraint (6.6) represents the production resources constraint, such as available labor and machine hours in each period. Constraints (6.7) to (6.10) assume that amount of inventory and backorder are zero in the initial and end of operation period. Constraints (6.11) and (6.12) convert the strategic production decision into hourly production rate, and  $\tau_p$  is the length of a production period.

### 6.3.3 Energy Demand Constraints

For each production hour, the electricity demand, and the charging and discharging of ES energy at a particular facility must match the sum of the power output of CHP and onsite renewable generation.

$$\begin{aligned} \tau_k L_{E,k} + \sum_{i=1}^I \sum_{n=1}^N (e_{ik} + q_v d_{kn} m_i) x_{itkn} + \sum_{n=1}^N q_v n_{ikn} d_{kn} w_v + B_{E,k(t-1)} - B_{E,kt} + P_{DA,kt} \\ = \sum_{g=1}^G \lambda_{gkt} P_k^c \tau_{gk} + P_{CHP,E,kt}, \end{aligned} \quad (6.13)$$

for  $\forall t$  and  $\forall k$

$$\begin{aligned} \tau_n L_{E,n} + \sum_{k=1}^K q_v n_{tkn} d_{kn} w_v + \sum_{i=1}^I \sum_{s=1}^S q_v \tilde{d}_{ims} m_i \tilde{x}_{itms} + \sum_{s=1}^S q_v \tilde{n}_{ims} \tilde{d}_{ns} w_v + B_{E,n(t-1)} - B_{E,nt} + P_{DA,nt} \\ = \sum_{g=1}^G \tau_{gn} \lambda_{tgn} P_{gn}^c + P_{CHP,E,nt}, \end{aligned} \quad (6.14)$$

for  $\forall t$  and  $\forall n$

$$\tau_s L_{E,s} + \sum_{n=1}^N q_v \tilde{n}_{tms} \tilde{d}_{ns} w_v + B_{E,s(t-1)} - B_{E,st} + P_{DA,st} = \sum_{g=1}^G \tau_{gs} \lambda_{tgs} P_{gs}^c + P_{CHP,E,st}, \quad (6.15)$$

for  $\forall t$  and  $\forall s$

Particularly, Constraints (6.13) to (6.15) represent the hourly electricity balance equation at the factories, warehouses, and stores, respectively. In constraint (6.13), the forward electric transportation is included for factories  $k$  where the battery of e-trucks is fully charged prior to departure. Constraint (6.14) defines the electricity balance of warehouses  $n$  including the forward electric transportation to stores and backward electric transportation to factories. Constraint (6.15) states electricity balance of stores  $s$  including the backward electric transportation to warehouses. Similarly, the thermal energy at each facility must be balanced by considering the demand, the charging and discharging of TS units, and the heat output of CHP unit.

$$P_{CHP,TH,kt} + B_{TH,k(t-1)} - B_{TH,kt} \geq \tau_k L_{TH,k}, \quad \text{for } \forall t \text{ and } \forall k \quad (6.16)$$

$$P_{CHP,TH,nt} + B_{TH,n(t-1)} - B_{TH,nt} \geq \tau_n L_{TH,n}, \quad \text{for } \forall t \text{ and } \forall n \quad (6.17)$$

$$P_{CHP,TH,st} + B_{TH,s(t-1)} - B_{TH,st} \geq \tau_s L_{TH,s}, \quad \text{for } \forall t \text{ and } \forall s \quad (6.18)$$

Constraints (6.16) to (6.18) represent the thermal balance conditions for factories, warehouses, and stores, respectively.

### 6.3.4 CHP Constraints

For CHP generator, the annual operation hours are limited based on their lifetime.

Once CHP is in running status, then the operation hour is counted for that period.

$$0 \leq \sum_{t=1}^T O_{CHP,k,t} \leq O_{CHP,k}^{\max}, \quad \text{for } \forall k \quad (6.19)$$

$$0 \leq \sum_{t=1}^T O_{CHP,n,t} \leq O_{CHP,n}^{\max}, \quad \text{for } \forall n \quad (6.20)$$

$$0 \leq \sum_{t=1}^T O_{CHP,s,t} \leq O_{CHP,s}^{\max}, \quad \text{for } \forall s \quad (6.21)$$

In Constraints (6.19) to (6.21),  $O_{CHP,k,t}$  is binary variable, if CHP generator is operated at time period  $t$ , then  $O_{CHP,k,t}$  equals 1, otherwise 0.

$$C_{CHP,kt} = \frac{C_{NGI,kt}}{\eta_k}, \quad \text{for } \forall t \text{ and } \forall k \quad (6.22)$$

$$C_{CHP,nt} = \frac{C_{NGC,nt}}{\eta_n}, \quad \text{for } \forall t \text{ and } \forall n \quad (6.23)$$

$$C_{CHP,st} = \frac{C_{NGC,st}}{\eta_s}, \quad \text{for } \forall t \text{ and } \forall s \quad (6.24)$$

Constraints (6.22) to (6.24) describe the relation of CHP operation cost with the natural gas price. For instance, if  $C_{NGC,kt} = \$7/\text{MWh}$ , and  $\eta_k = 50\%$ , the operating cost of CHP for electricity generation at factories  $k$  would be  $\$14/\text{MWh}$ .

$$P_{CHP,TH,kt} = \gamma_{CHP} P_{CHP,E,kt}, \quad \text{for } \forall t \text{ and } \forall k \quad (6.25)$$

$$P_{CHP,TH,nt} = \gamma_{CHP} P_{CHP,E,nt}, \quad \text{for } \forall t \text{ and } \forall n \quad (6.26)$$

$$P_{CHP,TH,st} = \gamma_{CHP} P_{CHP,E,st}, \quad \text{for } \forall t \text{ and } \forall s \quad (6.27)$$

The heat generated from CHP generators is calculated by multiplying the electricity output with the heat-to-power ratio  $\gamma_{CHP}$  of CHP generator in Constraints (6.25) to (6.27).

### 6.3.5 Capacity Constraints

The electricity and heat produced by the CHP generators over any period  $t$  at each facility cannot exceed their installed capacity as follows,

$$0 \leq P_{CHP,TH,kt} \leq P_{CHP,TH,k}^{\max}, \quad \text{for } \forall t \text{ and } \forall k \quad (6.28)$$

$$0 \leq P_{CHP,TH,nt} \leq P_{CHP,TH,n}^{\max}, \quad \text{for } \forall t \text{ and } \forall n \quad (6.29)$$

$$0 \leq P_{CHP,TH,st} \leq P_{CHP,TH,s}^{\max}, \quad \text{for } \forall t \text{ and } \forall s \quad (6.30)$$

$$0 \leq P_{CHP,E,kt} \leq P_{CHP,E,k}^{\max}, \quad \text{for } \forall t \text{ and } \forall k \quad (6.31)$$

$$0 \leq P_{CHP,E,nt} \leq P_{CHP,E,n}^{\max}, \quad \text{for } \forall t \text{ and } \forall n \quad (6.32)$$

$$0 \leq P_{CHP,E,st} \leq P_{CHP,E,s}^{\max}, \quad \text{for } \forall t \text{ and } \forall s \quad (6.33)$$

For the renewable generator, installation capacity constraints are given as follows,

$$0 \leq P_{gk}^c \leq P_{gk}^{\max}, \quad \text{for } \forall t \text{ and } \forall k \quad (6.34)$$

$$0 \leq P_{gn}^c \leq P_{gn}^{\max}, \quad \text{for } \forall t \text{ and } \forall n \quad (6.35)$$

$$0 \leq P_{gs}^c \leq P_{gs}^{\max}, \quad \text{for } \forall t \text{ and } \forall s \quad (6.36)$$

Both electricity and thermal energy storage constraints are considered at each facility.

$$0 \leq B_{E,kt} \leq B_k^c, \quad \text{for } \forall t \text{ and } \forall k \quad (6.37)$$

$$0 \leq B_{E,nt} \leq B_n^c, \quad \text{for } \forall t \text{ and } \forall n \quad (6.38)$$

$$0 \leq B_{E,st} \leq B_s^c, \quad \text{for } \forall t \text{ and } \forall s \quad (6.39)$$

Constraints (6.37) to (6.39) stipulate that the electricity stored in an ES unit should not exceed its capacity at time  $t$  as below.

$$0 \leq B_{TH,kt} \leq B_{TH,k}^{\max}, \quad \text{for } \forall t \text{ and } \forall k \quad (6.40)$$

$$0 \leq B_{TH,nt} \leq B_{TH,n}^{\max}, \quad \text{for } \forall t \text{ and } \forall n \quad (6.41)$$

$$0 \leq B_{TH,st} \leq B_{TH,s}^{\max}, \quad \text{for } \forall t \text{ and } \forall s \quad (6.42)$$

Similarly, Constraints (6.40) to (6.42) below stipulate that the thermal energy stored in a TS unit should not exceed its capacity at time  $t$ .

### 6.3.6 Chance Constraint

Normality assumption on product demands is often used in literature (Mula et al., 2006; Kok et al., 2018). Let  $\mu_{ijs}$  and  $\sigma_{ijs}$  be the mean and standard deviation of product demand  $D_{ijs}$ , the chance Constraint (6.5) can be converted into deterministic counterpart as follows,

$$\sum_{n=1}^N \tilde{x}_{ijns} + \sum_{n=1}^N z_{ijns} - \sum_{n=1}^N z_{i(j-1)ns} \geq \mu_{ijs} + z_{\alpha} \sigma_{ijs} , \quad \text{for } \forall i, \forall j, \text{ and } \forall s \quad (6.43)$$

where  $z_{\alpha}$  is the  $z$ -value of the standard normal distribution with probability  $\alpha$ . For instance,  $z_{\alpha}=1.28$  given  $\alpha = 90\%$  in this study.

## 6.4 Capacity Factor of WT and PV in Testing Cities

The total energy required to operate the facilities comes from the renewable energy sources and CHP. However, the generation of renewables is uncertain due to unpredictable climate conditions. The capacity factor (CF) is defined as the ratio between the actual output power of a WT or PV unit versus its capacity for a given period. Let  $\lambda_{tgs}$ ,  $\lambda_{tgn}$ , and  $\lambda_{tgs}$  represent the CF value between 0 and 1 depending on wind speed and sunshine conditions at time  $t$ . Ten cities are chosen because they represent a wide range of climate conditions. The hourly wind speed and weather states of each city from 2006 to 2016 are retrieved from the web portal of Weather Underground with total of 192,192 records (Weather Underground, 2017). The aggregate climate data of ten cities reaches 1.92 million. In this study, the value of CF is less than 0.2 called the low state. The medium state of CF covers the range between 0.2-0.4 and the remainder interval is called the high state. This allows for estimating the hourly CF values accurately. The CF of WT and PV for each city is summarized in Table 6.4.

Table 6.4: Capacity Factors of WT and PV in Five Cities.

No	City and State	Wind Turbine			Solar PV		
		Average	Std Dev	Category	Average	Std Dev	Category
1	Phoenix, AZ	0.12	0.051	Low	0.32	0.192	Medium
2	Reno, NV	0.17	0.214	Low	0.35	0.208	Medium
3	Las Vegas, NV	0.24	0.298	Medium	0.43	0.257	High
4	Salt Lake City, UT	0.26	0.277	Medium	0.22	0.140	Medium
5	San Jose, CA	0.14	0.148	Low	0.31	0.188	Medium

## 6.5. Numerical Experiments

### 6.5.1. Model Parameters

The network layout including the mileage between two adjacent cities is shown in Figure 6.2. Electric trucks (e-trucks) are employed to move the finished goods from the factories to the warehouses and further down to the stores. Factories 1 and 2 are placed in Phoenix and Reno, respectively. Las Vegas is the location for the warehouse. Stores 1 and 2 are sited in Salt Lake City and San Jose, respectively. Each factory is capable of manufacturing two Products, A and B. The production planning is scheduled on a weekly basis over one year, or 52 weeks. Assume the weekly product demands of stores 1 and 2 are normally distributed with the mean and standard deviation given in Table 6.5. The demand in each store should be met with  $\alpha = 90\%$  confidence.

Table 6.5: Weekly Product Demands from Stores.

Store	Product A		Product B	
	Mean	Standard Deviation	Mean	Standard Deviation
Salt Lake City	600	55	500	70
San Jose	400	60	350	50

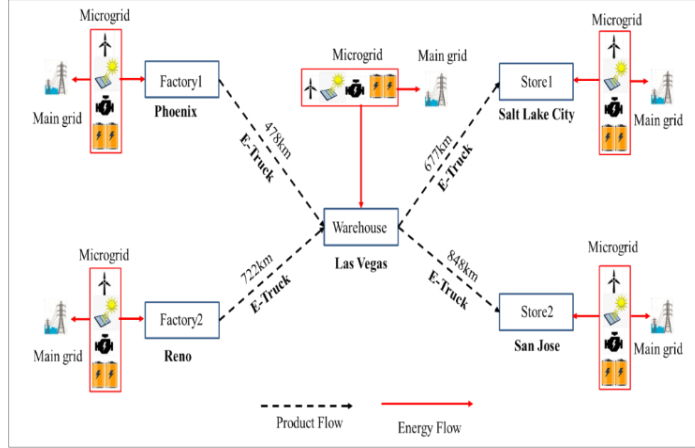


Figure 6.2: Energy, Product, and Transportation Flow across Facilities.

The distances between factories and warehouses, and warehouses and stores are recorded in kilometers. The homogeneous fleet of E-trucks have been applied to freight transportation in this study. Parameters for resources consumption to make and transport each item of Products A and B, such as energy use, labor and machine hour, inventory overhead, production, and transportation cost per item are given in Table 6.6.

Table 6.6: Parameters for Production Planning in Model.

Comments	Notation	Product A	Product B	Unit
		( $i=1$ )	( $i=2$ )	
Energy use	$e_i$	0.9	1.2	MWh/item
Production cost	$p_i$	400	600	\$/item
Holding cost	$h_i$	16	24	\$/item/week
Backorder cost	$b_i$	75	100	\$/item
Shipping cost	$\pi_i$	0.05	0.08	\$/item/km
Labor hour	$v_{i1}$	16	24	hour/item
Machine hour	$v_{i2}$	100	200	hour/item
Product weight	$m_i$	3	4	kg/item

Table 6.7 presents parameters of WT, PV, ES, e-trucks and bidding utility pricing. Though variations may exist, these values are adopted or estimated based on the reports from National Renewable Energy Laboratory (Stehly et al., 2018; Fu et al., 2018a; Fu et al., 2018b). The capital recovery factor of WT and PV,  $\phi_g$ , is estimated assuming 20 years

lifetime with the 5% interest rate. For ES,  $\varphi_{ES}$  is estimated assuming 10 years lifetime with the 5% interest rate. The self-weight of an e-truck  $w_v = 5,000$  kg, and the electricity intensity rate  $q_v = 1.19 \times 10^{-7}$  MWh/kg/km at 100 km/hour (Pham et al., 2019). The number of round trips between a factory and the warehouse is one trip per week, and the number of round trips between the warehouse and a store is also one trip per week. Both factories operate 24 hours a day and 7 days a week (i.e., 24/7 mode), and the electric load of a factory depends on the weekly production rate of Products, A and B.

Table 6.7: Parameter value in PSC-VPP.

DG	Notation	Value	Unit	Notation	Value	Unit
WT	$a_g$	1.5	\$/MWh	$T$	8736	hour
WT	$b_g$	8	\$/MWh	$n_{tkn}, \tilde{n}_{ms}$	1	trip/week
WT	$c_g$	0	\$/MWh	$\tau_w, \tilde{\tau}_s, \tau_{gk}, \tau_{gn}, \tau_{gs}$	1	hour
WT	$\phi_g$	0.0802	n/a	$\tau_p$	168	hour
PV	$a_g$	2	\$/MWh	$\rho_{DA}$	35	\$/MWh
PV	$b_g$	4	\$/MWh	$L_{E,kt}, L_{E,nt}, L_{E,st}$	2, 3, 5	MW
PV	$c_g$	10	\$/MWh	$L_{TH,kt}, L_{TH,nt}, L_{TH,st}$	5, 5, 2	MW
PV	$\phi_g$	0.0802	n/a	$\eta_k, \eta_n, \eta_s$	2, 2, 2	
ESS	$a_{BS}$	0.3	\$/MWh	$C_{NGI,kt}$	10	\$/MWh
ESS	$b_{BS}$	0.0075	\$/year	$C_{NGI,nt}$	20	\$/MWh
ESS	$\varphi_{ES}$	0.12	n/a	$C_{NGC,st}$	20	\$/MWh
E-Truck	$w_v$	5000	kg	$\gamma_{CHP}$	2	
E-Truck	$q_v$	$1.19 \times 10^{-7}$	MWh/kg/km	$\gamma_{bat}$	1	

### 6.5.2 Numerical Experiment Result for 2F-1W-2S Network

The network consists of two factories, one warehouse, and two stores, denoted as 2F-1W-2S. All the facilities participate in the VPP initiative, which the facilities realize energy self-sufficiency and bid in the day-ahead energy market to create profit by selling surplus energy. Assumed, CHP is already installed in the facilities and the capital cost is not considered in this study. The capacity of CHP is 25 MW, 10 MW, and 10 MW in the factory, warehouse, and store, respectively.

The total annualized cost in 2F-1W-2S network can be broken into two parts: 1) production-inventory, and 2) VPP system cost. The model contains 930 integer variables, 218,420 continuous variables, over 795,000 constraints. The model is coded in AMPL language. CPLEX solver is used to search for the optimal  $\mathbf{x}$ ,  $\mathbf{y}$ ,  $\mathbf{z}$ ,  $\mathbf{P}^c$ ,  $\mathbf{B}^c$ , and  $\mathbf{P}_{DA}$ . A personal computer with Intel Core i7 CPU (2.8 GHz), with 8.00 GB of RAM, is used for all implementations in this section. The running time ranges from 4 to 5 minutes for each case.

### 6.5.3 Result for Production Planning

The total cost in 2F-1W-2S network is \$ 81,831,023. The cost in production-inventory part is \$ 64,620,678, which represents around 78.9% of total cost of PSC-VPP model. Table 6.8 lists the experiment result and percentage of each category in production-inventory cost for Case 1.

Table 6.8: Production-inventory Cost.

Type	Amount	Proportion (%)
Production cost	\$54,683,200	84
Shipping cost	\$9,586,980	14
Inventory cost	\$191,323	0.29
Backorder cost	\$159,175	0.24

Figure 6.3 depicts the weekly production, inventory, and backorders of Products A and B, respectively. The energy consumption of Product B is higher than Product A. Product B has a more expensive shipping cost than A and a farther shipping distance from Factory 2 (Reno factory) to warehouse than Factory 1 (Phoenix). Most of Product B is still made from Factory 2, because Factory 2 has the stronger wind and solar resources compared with Factory 1. The backorder cost and holding cost are relatively high for both products. The model returns a solution with small amounts of backorders and inventory.

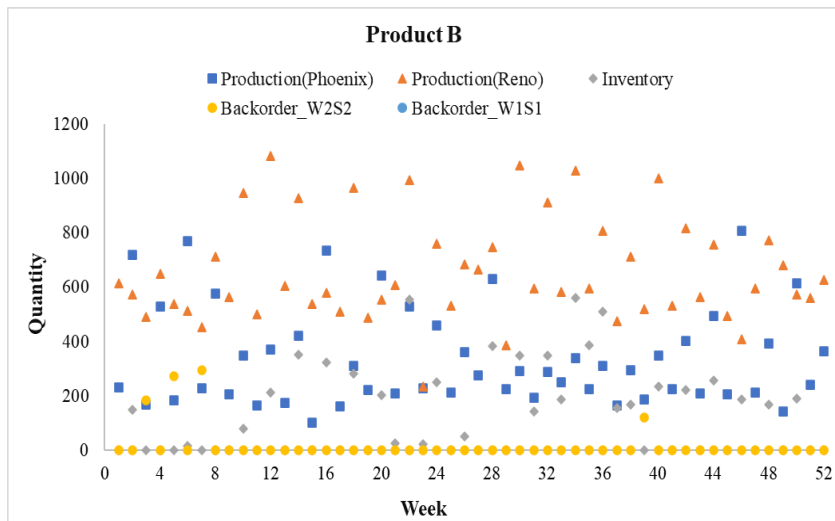
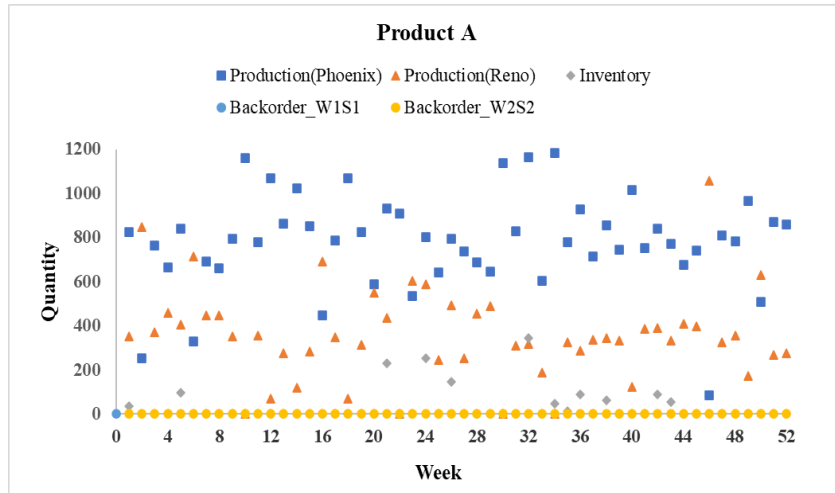


Figure 6.3 Production and Inventory Decision of the 2F-1W-2S Network.

Figure 6.4 plots the shipping amount of Products A and B from the warehouse to the stores. The shipping quantity of goods cannot always meet the demand of the store in each period, especially at the beginning of the year. The limited available energy triggers this phenomenon. The backorder in the beginning and end of the operation period is always zero.



Figure 6.4: Transportation between Warehouse and Stores of the 2F-1W-2S Network.

#### 6.5.4 Result for Microgrid Allocation and Scheduling

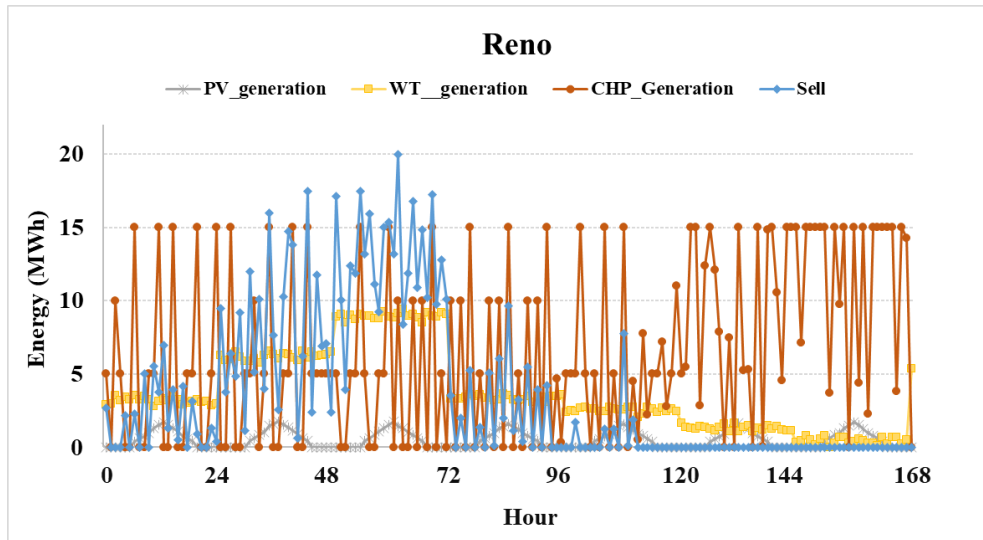
This section presents the optimal solution of WT, PV, ESS capacity, and the hourly selling energy amount in each facility. The capacity of WT, PV, ESS and energy sales of each facility is summarized in Table 6.9. The VPP system cost  $f(\mathbf{P}^c, \mathbf{B}^c, \mathbf{P}_{DA})$  is \$17,210,345 and selling income is \$4,676,490.

Table 6.9: Size of WT, PV and ESS for the 2F-1W-2S Network.

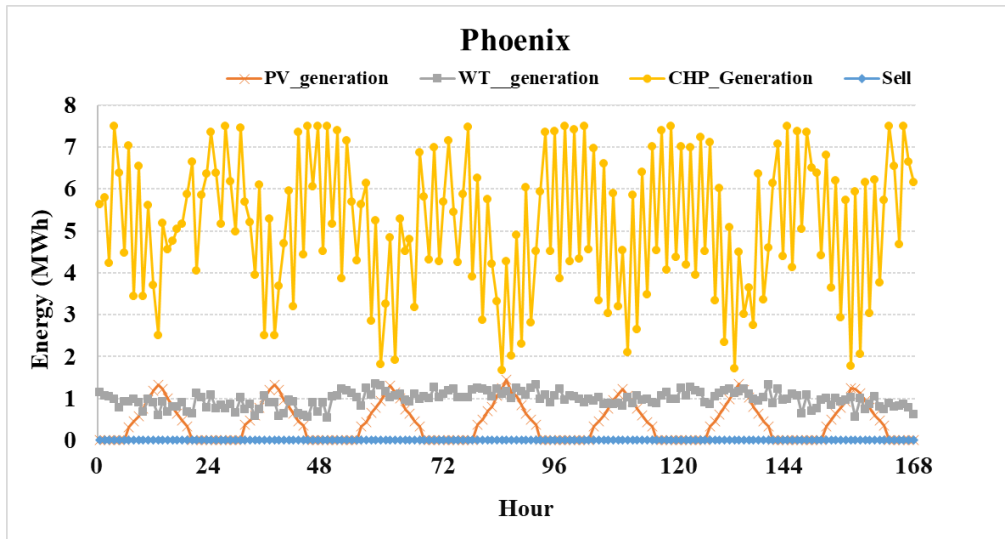
Type	Phoenix (Factory 1)	Reno (Factory 2)	Las Vegas (Warehouse)	Salt Lake City (Store 1)	San Jose (Store 2)
WT (MW)	13.322	21.359	10	15	9.899
PV (MW)	3.173	4.26	0.765	0	5.554
ESS (MWh)	1.58	5.054	0	0	0.01
Sell (MWh/Year)	2,070	35,460	41,364	41,295	13,425

The excess energy can be sold to the main grid via the day-ahead market. Figures 6.5 to 6.8 show the selling energy and the energy generation from the renewable and CHP units. Factories 1 and 2 sell about 2,035 MWh and 35,823 MWh in one year, respectively. There is a huge difference between these two cities because Reno has higher

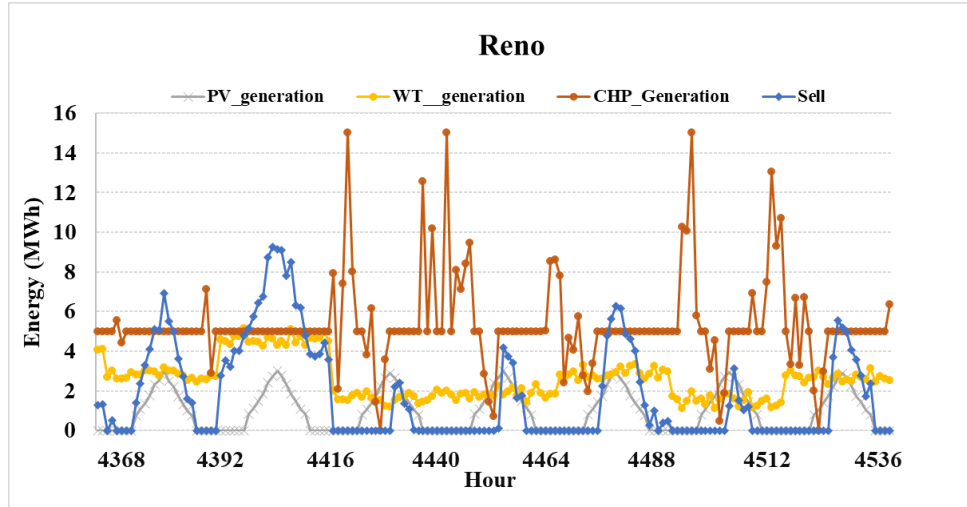
renewable capacity factors. Reno sells more electricity during the 2<sup>nd</sup> quarter as shown Figure 6.6, meanwhile Reno has strong seasonal wind speed.



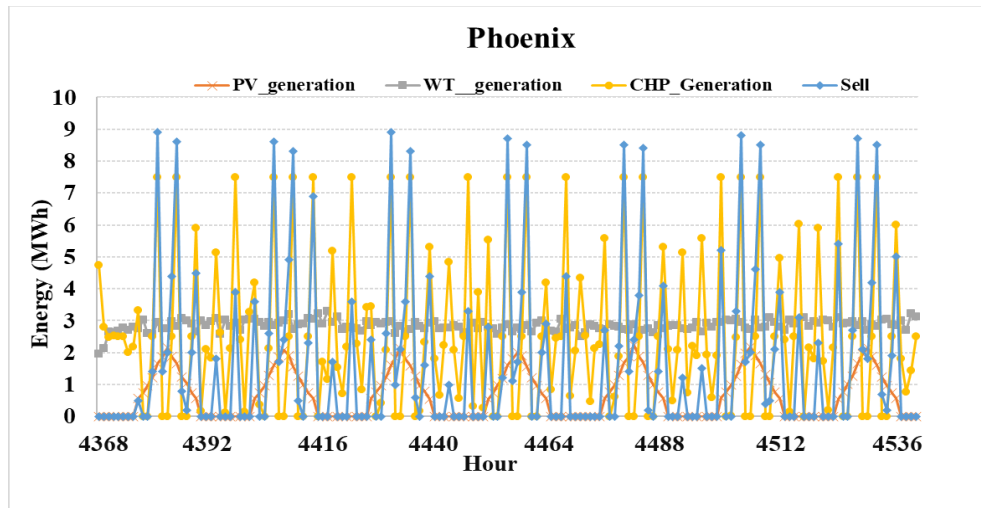
(a). 1<sup>st</sup> Quarter in Reno.



(b). 1<sup>st</sup> Quarter in Phoenix.



(c). 3<sup>rd</sup> Quarter in Reno.



(d). 3<sup>rd</sup> Quarter in Phoenix.

Figure 6.5: Hourly Energy Transactions in 1<sup>st</sup> and 3<sup>rd</sup> Quarter in Factories.

## 6.6 Sensitivity Analysis

The sensitivity analysis aims to quantify the importance of uncertain parameters regarding their contribution to model output variability, which investigates parameter importance by varying one parameter at a time, while keeping other parameters fixed. The sensitivity analysis is performed to investigate how: 1) the holding cost and backorder cost influence production and inventory decision; and 2) bidding electricity price, natural gas price, battery capacity cost, and PV capacity cost impact

VPP cost.

### 6.6.1 Sensitivity Analysis of Production Planning

The holding cost and the backorder costs vary by 50%, while energy consumption varies by 10% of Products A and B with respect to the benchmark. Model PSC-VPP is resolved and the new results are summarized in Table 6.10 along with the benchmark cost. It is found that the relative cost difference is quite small and between -7.56% and 7.6%. Hence the production decision is robust regardless of relatively large variations in holding cost, backorder cost and energy consumption of product.

Table 6.10: Sensitivity Analysis on Production Planning.

Scenario	$f(\mathbf{x}, \mathbf{y}, \mathbf{z}, \mathbf{P}^c, \mathbf{B}^c, \mathbf{P}_{DA})$ (\$)	Cost Difference(\$)	Relative Difference (%)
Benchmark	81,988,282	0	0
Increase $h_i$ by 50%	82,075,909	87,627	0.107
Decrease $h_i$ by 50%	81,888,786	-99,496	-0.121
Increase $b_i$ by 50%	82,061,053	72,771	0.089
Decrease $b_i$ by 50%	81,881,975	-106,307	-0.13
Increase product energy consumption by 10%	82,990,392	1,002,110	1.222
Decrease product energy consumption by 10%	81,032,590	-955,692	-1.16
Increase capacitor factory by 20%	79,798,707	-2,189,575	-2.76
Increase capacitor factory by 50%	75,817,468	-6,170,814	-7.56
Decrease capacitor factory by 20%	84,281,156	2,292,874	2.80
Decrease capacitor factory by 50%	88,243,784	6,255,502	7.60

## 6.6.2 Sensitivity Analysis on Microgrid Allocation

Sensitivity analysis is performed by varying the microgrid parameters, including natural gas price, energy selling price, capacity cost of battery, and capacity cost of solar PV. The cost of 14 variants is compared with the benchmark study (i.e., Case 1), and the results are summarized in Tables 6.11, 6.12, and 6.13.

Table 6.11: Comparisons of Annual Cost among Cases.

Case	$f(\mathbf{x}, \mathbf{y}, \mathbf{z}, \mathbf{P}^c, \mathbf{B}^c, \mathbf{P}_{DA})$	Cost Difference (\$)	Relative Difference(%)	Comments
1	81,988,282	0	0	Benchmark
2	86,846,889	4,858,607	5.9	Natural gas price increasing 50%
3	76,002,465	-5,985,817	-7.9	Natural gas price decreasing 50%
4	84,002,381	2,014,099	2.4	Natural gas price increasing 20%
5	79,820,509	-2,167,773	-2.9	Natural gas price decreasing 20%
6	70,694,424	-11,293,858	-13.8	Selling price increasing 100% \$70/MWh (9am-9pm), \$35/MWh other time
7	74,378,554	-7,609,728	-9.9	140/MWh (9am-9pm), \$70/MWh other time
8	46,485,620	-35,502,662	-49.9	\$0.05M/MWh for battery cost
9	81,513,437	-474,845	-0.6	\$0.1M/MWh for battery cost
10	81,727,544	-260,738	-0.3	\$1.8M/MW for PV (decreasing 10%)
11	81,618,883	-369,399	-0.5	\$1.5M/MW for PV(decreasing 25%)
12	80,623,336	-1,364,946	-1.7	\$1M/MW for PV(decreasing 50%)
13	77,360,401	-4,627,881	-5.6	CHP operation hour less than 6000hours/Y
14	82,205,092	216,810	0.3	

Five observations are found. First, the bidding price has more impact on the supply chain cost by comparing all cases. When the selling price increases by 100% from \$35/MWh to \$70/MWh, the system cost decreases by 13.8% in Case 6. When the rates for selling electricity to the grid vary from \$70/MWh during peak hour from 10 am - 9 pm to \$35/MWh during off-peak hour from 10 pm to next day 9 am, the system cost reduces by 9.3% in Case 7. The installation capacity of generations reaches the upper

limit and the amount of selling energy increases more than twice in Table 5.3. Second, Cases 9 and 10 show that reducing capacity cost of ES unit has little impact on the total operation cost. This observation is counterintuitive because ES is often treated as a good solution to mitigate the intermittency of wind and PV generation. Third, natural gas price not only influences the operation cost of CHP, but also affects the size of renewable generators as in Table 6.13. Fourth, the facility prefers to install more solar PV when the price of PV is down to \$0.5M/MW. Finally, it shows PSC-VPP is more efficient when multi-generator is selected through compared with Case 1 and Case 14. Without restricted operation, CHP unit cuts down cost.

Table 6.12: Size of WT, PV, and ESS form Case 1 to Case 7.

Cases	Type	Phoenix (Factory 1)	Reno (Factory 2)	Las Vegas (Warehouse)	Salt Lake City (Store 1)	San Jose (Store 2)
Bench mark	WT (MW)	13.322	21.359	10	15	9.899
	PV (MW)	3.173	4.26	0.765	0	5.554
	ESS (MWh)	1.58	5.054	0	0	0.01
2	WT (MW)	17.559	22.456	10	12	14.253
	PV (MW)	5.213	6.279	0.833	4.343	6.332
	ESS (MWh)	1.154	3.589	0.053	4.251	2.568
5	WT (MW)	10.662	16.632	10	15	3.745
	PV (MW)	0.738	3.225	0.354	1.295	4.57
	ESS (MWh)	2.059	8.878	0.053	4.251	4.721
3	WT (MW)	14.898	22.091	10	15	11.867
	PV (MW)	4.243	5.398	0.816	2.351	6.068
	ESS (MWh)	1.233	4.246	0.053	4.251	2.977
4	WT (MW)	11.753	20.078	10	15	8.06
	PV (MW)	0.856	2.569	0.683	1.295	5.739
	ESS (MWh)	2.258	6.213	0.053	4.251	3.787
6	WT (MW)	15.071	25	10	15	15
	PV (MW)	25	25	10	3.36	15
	ESS (MWh)	1.189	3.374	0.053	4.251	2.465
7	WT (MW)	19.835	25	10	15	15
	PV (MW)	25	25	10	7.005	15
	ESS (MWh)	1.298	3.454	0.053	4.251	2.465

Table 6.13: Size of WT, PV, and ESS from Case 8 to Case 14 .

Cases	Type	Phoenix (Factory 1)	Reno (Factory 2)	Las Vegas (Warehouse)	Salt Lake City (Store 1)	San Jose (Store 2)
8	WT (MW)	25	25	10	15	15
	PV (MW)	25	25	10	15	15
	ESS (MWh)	0.761	3.652	0.053	4.251	2.465
9	WT (MW)	2.796	9.248	0.758	15	5.311
	PV (MW)	8.816	7.44	10	1.295	9.003
	ESS (MWh)	17.404	14.63	0.053	4.251	20
10	WT (MW)	9.973	13.711	10	15	8.843
	PV (MW)	4.437	6.7	0.758	1.295	6.082
	ESS (MWh)	3.649	13.796	0.053	4.251	3.617
11	WT (MW)	12.361	19.391	10	15	9.16
	PV (MW)	5.251	6.538	10	2.093	6.907
	ESS (MWh)	1.857	6.425	0.053	4.251	3.548
12	WT (MW)	11.702	25	10	15	8.292
	PV (MW)	10.292	15.229	10	4.816	10.706
	ESS (MWh)	2.767	9.47	0.053	4.251	3.736
13	WT (MW)	9.996	15.442	10	15	7.977
	PV (MW)	25	25	10	15	15
	ESS (MWh)	2.663	9.622	0.053	4.251	3.805
14	WT (MW)	14.899	20.291	10	15	10.629
	PV (MW)	5.639	5.279	2.351	4.93	6.79
	ESS (MWh)	9.084	5.385	3.9	1.23	2.9

Normally, ES unit absorbs surplus energy at the highest output and releases stored energy when power is in shortage. After introducing the TOU rate or simply adjusting selling price, the status of ES has changed accordingly, such as in Cases 6 and 7. ES releases all the stored energy to generate profit in the peak hour and keeps a high storage

level in off-peak hours in Case 7. In Case 6, the status of ES is always at zero level in each operation step, even if solar PV has a high-power output between 10 am to 4 pm. The surplus energy directly exports to the main grid instead of storing it in ES units as shown in Figure 6.9.

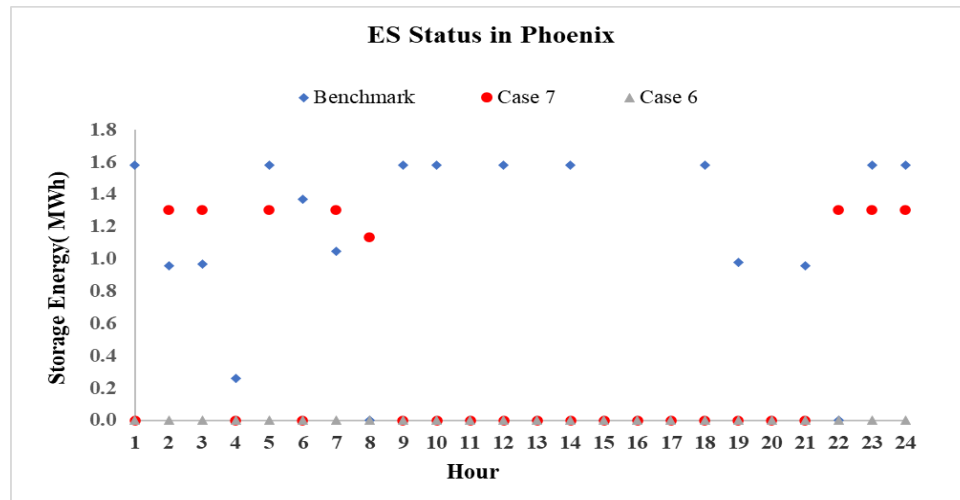


Figure 6.6: Status of ES in 24 hours.

### 6.6.3 Sensitivity Analysis on CHP Operation

CHP operation shedule is considered in Case 14 in oder to ensure the service life of unit. In this case, the operation hour of CHP in each facility has limitation, the total operation hour is assumed to be less than 6000 hrs/year considering the necessary downtime for maintenance. The experiment results show the operation hour of CHP in the first and the fourth quarter of a year is longer than the rest of a year. Limitation of CHP operation hour also affects the sizing of ES unit in the factories compared with Case 1 and Case 14.

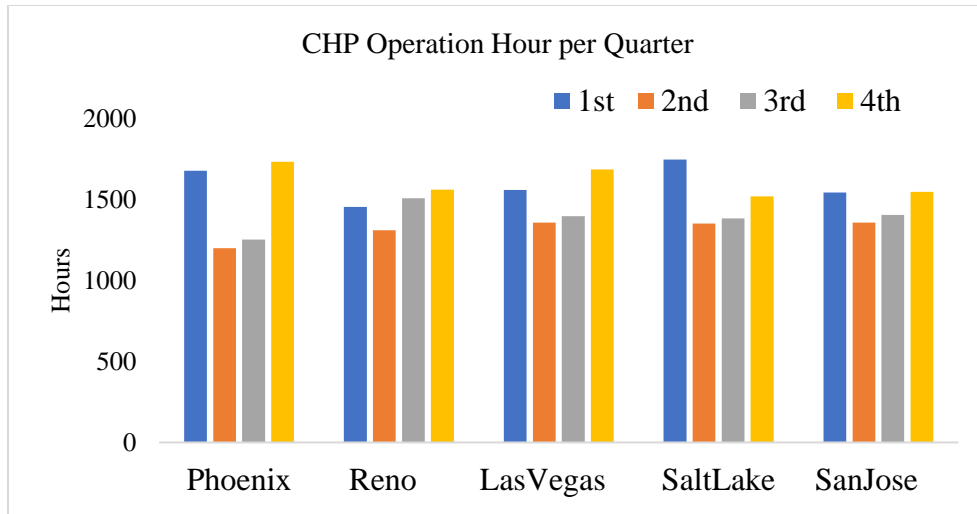


Figure 6.7: Scheduling CHP Operation Hours in One-year at Facilities.

## 6.7 Conclusions of Analysis

With a large number of the VPP implemented in the manufacturing plants, this study presents a mix-integer, production and energy planning model for the supply chain operations. The proposed model supports VPP economics and power management, which is essential for integration large-scale, on-site renewable generation, and CHP unit with thermal load. The main conclusions are as follows:

- 1) The sensitivity analysis of the electricity market price is performed in Cases 6-8. Higher electricity market prices yield higher profits and incentivize the facilities to install more renewable generators. The annual cost of VPP reduces due to more revenue income of energy sales. The electricity market price also impacts the behavior of ES, and surplus energy is more likely to be exported to main grid directly.
- 2) The sensitivity analysis of capacity cost of solar PV and battery in Cases 9 to 13 illustrates that changes in capacity cost only slightly impact the total system cost.

- 3) The available wind and solar resources of the factory affect the production plan. High energy consumption products will be made in factories with abundant natural resources, even if the shipping distance is longer and a higher shipping cost incurs between factory and warehouse.
- 4) The expense of the supply chain system increases when CHP has restricted operating hours. The result indicates that the VPP system works more efficiently when multiple generators are selected. It means that the PSC-VPP model works in a more efficient way when multiple generations are selected. CHP technique has a lower cost with higher economic savings.

## 7. BATTERY TECHNOLOGY DEVELOPMENT AND SIMULATION

### 7.1 Lithium-ion Electrochemical Energy Storage Device

Lithium-ion battery (LIB) technology was commercially introduced by Sony in the early 1990s based on the use of lithium intercalation compounds. As a main advantage, LIB can be recharged hundreds of times and more stable with a lower self-discharge rate than other rechargeable batteries. It has zero to minimal memory effect, unlike lead-acid battery. LIB has successfully applied in portable electronics and electrical vehicles. With the continued technical advances of LIB batteries, it has the capability to be utilized as the utility-scale energy storage for the intermittent renewable power system, i.e., wind and solar. Though the cost of LIB battery is constantly falling, it is still higher than that of Nickel-cadmium or lead-acid batteries.

The primary functional components of LIB include a carbon negative electrode (or cathode), a metal-oxide positive electrode (anode), an organic electrolyte with dissolved lithium ions, and a micro-porous polymer separator with high energy density and high dynamics. The electrochemistry process can be expressed by a formula below:



The electrons flow from the negative electrode to the positive electrode during the charging process inside of a battery, on the contrary, the discharging process is a reverse process. The charging and discharging process is shown in Figure 7.1.

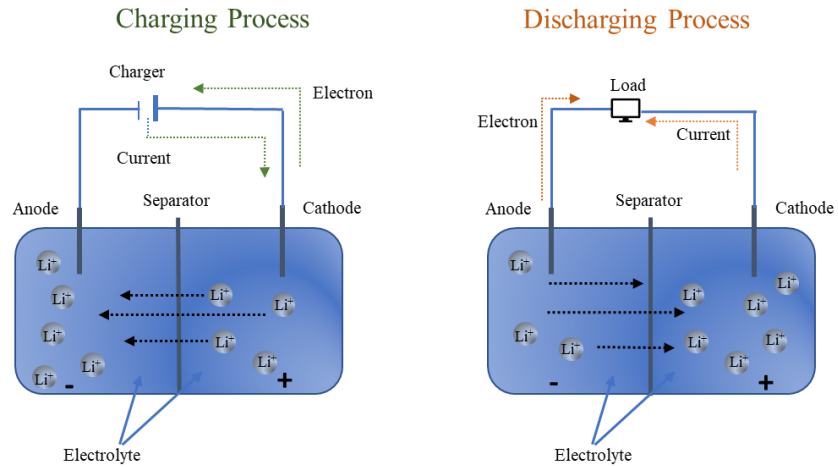


Figure 7.1: Charging and Discharging Process of Li-ion Battery.

## 7.2 Supercapacitor Energy Storage Device

Supercapacitor (SC) is a novel energy storage device that can be applied in many fields. The electrochemical performance of SC is governed by the electrode material. Therefore, more efforts have been paid to exploit electrode materials aimed at increasing specific capacitance as well as energy density. Graphene (GR) becomes the most promising material of energy storage devices due to the high surface area and electrical conductance.

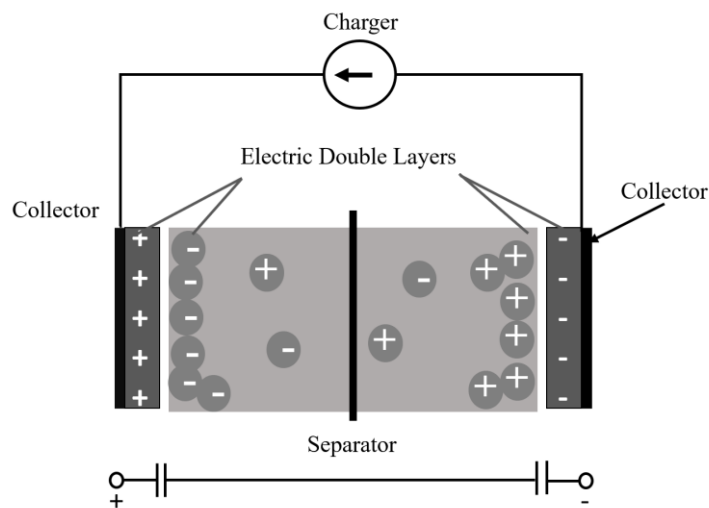


Figure 7.2: Schematic of an EDLC.

Based on the energy storage mechanism, SC can be classified into three types: electric double layer capacitor (EDLC), pseudocapacitor, and hybrid supercapacitor formed by a combination of EDLC and pseudocapacitor. The structure of EDLC is shown in Figure 7.2 with ions adsorption process. SC may be applied in consumer electronics, electric transportation systems (e.g., electric vehicle), and electric utility industry (e.g., improving grid system stability, quickly responding to the peak demands). The following equations (Luo et al., 2015) are used to estimate capacitance and energy of a capacitor, respectively.

$$C = \epsilon_0 \epsilon_r \frac{A}{d} \quad (7.2)$$

$$E = \frac{1}{2} CV^2 \quad (7.3)$$

where,

$C$  = Capacitance (F).

$A$  = Area of plate overlap ( $m^2$ ).

$D$  = Distance between plates in meters (m).

$\epsilon_0$  = Electric constant (F/m).

$\epsilon_r$  = Dielectric constant.

$V$  = Voltage across capacitor (V).

SC are polarized by design with either symmetric or asymmetric electrodes. Compared with symmetrical SC, the asymmetrical SC, consisting of two dissimilar electrodes, have the following advantages: higher specific capacitance, higher rated voltage, and corresponding to higher specific energy. In recent years, GR has significant characteristics such as large specific area, good flexibility, excellent electrical conductivity, good chemical and thermal stability, wide potential window, and abundant

surface functional groups (Zhu et al., 2010).

GR is a single, tightly packed layer of carbon atoms that are bonded together in a hexagonal honeycomb lattice. Researchers have proved that microchemically cleaved graphene has high mobility ( $15,000 \text{ cm}^2/\text{v/s}$ ) with  $1,013/\text{cm}^2$  electrons and holes concentration at room temperature (Warner et al., 2012, Neto et al., 2009, Charlier et al., 2007, Reina et al., 2008). Graphene can also form composites with other kinds of carbon such as graphene oxide, multi-walled carbon nanotubes, or electrochemically active materials such as polypyrrole and metal oxide.

From Bae et al. (2010), three major approaches have been used for GR synthesis: 1) Reduction of graphene oxide generated by the graphite oxide; 2) Exfoliation of graphite; and 3) Chemical-vapor deposition (CVD). At present, CVD method is most successful in synthesizing higher quality and large-scale graphene film or sheet up to meter scale. Typically, the CVD synthesis approach is involved in reactions between hydrocarbon gases, such as methane and metal substrate, by applying high temperature and low pressure. Graphene layer can be synthesized on a sheet of copper and transferred onto a flexible substrate. Besides the three major synthesis methods, there are several alternative methods available for graphene synthesis, such as graphene growth on SiC wafers, mechanical exfoliation of graphite to give graphene (Scotch-tape method), thermal annealing, flash reduction for graphene oxide. Details can be found in studies by Geim (2011), McAllister et al. (2007), and Cote et al. (2009).

### **7.3 Nanomaterial for SC Electrode**

SC can offer high power density, long cycle life, high charging-discharging rate, and low-cost properties. The working performance of SC is primarily decided by two

factors that are the electrode material and its structure. The surface area of electrode material is one of the most important variables to affect the value of capacitance. Table 7.1 illustrates the test results that the specific surface area that shows the significant influences on the capacitance. The high proportion of over 20 Å micro-pores result in carbon materials having large specific areas. The surface area of nano-sample is measured by Brunauer-Emmett-Teller (BET) technique.

Table 7.1: Comparisons of Specific Surface Area with EDLC Capacitance (Chen et al., 2015).

	Property of Activated Carbon Cloth			Characteristics of Electric Double Layer Capacitor	
	Specific Surface Area by BET	Strength	Proportion of micro-pores of diameter over 20 Å	Capacitance	Internal Resistance
Product of the invention	300 m <sup>2</sup> /g	Strong	50%	8 F	1 Ω
	300 m <sup>2</sup> /g	Strong	50%	8 F	1 Ω
	300 m <sup>2</sup> /g	Strong	80%	10 F	1 Ω

### 7.3.1 Graphene and graphene oxide

The GR-based SC have significantly increased both energy and power density. Theoretically, a single layer GR has the specific capacitance 21 uF/cm<sup>2</sup>. Xia et al. (2009) design a series of experiments to measure GR specific capacitance. Its practical value reaches 550 F/g when the entire surface area is fully utilized. Reduced graphene oxide (rGO) sheets have insulator property, with differential conductivity values of (1-5)×10<sup>3</sup> S/cm depending on the oxidation degree and highest specific capacitance of 175 F/g with aqueous electrolyte. rGO has been used as an electrode and solid separator material for SCs (Xia et.al., 2009).

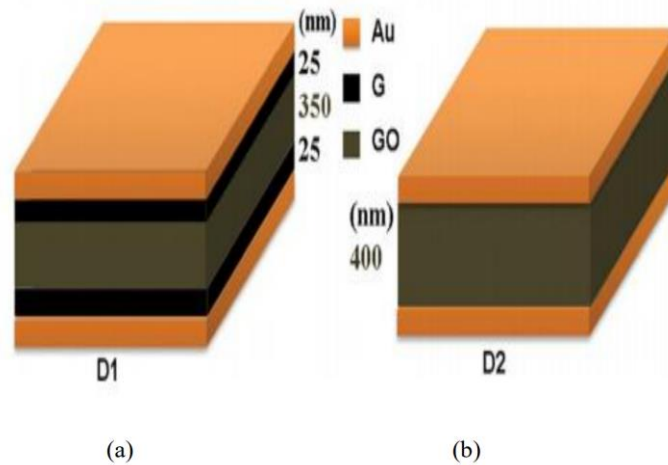


Figure 7.3: Schematic of Two Devices with Different Spacer Thickness (Liu et al., 2013).

The GR and rGO are deployed to make electrode and dielectric spacer components of SC, respectively. Liu et al. (2013) make two devices ( $D_1$  and  $D_2$ ) to investigate the GR electrode material to enhance the capacitance and the dielectric constant of rGO. The structure of  $D_1$  is shown in Figure 7.3(a), which is made of GR/GO/GR stacked films in which each graphene layer is 25 nm thickness and the thickness rGO spacer is 350 nm.  $D_2$  shown in Figure 7.3(b) is made from a 400 nm rGO film. The capacitance can be calculated by the cyclic voltammetry. Both have excellent working performance, however, capacitance of  $D_1$  is more than two times of  $D_2$ .

The results indicated that GR could be a good electrode material for SC and rGO because of its high dielectric constant that can be applied as a spacer in thin-film SC. Besides, rGO as the dielectric spacer can be used to fabricate all-solid-state SC device with no electrolyte leaks.

### 7.3.2 Graphene and Metal Oxide Nanocomposite Electrode

GR composites with Ni, Co, Mn, Ru, etc. oxide called transition metal are explored for SC electrode. The metal oxide uniform distributed on GR sheets can eliminate restacking of the sheets during the synthesis that stabilizes the volume change

in metal/metal oxide during charge-discharge cycles. An asymmetric SC is assembled by using nanocomposites as a positive electrode and GR as a negative electrode, which are constructed from carbon-based material with incorporated or deposited pseudocapacitive active materials like metal oxides and conducting polymers.

$\text{RuO}_2$  is considered as the most promising metal oxide material for SC electrode, due to its high conductivity, high reversible redox reaction, excellent electrochemical stability, and high specific capacity. However,  $\text{RuO}_2$  applications are limited because it is too expensive. Improving the utilization rate of  $\text{RuO}_2$  would help to reduce the cost of SC.

In Lee et al. (2010),  $\text{RuO}_2$  grown on GR sheets (GSs) composites has 570 F/g specific capacitance at 38.3 wt% Ru loading, 20.1 Wh/kg energy density at low charge-discharge current rate (100 mA/g) and retains 97.9% electrochemical stability after 1,000 cycles.

$\text{NiO}$  and  $\text{MnO}_2$  have attracted more attention as SC material due to their high energy density, low cost, environment compatibility. Nevertheless, the high charging-discharging rate becomes a main limit because of the poor electrical conductivity and low accessible surface area of  $\text{NiO}$ . Chen et al. (2016) conduct a test in which  $\text{NiO}$  is electrochemically deposited into the highly porous GR aerogel (GA) to form  $\text{NiO/GA}$  composites.  $\text{NiO/GA}$  electrodes own excellent electrochemical performance with the specific capacitance of 489.9 F/g at the charge-discharge current density of 1 A/g in 2M KOH electrolyte.

Theoretically, specific capacitance value of  $\text{MnO}_2$  is about 1,370F/g (Liu et al., 2014), however the poor reversibility of the electrochemical oxidation-reduction and the

low conductivity restrict its application. Many researchers have shown that  $\text{MnO}_2$  would have a good performance in neutral aqueous electrolyte solution within a wide potential window when it is doped with carbon material.  $\text{MnO}_2$  composited with GR is able to test the effects of electrochemical performance. Nanocomposite material has the larger reinforcement surface than conventional composite material. Zhang et al. (2014) conducts the experiment that GR– $\text{MnO}_2$  nanocomposite as positive electrode and GR as negative electrode reacted with a  $\text{KMnO}_4$  solution of 1.45 mol/L. It gives a high energy density of 23.9 Wh/kg and a good cycling performance of around 96% of the initial capacitance after 1,000 cycles. The results demonstrate that these composites nanomaterial have excellent electrochemical properties with eliminated restacking, and they are distinctly suitable for SC materials.

### 7.3.3 Graphene and CNT Flexible Electrode

At present, stainless steel and Indium tin oxide are most commonly used as materials for preparing SC electrodes. There are several drawbacks to using them, which include a lack of flexibility due to easily caused cracks under strain. Using flexible substrates as support for active materials is attracting great attention due to their low cost, high flexibility, and smooth surfaces. The large-scale fabrication of solid SC is not only limited by the fragility of electrode material, but also restricted by their cycling stability and electrochemical performance. GR/CNTs film shows unique electrical and mechanical properties as well as high stability in electrolyte due to combinations of properties of GR and CNTs. GR/CNT film would be directly used as the electrode without any binders and current collectors.

A CNT can carry current with the density of  $103 \text{ mA/cm}^2$ , and the electrical

resistivity of an individual CNT has  $1 \mu\Omega$ . A hybrid structure of GR foliates aligned along the multi-walled CNT (MWCNT) increases surface area for capacitors shown in Figure 7.4. CNT gives a backbone for a homogeneous distribution of metal oxide or electrically conducting polymers.

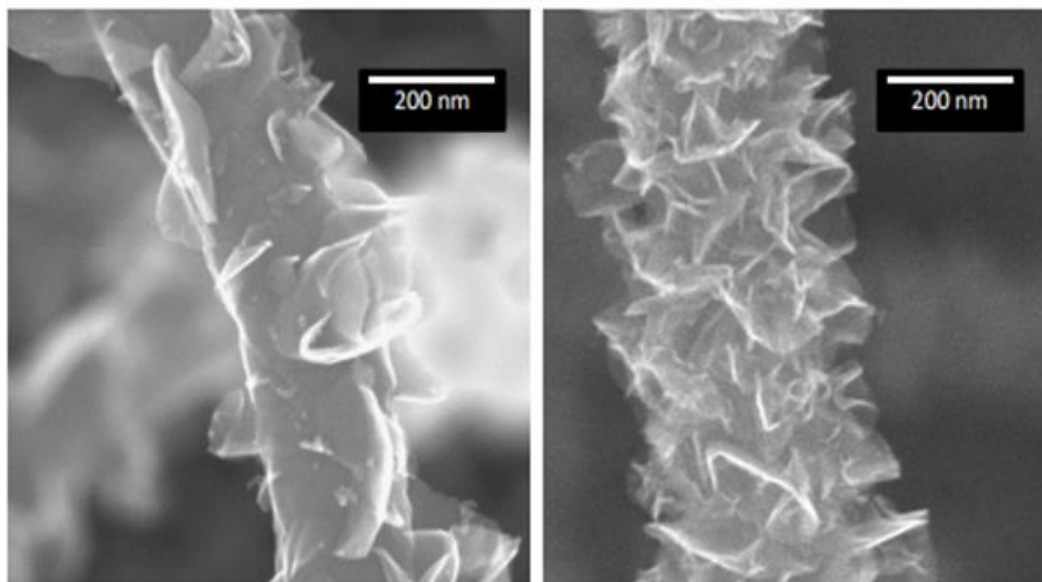


Figure 7.4: Graphitized MWCNT with Varying Foliate Density (Cui et al., 2000).

MWCNT in the composite films enhance transportation of electrolyte ions and electrons into the inner region of the electrode, in which CNT flexible film has a high specific capacitance of 256 F/g at the current density of 0.1A/g and after 2000 charge-discharge cycles, the specific capacitance still retains 97%. Dürkop et al. (2004) prove these electrodes with composite nanomaterial achieve higher capacitances than any other pure nanomaterials-based electrodes.

In most SC devices, binders must be used in order to hold the electrodes together. Due to without electrochemical activity and with the low specific capacitance, binders impact on the physical contact and charge transfer. GR/MnO<sub>2</sub>/CNT nanocomposites as the flexible electrodes allow high active material loading (71wt% MnO<sub>2</sub>), area density

(8.80 mg/cm<sup>2</sup>), and high specific capacitance 372 F/g without the current collectors and binders (Ubnoske et al., 2015).

In the experiment by Li et al. (2012), the results demonstrated GR/CNT film has an excellent electrochemical performance with the specific capacitance of (70-110) F/g at the low scan rate 1mV/s. The mass ratios of GR and CNT is defined in Table 7.2.

Table 7.2: Electrode Materials of SCs (Li et al., 2012).

Sample	Mass Ratios (GO to CNTs)	Samples after Annealing	BET-SSA (m <sup>2</sup> /g)	C <sub>g</sub> (F/g)
GO	1:0	Gr	1.9	119
GO <sub>2</sub> /CNT <sub>1</sub>	2:1	Gr <sub>2</sub> /CNT <sub>1</sub>	86.5	105
GO <sub>2</sub> /CNT <sub>1</sub>	1:1	Gr <sub>1</sub> /CNT <sub>1</sub>	91	111
GO <sub>2</sub> /CNT <sub>1</sub>	1:2	Gr <sub>1</sub> /CNT <sub>2</sub>	95.6	74

The test results indicate that the ratios between them affect the film resistance and specific capacitance because the CNT is used to improve film conductivity while providing bridge and compact effects. The Gr<sub>1</sub>/CNT<sub>1</sub> film with an appropriate ratio is the best choice. The scanning electron microscope image of the GR/CNT is presented on film around 30-40 μm thick. Hence, the large portion of GR should be adopted as prepared for GR/CNT film with high compactness. On the other hand, the increase of CNT content could reduce the stacking of GR.

#### 7.4 Simulate Performance of Lithium-ion Battery

The performance of a battery over its lifetime is affected not only by thermal and electrochemistry, but also by the battery management control system. To gain better control over the performance and life cycle of a battery, accurate modeling of battery characterization is essential. The numerical model is faster, safer, and less costly than building physical prototypes, and has been adopted to obtain a more detailed

understanding of the electrochemical system. Table 7.3 lists the parameters for this section.

Table 7.3: Notation of Parameters.

Notation	Description	Unit
$D_s$	Diffusion coefficient	$\text{m}^2/\text{s}$
$\varepsilon_{s,i}$	Volume fraction of the active particles	
$r_i$	Radius of particle size	m
$\alpha_i$	Specific surface area of particles	$\text{m}^2/\text{g}$
$K_{\text{pos}}$	Reaction rate coefficient positive electrode	m/s
$K_{\text{neg}}$	Reaction rate coefficient negative electrode	m/s
$\phi_l$	Potential of electrode	V
$N$	Cycle number	cycle
$\sigma_{s,eff}$	Conductivity	S/m
$R$	Universal gas constant	J/(mol·K)
$c_{s,i}$	Li-ion concentration	$\text{mol}/\text{m}^3$
$\rho$	Density of active material	$\text{g}/\text{m}^3$
$Q_o$	Initial capacity	$\text{C}/\text{m}^2$
$c_l$	Initial electrolyte salt concentration	$\text{mol}/\text{m}^3$
$F$	Faraday's constant	C/mol
$c_{s,max}$	Saturation concentration of Li ion in the solid phase	$\text{mol}/\text{m}^3$

The cell's output performance of specific capacity and energy efficiency is tested through the numerical model because the internal resistance of the cell changes with the cycling number. In the model, the variation of lithium concentration in the liquid phase along the current path can be neglected. The variation in the solid phase potential at the anode or at the cathode is also negligible because of the good conductivity of the electrode materials. It is also assumed that the active electrode materials are made from uniform spherical particles with a radius of  $r_p$  and that the diffusion is the only mechanism of lithium transport inside the particles. The total surface film resistance ( $R^f$ ) consists of initial film resistance ( $R_c$ ) and the resistance of the film formed due to the

parasitic reaction occurring at the anode surface as the new resistance  $R_s$ . That is,

$$R^f = R_c + R_s \quad (7.4)$$

The thickness of the film at the negative electrode changes with the times of charge-discharge cycle. Hence the resistance of the film grows as the cycle number increases. The film thickness function  $\delta_f$  under charge-discharge cycle number  $N$  in given below,

$$\frac{\partial \delta_f |_N}{\partial t} = \frac{J_s^{Li} |_N * M}{\rho * F} \quad (7.5)$$

where

$\rho$  = density of active material.

$M$  = molecular weight.

$F$  = Faraday's constant, 96,487 C/mol.

The specific surface area  $\alpha_i$  and  $S_i$  superficial surface area of electrode are given by following equations,

$$\alpha_i = \frac{3\varepsilon_i}{r_i} \quad i = \text{positive, negative} \quad (7.6)$$

$$S_i = \alpha_i V_i \quad i = \text{positive, negative} \quad (7.7)$$

where

$r_i$  = radius of particles.

$\varepsilon_i$  = volume fraction of a solid phase of electrode.

$V_i$  = volume of electrode.

The equation that describes the diffusion of lithium in the solid phase is given by Fick's 2nd law as follows,

$$\frac{\partial c_{s,i}}{\partial t} = \frac{1}{r_i^2} \frac{\partial c_{s,i}}{\partial r_i} + \frac{2D_{s,i}}{r_i} \frac{\partial c_{s,i}}{\partial r_i} \quad (7.8)$$

Butler-Volmer (BV) kinetics is used to describe lithium intercalation/deintercalation in the cell. Since the concentration variation in liquid phase is neglected, the current density of the parasitic reaction is given by the Tafel equation and  $\eta_s$  as the overpotential is given by

$$J_s^{Li} = J_{s,0}^{Li} \exp\left(\frac{0.5F}{RT} \eta_s\right) \quad (7.9)$$

$$\eta_s = \phi_l - U_{sq} - J_n S_n R^f \quad (7.10)$$

In the following discharging process, the dimensionless lithium concentration at the beginning is used as the initial condition for the diffusion equation in the solid phase. The surface film resistance ( $R_f$ ) is modified due to the parasitic reaction in the previous cycle. The loss of the capacity of the cell is estimated by the following equation,

$$Q_s = \int_T J_s^{Li} S_n dt \quad (7.11)$$

Capacity fade degree is an important way to test battery performance, which occurs under various conditions. The conditions are classified into two categories: electrode materials and status of use. Simulation approach is applied to analyze the effect of the conductivity of the newly formed surface film on charging and discharging performance of the battery. The simulations are carried out by charging the battery to 4.2 V. Figure 7.5 compares the capacity fade and the discharging performance under different cycles.

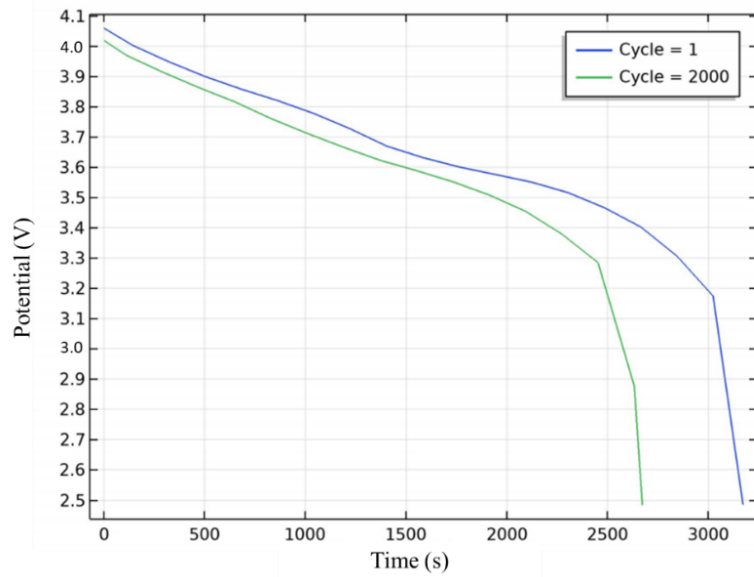


Figure 7.5: Discharge Curve Comparison under Various Cycle Numbers.

Depending on the status of usage, the number of charge-discharge cycles and the temperature influence the capacity loss as shown in Figure 7.6. The capacity loss is due to expansion/contraction of the active materials, and the rate of expansion/contraction is proportional to the local rate of expansion of the intercalation material.

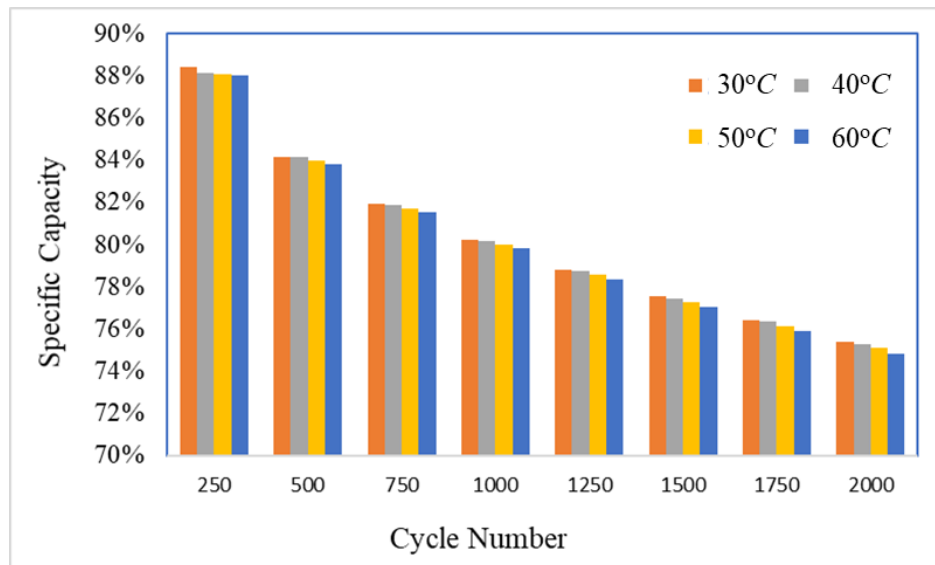


Figure 7.6: Specific Capacity under Various Conditions.

The results indicate that capacity fade is affected by at least two major processes: 1) loss of active lithium, and 2) impedance growth at the positive and negative electrodes. The rate capability is studied in terms of polarization (voltage loss) or the internal resistance growth. A battery cell with high-rate capability can generate a considerable amount of power, that is, it suffers from little voltage loss even at high current loads. In contrast, a low rate-capability cell has the opposite behavior. The porosity of electrodes, active material particle size, and state of charge (SOC) are considered as the factors in the model to simulate the internal resistance of cell under effect. Three parameters are explored: SOC, porosity of the positive electrode ( $\epsilon_s$ ), and the particle radius size of the positive active electrode material ( $r_p$ ). Each factor has three levels as in Table 7.4.

The energy efficiency is defined as the ratio between the power output ( $W_{disc}$ ) and input ( $W_{ch}$ ) as follows,

$$\eta_e = \frac{W_{disc}}{W_{ch}} = \frac{\int_{t=out} (I * U_{eq}) dt}{\int_{t=in} (I * U_{eq}) dt} \quad (7.12)$$

Table 7.4: Factors and Levels of Parameters in Model.

Level \ Factor	Low	Medium	High
$\epsilon_s$	0.1	0.4	0.6
$r_p$	$5 \times 10^{-7}$	$1 \times 10^{-6}$	$2 \times 10^{-6}$
SOC	0.4	0.6	0.8

The internal resistance decreases when the positive active material particle size is decreased and the porosity in the positive electrode is increased as shown in Figure 7.7.

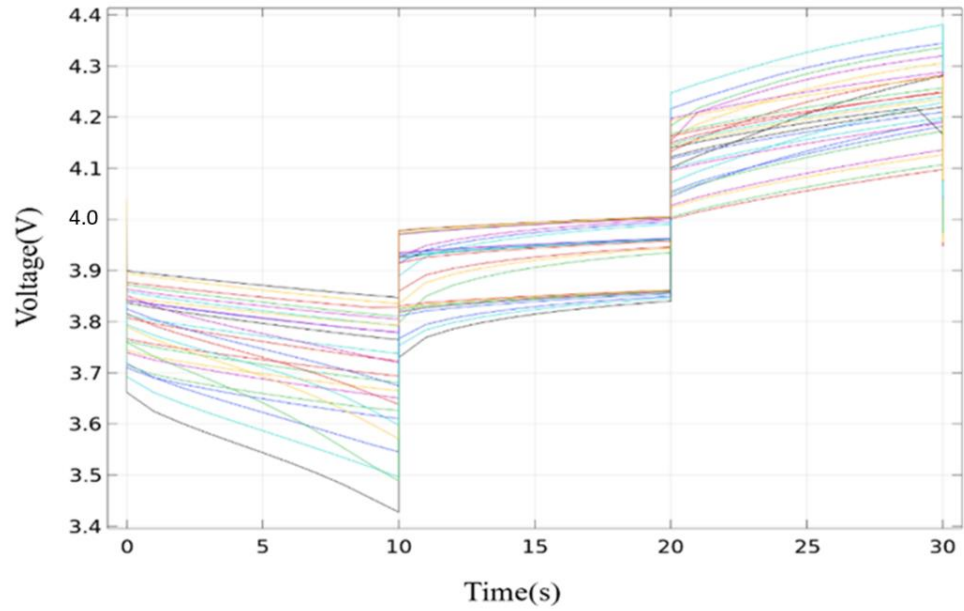


Figure 7.7: Voltage Behavior for Various Designs.

The simulation result of energy efficiency ( $\eta_e$ ) under 27 cases are compared in Table 7.5. The battery has the best performance when using the values from Case 21. Figure 7.8 also depicts the energy efficiency of Cases 1, 10, 9, and 21 in the temperature ( $^{\circ}\text{C}$ ) range of [0, 60]. Case 21 still has the best performance.

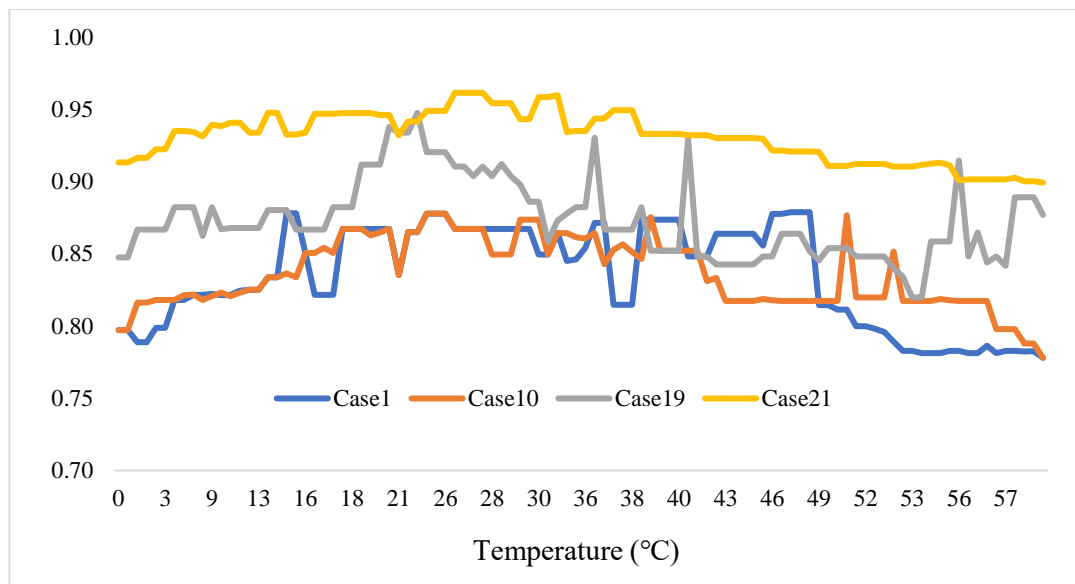


Figure 7.8: Energy Efficiency under Various Conditions.

Table 7.5: Simulation Result Based on Various Levels of Three Factors.

Case	SOC	$r_p$ (m)	$\varepsilon_s$	$\eta_e$
1	0.4	5.00E-07	0.1	0.878
2	0.4	5.00E-07	0.4	0.915
3	0.4	5.00E-07	0.6	0.919
4	0.4	1.00E-06	0.1	0.863
5	0.4	1.00E-06	0.4	0.903
6	0.4	1.00E-06	0.6	0.907
7	0.4	2.00E-06	0.1	0.843
8	0.4	2.00E-06	0.4	0.885
9	0.4	2.00E-06	0.6	0.889
10	0.6	5.00E-07	0.1	0.883
11	0.6	5.00E-07	0.4	0.920
12	0.6	5.00E-07	0.6	0.924
13	0.6	1.00E-06	0.1	0.868
14	0.6	1.00E-06	0.4	0.909
15	0.6	1.00E-06	0.6	0.913
16	0.6	2.00E-06	0.1	0.849
17	0.6	2.00E-06	0.4	0.894
18	0.6	2.00E-06	0.6	0.898
19	0.8	5.00E-07	0.1	0.886
20	0.8	5.00E-07	0.4	0.921
21	0.8	5.00E-07	0.6	0.925
22	0.8	1.00E-06	0.1	0.873
23	0.8	1.00E-06	0.4	0.910
24	0.8	1.00E-06	0.6	0.914
25	0.8	2.00E-06	0.1	0.857
26	0.8	2.00E-06	0.4	0.897
27	0.8	2.00E-06	0.6	0.901

Design of experiments is applied to investigate the capacity fade degree with three factors in this section. Three factors are SOC, the porosity of the positive electrode ( $\varepsilon_s$ ), and the particle radius size of the positive active electrode material ( $r_p$ ) and each factor has three levels. Through analysis of the simulation results, the battery will have better performance when the positive active electrode has a smaller size, while the porosity of the positive electrode and the SOC is at a high level.

## 7.5 Commercialization

The distributed generation (DG) systems with hybrid energy storage devices create new opportunities for large industrial consumers to save energy costs and achieve the environmental sustainability. The onsite generation can be applied in real life depending on the capacity cost of the device and local weather profile. However, the energy storage device plays a critical role in the communalization of such DG system. Schmidt et al. (2017) point out that an average annual cost prominently declining by 30% on the cell level can lead to 12% cutting on the system level in the energy storage system. Hajiaghasi et al. (2019) make a summary that hybrid energy storage performs better than battery-alone energy storage for a stand-alone PV system. Jing et al. (2016) testify that hybrid storage has the virtues of both high energy and power density, and such systems increase battery lifespan. They analytically demonstrate that the hybrid configuration extends power output and battery lifetime.

With the utility price increase, the onsite power system will be more competitive than the traditional power system. The cost of the onsite power system is also decreasing with the novel material applied and innovative technology developed. This section will illustrate the financial analysis of the products of supercapacitor and new generation of Li-ion battery.

### 7.5.1 Supercapacitor Penetration Rate Forecast

Supercapacitors (SC) are novel energy storage devices that can be applied in many fields due to their long-life cycle, high power density, and fast charge-discharge rate. The major applications of SC include consumer, public and industrial sectors, utility grid, and transportation. SC market is valued \$3.27 billion in 2019 and is expected to

reach \$16.95 billion by 2027, growing at a CAGR of 23.3% from 2020 to 2027.

The main gap between the SC with currently existing technologies is caused by the high cost of raw materials for both carbon and mixed metal oxide-based SC.

Currently, the cost of graphene ranges between \$50-200/kg, depending on quality and volume of purchase.

The capacity cost of SC is  $1.2 \times 10^6$ /MWh in this study. Suppose cuts the price to  $0.2 \times 10^6$ /MWh due to the decreasing of row material cost and manufacturing process improvement. The ratio of installation capacity between SC and battery dramatic changes when the capacity cost of SC trends down  $0.8 \times 10^6$ /MWh. The system is more preferred to install SC instead of battery, even the capacity cost of Li-ion battery ( $0.6 \times 10^6$ /MWh) is lower than SC. The reason is that there is no maintenance cost of SC and the impact of depth of discharging of SC technique is also ignored. Figure 7.9 plots the SC penetration rate. When the capacity cost of SC reaches  $0.2 \times 10^6$ /MWh, the penetration rate of SC is almost reaching 100%.

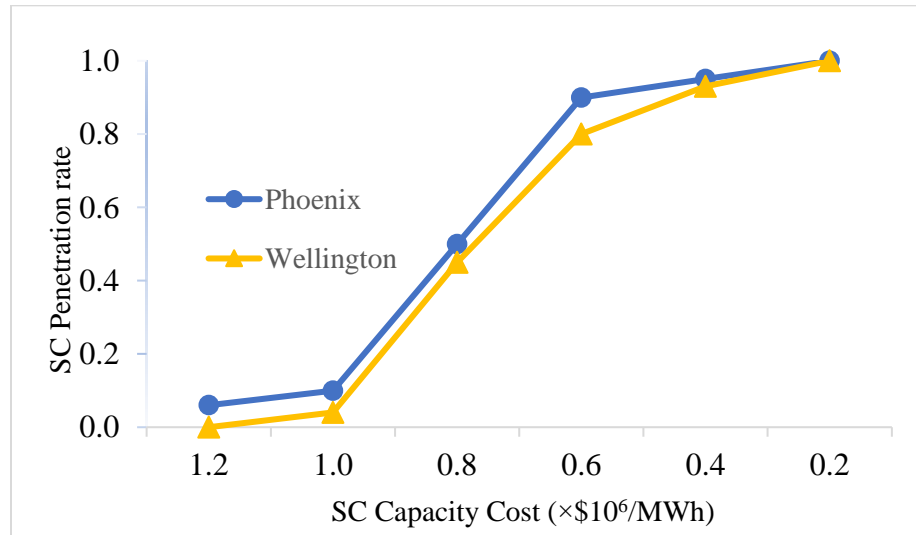


Figure 7.9: SC Penetration Rate vs. Capacity Cost.

### 7.5.2 Li-ion Battery Financial Forecast

The energy density and power density of lithium-ion battery has significantly increased in past decade. It is an important type of energy storage device covering a wide range of applications from consumer products to industrial applications, such as portable/wearable electrics, uninterruptible power supply system. It is the biggest potential profits. A new generation of lithium-ion battery with advanced graphene-based nanostructure material takes advantage of the opportunity for energy storage product, which has the biggest potential to dominate the battery market. At the inception, the new generation lithium-ion expects to have a 1% share of the U.S. market, which is worth \$20B around 80,000MWh volume. It is projected that the annual increase rate of market share will be 0.5% and the price of the new battery is \$180/kWh, which is reasonable and competitive.

The new generation Li-ion battery product adopts advanced fabrication processes and novel material. The battery will significantly cost less due to enhancement of existing processes, and adoption of new materials, reduction of waste, and optimization manufacturing process. It has the following specifications:

- 1). Competitive Price: customers would rather save 30% cost by opting.
- 2). More Safety: avoid the liquid leak toxic material out due to all solid components of battery and Graphene is environment-friendly materials in manufacturing.
- 3). Multiple Applications: it can be sealed with any shape to suit any application due to flexible electrodes.

The cost to manufacture battery consists of raw materials, operations, salaries, operation, product development, and depreciation. All of these can be divided into two

categories: fixed costs and variable costs. The variable costs of manufacture scale with the output volume of production. Figure 7.10 shows the percentage of the cost for one unit battery.

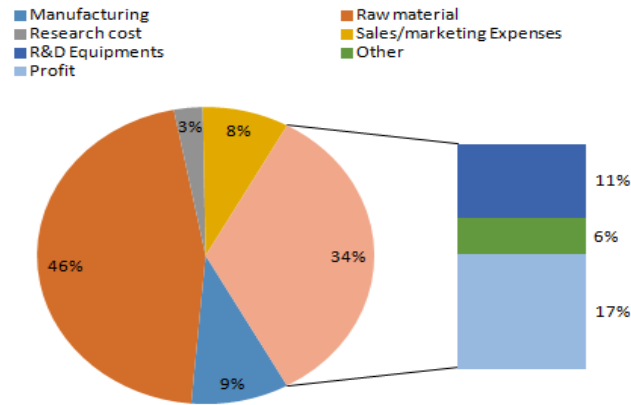


Figure 7.10: Cost Ratio (%).

Cash flow is the net amount of money and cash-equivalents being transferred into and out of a business, which show the capacity of the product to create value for shareholders. A cash flow is analyzed at the first 24 months and 5 years. Financial forecasts will allow the investor to see how costs, order amounts, and growth rate affect profitability. A 24-month cash flow as shown in Figure 7.11. The breakeven point turns up at the monthly product sale volume at 12,554 kWh and all expenses will be recovered by the sales.

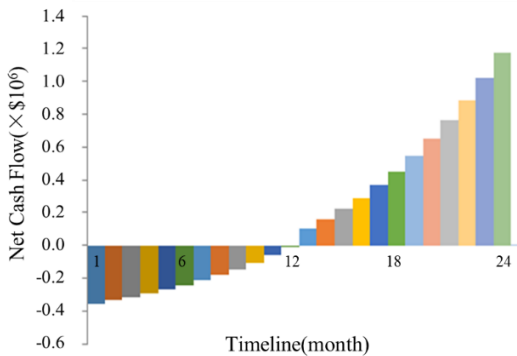


Figure 7.11: 24-Month Cash Flow.

The final finance forecasts that the break-even point will appear at the 13<sup>th</sup> month after initial product manufacturing. According to conservative estimates, the investment will have at least 100% return within 5<sup>th</sup> year of the financing period, and net income will be \$895,000 at the end of the 6<sup>th</sup> year.

Table 7.6 shows the 5-year cash flows statement with net present value (NPV) and the internal rate return (IRR) value. Both give the same evaluation for this product, which will bring profits for the investors. NPV is \$443,749 with an interest rate of 10% for 5 years. It is expected that the product can add value to the firm and therefore increase the wealth of the shareholders. The investment will be recovered after 4.02 years and the investors start to get the business's money back. The IRR is 25% when the NPV is equal to zero.

Table 7.6: Five Year Cash Flows Statement.

	Y1	Y2	Y3	Y4	Y5
Revenue(\$)	7,200,000	7,920,000	8,712,000	9,583,200	10,541,520
Cost of Goods Sold	4,560,000	4,268,000	4,694,800	5,164,280	5,680,708
Gross Profit	2,640,000	3,652,000	4,017,200	4,418,920	4,860,812
Operating expenses(\$)					
Payroll	880,000	880,000	880,000	900,000	900,000
Payroll Taxes(15%)	132,000	132,000	132,000	135,000	135,000
Rent	200,000	200,000	300,000	300,000	400,000
Utilities	500,000	500,000	600,000	600,000	600,000
Telephone	48,000	48,000	48,000	48,000	48,000
Professional Fees	250,000	250,000	250,000	250,000	250,000
Travel/entertainment	500,000	500,000	500,000	500,000	500,000
Phone and Internet	72,000	72,000	72,000	72,000	72,000
Dpreciation	1,000,000	1,000,000	1,000,000	1,000,000	1,000,000
total Operating Expense	3,582,000	3,582,000	3,782,000	3,805,000	3,905,000
Net Income(\$)	-942,000	70,000	235,200	613,920	955,812
Payback Period	4.02				
Net Present Value(r =10%)	443,749				
Internal Rate of Return(IRR)	0.24				

## 8. CONCLUSIONS AND FUTURE WORK

### 8.1 Conclusions

This research work addresses how to design an onsite grid-connect renewable power system, which provides reliable energy supply for manufacturing facilities under uncertain weather conditions. The optimization objective is to minimize the investment cost of the system, as well as the microgrid operating cost by considering the power reliability criterion and time of use (TOU) rate. The numerical experiment results demonstrate that a renewable power system integrating hybrid energy storage devices is cost-effective from a long-term perspective. Manufacturing facilities can be powered by wind turbine and solar PV so as to meet energy demand under required loss of loss probability criteria while lowering environmental impact. Sizing renewable generation comprised of hybrid energy storage system is also proposed in this study. Below the research activities and findings of each chapter are summarized.

In chapter 2, the historical weather data of multi-cities is retrieved from the weather underground web portal by open-source API. Python programming language is used to manipulate tons and tons of data and extract effective statistical information from the historical weather data. The wind speed and weather features are analyzed and interpreted by applying a statistical approach. Through processed and organized data, six testing cities are selected, which present diverse weather portfolios across the north and south hemispheres. For example, Wellington is the windiest city, but the weather is mostly cloudy; on the contrary, Phoenix has a low wind profile but mostly sunny. San Francisco has medium to large wind plus plenty of sunshine. On average, there are less than 3.33% incomplete and missing observations. In Wellington, about 75% of wind

direction is observed between the north and northwest. In San Francisco, around 50% of wind blows from the west and northwest. Wind speed distribution curve in Sanya can be described as the normal distribution. However, the distribution curve in the remaining cities follows the Weibull distribution.

Chapter 3 proposes the hybrid forecast models with multivariate input and multi-step output capability for the wind speed and weather feature, respectively. Several findings are obtained from the numerical experiment comparisons. First, wind direction is found to be the most significant feature in the multivariate model. It improves the prediction performance and leads to a much better forecast result. Second, the proposed model outperforms the benchmark results of ARIMA, persistence model, and univariate FNN model in 3-to-24 hours ahead prediction. Third, the proposed wind speed forecasting model does not show an obvious advantage in 1-hour ahead prediction. The prediction error of the hybrid model is typically 8% smaller than ARIMA and persistence models. All models result in good prediction if hourly wind speed does not have significant standard deviation, such as in Phoenix.

The weather condition prediction results show the seasonal prediction models and yearly forecasting models are drastically different. The forecasting result indicates the yearly models generates better performance across multiple cities than the seasonal models for their corresponding period due to the random distribution of states. The five-state forecasting model yields higher accuracy than the seven-state model. Furthermore, the model's prediction accuracy decreases when the feature retains more classes. The forecasting results show that the proposed model forecasting accuracy is 35.7% and 32% higher than the MM and HMM, respectively.

In chapter 4, the working principle of renewable generators and energy storage devices is illustrated. The renewable generation process, charging and discharging procedure, and capacity degradation of energy storage devices are converted into mathematic functions. The capacity factor is defined as the division of actual power output in one hour divided by the rated power capacity of generation. The generation of wind turbine and solar PV will be simulated based on the hourly capacity factors. The value of a capacity factor is between zero and one.

In chapter 5, the mixed-integer nonlinear programming is established to optimize the levelized cost of energy (LCOE). The objective function is solved by the AMPL compiler. To tackle the complex optimization problem, wind and solar generations are simulated hour-by-hour across a year first. Through running four operation modes in each of the testing cities, the experiment results demonstrate the renewable energy is cost-effective when the local wind resource is abundant or the capacity cost of solar PV is continuously reduced. LCOE is \$54.7/MWh below the utility price in Willington. The local wind speed and weather features ultimately determine the mix of renewable generation portfolios. The capacity of HESS is primarily impacted by the facility's operation mode, not necessarily the carbon credit and TOU policy. When a facility is operating during the night, the facility needs to install more energy storage devices to meet the power demand.

This model sets an example and provides a solution to design and operate a microgrid power system with onsite renewable technique, which is competitive, feasible, and has a minimum impact on the main grid. This model can be expanded to multi-nodes from manufacturing into commercial businesses, data centers, warehouses, and

distribution centers, which are energy-intensive industries.

In chapter 6, it provides a state-of-the-art decision model that integrates onsite generation into supply chain logistic planning with multi-echelon facilities. The supply chain model is proposed based on weekly production-inventory and hourly generation to size the renewable generation and energy storage unit. A long-term optimization decision problem can be formulated as mixed-integer linear programming model to minimize annual operation costs. The numerical example and sensitivity analysis reveal the effect of energy pricing policies, natural gas price, and product-inventory cost on the production processes and the sizing of renewable generators.

The sensitivity analysis of changes in the electricity market price are performed. The study finds higher electricity market prices yield higher profits and incentivize the supply chain system to install more renewable generators. The annual cost of supply chain system reduces due to revenue income of energy sales. The electricity market price also impacts the behavior of ES, surplus energy is more likely to export to the mind grid. The experiment results also reveal the available wind and solar resources of the factory affect the production plan. High energy consumption products will be made in factories with abundant natural resources, even if the shipping distance is longer and higher shipping cost incurs between factory and warehouse. The expense of the the supply chain system goes up when the combined power and heat unit has limited operating hours. The numerical experiment result indicates that the supply chain system will work more cost effectively when multiple generators are selected.

Chapter 7 investigates the capacity fade of the battery under various conditions. The simulation is carried out by charging the battery to the required voltage level with

COSMOS software. The model is designed to simulate the capacity fade and the charging and discharging performance of a battery up to 2,000 cycles. The results indicate that capacity fade is caused by the loss of active lithium at the negative. The porosity of electrodes, active material particle size, and state of charge are considered as three controllable factors in the model to simulate the internal resistance of the cell. The simulation results show the internal resistance decreases when the particle size of positive active material is decreased and the porosity in the positive electrode is increased.

## **8.2 Future Studies**

The future research could be explored from three directions: 1) constructing multi-objective optimization for virtual power plant (VPP) planning; 2) designing forecasting models to meet both long- and short-term prediction performance simultaneously; and 3) optimizing energy flow in the storage devices.

### **8.2.1 Multi-Objective Optimization Model**

Wind and solar are complementary in terms of renewable power generation. The wind speed and the weather feature are the key parameters that determine the output of local WT and PV equipment. The smart grid will be achieved by offering differential pricing electricity to encourage energy consumers to be switched from traditional energy resources. In the future study, multi-objective optimization models are formulated to minimize operation system cost and maximize environment benefit under power supply reliability criteria, when applied combined heat and power unit in the power system. Various design constraints from real life industry should be considered, including zero carbon footprint and the maximum amount of energy loss allowed in a one-year operation.

### 8.2.2 Joint Long- and Short-Term Forecasting Model

The production and capacity of renewable generation have been increasing in recent years. The manufacturers often purchase electricity from the day-ahead market. Hence, it is desirable to develop an integrated model that jointly forecasts long-term and short-term wind speed and weather features. The forecasting model with high accuracy is important to ensure the power supply and reduce manufacturing cost, which ensures the maximum profit in bidding on energy in the day-ahead market.

The fundamental prediction engine is the artificial neural network in this study. The particle swarm optimization algorithm or genetic algorithm technique can be efficient in tuning model parameters for a given neural network structure. The hyperparameters in the model also need to be optimized through an efficient way in the future study. However, there are limited studies focusing on the optimal selection of network structures, the number of hidden layers, and the number of neurons associated with a hidden layer. In the future, the study will focus on finding an effective way to determine the values of these hyperparameters of the model.

The forecasting model is still facing the challenges of which features can be selected as the input of model and what is the best way for imputing missing data or value. These would be the future tasks to design a high-performance model.

### 8.2.3 Energy Storage Technology

Hybrid energy storage system (HESS) is characterized by a beneficial coupling of two or more energy storage technologies with supplementary operating characteristics, such as energy and power density, self-discharge rate, efficiency, and lifetime. This study has discussed typical HESS applications, the energy storage coupling architectures, basic

energy management concepts, and a principal approach for the power flow decomposition.

The microgrid could be expanded to incorporate other energy forms such as small hydro, geothermal, and ocean wave energy. In future studies, HESS configurations will be adopted into four types: 1) fuel cell/battery, 2) hydrogen/battery, 3) compressed air energy storage/battery, and 4) flywheel/battery. These four types of HESS will be investigated in the power system management as well as "beyond Li-ion" technologies, such as lithium-sulfur and lithium-air chemistries. The "beyond Li-ion" technologies are potentially investing in, 1). Improving electrolyte/separator combinations so that they result in less dendrite growth when using Lithium metal anodes. 2). Developing advanced material coatings. 3). Developing new ceramic, polymer, and hybrid structures with high ionic conductivity, low electronic impedance, and high structural stability,

The new commercialization model of renewable energy is peer-to-peer energy (P2P) trading. Under the P2P business model, the buying and selling of energy takes place between two or more grid-connected parties instead of through a central market. Roy et al. (2016) state that peer-to-peer solar energy trading has considerable promise to generate benefits for both producers and consumers without intermediary at the agreed price. That means any excess energy can be transferred and sold to other users via a smart meter. This model encourages more manufacturers, commercial users, or homeowners to install renewable generation or empowers their right to choose suitable energy source or destination by themselves.

## APPENDIX SECTION

### Appendix A. Wind Speed Forecast Model in Chapter 3

The following Python code is for wind speed forecast model.

```
df=read_csv("Boston_Wind_Dataset.csv")
data1=df["Label_year_data"]
data1 = pd.DataFrame(data1)
data1=data1.replace(to_replace=0,value=1)
def series_to_supervised(data, n_in=1, n_out=1, dropnan=True):
    n_vars = 1 if type(data) is list else data.shape[1]
    df = pd.DataFrame(data)
    cols, names = list(), list()
    # input sequence (t-n, ... t-1)
    for i in range(n_in, 0, -1):
        cols.append(df.shift(i))
        names += [('var%d(t-%d)' % (j+1, i)) for j in range(n_vars)]
    # forecast sequence (t, t+1, ... t+n)
    for i in range(0, n_out):
        cols.append(df.shift(-i))
        if i == 0:
            names += [('var%d(t)' % (j+1)) for j in range(n_vars)]
        else:
            names += [('var%d(t+%d)' % (j+1, i)) for j in range(n_vars)]
    agg = concat(cols, axis=1)
    agg.columns = names
    # drop rows with NaN values
    if dropnan:
        agg.dropna(inplace=True)
    return agg
data2=series_to_supervised(data1,n_lag,n_seq)
#Feature scaling
scaler_1 = MinMaxScaler(feature_range=(0, 1))
scale_X =data2.iloc[:,0:n_lag]
scale_Y =data2.iloc[:,n_lag:(n_seq+n_lag+1)]
scalerX = scaler_1.fit(scale_X)
scalery = scaler_2.fit(scale_Y)
scaled_X = scalerX.transform(scale_X)
scaled_Y = scalery.transform(scale_Y)
scaled_Y = scaled_Y.astype('float32')
scaled_X = scaled_X.astype('float32')
X_train, X_test ,X_val= scaled_X[:-(len(scaled_X)-n_val-n_test)], scaled_X[-n_test:],
scaled_X[-(n_val+n_test):-n_test]
y_train, y_test,y_val = scaled_Y[:-(len(scaled_X)-n_val-n_test)], scaled_Y[-
n_test:],scaled_Y[-(n_val+n_test):-n_test]
```

```

X_train=X_train.reshape((X_train.shape[0],time_step, X_train.shape[1]))
X_test = X_test.reshape((X_test.shape[0], time_step, X_test.shape[1]))
X_val = X_val.reshape((X_val.shape[0], time_step, X_val.shape[1]))
# two hidden layers model
model = Sequential()
model.add(LSTM(n_hidden_1,return_sequences=True,activation='linear',stateful=True,
              activity_regularizer=l1(0.001),
              batch_input_shape=(n_batch, time_step, X_train.shape[2])))
model.add(Activation('relu'))
model.add(LSTM(n_hidden_2,batch_input_shape=(n_batch, time_step,
X_train.shape[2]), activation='relu',stateful=True))
model.add(Dense(y_train.shape[1]))
adam=optimizers.Adam(lr=0.0005)
model.compile(loss=losses.mean_squared_error, optimizer="adam")
checkpoint = ModelCheckpoint(filepath="best_weights_mod5.hdf5", monitor='val_acc',
verbose=1, save_best_only=True, mode='max')
callbacks_list = [checkpoint]
history = model.fit(X_train, y_train,
validation_data=(X_val,y_val),callbacks=callbacks_list, epochs=10, batch_size=n_batch,
verbose=2,shuffle=False)

# plot train and validation loss
plt.plot(history.history['loss'][30:])
plt.plot(history.history['val_loss'][30:])
plt.title('model train vs validation loss')
plt.ylabel('loss')
plt.xlabel('epoch')
plt.legend(['train', 'validation'], loc='upper right')
plt.show()

verbose=1
losses = []
val_losses = []
min_val_loss = (99999,999999)
for i in range(training_epochs):
    if verbose!=0:
        print(i)
    history = model.fit(X_train, y_train, validation_data=(X_val,y_val), epochs=2,
batch_size=n_batch, verbose=2, shuffle=False)
    losses.append(history.history['loss'])
    val_losses.append(history.history['val_loss'][0])
    if val_losses[-1] < min_val_loss[0]:
        min_val_loss = (val_losses[-1], i)
# model.reset_states()
print('best val_loss and epoch:',min_val_loss)
plt.title('loss')

```

```
plt.plot(losses,color="blue")
plt.plot(val_losses, color='red')
plt.show()

# forecasting
pred_y = model.predict(X_test,batch_size=n_batch)
inv_yhat = scaler.inverse_transform(pred_y)
real_test=scale_Y[-n_test:]

# calculate MSE with scaled
mse = 0
rmse = 0
for i in range(n_seq):
    RMSE = sqrt(mean_squared_error(y_test, pred_y))
    MAE=mean_absolute_error(y_test, pred_y)
    print('t+%d RMSE: %f % ((i+1), rmse))
    print('t+%d MAE: %f % ((i+1), MAE))
```

## Appendix B. Weather Feature Forecast Model in Chapter 3

The following Python code is for weather feature forecast model.

```
df=read_csv("Phoneix_Finalclean.csv",index_col='new.UTC')
scaler = MinMaxScaler(feature_range=(0, 1))

def encode(data, col, max_val):
    data[col + '_sin'] = np.sin(2 * np.pi * data[col]/max_val)
    data[col + '_cos'] = np.cos(2 * np.pi * data[col]/max_val)
    return data
x = encode(x, 'Hour', 23)
x=x.drop(["Hour"],axis=1)
ax = x.plot.scatter('Hour_sin', 'Hour_cos').set_aspect('equal')

def series_to_supervised(data, n_in=1, n_out=1, dropnan=True):
    n_vars = 1 if type(data) is list else data.shape[1]
    df = DataFrame(data)
    cols, names = list(), list()
    # input sequence (t-n, ... t-1)
    for i in range(n_in, 0, -1):
        cols.append(df.shift(i))
        names += [('var%d(t-%d)' % (j+1, i)) for j in range(n_vars)]
    # forecast sequence (t, t+1, ... t+n)
    for i in range(0, n_out):
        cols.append(df.shift(-i))
        if i == 0:
            names += [('var%d(t)' % (j+1)) for j in range(n_vars)]
        else:
            names += [('var%d(t+%d)' % (j+1, i)) for j in range(n_vars)]
    agg = concat(cols, axis=1)
    agg.columns = names
    if dropnan:
        agg.dropna(inplace=True)
    return agg

rnn_data=series_to_supervised(x,3,1)
rnn_data=rnn_data.drop(["var7(t-1)","var8(t-1)",
    "var7(t-2)","var8(t-2)","var7(t-3)","var8(t-3)"],axis=1)

rnn_data.rename(columns={'var1(t)': 'Sea_Level_PressureIn_N(t)', 'var2(t)':
"Humidity_N(t)",
'var3(t)': 'Dew_PointF_N(t)', 'var4(t)':'Wind_Speed_mps(t)', 'var5(t)':
"Temperature_C_N(t)",
'var6(t)':'Conditions_Name(t)',
'var1(t-1)': 'Sea_Level_PressureIn_N(t-1)', 'var2(t-1)': "Humidity_N(t-1)",
```

```

'var3(t-1)': 'Dew_PointF_N(t-1)', 'var4(t-1)': "Wind_Speed_mps(t-1)", 'var5(t-1)':
"Temperature_C_N(t-1)",
'var6(t-1)': 'Conditions_Name(t-1)',
'var1(t-2)': 'Sea_Level_PressureIn_N(t-2)', 'var2(t-2)': "Humidity_N(t-2)",
'var3(t-2)': 'Dew_PointF_N(t-2)', 'var4(t-2)': "Wind_Speed_mps(t-2)", 'var5(t-2)':
"Temperature_C_N(t-2)",
'var6(t-2)': "Conditions_Name(t-2)",
'var1(t-3)': 'Sea_Level_PressureIn_N(t-3)', 'var2(t-3)': "Humidity_N(t-3)",
'var3(t-3)': 'Dew_PointF_N(t-3)', 'var4(t-3)': "Wind_Speed_mps(t-3)", 'var5(t-3)':
"Temperature_C_N(t-3)",
'var6(t-3)': "Conditions_Name(t-3)",
'var7(t)': 'Hour_sin', 'var8(t)': 'Hour_cos'}, inplace=True)

```

```

encoder = LabelEncoder()
rnn_data["Conditions_Name(t-
1)"]=encoder.fit_transform(rnn_data["Conditions_Name(t-1)"].astype("str"))
rnn_data["Conditions_Name(t-
2)"]=encoder.fit_transform(rnn_data["Conditions_Name(t-2)"].astype("str"))
rnn_data["Conditions_Name(t-
3)"]=encoder.fit_transform(rnn_data["Conditions_Name(t-3)"].astype("str"))

```

```

rnn_data[["Conditions_Name(t-1)", "Conditions_Name(t-2)", "Conditions_Name(t-3)"]]
= scaler.fit_transform(rnn_data[["Conditions_Name(t-1)", "Conditions_Name(t-
2)", "Conditions_Name(t-3)"]])

```

```

def encode_text_index(df, name):
    le = LabelEncoder()
    df[name] = le.fit_transform(df[name])
    return le.classes_
def to_xy(df, target):
    result = []
    for x in df.columns:
        if x != target:
            result.append(x)
    target_type = df[target].dtypes
    target_type = target_type[0] if hasattr(
        target_type, '__iter__') else target_type
    if target_type in (np.int64, np.int32):
        # Classification
        dummies = pd.get_dummies(df[target])
        return df[result].values.astype(np.float32), dummies.values.astype(np.float32)

```

```

dataset1=rnn_data.loc[:,['Sea_Level_PressureIn_N(t-3)',
'Dew_PointF_N(t-3)', 'Wind_Speed_mps(t-3)', 'Temperature_C_N(t-
3)', "Conditions_Name(t-3)",
'Sea_Level_PressureIn_N(t-2)', 'Humidity_N(t-2)', 'Dew_PointF_N(t-2)',

```

```

'Wind_Speed_mps(t-2)', "Conditions_Name(t-2)",
'Sea_Level_PressureIn_N(t-1)', 'Humidity_N(t-1)',
'Dew_PointF_N(t-1)', 'Wind_Speed_mps(t-1)', "Conditions_Name(t-1)"
'Sea_Level_PressureIn_N(t)',
'Humidity_N(t)', 'Dew_PointF_N(t)', 'Wind_Speed_mps(t)',
'Temperature_C_N(t)', 'Hour_sin', 'Hour_cos', "Conditions_Name(t)"]].values

# PCA
X =
x.loc[100000:,[ "Month", "Day", "Hour", "Sea_Level_PressureIn_N", "Humidity_N", "Dew_
PointF_N", "Wind_Speed_mps", "Temperature_C_N" ]]
Y = x.loc[100000:,[ "Conditions_Name" ]]
Y = pd.Categorical(Y)
my_color = Y.cat.codes
my_color = ['r', 'g', 'm']

X = scaler.fit_transform(X)
from sklearn.decomposition import PCA
pca = PCA(n_components=3)

principalComponents = pca.fit_transform(X)
result = DataFrame(data = principalComponents
                    , columns = ['PCA%i' % i for i in range(3)], index=X.index)
from mpl_toolkits.mplot3d import Axes3D
fig = plt.figure()
ax = fig.add_subplot(111, projection='3d')
ax.scatter(result['PCA0'], result['PCA1'], result['PCA2'], c=my_color,
           cmap="Conditions_Name", s=60)

# create the model with the best params
dataset1 = rnn_data.loc[:, [
    'Sea_Level_PressureIn_N(t-1)',
    'Humidity_N(t-1)',
    'Dew_PointF_N(t-1)',
    'Wind_Speed_mps(t-1)',
    'Temperature_C_N(t-1)',
    'Hour_sin', 'Hour_cos',
    'Conditions_Name(t-1)',
    'Conditions_Name(t)']]

Conditions_Name = encode_text_index(dataset1, "Conditions_Name(t)")
X, Y = to_xy(dataset1, "Conditions_Name(t)")
X_train, X_test, Y_train, Y_test = train_test_split(X, Y, test_size=0.2)
n_epochs = 20
n_batch = 1
model = Sequential()

```

```

model.add(Dense(100, input_dim=X_train.shape[1], activation='relu'))
model.add(Dense(100, activation='relu'))
model.add(Dense(100, kernel_regularizer=regularizers.l2(0.01),
                activity_regularizer=regularizers.l1(0.01),
                activation='relu'))

# Compile model
adam=keras.optimizers.Adam(lr=0.01, beta_1=0.99, beta_2=0.99, epsilon=None,
decay=0.0)
model.compile(loss='categorical_crossentropy', optimizer="adam", metrics=['accuracy'])
checkpoint = ModelCheckpoint(filepath="best_weights_mod5.hdf5", monitor='val_acc',
verbose=1, save_best_only=True, mode='max')
callbacks_list = [checkpoint]
history =
model.fit(X_train,Y_train,validation_data=(X_test,Y_test),callbacks=callbacks_list,verbo
se=1,epochs=n_epochs,batch_size=n_batch)

#predicted
loss, acc = model.evaluate(X_test,Y_test)
pred = model.predict(X_test)

from sklearn import metrics
pred_y = np.argmax(pred,axis=1)
real_y = np.argmax(Y_test,axis=1)
score=metrics.accuracy_score(real_y,pred_y)
score=metrics.accuracy_score(real_y,index)
print("accuracy score: {}".format(score))

```

## Appendix C. Model 5.1: MLCOE in Chapter 5

The following AMPL code is for Model 5.1: MLCOE.

```

set prods:={"WT", "PV"};
set HESS:={"BS", "SC"};
param T;
set periods:= 0..T by 24;
set index;
param Y;
param r;
param Q=(r*(1+r)^Y)/((1+r)^Y-1);
param Alpha;
param Delta;
param mean;
param sigma;
param a1_G{n in prods};
param a1_HESS{j in HESS};
param a2_G{n in prods};
param a2_HESS;
param a3_G;
param D{t in 1..T};
param Coff{t in 1..T,n in prods};
param E{t in 1..T};
param W{t in 1..T};
param c_buy;
param c_sale;
param SOC_min;
param SOC_max{j in HESS};
param SOC_ini{j in HESS};
param HESS_capacity{j in HESS};
param DoD;
var P_G{n in prods}>=0;
var P_HESS{j in HESS}>=0;
var E_jt{j in HESS,t in 0..T};
var E_Ch_jt{j in HESS,t in 1..T}>=0;
var E_Disch_jt{j in HESS,t in 1..T}>=0;
var P_buy{t in 1..T}>=0;
var P_sale{t in 1..T}>=0;
var P_buy_pos{t in 1..T}binary;
var cost_cap_G=sum{n in prods}Q*a1_G[n]*P_G[n];
var cost_cap_HESS=sum{j in HESS}Q*a1_HESS[j]*P_HESS[j];
var OM_cost_G=sum{n in prods,t in 1..T}a2_G[n]*P_G[n]*Coff[t,n];
var OM_cost_HESS=sum{t in 1..T}E_Disch_jt["BS",t]*a2_HESS;
var carbontax_reward=sum{n in prods, t in 1..T}P_G["WT"]*Coff[t,"WT"]*a3_G;
var Cost_buy=sum{t in 1..T}P_buy[t]*c_buy;

```

```

var generation=sum{n in prods,t in 1..T}P_G[n]*Coff[t,n];

minimize LCOE_cost:
(cost_cap_G+cost_cap_HESS+OM_cost_G+OM_cost_HESS-
carbontax_rewardIncome_sale)/generation;

subject to initial_state{j in HESS}:
    E_jt[j,0]= P_HESS[j]*SOC_ini[j];
subject to initial_end{j in HESS, t in 1..T}:
    E_jt[j,T]= P_HESS[j]*SOC_ini[j];
subject to SOC_MAX {j in HESS,t in 1..T}:
    E_jt[j,t]-SOC_max[j]* P_HESS[j]<=0;
subject to SOC_MIM {j in HESS,t in 1..T}:
    E_jt[j,t]-SOC_min* P_HESS[j]>=0;
subject to SOC_Process{j in HESS,t in 1..T}:#: ord(t)>1
    E_jt[j,t]=E_jt[j,t-1]+E_Ch_jt[j,t]-E_Disch_jt[j,t];
subject to energy_conservation:
    sum{n in prods, t in 1..T}P_G[n]*Coff[t,n]+sum{t in 1..T}P_buy[t]-sum{t in
1..T}P_sale[t]=sum{t in 1..T}D[t];
subject to anytimeEnergy_onservation{t in 1..T}:
    sum{n in prods}(P_G[n]*Coff[t,n])+P_buy[t]-P_sale[t]+sum{j in
HESS}(E_Disch_jt[j,t]-E_Ch_jt[j,t])=D[t];

subject to P_buy_pos_defn{t in 1..T}:
P_buy[t] <= 37*P_buy_pos[t];

subject to buy_times:
sum{t in 1..T}P_buy_pos[t]<=T*Alpha;

subject to buy_amount:
    sum{t in 1..T}P_buy[t]<=0.01*sum{t in 1..T}D[t];

```

Appendix D. Model 6.1: PSC-VPP in Chapter 6

The following AMPL code is for Model 6.1: PSC-VPP.

```
set Gens:={"WT", "PV"};
set Factory:={"Pho", "Reno"};
set Warehouse:={"LasV"};
set Store:={"SaltLake","SanJose" };
set Prod_typ:={"p1","p2"};
set Prod_res:={"Labor","MachHour"};
set LINKS_FW within {Factory,Warehouse};
set LINKS_WS = {Warehouse,Store};
set periods:= 1..T by 1 ordered;
set steps:=0..T by 1 ordered;
set prod_period0 := 0..J by 1;
set prod_period1 := 1..J by 1;
param T:=8736;
param J:=52;
param Q_GEN;
param Q_ESS;
param a1_G{n in Gens};
param a1_ESS;
param a2_G{n in Gens};
param a2_ESS;
param a3_G{n in Gens};
param CHP_eff;
param gas_price;
param gas_price_I;
param gas_price_C;
param a2_CHP_I=gas_price_I/CHP_eff;
param a2_CHP_C=gas_price_C/CHP_eff;
param CF_F{t in periods,f in Factory,n in Gens};
param CF_W{t in periods,w in Warehouse,n in Gens};
param CF_S{t in periods,s in Store,n in Gens};
param Price_DA_F{t in periods,f in Factory};
param Price_DA_W{t in periods,w in Warehouse};
param Price_DA_S{t in periods,s in Store};
param Weight_item{p in Prod_typ};
param E_use_item {p in Prod_typ};
param Making_cost_item{p in Prod_typ};
param dist_FW{f in Factory, w in Warehouse};
param dist_WS{w in Warehouse, s in Store};
param shipping_cost{p in Prod_typ};
param holding_cost{p in Prod_typ};
param backorder_cost{p in Prod_typ};
param Truck_intensity;
```

```

param Truck_wight;
param trips_FW
param trips_WS;
param operate_hour_W{w in Warehouse};
param operate_hour_S{s in Store};
param E_demand_F{f in Factory};
param E_demand_W{w in Warehouse};
param E_demand_S{s in Store};
param T_demand_F{f in Factory};
param T_demand_W{w in Warehouse};
param T_demand_S{s in Store};
param Prod_demand_S{j in 1..J, s in Store, p in Prod_typ};
param Prod_demand_mean{p in Prod_typ, s in Store};
param Prod_demand_Std{p in Prod_typ, s in Store};
param Prod_demand_probility{p in Prod_typ};
param Available_res{t in prod_period1,f in Factory, r in Prod_res } ;
param Prod_need_res{p in Prod_typ, r in Prod_res } ;
param Prod_MAX {p in Prod_typ,s in Store};
param CHP_TtoE_F;
param CHP_TtoE_W;
param CHP_TtoE_S;
param ESS_E_F_max{f in Factory
param ESS_E_W_max{w in Warehouse};
param ESS_E_S_max{s in Store};
param ESS_T_F_max{f in Factory};
param ESS_T_F_min{f in Factory};
param ESS_T_W_max{w in Warehouse
param ESS_T_W_min{w in Warehouse};
param ESS_T_S_max{s in Store};
param ESS_T_S_min{s in Store};
param transport_E_SW {t in prod_period1,s in Store}
    = sum{w in Warehouse}Truck_intensity*dist_WS[w,s]*Truck_wight*trips_WS;
param transport_E_SW_hourly{t in 1..T,s in Store}=transport_E_SW[ceil(t/(T/J)),s];
var G_F{g in Gens,f in Factory}>=0,<=25;
var G_W{g in Gens,w in Warehouse}>=0,<=10;
var G_S{g in Gens,s in Store}>=0,<=15;
var Prod_shipped_FW{t in prod_period1, p in Prod_typ, f in Factory,w in Warehouse}
integer >=0;
var Prod_shipped_WS{t in prod_period1, p in Prod_typ, w in Warehouse, s in Store}
integer >=0;
var backorder_W{t in prod_period0, p in Prod_typ, w in Warehouse, s in Store} integer
>=0;
var inventory_W{t in prod_period0, p in Prod_typ, w in Warehouse} integer >=0;
var shipped{t in prod_period1, p in Prod_typ,w in Warehouse, s in Store}integer >=0;
var CHP_trade_F{t in periods,f in Factory}>=0;
var CHP_trade_W{t in periods,w in Warehouse}>=0;

```

```

var CHP_trade_S{t in periods,s in Store}>=0;
var ESS_F{f in Factory}>=0;
var ESS_W{w in Warehouse}>=0;
var ESS_S{s in Store}>=0;
var ESS_E_F{t in steps,f in Factory}>=0;
var ESS_E_W{t in steps,w in Warehouse}>=0;
var ESS_E_S{t in steps,s in Store}>=0;
var ESS_T_F{t in steps,f in Factory}>=0;
var ESS_T_W{t in steps,w in Warehouse}>=0;
var ESS_T_S{t in steps,s in Store}>=0;
var CHP_T_F{t in periods,f in Factory}>=0;
var CHP_T_W{t in periods,w in Warehouse}>=0;
var CHP_T_S{t in periods,s in Store}>=0;

var Prod_transport_FW{t in prod_period1,f in Factory}
= sum{p in Prod_typ,w in Warehouse}E_use_item[p]*Prod_shipped_FW[t,p,f,w]
+ sum{w in Warehouse, p in Prod_typ}Truck_intensity*dist_FW[f,w]*trips_FW*
Weight_item[p]*Prod_shipped_FW[t,p,f,w] + sum{w in Warehouse}
Truck_intensity *dist_FW[f,w] * Truck_wight*trips_FW;
var transport_E_WF{t in prod_period1,w in Warehouse}
= sum{f in Factory}Truck_intensity*dist_FW[f,w]*Truck_wight*trips_FW
+ sum{s in Store,p in Prod_typ}Truck_intensity * dist_WS[w,s] *
trips_WS*Weight_item[p]*Prod_shipped_WS[t,p,w,s]+ sum{s in
Store}Truck_intensity*dist_WS[w,s]*Truck_wight*trips_WS;

var Prod_transport_FW_hourly{t in 1..T,f in Factory} =
Prod_transport_FW[ceil(t/(T/J)),f];
var transport_E_WF_hourly{t in 1..T,w in Warehouse}=
transport_E_WF[ceil(t/(T/J)),w];
var cap_cost_Gens = sum{n in Gens,f in Factory}Q_GEN*a1_G[n]*G_F[n,f]
+ sum{n in Gens,w in Warehouse}Q_GEN*a1_G[n]*G_W[n,w]
+ sum{n in Gens,s in Store}Q_GEN*a1_G[n]*G_S[n,s];
var cap_cost_ESS= sum{f in Factory}Q_ESS*a1_ESS*ESS_F[f]
+ sum{w in Warehouse}Q_ESS*a1_ESS*ESS_W[w]
+ sum{s in Store}Q_ESS*a1_ESS*ESS_S[s];
var OM_cost_G = sum{t in 1..T,f in Factory}(a2_G["WT"] * G_F["WT",f] *
CF_F[t,f,"WT"] + a2_G["PV"] * G_F["PV",f] * CF_F[t,f,"PV"]) +
sum{t in 1..T,w in Warehouse}(a2_G["WT"]*G_W["WT",w]
*CF_W[t,w,"WT"]+a2_G["PV"]*G_W["PV",w]* CF_W[t,w,"PV"])
+ sum{t in 1..T,s in Store}(a2_G["WT"]*G_S["WT",s]*
CF_S[t,s,"WT"]+ a2_G["PV"]*G_S["PV",s] *CF_S[t,s,"PV"]);

var OM_cost_ESS = sum{f in Factory}a2_ESS*ESS_F[f] + sum{w in
Warehouse}a2_ESS*ESS_W[w]
+ sum{s in Store}a2_ESS*ESS_S[s];

```

```

var OM_cost_CHP = (sum{f in Factory,t in 1..T}CHP_T_F[t,f]*a2_CHP_I
+sum{w in Warehouse,t in 1..T}CHP_T_W[t,w]*a2_CHP_C
+sum{s in Store,t in 1..T}CHP_T_S[t,s]*a2_CHP_C);

var CC_income = sum{t in 1..T,f in Factory}(a3_G["WT"]*G_F["WT",f]
*CF_F[t,f,"WT"]+a3_G["PV"]*G_F["PV",f]*CF_F[t,f,"PV"])
+sum{t in 1..T,w in Warehouse}(a3_G["WT"]*G_W["WT",w]
*CF_W[t,w,"WT"]+a3_G["PV"]*G_W["PV",w]*CF_W[t,w,"PV"])
+sum{t in 1..T,s in Store}(a3_G["WT"]*G_S["WT",s]*
CF_S[t,s,"WT"]+a3_G["PV"]*G_S["PV",s]*CF_S[t,s,"PV"]);
var selling_income = sum{f in Factory,t in 1..T}CHP_trade_F[t,f]*Price_DA_F[t,f]
+ sum{w in Warehouse,t in 1..T}CHP_trade_W[t,w] *Price_DA_W[t,w]+
sum{s in Store,t in 1..T}CHP_trade_S[t,s]*Price_DA_S[t,s];

var cost_proding_F = sum{t in prod_period1, p in Prod_typ, f in Factory,w in
Warehouse}Prod_shipped_FW[t,p,f,w]*Making_cost_item[p];
var cost_shipping_FW = sum{t in prod_period1, p in Prod_typ, f in Factory,w in
Warehouse}Prod_shipped_FW[t,p,f,w]*shipping_cost[p]*dist_FW[f,w];
var cost_holding_W = sum{t in prod_period1, p in Prod_typ,w in
Warehouse}holding_cost[p]*inventory_W[t,p,w];
var cost_backorder_W =sum{t in prod_period1, p in Prod_typ,w in Warehouse, s in
Store} backorder_cost[p]*backorder_W[t,p,w,s];
var cost_shipping_WS = sum{t in prod_period1, p in Prod_typ,w in Warehouse, s in
Store}Prod_shipped_WS[t,p,w,s]*shipping_cost[p]*dist_WS[w,s];
minimize PSC-VPP cost:
cap_cost_Gens+cap_cost_ESS+(OM_cost_G+OM_cost_ESS+OM_cost_CHP)-
CC_income - selling_income + cost_proding_F + cost_shipping_FW + cost_holding_W
+cost_backorder_W +cost_shipping_WS ;

subject to 1_inventory_balance{ p in Prod_typ,w in Warehouse, j in 1..J }:
sum{f in Factory}Prod_shipped_FW[j,p,f,w] + inventory_W[j-1,p,w] -
inventory_W[j,p,w] +sum{s in Store}(backorder_W[j,p,w,s]-backorder_W[j-1,p,w,s]) =
sum{s in Store}shipped[j,p,w,s];

subject to 2_product_demand{j in 1..J, p in Prod_typ,s in Store}:
sum{w in Warehouse}shipped[j,p,w,s]
>=Prod_demand_mean[p,s]+1.2*Prod_demand_Std[p,s];
subject to 3_product_demand{j in 1..J, p in Prod_typ,s in Store}:
sum{w in Warehouse}shipped[j,p,w,s]- sum{w in Warehouse}backorder_W[j,p,w,s]
+ sum{w in Warehouse}backorder_W[j-1,p,w,s] = sum{w in
Warehouse}Prod_shipped_WS[j,p,w,s];

subject to 3_resource{r in Prod_res, j in 1..J, f in Factory}:
sum{w in Warehouse,p in Prod_typ}Prod_shipped_FW[j,p,f,w]*Prod_need_res[p,r]
<= Available_res[j,f,r];
subject to 4_inv_inventory{p in Prod_typ,w in Warehouse}:

```

$inventory\_W[0, p, w] = 0;$   
subject to 4\_end\_inventory{p in Prod\_typ,w in Warehouse}:  
 $inventory\_W[J, p, w] = 0;$   
subject to 5\_inv\_backorder{p in Prod\_typ,w in Warehouse,s in Store}:  
 $backorder\_W[0, p, w, s] = 0;$   
subject to 5\_end\_backorder{p in Prod\_typ,w in Warehouse,s in Store}:  
 $backorder\_W[J, p, w, s] = 0;$   
subject to 6\_energy\_balance\_factory{f in Factory, t in 1..T}:  
 $sum\{g in Gens\}(G\_F["WT",f]*CF\_F[t,f,"WT"]+G\_F["PV",f]*CF\_F[t,f,"PV"])$   
 $+ESS\_E\_F[t,f]-ESS\_E\_F[t-1,f]+CHP\_T\_F[t,f]/2$   
 $= 0.0058*Prod\_transport\_FW\_hourly[t,f]+E\_demand\_F[f]+CHP\_trade\_F[t,f];$   
subject to 7\_energy\_balance\_warehouse{w in Warehouse, t in 1..T}:  
 $sum\{g in Gens\}(G\_W["WT",w]*CF\_W[t,w,"WT"]+G\_W["PV",w]*$   
 $CF\_W[t,w,"PV"])+ESS\_E\_W[t,w]-ESS\_E\_W[t-1,w]+CHP\_T\_W[t,w]/2$   
 $= 0.0058*transport\_E\_WF\_hourly[t,w]+E\_demand\_W[w]+CHP\_trade\_W[t,w];$   
subject to 8\_energy\_balance\_Store{s in Store, t in 1..T}:  
 $sum\{g in Gens\}(G\_S["WT",s]*CF\_S[t,s,"WT"]+G\_S["PV",s]*CF\_S[t,s,"PV"])$   
 $+ESS\_E\_S[t,s]-ESS\_E\_S[t-1,s]+CHP\_T\_S[t,s]/2$   
 $= 0.0058*transport\_E\_SW\_hourly[t,s]+E\_demand\_S[s]+CHP\_trade\_S[t,s];$   
subject to 9\_thermal\_balance\_factory{f in Factory, t in 1..T}:  
 $ESS\_T\_F[t,f]-ESS\_T\_F[t-1,f]+CHP\_T\_F[t,f]>=T\_demand\_F[f];$   
subject to 10\_thermal\_balance\_warehouse{w in Warehouse, t in 1..T}:  
 $ESS\_T\_W[t,w]-ESS\_T\_W[t-1,w]+CHP\_T\_W[t,w]>=T\_demand\_W[w];$   
subject to 11\_thermal\_balance\_Store{s in Store, t in 1..T}:  
 $ESS\_T\_S[t,s]-ESS\_T\_S[t-1,s]+CHP\_T\_S[t,s]>=T\_demand\_S[s];$   
subject to ESS\_Max\_electricity\_Factory{t in steps, f in Factory}:  
 $ESS\_E\_F[t,f]<=ESS\_F[f];$   
subject to ESS\_Max\_electricity\_Warehouse{t in steps, w in Warehouse}:  
 $ESS\_E\_W[t,w]<=ESS\_W[w];$   
subject to ESS\_Max\_electricity\_store{t in steps, s in Store}:  
 $ESS\_E\_S[t,s]<=ESS\_S[s];$   
subject to initial\_state\_f{f in Factory}:  
 $ESS\_E\_F[0,f]=0;$   
subject to initial\_state\_w{w in Warehouse}:  
 $ESS\_E\_W[0,w]=0;$   
subject to initial\_state\_s{s in Store}:  
 $ESS\_E\_S[0,s]=0;$   
subject to initial\_state\_T\_f{f in Factory}:  
 $ESS\_T\_F[0,f]=0;$   
subject to initial\_state\_T\_w{w in Warehouse}:  
 $ESS\_T\_W[0,w]=0;$   
subject to initial\_state\_T\_F{s in Store}:  
 $ESS\_T\_S[0,s]=0;$

Appendix E. Available Labor and Machine Hours for 2F-1W-2S Network for Chapter 6

Table E: Resource Data for 2F-1W-2S Network (Note: F1=Factory 1, F2=Factory 2)

Week	Labor		Machine		Week	Labor		Machine	
	F1	F2	F1	F2		F1	F2	F1	F2
1	17871	19412	122693	150577	27	17567	19081	122998	150953
2	23963	26028	161238	197883	28	27251	29599	185471	227623
3	15531	16870	105179	129084	29	15008	16302	104506	128257
4	23810	25862	164141	201447	30	24055	26129	164533	201928
5	17020	18487	115050	141198	31	17082	18554	116094	142480
6	25516	27715	178157	218648	32	24361	26462	166074	203818
7	15806	17167	109757	134701	33	14922	16208	105226	129142
8	24907	27054	172894	212188	34	25848	28076	177572	217930
9	16817	18266	115034	141178	35	17068	18539	117494	144198
10	25744	27963	177118	217372	36	21218	23047	147419	180923
11	15654	17004	105661	129674	37	14681	15946	99626	122268
12	24750	26883	173807	213307	38	19834	21544	137372	168593
13	17130	18607	115341	141554	39	15590	16934	106354	130525
14	26236	28498	177504	217847	40	23474	25497	164676	202102
15	15336	16657	105793	129836	41	16581	18011	114349	140338
16	26527	28814	182681	224199	42	22794	24759	157022	192708
17	15736	17093	106150	130276	43	16545	17971	113408	139182
18	23364	25378	160770	197309	44	22714	24673	158422	194427
19	17637	15964	120826	148288	45	15986	17364	109791	134743
20	26231	28492	178312	218837	46	23443	25465	161554	198270
21	18956	20590	128436	157626	47	17212	18696	117720	144474
22	27107	29443	187268	229829	48	21403	23247	149436	183400
23	13394	14549	94626	116132	49	17975	19524	119144	146222
24	24284	26377	163848	201087	50	23839	25895	165547	203171
25	14600	15859	101396	124441	51	18728	16952	128554	157771
26	21334	23173	144616	177482	52	22326	24251	151885	186404

## REFERENCES

- Alkholidi, A. G (2013). Renewable energy solution for electrical power sector in Yemen. *International Journal of Renewable Energy Research (IJRER)*, vol.3, no.4, pp. 803-811.
- Amellas, Y., El Bakkali, O., Djebli, A., Echchelh, A. (2020). Short-term wind speed prediction based on MLP and NARX networks models. *Indonesian Journal of Electrical Engineering and Computer Science*, vol.18, no.1, pp. 150-157.
- Azzouzi, M., Popescu, D., Bouchahdane, M. (2016). Modeling of electrical characteristics of photovoltaic cell considering single-diode model. *Journal of Clean Energy Technologies*, vol.4, no.6, pp. 414-20.
- Bae, S., Kim, H., Lee, Y., Xu, X., Park, J. S., Zheng, Y., Kim, Y. J. (2010). Roll-to-roll production of 30-inch graphene films for transparent electrodes. *Nature nanotechnology*, vol. 5, no. 8, pp. 574-578.
- Bahramirad, S., Reder, W., Khodaei, A. (2012). Reliability-constrained optimal sizing of energy storage system in a microgrid. *IEEE Transactions on Smart Grid*, vol.3, no.4, pp. 2056-2062.
- Barbounis, T. G., Theocharis, J. B., Alexiadis, M. C., Dokopoulos, P. S. (2006). Long-term wind speed and power forecasting using local recurrent neural network models. *IEEE Transactions on Energy Conversion*, vol.21, no.1, pp. 273-284.
- Berger, M. A. (2012). *An introduction to probability and stochastic processes*. Springer Science & Business Media.
- Bhandari, V., Rose, S., Wilson, E. J. (2019). Non-financial barriers to combined heat and power in the United States-a qualitative study. *The Electricity Journal*, vol.32, no.3, pp. 49-56.
- Box, G., Jenkins, G., (1970). *Time Series Analysis: Forecasting and Control*. Holden Day: San Francisco, CA, USA.
- Box, G. E., Jenkins, G. M., Reinsel, G. C., Ljung, G. M. (2015). *Time Series Analysis: Forecasting and Control*. John Wiley & Sons.
- Cadenas, E., Rivera, W. (2010). Wind speed forecasting in three different regions of Mexico using a hybrid ARIMA-ANN model. *Renewable Energy*, vol.35, no.12, pp. 2732-2738.
- Carnegie, R., Gotham, D., Nderitu, D., Preckel, P. V. (2013). *Utility Scale Energy Storage Systems: Benefits, Applications, and Technologies*. State Utility Forecasting Group. Tech. Rep.

- Carvalho, D., Rocha, A., Gómez-Gesteira, M. Santos, C., (2012). A sensitivity study of the WRF model in wind simulation for an area of high wind energy. *Environmental Modelling & Software*, 33, 23-34.
- Charlier, J. C., Blase, X., Roche, S. (2007). Electronic and Transport Properties of Nanotubes. *Reviews of modern physics*, vol.79, no.2, pp. 677.
- Chen, H., Cong, T.N., Yang, W., Tan, C., Li, Y., Ding, Y. (2009). Progress in electrical energy storage system: A Critical Review. *Progress in Natural Science*, vol. 19, no. 3, pp. 291–312.
- Chen, S. X., Gooi, H. B., Wang, M. (2012). Sizing of energy storage for microgrids. *IEEE Transactions on Smart Grid*, vol.3, no.1, pp. 142-151.
- Chen, W., Gui, D., Yu, S., Liu, C., Zhao, L., Liu, J. (2016). Preparation of nickel oxide/graphene aerogel composites and its electrochemical performance for supercapacitor. In proceeding of 17th IEEE International Conference on Electronic Packaging Technology (ICEPT), pp. 249-252.
- Chen, Y., Du, L., Yang, P., Sun, P., Yu, X., Mai, W. (2015). Significantly enhanced robustness and electrochemical performance of flexible carbon nanotube-based supercapacitors by electrodepositing polypyrrole. *Journal of Power Sources*, vol.287, pp. 68-74.
- Cochrane, J. H. (2005). Time series for macroeconomics and finance. Manuscript, University of Chicago, pp. 1-136.
- Costa, A., Crespo, A., Navarro, J., Lizcano, G., Madsen, H., Feitosa, E., (2008). A review on the young history of the wind power short-term prediction. *Renewable and Sustainable Energy Reviews*, 12(6), 1725-1744.
- Cote, L. J., Cruz-Silva, R., Huang, J. (2009). Flash reduction and patterning of graphite oxide and its polymer composite. *Journal of the American Chemical Society*, vol.131, no.31, pp. 11027-11032.
- Croonenbroeck, C., Stadtmann, G. (2019). Renewable generation forecast studies—Review and good practice guidance. *Renewable and Sustainable Energy Reviews*, vol.108, pp. 312-322.
- Cui, H. T., Zhou, O., Stoner, B. R. (2000). Deposition of aligned bamboo-like carbon nanotubes via microwave plasma enhanced chemical vapor deposition. *Journal of Applied Physics*, vol.88, no.10, pp. 6072-6074.
- Damousis, I. G., Alexiadis, M. C., Theocharis, J. B., Dokopoulos, P. S. (2004). A fuzzy model for wind speed prediction and power generation in wind parks using spatial correlation, *IEEE Transactions on Energy Conversion*, vol. 19, no. 2, pp.352-361.

- Datta, T. K. (2017). Effect of green technology investment on a production-inventory system with carbon tax. *Advances in operations research*, 2017.
- Development of Energy (DOE) Global Energy Storage Database. (2017). Available at <https://www.energystorageexchange.org/>, (access on Sep 2018).
- Dong, N., Chang, J. F., Wu, A. G., Gao, Z. K. (2020). A novel convolutional neural network framework based solar irradiance prediction method. *International Journal of Electrical Power & Energy Systems*, vol.114, pp. 105411.
- Dougal, R. A., Liu, S., & White, R. E. (2002). Power and life extension of battery-ultracapacitor hybrids. *IEEE Transactions on Components and Packaging Technologies*, vol.25, no.1, pp.120-131.
- Duarte, J. L. R., Fan, N., Jin, T. (2020). Multi-process production scheduling with variable renewable integration and demand response. *European Journal of Operational Research*, vol.281, no.1, pp. 186-200.
- Dunn, B., Kamath, H., Tarascon, J. M. (2011). Electrical energy storage for the grid: a Battery of Choices. *Science*, vol.334, no.6058, pp. 928-935.
- Dürkop, T., Getty, S. A., Cobas, E., Fuhrer, M. S. (2004). Extraordinary mobility in semiconducting carbon nanotubes. *Nano letters*, vol.4, no.1, pp. 35-39.
- Fang, S., Chiang, H. D., (2016). Improving supervised wind power forecasting models using extended numerical weather variables and unlabelled data. *IET Renewable Power Generation*, 10(10), 1616-1624.
- Fattahi, M., Mosadegh, H., Hasani, A. (2018). Sustainable planning in mining supply chains with renewable energy integration: A real-life case study. *Resources Policy*.
- Fu, R., Feldman, D., Margolis, R., Woodhouse, M., Ardani, K. (2018) The U.S. Solar Photovoltaic System Cost Benchmark: Q1 2017. National Renewable Energy Laboratory Report. Available at <https://www.nrel.gov/docs/fy17osti/68925.pdf>, (accessed on September 4, 2020).
- Fu, R., Remo, T., Margolis, R. (2018) The 2018 U.S. Utility-scale Photovoltaics-Plus-Energy Storage System Costs Benchmark. National Renewable Energy Laboratory Report. Available at <https://www.nrel.gov/docs/fy19osti/71714.pdf>, (accessed in September 4, 2019).
- Gao, M., Li, J., Hong, F., Long, D. (2019). Day-ahead power forecasting in a large-scale photovoltaic plant based on weather classification using LSTM. *Energy*, vol.187, pp. 115838.

- Geim, A. K. (2011). Nobel Lecture: Random walk to graphene. *Reviews of Modern Physics*, vol.83, no.3, pp. 851.
- Glavin, M. E., Chan, P. K., Armstrong, S., Hurley, W. G. (2008). A stand-alone photovoltaic supercapacitor battery hybrid energy storage system. In proceeding of IEEE Power Electronics and Motion Control Conference, pp. 1688-1695.
- Global Wind Energy Council. Global wind statistics (2019). Available at: [www.gwec.net/wpcontent/uploads/vip/GWEC\\_PRstats2018\\_EN\\_WEB.pdf](http://www.gwec.net/wpcontent/uploads/vip/GWEC_PRstats2018_EN_WEB.pdf). (access on Step 2018).
- Golari, M., Fan, N., Jin, T. (2017) Multistage stochastic optimization for production-inventory planning with intermittent renewable energy. *Production and Operations Management*, vol. 26, no. 3, pp. 409-425.
- González, A., Riba, J. R., Rius, A., Puig, R. (2015). Optimal sizing of a hybrid grid-connected photovoltaic and wind power system. *Applied Energy*, vol.154, pp. 752-762.
- Guyon, I., Elisseeff, A. (2003). An introduction to variable and feature selection. *Journal of machine learning research*, vol.3, pp. 1157-1182.
- Hadjipaschalis, I., Poullikkas, A., Efthimiou, V. (2009). Overview of current and future energy storage technologies for electric power applications. *Renewable and sustainable energy reviews*, vol.13, pp. 1513-1522.
- Hajiaghahi, S., Salemnia, A., Hamzeh, M. (2019). Hybrid energy storage system for microgrids applications: A review. *Journal of Energy Storage*, vol.21, pp. 543-570.
- Hanaei, H., Assadi, M. K., Saidur, R. (2016). Highly efficient antireflective and self-cleaning coatings that incorporate carbon nanotubes (CNTs) into solar cells: A review. *Renewable and Sustainable Energy Reviews*, vol.59, pp. 620-635.
- Hart, D., Sarkissian, A. (2016). Deployment of grid-scale batteries in the united states. unpublished case study prepared for DOE Office of Energy Policy and Strategic Analysis, Washington, DC.
- Hasani, A., Mokhtari, H., Fattahi, M. (2020). A multi-objective optimization approach for green and resilient supply chain network design: a real-life Case Study. *Journal of Cleaner Production*, vol.278, pp. 123199.
- Hesse, H. C., Schimpe, M., Kucevic, D., Jossen, A. (2017). Lithium-Ion Battery Storage for the Grid: A Review of Stationary Battery Storage System Tailored for Applications in Modern Power Grids. *Energies*, vol.10. no.12.

- Hipel, K. W., McLeod, A. I. (1994). Time series modelling of water resources. Available at: <http://www.energystorageexchange.org>, (accessed on Dec 2017).
- Huang, S., Manikandan, G. J., Ramachandran, A., Rupnow, K., Hwu, W. M. W., & Chen, D. (2017, February). Hardware acceleration of the pair-HMM algorithm for DNA variant calling. In Proceedings of the 2017 ACM/SIGDA International Symposium on Field-Programmable Gate Arrays (pp. 275-284).
- Ilinka, A., McCarthy, E., Chaumel, J.L., Retiveau, J.L. (2003). Wind potential assessment of Quebec Province. *Renewable Energy*, vol.28, no.12, pp. 1881-1897.
- IEA (2020). *Renewables 2020*. International Energy Agency. Available at: <https://www.iea.org/reports/renewables-2020>, (accessed on Nov 5, 2020).
- Jangamshetti, S. H., Rau, V. G. (2001). Normalized power curves as a tool for identification of optimum wind turbine generator parameters. *IEEE Transactions on Energy Conversion*, 16(3), 283-288.
- Jin, T., Pham, A., Novoa, C., Temponi, C. (2017). A zero-carbon supply chain model: minimising levelised cost of onsite renewable generation. In *Supply Chain Forum: An International Journal* (Vol. 18, No. 2, pp. 49-59). Taylor & Francis.
- Jing, W., Lai, C. H., Wong, S. H. W., Wong, M. L. D. (2016). Battery-supercapacitor hybrid energy storage system in standalone DC microgrids. *IET Renewable Power Generation*, vol.11, no.4, pp. 461- 469.
- Ju, L., Tan, Z., Yuan, J., Tan, Q., Li, H., Dong, F. (2016). A bi-level stochastic scheduling optimization model for a virtual power plant connected to a wind–photovoltaic–energy storage system considering the uncertainty and demand response. *Applied energy*, vol.171, pp. 184-199.
- Justus, C. G., Hargraves, W. R., Mikhail, A., Graber, D., (1978). Methods for estimating wind speed frequency distributions. *Journal of Applied Meteorology*, 17(3), 350-353.
- Kamadinata, J. O., Ken, T. L., Suwa, T. (2019). Sky image-based solar irradiance prediction methodologies using artificial neural networks. *Renewable Energy*, vol.134, pp. 837-845.
- Kamruzzaman, J., Begg, R., Sarker, R. (2006). *Artificial neural networks in finance and manufacturing*. IGI Global.
- Kavasserri, R. G., Seetharaman, K., (2009). Day-ahead wind speed forecasting using f-ARIMA models. *Renewable Energy*, 34(5), 1388-1393.

- Khashei, M., Bijari, M., (2010). An artificial neural network (p, d, q) model for timeseries forecasting. *Expert Systems with Applications*, 37(1), 479-489.
- Khiatani, D., Ghose, U. (2017). Weather forecasting using hidden Markov model. In proceeding of 2017 International Conference on Computing and Communication Technologies for Smart Nation (IC3TSN), pp. 220-225.
- Kline, D. M., Zhang, G. P. (2004). Methods for multi-step time series forecasting with neural networks. *Neural Networks in Business Forecasting*, pp. 226-250.
- Koeler, B, CIO Weather Channel, Data Structure for Representation of Big Data of Weather Forecasting. Available at <http://www.nasdaq.com/article/big-datadelivers-fewer-hunchesmore-facts-toweather-channel-20130211-00763>, (accessed on Dec 20, 2017).
- Kok, T., Grob, C., Laumanns, M., Minner, S., Rambau, J., Schade, K. (2018) A typology and literature review on stochastic multi-echelon inventory models. *European Journal of Operational Research*, vol. 269, no. 3, pp. 955-983.
- Kuha, J. (2004). AIC and BIC: Comparisons of assumptions and performance. *Sociological methods & research*, 33(2), 188-229.
- Kuznia, L., Zeng, B., Centeno, G., Miao, Z. (2013). Stochastic optimization for powersystem configuration with renewable energy in remote areas. *Annals of Operations Research*, vol.210, no.1, pp. 411-432.
- Lee, H., Cho, M. S., Kim, I. H., Do Nam, J., Lee, Y. (2010). RuOx/polypyrrolenanocomposite electrode for electrochemical capacitors. *Synthetic Metals*, vol.160, no.9-10, pp. 1055-1059.
- Lee, T. Y., Chen, N. (1995). Determination of optimal contract capacities and optimal sizes of battery energy storage systems for time-of-use rates industrial customers. *IEEE Transactions on Energy Conversion*, vol.10, no.3, pp. 562-568.
- Lei, M., Shiyan, L., Chuanwen, J., Hongling, L., Yan, Z. (2009). A review on the forecasting of wind speed and generated power. *Renewable and Sustainable Energy Reviews*, vol.13, no.4, pp. 915-920.
- Li, B., Tian, Y., Chen, F., Jin, T. (2017). Toward net-zero carbon manufacturing operations: an onsite renewables solution. *Journal of the Operational Research Society*, vol.68, no.3, pp. 308-321.
- Li, J. J., Ma, Y. W., Jiang, X., Feng, X. M., Fan, Q. L., Huang, W. (2012). Graphene/carbon nanotube films prepared by solution casting for electrochemical energy storage. *IEEE Transactions on Nanotechnology*, vol.11, no.1, pp. 3-7.

- Li, S., Wunsch, D. C., O'Hair, E. A., Giesselmann, M. G., (2001). Using neural networks to estimate wind turbine power generation. *IEEE Transactions on Energy Conversion*, 16(3), 276-282.
- Li, X., Wen, J., Malkawi, A. (2016). An operation optimization and decision framework for a building cluster with distributed energy systems. *Applied Energy*, vol.178, pp. 98-109.
- Lin, J.-Y., Zhou, S. X., Gao, F. (2019). Production and technology choice under emissions regulation: Centralized vs decentralized supply chains, *IIEE Transactions*, vol.51, no.1, pp. 57-73.
- Liu, C., Gui, D., Liu, J. (2014). Preparation of MnO<sub>2</sub>/graphene nanocomposite for the application of supercapacitor. In proceeding of 15th IEEE International Conference on Electronic Packaging Technology (ICEPT), pp. 177-182.
- Liu, J., Galpaya, D., Notarianni, M., Yan, C., Motta, N. (2013). Graphene-based thin film SC with rGO as dielectric spacer. *Applied Physics Letters*, vol.103, no.6, pp. 063108.
- Liu, H., Tian, H. Q., Li, Y. F., (2012). Comparison of two new ARIMA-ANN and ARIMA-Kalman hybrid methods for wind speed prediction. *Applied Energy*, 98, 415-424.
- Luo, X., Wang, J., Dooner, M., Clarke, J. (2015). Overview of current development in electrical energy storage technologies and the application potential in power system operation. *Applied Energy*, vol.137, pp. 511-536.
- Mabel, M. C., Fernandez, E., (2008). Analysis of wind power generation and prediction using ANN: A case study. *Renewable Energy*, 33(5), 986-992.
- McAllister, M. J., Li, J. L., Adamson, D. H., Schniepp, H. C., Abdala, A. A., Liu, J., Aksay, I. A. (2007). Single sheet functionalized graphene by oxidation and thermal expansion of graphite. *Chemistry of materials*, vol.19, no.18, pp. 4396-4404.
- Mohammadi, M., Hosseinian, S. H., Gharehpetian, G. B. (2012). Optimization of hybrid solar energy sources/wind turbine systems integrated to utility grids as microgrid (MG) under pool/bilateral/hybrid electricity market using PSO. *Solar energy*, vol.86, no.1, pp. 112-125.
- Mohandes, M. A., Halawani, T. O., Rehman, S. Hussain, A. A., (2004). Support vector machines for wind speed prediction. *Renewable Energy*, 29(6), 939-947.

- Moon J-Y., Park J (2014). Smart production scheduling with time dependent and machine-dependent electricity cost by considering distributed energy resources and energy storage. *International Journal of Production Research*, vol.52, no.13, pp. 3922–3939.
- Mula, J., Poler, R., Garca-Sabater, J. P., Lario, F. C. (2006) Models for production planning under uncertainty: A review. *International Journal of Production Economics*, vol. 103, no. 1, pp. 271-285.
- Navaeefard, A., Tafreshi, S.M.M., Barzegari, M., Shahrood, A.J. (2010). Optimal sizing of distributed energy resources in microgrid considering wind energy uncertainty with respect to reliability. In *Proceedings of IEEE Conference on Energy*, pp. 820–825.
- Naval, N., Sánchez, R., Yusta, J. M. (2020). A virtual power plant optimal dispatch model with large and small-scale distributed renewable generation. *Renewable Energy*, vol.151, pp. 57-69.
- Neto, A. C., Guinea, F., Peres, N. M., Novoselov, K. S., & Geim, A. K. (2009). The electronic properties of graphene. *Reviews of modern physics*, vol.81, no.1, pp. 109.
- Notton, G., Voyant, C., Fouilloy, A., Duchaud, J. L., & Nivet, M. L. (2019). Some applications of ANN to solar radiation estimation and forecasting for energy applications. *Applied Sciences*, 9(1), 209.
- Palaz, D., Magimai-Doss, M., & Collobert, R. (2019). End-to-end acoustic modeling using convolutional neural networks for HMM-based automatic speech recognition. *Speech Communication*, 108, 15-32.
- Peng, H., Liu, F., Yang, X., (2013). A hybrid strategy of short-term wind power prediction. *Renewable Energy*, 50, 590-595.
- Pham, A., Jin, T., Novoa, C., Qin, J. (2019). A multi-site production and microgrid planning model for net-zero energy operations. *International Journal of Production Economics*, vol. 218, pp. 260-274.
- Pho, K. H., Ly, S., Ly, S., Lukusa, T. M. (2019). Comparison among Akaike information criterion, Bayesian information criterion and Vuong's test in model selection: A case study of violated speed regulation in Taiwan. *Journal of Advanced Engineering and Computation*, 3(1), 293-303
- Powers, J. G., Klemp, J. B., Skamarock, W. C., Davis, C. A., Dudhia, J., Gill, D. O., Coen, J. L., Gochis, D. J., Ahmadov, R., Peckham, S. E., Grell, G. A., (2017). The weather research and forecasting model: Overview, system efforts, and future directions. *Bulletin of the American Meteorological Society*, 98(8), 1717-1737.

- Provost, F., & Kohavi, R. (1998). Glossary of terms. *Journal of Machine Learning*, 30(2-3), 271-274.
- Ralon, P., Taylor, M., Ilas, A., Diaz-Bone, H., Kairies, K. (2017). Electricity storage and renewables: Costs and markets to 2030. International Renewable Energy Agency: Abu Dhabi, UAE.
- Rao, C. N. R., Sood, A. K. (Eds.). (2013). *Graphene: synthesis, properties, and phenomena*. John Wiley & Sons.
- Reina, A., Jia, X., Ho, J., Nezich, D., Son, H., Bulovic, V., Kong, J. (2009). Large area, few-layer graphene films on arbitrary substrates by chemical vapor deposition. *Nano letters*, vol.9, no.1, pp. 30-35.
- Ren, Y., Suganthan, P. N., Srikanth, N. (2014). A comparative study of empirical mode decomposition-based short-term wind speed forecasting methods. *IEEE Transactions on Sustainable Energy*, 6(1), 236-244.
- Roy, A., Bruce, A., MacGill, I. (2016). The potential value of peer-to-peer energy trading in the Australian national electricity market. In *Asia-Pacific solar research conference*.
- Ruangpattana, S., Klabjan, D., Arinez, J., Biller, S. (2011). Optimization of on-site renewable energy generation for industrial sites. In *Proceedings of 2011 IEEE Power Systems Conference and Exposition*, pp. 1-8.
- Sanders, L., Lopez, S., Guzman, G., Jimenez, J., Jin, T. (2012). Simulation of a green wafer fab featuring solar photovoltaic technology and storage system. In *Proceedings of 2012 IEEE Winter Simulation Conference (WSC)*, pp. 1-12.
- Sanjari, M. J., & Gooi, H. B. (2016). Probabilistic forecast of PV power generation based on higher order Markov chain. *IEEE Transactions on Power Systems*, 32(4), 2942-2952.
- Schmidt, O., Hawkes, A., Gambhir, A., Staffell, I. (2017). The future cost of electrical energy storage based on experience rates. *Nature Energy*, vol.2, no.8, pp. 17110.
- Seguro, J. V., Lambert, T. W., (2000). Modern estimation of the parameters of the Weibull wind speed distribution for wind energy analysis. *Journal of Wind Engineering and Industrial Aerodynamics*, 85(1), 75-84.
- Senjyu, T., Yona, A., Urasaki, N., Funabashi, T. (2006). Application of recurrent neural network to long-term-ahead generating power forecasting for wind power generator. In *Proceedings of 2006 IEEE Power Systems Conference and Exposition*, pp. 1260-1265.

- Shah, K. K., Mundada, A. S., Pearce, J. M. (2015). Performance of US hybrid distributed energy systems: Solar photovoltaic, battery and combined heat and power. *Energy Conversion and Management*, vol.105, pp. 71-80.
- Shi, J., Lee, W. J., Liu, Y., Yang, Y., Wang, P. (2012). Forecasting power output of photovoltaic systems based on weather classification and support vector machines. *IEEE Transactions on Industry Applications*, vol.48, no.3, pp. 1064-1069.
- Stehly, T., Beiter, P., Heimiller, D., Scott, G. (2018). The 2017 Cost of Wind Energy Review. National Renewable Energy Laboratory Report. Available at <https://www.nrel.gov/docs/fy18osti/72167.pdf>, (accessed on September 10, 2019).
- Sullivan, L. R., Liu-Sullivan, N. Y. (2019). *Historical Dictionary of the Chinese Environment*. Rowman Littlefield.
- Supply chain dive (2019). Nike opens new distribution center running on 100% renewable energy. Retrieved from: <https://www.supplychaindive.com/news/nike-distribution-center-100-renewable-energy/563497/> (accessed on Feb 4, 2020).
- Taboada, H., Xiong, Z., Jin, T., Jimenez, J. (2012). Exploring a solar photovoltaic-based energy solution for green manufacturing industry. In *Proceedings of 2012 IEEE International Conference on Automation Science and Engineering (CASE)*, pp. 40-45
- U.S. Energy Information Administration (2020). Available at <https://www.eia.gov/naturalgas>, (accessed on September 4, 2020).
- U.S. Energy Information Administration (2016), Annual Electric Generator Report.. Available at <https://www.eia.gov/todayinenergy>, (accessed on Dec 4, 2019).
- U.S. Energy Information Administration (2017). Updated Capital Cost Estimates for Electricity Generation Plants. Available at <https://www.eia.gov/analysis/studies/powerplants/>, (accessed on September 29, 2017).
- Ubnoske, S. M., Raut, A. S., Parker, C. B., Glass, J. T., Stoner, B. R. (2015). Role of nanocrystalline domain size on the electrochemical double-layer capacitance of high edge density carbon nanostructures. *MRS Communications*, vol.5, no.02, pp. 285-290.
- Vafaei, M., Kazerani, M. (2011). Optimal unit-sizing of a wind-hydrogen-diesel microgrid system for a remote community. in *Proceedings of IEEE Power Tech Conference, Trondheim* (pp. 1-7).
- Van der Hoeven, M. (2013). *World energy outlook 2012*. International Energy Agency: Tokyo, Japan.

- Villarreal, S., Jimenez, J. A., Jin, T., Cabrera-Rios, M. (2013). Designing a sustainable and distributed generation system for semiconductor wafer fabs. *IEEE Transactions on Automation Science and Engineering*, vol.10, no.1, pp. 16-26.
- Viterbi, A. (1967). Error bounds for convolutional codes and an asymptotically optimum decoding algorithm. *IEEE transactions on Information Theory*, vol.13, no.2, pp. 260-269.
- Waldemarsson, M., Lidestam, H., Rudberg, M. (2013). Including energy in supply chain planning at a pulp company. *Applied energy*, vol.112, pp. 1056-1065.
- Wang, H. Z., Li, G. Q., Wang, G. B., Peng, J. C., Jiang, H., Liu, Y. T. (2017). Deep learning based ensemble approach for probabilistic wind power forecasting. *Applied energy*, vol.188, pp. 56-70.
- Wang, Y., Ai, X., Tan, Z., Yan, L., Liu, S. (2015). Interactive dispatch modes and bidding strategy of multiple virtual power plants based on demand response and game theory. *IEEE Transactions on Smart Grid*, vol.7, no.1, pp. 510-519.
- Wang, Z. R., Du, J., Wang, J. M. (2020). Writer-aware CNN for parsimonious HMM-based offline handwritten Chinese text recognition. *Pattern Recognition*, vol.100, pp. 107102.
- Warner, J. H., Schaffel, F., Rummeli, M., Bachmatiuk, A. (2012). *Graphene: Fundamentals and emergent applications*. Newnes.
- Weather Underground Databases. <https://www.wunderground.com/> (accessed on September 29, 2017)
- Wu, Y.K., Hong, J.S., (2007). A literature review of wind forecasting technology in the world. In *Proceedings of 2007 IEEE Lausanne Power Tech*, pp. 504-509.
- Xia, J., Chen, F., Li, J., Tao, N. (2009). Measurement of the quantum capacitance of graphene. *Nature nanotechnology*, vol.4, no.8, pp. 505-509.
- Yamchi, H. B., Shahsavari, H., Kalantari, N. T., Safari, A., Farrokhifar, M. (2019). A cost-efficient application of different battery energy storage technologies in microgrids considering load uncertainty. *Journal of Energy Storage*, vol.22, pp. 17-26.
- Yang, H. T., Huang, C. M., Huang, Y. C., Pai, Y. S. (2014). A weather-based hybrid method for 1-day ahead hourly forecasting of PV power output. *IEEE transactions on sustainable energy*, vol.5, no.3, pp. 917-926.

- Zhang, C., Wei, H., Zhao, J., Liu, T., Zhu, T., Zhang, K., (2016). Short-term wind speed forecasting using empirical mode decomposition and feature selection. *Renewable Energy*, 96, 727-737.
- Zhang, G., Patuwo, B. E., Hu, M. Y. (1998). Forecasting with artificial neural networks: The state of the art. *International journal of forecasting*, vol.14, no.1, pp. 35-62.
- Zhang, G., Ren, L., Deng, L., Wang, J., Kang, L., Liu, Z. H. (2014). Graphene–MnO<sub>2</sub> nanocomposite for high-performance asymmetrical electrochemical capacitor. *Materials Research Bulletin*, vol.49, pp. 577-583.
- Zhang, G., Tang, X., Qi, Z. (2010). Research on battery supercapacitor hybrid storage and its application in microgrid, in *Proceeding of Power and Energy Engineering Conference (APPEEC), Asia-Pacific* (pp. 1-4).
- Zhang, H., Cai, J., Fang, K., Zhao, F., Sutherland, J. W. (2017). Operational optimization of a grid-connected factory with onsite photovoltaic and battery storage systems. *Applied Energy*, vol.205, pp. 1538-1547.
- Zhou, H., Bhattacharya, T., Tran, D., Siew, T. S. T., Khambadkone, A. M. (2011). Composite energy storage system involving battery and ultracapacitor with dynamic energy management in microgrid applications. *IEEE Transactions on Power Electronics*, vol.26, no.3, pp. 923-930.
- Zhou, Q., Wang, C., Zhang, G. (2019). Hybrid forecasting system based on an optimal model selection strategy for different wind speed forecasting problems. *Applied Energy*, vol.250, pp. 1559-1580.
- Zhu, Y., Murali, S., Cai, W., Li, X., Suk, J. W., Potts, J. R., Ruoff, R. S. (2010). Graphene and graphene oxide: synthesis, properties, and applications. *Advanced materials*, vol.22, no.35, pp. 3906-3924.
- Zidan, A., Gabbar, H. A., Eldessouky, A. (2015). Optimal planning of combined heat and power systems within microgrids. *Energy*, vol.93, pp. 235-244.
- Ziel, F., Croonenbroeck, C., Ambach, D. (2016). Forecasting wind power—modeling periodic and non-linear effects under conditional heteroscedasticity. *Applied Energy*, vol.177, pp. 285-297.